



HAL
open science

Aspects microstructuraux de l'oxydation d'alliages de Zirconium

Christian Proff

► **To cite this version:**

Christian Proff. Aspects microstructuraux de l'oxydation d'alliages de Zirconium. Autre. Université de Grenoble, 2011. Français. NNT : 2011GRENI027 . tel-00609232

HAL Id: tel-00609232

<https://theses.hal.science/tel-00609232v1>

Submitted on 18 Jul 2011

HAL is a multi-disciplinary open access archive for the deposit and dissemination of scientific research documents, whether they are published or not. The documents may come from teaching and research institutions in France or abroad, or from public or private research centers.

L'archive ouverte pluridisciplinaire **HAL**, est destinée au dépôt et à la diffusion de documents scientifiques de niveau recherche, publiés ou non, émanant des établissements d'enseignement et de recherche français ou étrangers, des laboratoires publics ou privés.

THÈSE

Pour obtenir le grade de

DOCTEUR DE L'UNIVERSITÉ DE GRENOBLE

Spécialité : **Matériaux, Mécanique, Génie civil, Electrochimie**

Arrêté ministériel : 7 août 2006

Présentée par

Christian PROFF

Thèse dirigée par **Clément LEMAIGNAN** et
codirigée par **Sousan ABOLHASSANI**

préparée au sein du **Laboratory for Nuclear Materials**
Paul-Scherrer-Institut,
5232 Villigen, Suisse

dans l'École Doctorale I-MEP2

Aspects microstructuraux de l'oxydation d'alliages de zirconium

Thèse soutenue publiquement le **06.05.2011**,
devant le jury composé de :

Dr. Pierre BARBERIS

HDR, CEZUS UGINE, Rapporteur

Prof. Arthur MOTTA

Professeur Penn State University, Rapporteur

Dr. Didier GILBON

Directeur Laboratoire Matériaux, Président

Dr. Sousan ABOLHASSANI

Directeur Zr Laboratoire Matériaux PSI, Membre

Prof. Clément LEMAIGNAN

Professeur, INPG Dir. Recherche CEA, Membre



Abstract

This thesis is focused on the microstructural characterisation of precipitates in the oxide of binary zirconium alloys (1 wt.% Fe, Cr or Ni or 0.6 wt.% Nb) under different oxidation conditions at 415°C. The samples were oxidised in autoclave in air and steam and in an environmental scanning electron microscope in water vapour.

The microstructural evolution of the precipitates during oxidation was characterised using electron microscopy.

The findings from the analysis are the following:

- Two types of oxidation behaviour are observed for precipitates.
- Pilling-Bedworth ratio of precipitates is higher than that of the zirconium matrix.
- Formation of pure iron oxide crystals on the surface for iron bearing precipitates close to or at the surface.

From these observations it is concluded that the precipitate oxidation behaviour can be correlated to precipitate composition and oxidation tendency of the elements in the precipitates. Iron exhibits clearly different behaviour.

Keywords: binary zirconium alloys, precipitates, corrosion, oxide, TEM, microstructure

An electronic version of the thesis can be found on the following server:

<http://tel.archives-ouvertes.fr> (please give title and author name to find the thesis)

dedicated to my beloved parents and Sonja

Acknowledgements

First I would like to thank Dr. M.M. Dadras from CSEM in Neuchâtel, and M. Leboeouf, who made the in situ oxidation experiments possible and taught me the use of AFM and the in situ heating stage and were there when I needed help with my experiments. Also thank you very much for the support and your contribution (in particular that of Dr. V. Spassov) for performing the bulge tests, which turned out to be more time consuming than expected.

I would like to thank very much the financial contribution from *swissnuclear* for the project which was a constant support for this thesis.

It was an honour to work with my supervisor Dr. Sousan Abolhassani, who guided me through the world of electron microscopy and zirconium alloy corrosion and shared with me her knowledge in this field. I appreciated the high degree of freedom I enjoyed, allowing me to perform all the interesting experiments that I wanted to. Her patience with me when things went not as they should was endless, as well as her support, scientific as personal.

I would like to thank Prof. Clément Lemaignan for accepting to supervise this project, many stimulating discussions, his external view on the work that helped to see the broader context and his valuable feedback during the write-up of the thesis.

The contribution from Dr. Pierre Barberis from CEZUS is acknowledged, who provided the material for this study and accepted to be part of the PhD jury.

Dr. VenkatRao Mallipudi was a great help with his expert ANSYS knowledge, indispensable for the creation of the macro for evaluating precipitate influence on the stresses in the oxide scale.

Dr. Manuel Pouchon I would like to thank for all his assistance with nanoindentation.

I am indebted to E. Minikus, who was a great help with minor and major issues concerning the TEM operation and the sample preparation laboratory. J. Krbanjevic is thanked for the time she spent teaching me the use of the FIB/SEM and preparing my first TEM specimens. Thanks also to the other helpful persons in the microscopy lab, who helped to quickly solve problems. It was a pleasure to work with Röbi, who was always ready to provide assistance to the autoclave experiments, training of our Master student Bhadri and with computer issues. The same should be said about other people from the Hotlab, Andrej Bullemer, Agathe Waelchli and Marcus Keller, who provided support in technical issues.

I would also express my gratitude to my roommates Paul, Sebastiano, Hygreeva, VenkatRao and Cyprian for the nice atmosphere in our office and the valuable help with all kinds of problems and my friends from the lunch group, Iza, Per, Cedric, Maria, Dorota, Christian and Tatjana, for the nice atmosphere and distraction, which was helpful to see things from a different perspective.

Dr. Johannes Bertsch, Dr. Stephane Valance and Dr. Cedric Cozzo are thanked for their help with the translation of parts of this thesis into French.

This would not have been possible without the support and love from my family and Sonja, who had to accept me being distracted by things completely foreign to them.

Table of content

Abstract.....	1
Acknowledgements	4
Table of content.....	5
Abbreviations	9
1 Introduction	11
2 Literature	13
2.1 Development of zirconium alloys for nuclear applications	13
2.2 Microstructure of zirconium alloys	15
2.2.1 Heat treatment	15
2.2.2 Secondary phase particles	17
2.3 Oxidation of zirconium and its alloys	19
2.3.1 Testing conditions in water and steam	20
2.3.2 Testing conditions in air	21
2.3.3 Corrosion kinetics	21
2.3.4 Matrix oxidation.....	23
2.3.5 Precipitate oxidation.....	28
2.4 Zirconium oxide and its properties.....	31
2.4.1 Mechanical aspects of the oxidation of zirconium alloys	33
2.4.2 Mechanical properties of zirconia	34
2.5 Open questions concerning corrosion of (binary) zirconium alloys	36
3 Materials and methods	37
3.1 Materials.....	37
3.1.1 Binary alloys	37
3.1.2 Pure zirconium, Zircaloy-2 and Zircaloy-4.....	38
3.1.3 Overview of available samples	38
3.2 Oxidation experiments	39
3.2.1 In situ oxidation campaigns.....	39
3.2.2 Autoclave oxidation	41
3.2.3 Furnace oxidation in air.....	42
3.3 Sample preparation.....	43
3.3.1 Sample cutting and surface polishing.....	43
3.3.2 Mechanical preparation of transverse sections.....	43
3.3.3 In situ oxidation experiment samples.....	43
3.3.4 Electropolished TEM samples	43
3.3.5 Focused ion beam.....	44
3.3.6 Preparation of freestanding oxide membranes	47
3.4 Characterisation methods	49
3.4.1 Atomic force microscopy	49
3.4.2 Scanning electron microscopy	49
3.4.3 Environmental scanning electron microscopy	49

3.4.4	Transmission electron microscopy	50
3.4.5	Energy dispersive x-ray spectroscopy	51
3.4.6	Microhardness	51
3.4.7	Nanoindentation	52
3.4.8	Bulge test.....	52
4	Characterisation of as received material and oxidation experiments.....	55
4.1	Characterisation of precipitates in as received material.....	55
4.1.1	Precipitate size.....	55
4.1.2	Precipitate composition	57
4.2	Oxidation experiments	59
4.2.1	In situ oxidation in ESEM.....	59
4.2.2	Autoclave oxidation	60
4.2.3	Furnace oxidation in air.....	60
5	Microstructure of in situ oxidised alloys.....	61
5.1	In situ oxidation at 415°C.....	61
5.1.1	Zr1%Fe.....	61
5.1.2	Zr1%Ni with diamond finish.....	67
5.1.3	Zr1%Ni with Vibratory polisher finish	72
5.1.4	Zr1%Cr – as received.....	75
5.1.5	Zr1%Cr – annealed 48 hours at 730°C.....	78
5.1.6	Zr0.6%Nb.....	81
5.1.7	Pure zirconium	83
5.2	Summary of in situ oxidation results at 415°C	85
6	Microstructure of alloys oxidised in autoclave	89
6.1	Oxidation for 3 days in air at ambient pressure	89
6.1.1	Zr1%Fe.....	89
6.1.2	Zr1%Ni.....	91
6.1.3	Zr1%Cr.....	93
6.1.4	Zr0.6%Nb oxidised for 55 days in air	93
6.1.5	Pure zirconium	95
6.2	Oxidation for 3 days in steam at ambient pressure	96
6.2.1	Zr1%Fe.....	96
6.2.2	Zr1%Ni.....	100
6.2.3	Pure zirconium	101
6.3	Oxidation for 110 days in steam at 10.5 MPa.....	103
6.3.1	Zr1%Fe.....	103
6.3.2	Zr1%Ni.....	107
6.3.3	Zr1%Cr.....	109
6.3.4	Zr0.6%Nb (for 40 days)	111
6.4	Oxygen diffusion zone in the metal as a function of the oxidation time	113
7	Comparison of oxidation behaviour of binary alloys.....	117
8	Other selected oxidations	121

8.1	Other selected oxidation conditions of the binary alloys	121
8.1.1	Furnace oxidation for 1 hour in air.....	121
8.1.2	Furnace oxidation for 24 hours in air	123
8.2	Autoclave oxidation of Zircalloys in steam at 415°C	124
8.2.1	Zr ₂ (Fe,Ni) precipitates.....	124
8.2.2	Zr(Fe,Cr) ₂ precipitates.....	125
8.2.3	Comparison of binary zirconium alloys and Zircalloys	126
9	Mechanical properties of zirconia layers formed on binary alloys	127
10	Discussion	129
10.1	Introduction	129
10.2	Influence of surface preparation on results	129
10.3	Quantitative EDS measurements.....	130
10.3.1	Precipitate-matrix geometries in TEM specimens	130
10.3.2	Influence of precipitate-sample geometry in TEM on obtained results	132
10.3.3	Quantitative EDS results	133
10.4	Change of surface topography during oxidation	136
10.4.1	Protrusions on the surface	136
10.4.2	Pilling-Bedworth ratio of intermetallics.....	136
10.4.3	Cases modelled with ANSYS	138
10.5	Influence of oxidation conditions on precipitate oxidation.....	140
10.5.1	Influence of pressure	140
10.5.2	Influence of temperature	141
10.6	Precipitate oxidation behaviour.....	142
10.6.1	Precipitate oxidation behaviour in the oxide of binary alloys.....	142
10.6.2	Precipitate oxidation behaviour in the oxide of commercial alloys	143
10.6.3	Cracks on precipitates exhibiting delayed oxidation.....	144
10.6.4	Possible parameters affecting precipitate oxidation behaviour.....	148
10.7	Precipitate oxidation at the surface	155
10.8	Iron oxide formation at the surface	156
10.9	Iron migration to the surface	159
11	Conclusions	163
12	Outlook.....	165
13	References	167
14	Appendix I – Estimation of precipitate oxygen content for small precipitates	183
15	Appendix II – In situ experiments at 700°C.....	185
16	Appendix III – Mechanical properties of oxide on binary alloys	187
17	Appendix IV – Modelling of oxide with different precipitate oxidation	189
18	Résumé de thèse en français.....	193
18.1	Résumé	193
18.2	Introduction	194
18.3	Littérature	195
18.4	Matériaux et Méthodes.....	195

18.4.1	Matériaux	195
18.4.2	Expériences d'oxydation	197
18.5	Méthodes de caractérisation	197
18.5.1	Préparation d'échantillons.....	198
18.6	Caractérisation du matériau original et expériences d'oxydation	198
18.6.1	Caractérisation des précipités dans le matériau original	198
18.6.2	Résultats des expériences d'oxydation supplémentaires.....	198
18.7	Microstructure d'alliages oxydés in-situ	198
18.7.1	Oxydation in situ à 415°C	200
18.8	Microstructure des alliages oxydés en autoclave	202
18.8.1	Oxydation pendant 3 jours dans l'air à la pression ambiante.....	202
18.8.2	Oxydation sous vapeur pendant 3 jours à pression ambiante.....	204
18.8.3	Oxydation sous vapeur à 10.5 MPa pendant 110 jours	208
18.8.4	Comparaison du comportement du fer sous différentes conditions d'oxydation.....	210
18.8.5	Comparaison des différents alliages binaires et de leur conditions d'oxydation.....	210
18.9	Autres conditions d'oxydation choisies	212
18.9.1	Autres conditions d'oxydation pour les alliages binaires.....	212
18.9.2	Oxydation des Zircaloy en autoclave sous vapeur à 415°C.....	212
18.10	Discussion	212
18.10.1	Influence de la préparation de la surface sur les résultats	212
18.10.2	Mesures EDS quantitatives	212
18.10.3	Changement de la topographie de surface Durant l'oxydation	213
18.10.4	Influence des conditions d'oxydation sur l'oxydation de précipité	214
18.10.5	Le comportement des précipités à l'oxydation	214
18.10.6	Oxydation des précipités à la surface	216
18.10.7	Formation d'oxyde de fer à la surface.....	216
18.10.8	Migration de fer vers la surface.....	218
18.11	Conclusions	219
18.12	Perspectives.....	222

Abbreviations

AES	Auger electron spectroscopy
AFM	atomic force microscopy
ASTM	American Society for Testing and Materials
BF	bright field contrast
BSE	backscattered electrons
BWR	boiling water reactor
CANDU	CANada Deuterium Uranium
DF	dark field contrast
EDS	energy dispersive x-ray spectroscopy
EELS	electron energy loss spectroscopy
ESEM	environmental scanning electron microscope
FIB	focused ion beam microscopy
GSE	gaseous secondary electron (detector)
IAEA	International Atomic Energy Agency
LEED	low energy electron diffraction
P-B ratio	Pilling-Bedworth ratio
PWR	pressurised water reactor
SE	secondary electrons
SEM	scanning electron microscopy
SIMS	secondary ion mass spectrometry
SOCAP	second order cumulative annealing parameter
SPP	secondary phase particle
TEM	transmission electron microscopy
TEP	thermoelectric power
XPS	x-ray photoelectron spectroscopy
XRD	x-ray diffraction
Zry-2	Zircaloy-2
Zry-4	Zircaloy-4

1 Introduction

Zirconium alloys are used in nuclear power plants for example as fuel cladding. This type of alloys had been chosen because they exhibit among other important properties a low thermal neutron absorption cross section and a high corrosion resistance in water and steam at elevated temperatures and pressures. As unalloyed zirconium does not meet the requirements, alloying elements are added, of which some are soluble in the zirconium matrix at the added level and others are practically insoluble and therefore form precipitates.

The precipitates in zirconium alloys are either intermetallics formed by the alloying elements with zirconium or an alloying element phase with zirconium in solid solution. These precipitates have been shown to be correlated to the corrosion resistance of zirconium alloys. In the typical precipitates of zirconium alloys, one alloying element can be replaced to a certain extent by another alloying element, so that the precipitate composition is dependent on alloy composition and production parameters. The $Zr_2(Fe,Ni)$ and $Zr(Fe,Cr)_2$ precipitates in the so called Zircaloy are typical examples.

The precipitate oxidation behaviour in commercial zirconium alloys is phenomenologically known, however, the understanding of the precipitate oxidation behaviour is still limited and the influence of different alloying elements is not fundamentally understood. Due to the importance of the precipitates for the corrosion resistance of the zirconium alloys, it is of interest to understand the behaviour of the precipitates during the oxidation process and their influence on the oxidation behaviour of the whole alloy.

In the complex commercial zirconium alloys the interference of the alloying elements with each other will mask the behaviour of single alloying elements; the extent of this interference was not known till present due to the absence of data for single alloying element precipitates. Therefore binary zirconium alloys were chosen to be able to study the behaviour of a specific alloying element during oxidation in different oxidation environments without interference of other alloying elements. The oxidised binary alloys were characterised at the microstructural level with respect to the alloying element behaviour in the different oxidation environments, as the information is not available so far.

An overview of the known facts in the field of zirconium alloys and their oxidation is provided in the literature part of the thesis. In the next part the investigated material and the experimental approach are described. The experimental results are presented ordered by the different oxidation environments studied. The discussion part is divided into the evaluation of the limitations of the experimental results and the consequences of the results with respect to the understanding of precipitate oxidation. The conclusions summarise the used experimental approach and the most important findings of this work.

2 Literature

This chapter will give an introduction to the relevant literature available for this work on the oxidation of binary zirconium alloys and their precipitates. As mentioned before, the focus of this work is on the precipitate oxidation in the binary zirconium alloys and the impact of the precipitate oxidation on the oxide formed on the binary alloys. To outline the relevance of precipitate oxidation to the overall behaviour of zirconium alloys, first an introduction to the development of zirconium alloys for nuclear applications is provided and then processing parameters with significance to corrosion are presented. The different types of corrosion testing applied to zirconium alloys are reviewed with respect to their conditions and scope of their application. The description of the kinetics of oxidation of zirconium alloys is presented with respect to the oxidation of the zirconium matrix at the different stages of oxidation. The precipitate oxidation in zirconium alloys is reviewed with respect to the commercial alloys and binary alloys presented in the literature, with special focus on the reported microstructural results wherever available. The mechanical aspects which are connected to the oxidation of zirconium alloys and the formation of zirconia are addressed. The properties determined for bulk zirconia and zirconia films are compared for different preparation procedures and compositions in order to evaluate the variation in mechanical properties encountered for different types of zirconia.

At the end of this chapter open questions concerning the influence of precipitates on the formed oxide layer are addressed, which will be dealt with in this work.

2.1 Development of zirconium alloys for nuclear applications

The materials used in light and heavy water nuclear reactors as structural materials and fuel cladding have to meet several requirements: good corrosion resistance, adequate mechanical strength, high thermal conductivity and a low neutron capture cross-section for thermal neutrons. None of the conventional construction materials satisfied all these requirements and finally zirconium was chosen, as it has a low neutron capture cross-section, the mechanical properties fulfil the requirements and the fabrication costs are within tolerable limits. However, the corrosion properties of zirconium in high temperature water and steam were not sufficiently known at that time [1]. Therefore the corrosion resistance of pure zirconium and zirconium based alloys was investigated to find suitable alloys and improve the corrosion resistance. Some of these investigations focussed on the effect of different alloying elements, either by varying the concentration of one alloying element in tested alloys or by studying binary alloys containing the alloying element of interest.

Pure zirconium exhibits good high temperature corrosion properties in oxygen [2], however, it turned out to show much higher corrosion rates when tested in steam. Much effort was taken to identify and reduce the impurities, which were first believed to be the cause for the worse corrosion behaviour of pure zirconium in steam compared to oxygen. As arc-melting for purifying zirconium to sufficiently low levels of detrimental impurities is economically unfavourable to the Kroll-processed sponge zirconium, alloying was the first solution to increase the corrosion resistance [1]. The presence of elements such as Cr, Fe and

Ni was found to improve corrosion resistance of zirconium exposed to steam [3]. Additions of Sn and Nb were found to compensate for the accelerated corrosion caused by the impurity content of nitrogen [1], which was most difficult to remove at the time of the development of the first zirconium alloys for nuclear applications [3]. The zirconium alloys developed at that time in the USA were the so called Zircalloys, of which Zircaloy-2 (Zry-2) and Zircaloy-4 (Zry-4) are the ones which exhibited desired properties. They were developed in the 1950s with small additions of Cr, Fe, and in Zry-2 also Ni (see Table 1 for their specified composition range), in a matrix consisting of Zr, Sn and O, exhibiting good corrosion and creep resistance. The alloying elements Fe, Cr and Ni form intermetallic precipitates with Zr, owing to their low solubility in the α -Zr matrix, which are of $Zr(Fe,Cr)_2$ - and $Zr_2(Fe,Ni)$ -type [4].

Alloys containing Nb were developed in Canada (Zr-2.5Nb) and the Soviet Union (e.g. E110). More recent developments such as ZIRLO™, MDA (Mitsubishi developed alloy) and the HANA-alloys (high performance alloy for nuclear application) contain Sn, Nb and Fe [5] or Nb and Fe as M5™. Other elements being considered so far as alloying elements for zirconium alloys are V, Ta, Mo and Cu [6-9]. The question, which of the low solubility alloying elements forming precipitates in the Zircalloys (Fe, Cr and Ni), is most beneficial for corrosion inhibition, is still debated, as different groups found dissimilar beneficial orders for the elements in question e.g. [6, 10].

The optimal Sn-concentration in the Zircalloys was originally determined by the need to neutralize the nitrogen contained in zirconium processed at the time of their development. It is nowadays too high for optimal corrosion resistance of zirconium with low nitrogen impurity levels [11-14]. Therefore the Sn levels have been reduced within the Zry-2 and Zry-4 specifications, which already has consequences for the thermal creep resistance of the fuel cladding even though the changes are small [15]. For this reason the reduced thermal creep resistance has to be traded with respect to the reduced corrosion rate of lower tin contents at higher temperatures [1, 16].

Table 1: Compositions of some zirconium alloys with Zr in balance [1, 17-20]

Alloy	Sn / wt.%	Nb / wt.%	Fe / wt.%	Cr / wt.%	Ni / wt.%	O / wt.%
Zircaloy-2 (Zry-2) [1]	1.20 - 1.70		0.07 - 0.20	0.05 - 0.15	0.03 - 0.08	
Zircaloy-4 (Zry-4) [1]	1.20 - 1.70		0.18 - 0.24	0.07 - 0.13	< 70 ppm	0.09 - 0.13
Zircaloy-4 high tin [17]	1.5		0.2	0.1		0.09 - 0.16
Zircaloy-4 low tin [17]	1.3		0.2	0.1		0.11 - 0.16
ELS (extra low tin) [17]	0.8		0.2	0.1		
E110 [17]		0.9 - 1.1	0.014	<0.003		0.06
E125 [20]		2.5	0.015		0.007	0.05
Zr2.5%Nb [17]		2.5	<0.15			0.09 - 0.13
E635 [17]	1.10 - 1.40	0.9 - 1.1	0.30 - 0.50			0.05 - 0.07
ZIRLO™ [18]	0.9 - 1.2	0.9 - 1.13	0.1			0.09 - 0.13
optimised ZIRLO™ [17]	0.67	1	0.1	0.08		0.1
M5™ [18]		0.8 - 1.2	0.015 - 0.06			0.120
MDA [17]	0.8	0.5	0.2	0.1		
HANA-4 [19]	0.4	1.5	0.2	0.1		
HANA-5 [19]	0.8	0.4	0.35	0.15	Cu 0.1	

2.2 *Microstructure of zirconium alloys*

The microstructure of zirconium alloys consists of two features: the matrix and the precipitates, which are called secondary phase particles (SPP). The volume fraction of the precipitates depends mainly on their composition; a minor factor is their crystal structure. In the case of a binary zirconium alloy with 1 wt.% Fe, the precipitates account for ca. 5.6 vol% if all iron is assumed to be present in Zr_3Fe precipitates. For the other typical alloying elements the volume fraction is smaller, as their precipitates have higher alloying element to zirconium ratio than the Zr_3Fe precipitates.

The presence of precipitates is of importance for the good corrosion properties of the zirconium alloys, materials with all alloying elements in solution and not in precipitates (quenched material with supersaturated matrix) did show much worse oxidation resistance [21]. The size and distribution of the precipitates in the zirconium alloys, which depend on the heat treatment, determine for which corrosion conditions the alloys are best suited.

2.2.1 Heat treatment

The heat treatment of zirconium alloys is, beside the composition, the factor that determines the corrosion resistance. An example of the applied heat treatment is given for the Zircalloys, pointing out the various factors influencing the finished material.

The Zircalloys within their standardized composition ranges (Table 1) are manufactured following a standard processing route for the cladding tubes (see Figure 3 in [22]). This processing comprises a β -quench and subsequent pilgering and several annealing steps in the α -phase region, yielding a homogenous precipitate distribution [22].

The usual β -quenching rate for the fabrication of cladding tubes is lower than that required for complete suppression of precipitation. The subsequent heating of the quenched alloy in the α -phase will result in grain growth and growth of precipitates in the matrix. The heat treatment procedure during production has distinct consequences for the corrosion resistance for nodular and/or uniform corrosion, which are almost contrary in the required optimal heat treatment; the accumulated heat treatment for optimized nodular corrosion resistance is lower than the minimum accumulated heat treatment required for optimized uniform corrosion resistance (Figure 1). Small densely distributed precipitates as produced by a late β -quench are optimal for nodular and detrimental for uniform corrosion resistance (see p. 143-144 [20] and reference [23]). Nodular corrosion resistance is important for materials intended for application in boiling water reactors (BWR), while in pressurized water reactors (PWR) uniform corrosion resistance is of interest. These two different critical corrosion phenomena are a consequence of the different environments encountered in these two types of reactors.

As the uniform corrosion resistance is of interest in this project, the different aspects of this type of corrosion affected by the heat treatment will be presented. For optimized resistance to uniform corrosion a critical amount of heat treatment needs to be accumulated, which can be achieved by increased annealing time and temperature in the α -phase region (see p. 145 [20]). To assess the amount of accumulated heat treatment for optimal uniform corrosion resistance, several methods for comparing different production procedures have been developed. Common to the annealing parameters proposed is their description of mechanical properties

or the precipitate growth, which are correlated but not identical to the corrosion properties (see p. 144 [20]).

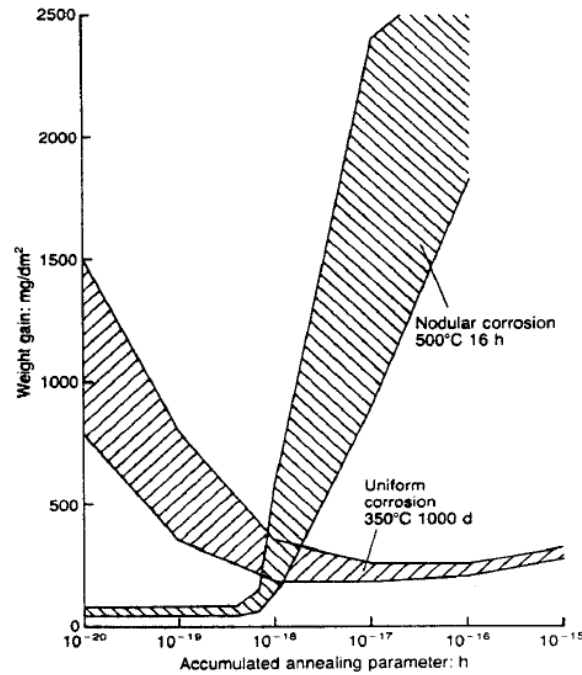


Figure 1: Influence of annealing parameter on resistance to nodular and to uniform corrosion at the given oxidation temperatures from [24].

After the last β -quench, which freezes the existing precipitate distribution, heat treatments are applied in the α -phase region, changing precipitate size and distribution. Two annealing parameters describing the precipitate evolution with the heat treatment are presented in the following. The so called cumulative annealing parameter A has been first introduced by Charquet et al. [25] and Weidinger et al. [26], where Q/R is 40000 K, in another work 31700 K [27] has also been suggested. A is defined as:

$$\sum A = \sum t_i e^{\frac{-Q}{RT_i}}$$

Equation 1: Q is the activation energy, t_i the time and T_i the temperature of the i^{th} heat treatment after the last β -quench [25].

The so called second order cumulative annealing parameter (SOCAP) has been proposed by Gros and Wadier [28], with a lower activation energy than for A, corresponding to slower growth kinetics than for the diffusion and interface transfer process. The effect of the heat treatment on the precipitate growth (Ostwald ripening) is compared by this parameter, which is also a possible parameter for the description of the corrosion resistance. The definition of SOCAP is given in Equation 2.

$$d^3 - d_0^3 = \left(\frac{K}{T^2} e^{\frac{-Q}{RT}} \right) \cdot t$$

Equation 2: Second order cumulative annealing parameter (SOCAP), in which d_0 stands for the initial precipitate diameter, d for the final precipitate diameter, K equals $1.11 \times 10^{-11} \text{ m}^3 \text{ s}^{-1} \text{ K}^2$ and Q/R equals 18700 K for standard Zry-4 and t is the annealing time in seconds [28].

Van Swam et al. [29] compared those two parameters for their efficiency to predict the corrosion resistance from the annealing parameter; for the material studied they could not establish a direct relationship between precipitate size and corrosion resistance. Their proposed corrosion parameter E' takes the burn-up of the cladding into account to allow comparison of materials having experienced a different burn-up [29]. Bradley et al. [14] concluded from an experimental study, that the assumptions for the validity of the cumulative annealing parameter, the order dependence of particular anneals and the equivalence of a long time and low-temperature anneal with a short time and high temperature anneal, do not hold for the experimental results obtained. A comparison of the cumulative annealing parameter to the precipitate size by Andersson and Thorvaldsson [27] showed the first to be more significant for good uniform corrosion resistance.

Due to the lack of strong correlation between heat treatment and resulting precipitate size to the corrosion resistance, the matrix concentration of the precipitate forming elements was investigated [30-35]. Even though the solubility of some of the alloying elements in the zirconium matrix is very low, there is a small but measureable amount remaining dissolved in the matrix. Materials exhibiting high alloying element content remaining in the matrix and Fe/Cr ratios below 1 were found to have a higher nodular corrosion resistance compared to materials with same composition but considerably lower matrix alloying element content [30]. For uniform corrosion resistance the optimal conditions are converse, with larger precipitates an Fe/Cr ratio above 2 and a matrix depleted in alloying element content being advantageous, however, the depletion in alloying elements should not exceed a certain level corresponding to an Fe/Cr ratio above 8 [31]. The alloying element investigated in more detail than the others was iron [32-35].

Also the relationship between beneficial changes in heat treatment and composition is quite complex. For a better uniform corrosion resistance of alloys containing Fe and Cr a higher Fe/Cr ratio for the $Zr(Fe,Cr)_2$ precipitates has been recommended by Strasser [31] and Charquet [12], which is achievable by changing the applied heat treatment between cold rolling steps. In the data presented by Strasser [31] it is not clear for some data sets, if the variation in Fe/Cr ratio is due to changes in the alloy composition or the heat treatment.

2.2.2 Secondary phase particles

Zirconium alloys contain precipitate forming elements such as Fe, Cr, Ni and Nb, which exhibit a low solubility in the Zr-matrix, and elements being present in solid solution such as tin and oxygen. For the alloying elements Fe, Cr and Ni, the presence in form of secondary phase particles (SPP) in zirconium alloys is well established [12, 36-42]. According to Charquet et al. [36] the solubility of these elements together is below 150 ppm at 800°C in the α -phase of the Zr1.4%Sn matrix. Consequently Fe, Cr and Ni are predominantly present in the precipitates with a precipitate composition and structure dependent on the alloy composition. In binary alloys these are Zr_3Fe precipitates for zirconium with small Fe additions, $ZrCr_2$ precipitates for zirconium with small Cr additions, Zr_2Ni precipitates for zirconium with small Ni additions, and in the commercial Zircalloys $Zr_2(Fe,Ni)$ in Zircaloy-2 and $Zr(Fe,Cr)_2$ in Zircaloy-2 and Zircaloy-4.

The influence of the production procedure on the alloying element ratio in the more complex precipitates has been addressed in 2.2.1.

To avoid precipitation of those elements inside the grains of α -Zr (bainite transition), a higher quenching rate than 1500 K/s is recommended from the β -phase [43], resulting in a microstructure with fine α -phase needles with a supersaturated α -matrix (martensite). The solubility of the alloying elements in β -phase is 6.75 at.% for Fe and 7.5 at.% for Cr [44]. A heat treatment at 600°C of such a β -quenched material will result in precipitation at the α -phase grain boundaries within a few minutes [34, 45]. The high interstitial diffusion rate is responsible for this fast precipitation of transition metals in α -Zr [46, 47]. For Zircalloys a matrix depleted in precipitate forming alloying elements was found, which corresponds to their low solubility and the results of diffusion measurements [32-35]. Niobium exhibits a higher solubility in the α -Zr matrix than Fe, Cr and Ni (around 0.6 wt.%) [48].

2.2.2.1 Commercial zirconium alloys

In the Zircalloys, which are the typical alloys containing Fe, Cr and Ni as alloying elements forming precipitates, two types of precipitates are generally found, $ZrCr_2$ -type precipitates with Laves phase structure with Fe substituting Cr atoms and $Zr_2(Fe,Ni)$ -type precipitates with Zintl-phase structure with Fe substituting Ni. The bulk composition and the final heat treatment of the alloys determine the Fe to Cr ratio in the precipitates, for standard Zircaloy-4 it is 2-1 [12, 49]. In Zircaloy-2 also a tetragonal $Zr_2(Fe,Ni)$ phase is also present [4].

The corrosion resistance of zirconium alloys containing precipitate is highly dependent on the distribution of the alloying elements mainly present in the precipitates [21], which is controlled by the heat treatment schemes during production. The matrix concentration in as-produced alloys is controlled by the solubility of the precipitate-forming elements in the matrix phase and the applied heat treatment. For example the solubility of Fe in an α -Zr matrix was measured by different techniques: Mössbauer spectroscopy by Stupel et al. [32] (0.04 and 0.2 wt.% Fe in Zr), atom probe by Wadman et al. [33] (Zircaloy-4) and thermoelectric power (TEP, 0.0036-0.0556 wt.% Fe in Zr and Zircaloy-4) by Borelly et al. [35], which all reported matrix concentrations of 150 wppm or less, depending on the temperature during the measurements. These solubility measurements yielded a solubility limit of 0.004 wt.% at 440°C [32] with Mössbauer spectroscopy and much lower solubility by TEP (5 ppm at 600°C in Figure 11a in [35]), who also claimed the data in [32] to be too high.

Loucif et al. [34] studied the precipitation behaviour of Fe in different zirconium alloys by TEP and concluded that the presence of tin and especially oxygen retard the precipitation process compared to pure zirconium.

Niobium also forms precipitates if added above the solubility limits, forming in binary Zr-Nb alloys either the metastable β -Zr phase containing 18-20 wt.% Nb at the grain boundaries, being held responsible for accelerated corrosion [50], or the β -Nb (80 wt.% Nb) phase, which is claimed to delay the oxidation process [51]. The solubility of Nb in the α -Zr matrix has been given by Lundin and Cox to be 0.6 wt.% in α -Zr [48]. The Nb content for optimal corrosion resistance seems to be determined by the solubility in the α -Zr matrix [52], which explains why alloys with Nb additions somewhat above this solubility limit are performing

quite well (e.g. E110, E635, ZIRLO™ and M5™ in Table 1). In a quaternary alloy (Zr-0.1-20wt% Nb with 1400 ppm O and 700 ppm Fe) Kim et al. [53] found a solubility limit of 0.2 wt.%Nb in the matrix and they suggested the Fe content of the quaternary alloy to be the cause for the reduced solubility compared to the solubility in the pure Zr matrix. Zr-Nb alloys containing also Fe as alloying element form $Zr(Fe,Nb)_2$ [54-56] and $(Zr,Nb)_2Fe$ precipitates [55, 56] beside the β -Nb precipitates.

Tin is unlike many other alloying elements dissolved in the α -matrix and has only rarely been shown to form precipitates (Zr_4Sn) [57-59]. The distribution of Sn in the matrix has been reported to vary strongly between different alloys of the Zircaloy family [60].

2.2.2.2 Binary zirconium alloys

In binary zirconium alloys with small additions of the alloying elements Fe, Cr and Ni, the following intermetallic compounds have been reported: Zr_2Fe [58, 59, 61, 62] (body centred tetragonal [63]) and Zr_3Fe [10, 61, 62, 64-66] (orthorhombic [63]), Zr_2Ni [10, 58, 59, 64] (tetragonal [10]) and $ZrCr_2$ [10, 59] (cubic). In the case of Zr-Ni and Zr-Cr only one precipitate type is observed for low alloying element contents. For the Zr-Fe system there are two possible precipitate types, of which according to Aubertin et al. [63] and Stein et al. [67] only Zr_3Fe should be stable at room temperature, as Zr_2Fe is a high temperature phase only stabilised by oxygen impurities down to room temperature [67]. The phase Zr_4Fe as given by [68] is claimed by Stein et al. [67] not to exist.

2.3 Oxidation of zirconium and its alloys

The oxidation of zirconium alloys proceeds by the diffusion of oxygen species to the metal-oxide interface, where the oxidation of the metal takes place [69]. In the water containing atmospheres the oxidation process produces also two hydrogen atoms per consumed oxygen atom ($Zr + 2 H_2O \rightarrow ZrO_2 + 4 H$), which can then form hydrides with zirconium, being detrimental for the long-term mechanical integrity of the cladding.

The oxidation of the zirconium alloys in reactor limits the time the fuel can be safely used, and therefore the burn-up achievable, as it reduces the thickness of the remaining cladding and, thus, the mechanical strength. The reduction of the fuel costs by increased average burn-up puts higher demands on the materials, due to the longer stay in the reactor. In addition for achieving higher thermal cycle efficiency, higher coolant temperatures could be desirable, which requires higher corrosion resistance, as at higher temperatures the oxidation kinetics accelerates.

Those requirements ask for reduced uniform corrosion and lower hydrogen uptake for the existing alloys and the development of new materials meeting those requirements. The corrosion of zirconium alloys has been studied now for more than 60 years, but still the knowledge about the underlying mechanism is to be regarded as not complete. There is no thorough understanding of the mechanism, since no direct mechanistical relationship between corrosion properties, alloy composition and alloy properties has been established yet. Several models have been proposed, both for zirconium alloy corrosion in water and steam [70-74], which will probably turn out to be parts of a phenomenological description of the underlying

mechanism. A general description of the problem has been given by Cox [75, 76] and several years ago in technical reviews by the IAEA [20, 77].

The corrosion problems encountered with zirconium alloys are dependent on a number of parameters, which can be connected either to the alloy or the type of power plant and sometimes both. Examples for alloy composition optimisation are the reduction of tin content in the Zircalloys to the lower limit of the specification to increase the corrosion resistance [78, 79] and the development of Zircaloy-4 to avoid the increased hydrogen uptake, which has been found for alloys containing nickel [1, 80], being therefore not added as alloying element in other commercial alloys than Zircaloy-2.

The type of corrosion attack limiting the cladding lifetime under normal operation is depending on the type of reactor. In boiling water reactors (BWR) localized corrosion attack on the cladding material in form of oxide nodules is a limiting factor, this type of attack is therefore called nodular corrosion. The nodule formation has been correlated in some studies to the presence of large precipitates or clusters of precipitates [70], in materials with small precipitates (<175 nm [70]) nodule formation is virtually absent, however a sound experimental proof of the nodule initiation sites is not available [20]. In a report by Cox [81] a plot showing the corrosion rate and hydrogen uptake in-reactor versus the hydrogen to oxygen ratio (H:O) is presented, indicating that below a H:O ratio of approximately 10 nodular corrosion is enhanced with respect to higher H:O ratios. For the pressurized water reactors (PWR) uniform corrosion attack was long time the lifetime limiting factor from the corrosion point of view. In this type of reactor Zircaloy-4 with no Ni additions and increased Fe and Cr content compared to Zircaloy-2 is used, as the high hydrogen pressure present would otherwise cause increased hydrogen uptake.

However, there are examples in the literature, reporting results contradicting the general findings mentioned above. For example Zircaloy-2 exhibited better corrosion properties than Zircaloy-4 with a similar hydrogen uptake in a PWR simulation environment [82].

2.3.1 Testing conditions in water and steam

The test of materials at reactor conditions requires testing for several years, being not practical for screening candidate alloys for nuclear applications. To simulate the long-term corrosion behaviour to be expected in the reactor, higher temperatures and higher pressures than encountered in the reactor are used in autoclave testing to compensate for the shorter exposure time in order to be able to compare different materials for in reactor corrosion results. The standard procedure for testing corrosion properties of Zirconium alloys in water and steam is ASTM G2 [83]. This test procedure recommends different testing conditions in autoclave for zirconium alloys to predict their in-reactor behaviour, being different for BWR and PWR environments. The long-term test conditions for PWRs are 350-370°C in water and 400-420°C in steam at 10 MPa and for BWRs 450-520°C at pressures above 6 MPa. The actual pressure and temperature in reactor are ca. 15 MPa and 284 to 294°C inlet temperature and 310 to 330°C outlet temperature for PWR and 7 MPa and 288°C outlet temperature for BWR [84] at a pH close to 7.

For Nb-containing alloys similar testing conditions have been applied [78], being not a standard listed in ASTM G2 [83]. Those testing parameters for zirconium alloys have been found empirically to best predict the in-reactor behaviour. Corrosion tests with lithiated water are conducted in some studies, as lithium used to control the coolant pH has been shown to have a detrimental effect on the corrosion resistance. It has been claimed to cause pore formation in the oxide layer [85].

The corrosion rate is commonly measured as weight gain and, for the usual procedure, the samples have to be taken out, weighed, and put back to the autoclave again in regular intervals (typically 14-30 days [22]), which results in thermal cycling of the samples each time the samples are taken out for measurements. Typical in-reactor conditions do not result in so many thermal cycles and more realistic testing would involve a temperature gradient over the tube wall, as existent over the tube wall from fuel pellets to cooling water. A hydrogen overpressure is suggested by Garde [86], to obtain an environment more similar to the PWRs.

The determination of the oxidation kinetics by weight gain is problematic for several reasons. The weight gain is only representative of the oxygen uptake of the sample if no spalling has occurred, which should be confirmed by inspection of the sample surface. The partition of the oxygen in the oxide and the subjacent metal should be known to be able to convert the weight gain into average oxide thickness, as with increasing temperature more oxygen is dissolved in the metal.

2.3.2 Testing conditions in air

Besides the standard ASTM G2 [83] test in water and steam, zirconium alloys have been also oxidised in air [10, 87-91]. These testing conditions are not used to evaluate the performance at normal operating conditions in reactor. The oxidation behaviour at those much higher temperatures than typical for reactors has been investigated to learn about the performance during loss of coolant accidents (LOCA) with air ingress [87-90]. The alloys investigated under such conditions were commercial alloys, as the tests are part of safety assurance tests. Depending on the study, the alloys have been pre-oxidised in steam before the exposure to air at high temperatures. Under such conditions the formation of zirconium nitride is a further factor influencing the formed oxide scale on zirconium alloys.

In more fundamental studies in oxygen at 750°C pure zirconium showed lower weight gains than binary zirconium alloys [91], except for the binary zirconium-copper alloy, performing similar to pure zirconium. Similar results were also obtained at 700°C [2]. Lower temperatures for oxidation tests are mainly used to separate the influence of hydrogen on the corrosion from the oxidising species present in the test environment.

2.3.3 Corrosion kinetics

The initial oxide formed on zirconium and its alloys is an adherent black oxide film growing with a cubic [2] or parabolic [92] rate equation, see Equation 3. This initially protective behaviour changes with oxidation time to an approximately linear behaviour ($n=1$), see also weight gain curves in Figure 2.

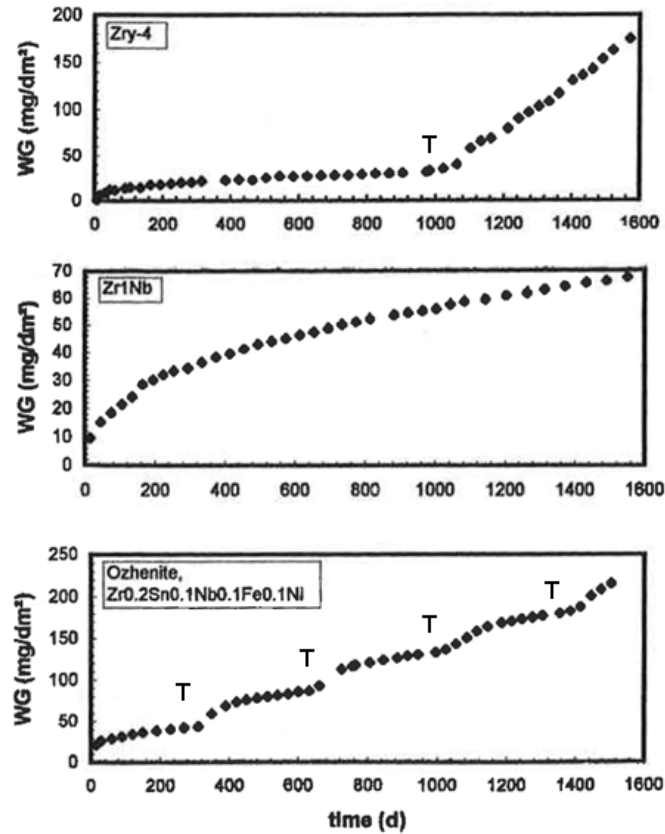


Figure 2: Corrosion kinetics encountered in zirconium alloys from Göhr et al. [93]. Kinetic transitions marked with T on weight gain curves of Zircaloy-4 and Ozhenit (these markings have been added in this thesis for clarification).

The two regimes in kinetics are termed pre-transition and post-transition. The critical thickness for the transition is reached with an oxide thickness exceeding 2-3 μm and a colour change from black to white, which is regarded as an indication for non-protective stoichiometric ZrO_2 [94].

$$\Delta w \propto t^{1/n}$$

Equation 3: With weight gain being Δw and t the oxidation t and the exponential factor n ranging from 3 to 2 for cubic to parabolic oxidation kinetics [95].

The average oxide thickness from weight gain data is usually calculated to be 15 mg/dm^2 for 1 μm of oxide, neglecting possible oxygen and hydrogen diffusion into the metal and sub-stoichiometry of the formed oxide as well as oxide spallation. The main corrosion product of zirconium alloys is zirconia, ZrO_2 , which is known to exist in seven crystallographic polymorphs [96, 97], of which the monoclinic, tetragonal and cubic have been reported for the oxide films [98].

Studies comparing the influence of the oxygen partial pressure on the oxidation kinetics of zirconium and its alloys found a small influence for the initial oxidation with lower oxygen pressures resulting in lower weight gains. This influence of oxygen partial pressure on oxidation kinetics increased with decreasing oxidation temperature from 700 $^\circ\text{C}$ [71] (small) over 500 $^\circ\text{C}$ [99] (higher) to 375 $^\circ\text{C}$ [92] (highest for reported studies).

For zirconium oxidation the oxide growth direction is inwards, as the mobile species has been shown to be oxygen in marker studies [69, 100] and diffusion experiments with oxygen

[101, 102]. The formation of the new oxide is therefore at the metal oxide interface (inwards), and not at the inner and the outer surface of the oxide, as for example on stainless steels, whose oxide grows inwards and outwards by cation and anion diffusion.

The oxygen taken up by zirconium is not fully converted into oxide, due to the high affinity of zirconium for oxygen and the ability to dissolve up to 30 at.% of oxygen in the α -matrix [103]. At high temperatures a considerable amount can be present in solution. To accommodate the oxygen in the lattice, the c-axis length increases over the whole concentration range, while the a-axis reaches its maximum length at $ZrO_{0.25}$ [104]. A diffusion zone is observed in the metal for high temperature oxidation in oxidizing environments with a diffusion rate being significant when compared to the advance of the metal-oxide interface above 300 °C [105]. As this dissolved oxygen leads to solution-hardening, micro-hardness testing can provide information about the diffusion zone [106-108]. The inward oxygen diffusion into zirconium is thought to be either interstitial lattice or grain boundary diffusion [109]. At temperatures lower than 700°C a decrease in oxygen diffusion rate was measured, grain boundary diffusion has been claimed to be the only mechanism active in this temperature range [110, 111]. The weight gain due to oxygen dissolution in the metal was measured to be 7.5% of the overall weight gain at 600°C, 17.5% at 750 °C [112] and 62% at 850°C [113], a similar increase is given on p. 37 in [20]. The oxidation of the metal could be therefore assumed to compete with the diffusion of oxygen into the metal, so that zirconium with a high corrosion rate will generally exhibit only a thin diffusion zone below the oxide scale [112]. The opposite has been shown to be valid for materials oxidised in reactor [114], for which the fastest corroding alloy also had the largest oxygen diffusion zone.

Zr_6O [107] and Zr_3O [107, 115, 116] (360°C up to 850°C) are compositions of ordered sub-oxides formed at the metal-oxide interface; oxygen concentrations exceeding those concentrations result in a partly ordered solution of Zr_3O_{1+y} , which will saturate at $ZrO_{0.44}$ [103] before the metal is converted to zirconia (for oxidation at room temperature).

2.3.4 Matrix oxidation

Zirconium and its alloys always form a thin protective layer when exposed to air at room temperature, preventing further oxidation under these conditions. However, at higher temperatures the oxidation proceeds and a thicker protective oxide is formed with cubic to parabolic kinetics until eventually the oxide becomes non-protective and the oxidation rate increases. The oxidation up to the first kinetic transition is called pre-transition stage and beyond this point post-transition. The oxide thickness before the first transition is in the range of 2-3 μm [117], depending mainly on the material. A barrier layer is reported at the metal-oxide interface, being dense and containing no cracks; however, the thickness and the structure of this layer are debated.

2.3.4.1 Low-temperature oxidation

The initial stage of the adsorption of oxygen on pure Zr has been studied in ultra high vacuum using Auger electron spectroscopy, LEED, XPS and SIMS [101-103, 105, 118-124]. It is generally agreed that oxygen dissolves first in zirconium at low oxygen partial pressures and high temperatures. The reaction of oxygen with zirconium is at high temperatures a

competition of oxygen adsorption on the surface and absorption with dissolution in the bulk. The absorption of oxygen was found to be hindered by adsorbed oxygen on the surface [125]. The oxide phase starts to nucleate, when a coverage of 0.6 to 1 monolayer is reached at room temperature ([101, 126]. The type of oxide growth studied on Zr(0001) surfaces was found to be temperature dependent, at 90 K a layer-by-layer growth was observed, at room temperature a mixture of layer-by-layer and island growth and at 200°C only island growth [105].

The thickness of oxide layers formed at room temperature in oxygen was found to be 1.6-2 nm [119, 122, 127]. The initial sub-stoichiometric oxide (ZrO_{2-x}) formed in air on all zirconium alloys is an adherent 2-3 nm thick black and protective oxide, being an efficient barrier against further oxidation in air at room temperature. The grain size of this microcrystalline film is in the range of the oxide layer thickness, and therefore it was previously thought to be at least partially amorphous [128]. XPS and soft x-ray absorption spectroscopy showed the presence of sub-oxide layers during initial oxidation of Zircaloy [129], which remained in the metal-oxide interface and transformed at some distance from the interface to ZrO_2 , while at 2 nm distance from the interface still some sub-oxide could be found.

2.3.4.2 Oxidation at pre-transition stage

The oxide thickness formed on zirconium saturated with oxygen increases with respect to non-saturated zirconium [103]. Sub-oxides reported by some authors are usually present close to the metal-oxide interface. Ordered layers of Zr_3O were shown to be present at low oxygen partial pressures [102, 119], which was also reported for the metal-oxide interface [107, 115] on test specimens under typical test conditions. The presence of sub-oxides could not be verified in all studies, for example Tanabe et al. [124] found no evidence of their presence using AES as Abolhassani et al. [130] with TEM.

At 450°C exposure to water the oxidation reaction had an “induction period” [129], during which the diffusion and dissolution in the metal were fast enough to delay further oxidation. During the pre-transition stage the interface remains quite even and smooth. The oxide thickness observed on the grains is lower than the one on the grain boundaries and sub-boundaries [131]. Among the first studies of cross-sections of the metal-oxide interface studied in TEM is the one by Urquart and Vermilyea [132] on Zircaloy-2 oxidized in oxygen at 600°C. A fine grained columnar structure was observed at some distance from the metal-oxide interface, being oriented parallel to the oxide growth direction. Motta et al. [8] calculated the kinetic rate exponent n for the initial protective stage for corrosion at 500°C in water and supercritical water for a series of alloys. It was in the range of $n = 2.3-2.8$ following the definition of n in Equation 3 for all but the Nb containing alloys (1.4-2.3) with faster oxidation kinetics (weight gain law was expressed as $A \cdot t^n$ in [8], so that their n corresponds to $1/n$ in Equation 3, so 0.25-0.36 and 0.43-0.71).

2.3.4.3 Transition of oxidation kinetics

The transition from a parabolic/cubic to a linear or cyclic oxidation behaviour was shown to be correlated to the formation of cracked layers in the oxide [133-136] and a variation of the thickness of the dense innermost oxide layer [135, 137]. A cyclic variation of the

tetragonal zirconia content [133] was observed in the oxide scale, which shows that beside cracks also the oxide structure is changing with proceeding oxidation and the transitions. The relationship between these observations of features in the oxide scale and the kinetic transition is so far not understood, as the cause and the consequence cannot be named for the made observations. So the relationship between the time to transition of different alloys and the spacing between the cracked layers is clearly observed [117, 133, 138].

2.3.4.4 Post-transition oxidation

After the change to the post-transition kinetics, no smooth metal-oxide interface can be observed any more. Post-transition oxides are usually composed of a layered structure, reflecting the cyclic weight gain behaviour in the post-transition regime [133-136]. The density of the formed oxide and the tetragonal content are among those parameters that have been shown to correlate to the layered structure, being already visible in optical micrographs. The average spacing of the layered structure is inversely proportional to the corrosion rate, indicating a beneficial effect of a delayed transition [133].

The influence of the oxidation environment on the microstructure of the formed oxide is illustrated by the difference in grain sizes for post-transition films reported for different water containing environments; in water-formed oxide films large oxide grains sizes of up to 100-500 nm were observed at the metal-oxide interface, while for oxides grown in steam the maximum grain size observed was 50 nm [139, 140]. Sabol et al. [139, 140] concluded from this an oxide growth initiated by many small nuclei having a preferential growth direction, in which the growth continues upon increasing film thickness. When a critical oxide grain size is reached, the film growth continues by re-nucleation of new oxide grains at the growth front at the metal oxide interface. From the different grain sizes observed for the different oxidation temperatures, it was assumed that lower temperatures favour continued grain growth, while higher temperatures do so for re-nucleation [140]. However, for oxidation of pure zirconium in air Lightstone and Pemsler [141] observed between 500-1000°C an increase of the oxide grain size for higher oxidation temperatures using XRD.

On new Nb-containing alloys studied by Wadman et al. [142], an intermediate sub-oxide could be found in some parts of the metal-oxide interface region, while in other regions it was comparable to the interface type observed on Zry-4. The microstructure of Zry-2.5wt.%Nb alloys, which are used in CANDU reactors, consist of elongated α -Zr grains with 1 at.% Nb and thin intermediate layers of β -Zr, containing 20 at.% Nb and segregations of impurities such as Fe. For the microstructure of the oxide formed on niobium containing alloys on α -Zr grains containing with Nb larger grains (40-60 nm) and a higher porosity were found than on β -Zr grains (15 nm) by several studies [143-145], while Elmoselhi [146] reported a Nb-rich oxide containing pores and no pores in the matrix oxide.

2.3.4.5 The barrier layer

A so called barrier layer concept has been proposed, as the protectiveness of the oxide is retained even though the oxide film degrades with progressing oxidation time. The problem that arises is, how to define the thickness of the barrier layer. Different investigations using SEM [147], impedance measurements [148-150] indicated the presence of a dense layer at the

metal-oxide interface. The thickness of this barrier layer is debated, as different measurements gave thicknesses from 10 nm [150] up to 2 μm [148], alike Cox [151] claimed from mercury intrusion measurements, that some pores extended right to the metal, so there would be no barrier layer at all. In general it is accepted, that there is a protective layer close to the metal-oxide interface restricting the access of the oxidising species to the interface e.g. [114].

However, it should be noted that transmission electron microscopy investigations of the metal-oxide interface of uniform oxide layers did not reveal a specific structure at the metal oxide interface being possible to relate to a barrier layer. There are reports of an amorphous oxide at the metal-oxide interface [149, 152], but this has been especially present on samples exhibiting accelerated corrosion [149]. For the Zircalloys a thinner barrier layer than for Zr2.5%Nb-alloys is expected [51, 144, 152], however except for the amorphous layer reported for Zr2.5%Nb [144], no other studies report such a layer at low uniform corrosion rates. Wadman et al. [142] reported for the oxide studied for pre-transition stage a uniform layer of 0.8 μm thickness and for post-transition a 150 nm thick layer without cracks and pores at the metal oxide interface. The tetragonal zirconia observed [72, 133, 153-158] has been suggested by Godlewski [157, 158] to form the barrier layer, as the tetragonal content is highest close to the metal-oxide interface. The tetragonal fraction was found to be highest close to the interface and decrease towards the outer surface [159].

2.3.4.6 Metal-oxide interface

The disparity between metal and oxide lattice parameters induces stresses in the interface, as the oxide is growing in compression and the metal is under tensile stress [159]. The undulated interface shape has been suggested to minimize the compressive stresses [160] in the interface, while the stress in the oxide close to the metal-oxide interface is also claimed to be a parameter stabilizing the tetragonal phase [158].

Different techniques are used to study the metal-oxide interface, fracturing the oxide and observing the different spalled layers [161] or the more frequently applied etching of the metal to be able to study the remaining oxide side of the interface in the SEM [131]. The study of the metal-oxide interface in TEM is a more recent technique due to the difficulties in sample preparation caused by the different properties of the phases at the interface.

The cauli-flower like metal-oxide interface shape observed for later stages of oxidation by Stehle et al. [147] seems to be a real feature and not an artefact, as TEM examinations of cross-sections also exhibit similar interface shapes e.g. [162]. Two different types of solutions have been reported in the literature for the removal of the metal to be able to study the metal-oxide interface. One type of solution contains hydrofluoric acid, as in the study of Stehle et al. [147] and others [131, 163] and the other bromine in methanol [163-165]. In the case of the bromine in methanol solution small needle like features were observed additionally to the general appearance observed after etching with the hydrofluoric acid solution. Cox [166] claimed that these needles [163-165] might be hydrides, as the bromine containing methanol solutions do not dissolve zirconium hydrides and therefore the small needles observed at the metal-oxide interface might well be hydrides [166]. Dissolution of zirconia at the metal-oxide interface and redeposition of oxide during stripping of the metal by preferential dissolution

was deemed not likely, in case fresh hydrofluoric acid containing solutions are applied for less than 15 minutes. Oskarsson et al. [163] also claimed after applying both types of solutions that the needles were dissolved (or not present) in the case of hydrofluoric acid containing etchants. The needles reported are usually not observed in TEM sections containing the metal-oxide interface which agrees with the finding of both Oskarsson et al. [163] and Cox [166] that these are artefacts from the etching process.

For thicker oxides ion-milling has been applied to study in-plane and cross-section samples of the oxide and the metal-oxide interface e.g. [132, 162]. Abolhassani et al. [162, 167] have been among the first applying the focused ion beam (FIB) technique to prepare cross-sections of oxides grown on zirconium alloys to investigating the metal-oxide interface. The interface shape is not analogous for different alloys, supporting a chemical influence of the alloying elements on the oxide properties, see scanning electron microscope investigations of Bossis et al. [168] and transmission electron microscope investigations of the metal oxide interface by Abolhassani et al. [162].

The presence of columnar oxide grains at the metal oxide interface was shown to be characteristic for uniform corrosion at low corrosion rates, while equiaxed oxide grains were associated with accelerated or nodular corrosion [142, 149]. The reason for the higher crack density in the latter might be that equiaxed oxide grain regions facilitate intergranular crack propagation with their interlinked grain boundary network, while a columnar grain structure provides more resistance. If the formation of equiaxed grains is a consequence of the accelerated corrosion or the cause is not yet resolved.

A recrystallised metal grain region exhibiting much smaller grain sizes than the 10 μm in the bulk metal was observed close to the metal-oxide interface by Urquart and Vermilyea [132] on Zircaloy-2 oxidized in oxygen at 600°C and Anada et al. [169] at 400°C in steam. This observation can be due to the high stresses at the metal-oxide interface.

Ding and Northwood [145] studied on Zr2.5wt.%Nb alloys the metal-oxide interface and could show stabilized tetragonal zirconia in the oxide scale, suggested to be stabilized by the small grain size, compressive stresses from the metal and dissolved Fe and Nb. On specimens of the oxide prepared by stripping from the metal the transformation of some tetragonal oxide to monoclinic oxide could be detected. From their observations they proposed a growth model, where the oxide is initially amorphous and transforms with decreasing stresses over a mosaic structure of crystallites to equiaxed tetragonal and finally to columnar monoclinic grains oriented in growth direction.

2.3.4.7 Microstructure of oxide films formed

The growth of all oxides in the different atmospheres at high temperatures (air, oxygen, water and steam) is dependent on the transport of oxygen through the oxide scale already formed. Under the oxide layer formed in air present on all alloys, a new crystallite layer [170] has to be formed. The oxide layer growth will proceed by nucleation of new oxide crystallites, changing to a more columnar growth during the pre-transition regime with grain sizes of 10-30 nm width and 50-200 nm length perpendicular to the metal-oxide interface [142]. These first oxide layers remain parallel sided and uniform, with a crystallographic oxide grain

orientation depending on the crystallographic orientation of the underlying metal grains [170-174]. The thickness of the formed oxide scale, i.e. the oxidation rate also depends on the orientation of the metal [170].

The orientation relationship between metal structure and formed oxide was investigated by Ploc [172-175] on surfaces of oxidized sheets and single crystals. The initial oxide formed was found to have a grain size of 5 nm with an orientation dependent on the orientation of the underlying Zr grains. Ploc found different possible oxide orientations for one metal orientation, however only for thin oxides an epitaxial growth was considered to be valid, while for thicker oxides the internal stresses seem to be most influential on the orientation.

Sabol et al. [139, 140] found in the transmission electron microscope the oxide grain size formed on Zry-4 in water at 360°C and steam at 427°C to increase from approximately 5 nm near the outer surface to 20 nm in pre-transition oxide layers and to 100 nm in post-transition close to the metal-oxide interface, changes in the oxidation kinetics are also reflected in the oxide grain size.

The partial amorphous regions found in the metal oxide interface are believed to be caused by the strain induced by the tensile stresses in the metal side of the interface. Those observed close to the metal oxide interface using TEM were claimed to be due to the type of corroding atmosphere present by Garzarolli et al. [149]. The extensive presence of amorphous oxide was only observed in case of nodular oxide or accelerated corrosion, however not in case of uniform oxide layers [149].

2.3.5 Precipitate oxidation

The oxidation behaviour of precipitates in zirconium alloys, containing the alloying elements in intermetallics formed with zirconium, was studied with a variety of methods, which can be divided in two categories: methods studying the average precipitate behaviour, such as electrochemical methods applied to the surface [176-178], and methods studying individual precipitates, such as transmission electron microscopy [179] and Auger spectroscopy [64, 180-182]. Of these methods only transmission electron microscopy and the latest scanning Auger microscopes have the spatial resolution capacity for chemical analysis, which allow studying precipitates with a size of few tens of nanometres. Atom probe tomography would also have the resolution, however the specimen preparation for precipitates located at the probe tip would be very difficult and the number of precipitates possible to study with reasonable effort would be limited. Of the presented methods only transmission electron microscopy allows the characterisation of individual precipitates and their microstructure with reasonable numbers of precipitates and time for sample preparation.

Therefore in the following the focus is on available TEM results on precipitate oxidation behaviour, first on commercial alloys with ternary intermetallic precipitates and then on binary model alloys with binary intermetallic precipitates. Results obtained by other methods will be also presented if of interest for comparison, especially for those cases, for which no TEM results have been found in the literature.

2.3.5.1 Characterisation of precipitate oxidation in commercial zirconium alloys

Although there are several studies reporting the precipitate oxidation during the oxidation

process of zirconium alloys, no fundamental description of the precipitate oxidation behaviour has been presented to our knowledge. Therefore a description of the precipitate oxidation as presented in the literature will be provided to allow an overview of the known facts.

Zr(Fe,Cr)₂ precipitates contained in Zircaloy-2 and Zircaloy-4 were found to be delayed in comparison to the matrix oxidation [117, 169, 179, 183-189]. Most of these precipitates oxidize only when surrounded by the oxidized matrix some hundred nanometres away from the metal-oxide interface. The Zr₂(Fe,Ni) precipitates contained in Zircaloy-2 have been reported by all authors to be oxidised when incorporated into the oxide, e.g. [186, 190, 191].

The microstructure of the oxidized precipitates was found to comprise some tetragonal zirconia being most probably stabilized by the small grain size and additions of remaining alloying elements in the precipitate site. Fe has been observed to form pure iron agglomerates at the edge of the precipitates during oxidation in steam at 400°C [179] and between 350 and 500°C by Garzarolli et al. [149], while the other alloying elements were not reported to form pure metal agglomerates. Also for Nb containing precipitates reports of unoxidized precipitates in the oxide are found in the literature [54, 117, 138, 184, 192, 193], but also Nb containing precipitates oxidizing directly when incorporated into the oxide [54, 55]. Oxidised β-Nb precipitates were generally reported to be amorphous [54, 117, 138, 184, 192, 193]. For vanadium and iron containing precipitates Pecheur [184] reported unoxidized precipitates in the oxide. Mixed oxides of alloying element and zirconium were reported for Nb [144]. Also other authors have studied precipitates in the oxide layer e.g. [194, 195].

The diffusion of the alloying elements out of oxidised precipitates into the surrounding zirconia matrix was observed for both Zr(Fe,Cr)₂ and Zr₂(Fe,Ni) type precipitates in the Zircalloys [149, 179, 187, 190, 196, 197]. The overall order being Fe > Ni >> Cr [187, 197], with Fe being more mobile than Ni [190, 197] and both much more mobile than Cr [197]. From the comparison of the results of these different studies one can conclude that no special difference was reported for the Zr(Fe,Cr)₂ precipitate behaviour in Zircaloy-2 and Zircaloy-4.

Cox and Sheikh [197] showed that the dissolution of the alloying elements in the matrix oxide formed on Zircaloy-2 is temperature and alloying element dependent. Iron segregates already during oxidation at 400°C to the interface of the oxidised precipitates and the surrounding matrix and forms local agglomerates of almost pure iron oxide (identified by EDS measurements). At 500°C iron is observed to segregate further from the precipitates and no pure iron oxide agglomerates are observed and Zr₂(Fe,Ni)-precipitates show also the segregation of nickel, for precipitates above 1 μm diameter both also segregate within the precipitates and form zirconia enriched in iron and nickel. Chromium is observed to remain within the precipitates. After oxidation at 600°C iron, chromium and nickel are observed to dissolve into the surrounding oxide matrix without forming agglomerates of pure alloying element oxide.

On the surface of oxidised Zircalloys the presence of pure alloying element oxides was reported [177, 198-200]. In the case of Zircaloy-4 [198, 200] a chromium oxide layer was observed on the surface above an oxidised Zr(Fe,Cr)₂ precipitate, in one case with an iron oxide layer underneath the chromium oxide layer [198]. In the case of Zircaloy-2 [177, 199] only iron oxide could be detected by potential reduction on Zircaloy-2. Tests in deoxygenated

environments showed not such an iron oxide formation in these environments [177]. Interesting is that the iron oxide layer thickness increased with oxidation time in all studies including different oxidation times [177, 199], while the chromium oxide layer thickness remained constant [200].

For the presence of the alloying element oxide on the surface Hatano and Sugisaki [199, 200] presented an explanation based on the oxygen partial pressure in the oxide. The alloying element with the highest oxygen partial pressure required for oxidation in the respective precipitate forms the surface oxide, which in the case of the Zircalloys explains their observations for the alloying elements Cr, Fe and Ni [199, 200]. At the beginning of the oxidation process they [199, 200] suggest a thin zirconia layer to form on top of the precipitates and the metallic alloying element atoms to be released into the precipitate. The raising oxygen partial pressure reaches then during further oxidation the pressure necessary to oxidise the alloying element with the higher oxygen affinity, which might be below the one required to oxidise the massive alloying element, as Davison et al. [201] showed for iron in ZrO_2 to be more difficult to be reduced than pure Fe_2O_3 . Hatano and Sugisaki [199, 200] suggested the metallic alloying element atoms to be dissolved into the surrounding zirconia, however the concentration being higher than the solubility limit, leaving considerable amounts of metallic alloying element atoms which then could segregate to the surface, where the oxygen partial pressure required for oxidation would be exceeded, to form alloying element oxide. The alloying element with the higher oxygen potential required for oxidation diffuses into the zirconia matrix, leading to a depletion of the outer precipitate part in this alloying element. This explains the observations for the precipitates in the Zircalloys, however, for the binary zirconium alloys this explanation is not sufficient, which will be presented in the next section.

Independent of the oxidation state of the whole precipitate, the oxidation state of the alloying elements in the oxide is sometimes reported as metallic in a number of studies in the oxide film [62, 190, 200], in the case of $Zr_2(Fe,Ni)$ -precipitates they were reported to be oxidized in one [199] and metallic in another one [190], which does not clarify the situation.

2.3.5.2 Characterisation of precipitate oxidation in binary zirconium alloys

Binary alloys containing only one alloying element besides the impurities have been studied to investigate the specific influence of the alloying elements on the corrosion properties [6, 10, 58, 59, 64, 80, 91, 176-178, 180-182, 184, 202-210]. However, beside the study by Pecheur [184] on Zr1%Nb, no study could be found reporting the microstructural investigation of precipitates in the oxide layer of a binary alloy.

Concerning the chemical analysis of precipitates in the oxide using scanning auger microscopy, Ploc et al. [64, 180-182] claimed, that with respect to the Zr matrix Zr_2Ni precipitates exhibited a delayed oxidation and Zr_3Fe precipitates an accelerated oxidation.

On the surface of binary zirconium alloys containing iron the presence of pure iron oxide has been reported by several authors [64, 177], they do not provide an explanation for the formation of the iron oxide. Shirvington [177] showed that this formation of iron oxide (magnetite) is only observable in not deoxygenated environments.

In the case of binary zirconium alloys (with Cr, Fe, Ni and Sn) [177] only iron oxide could be detected by potential reduction on the Zr0.7wt%Fe samples, chromium and nickel oxide appeared to be present on the respective alloys, however, their quantities were much lower than the ones observed for iron. The explanation presented by Hatano and Sugisaki [199, 200] for the formation of alloying element oxide on the surface would rather indicate a formation of alloying element oxides on the surface of every binary alloy, which so far was not observed. For Ni in Auger no indications have been observed for a Ni rich oxide at the surface, rather for a depletion in Ni [64].

In the case of Zr-Cr and Zr-Ni binary alloys, such oxides of alloying elements have also been reported, however, to a much smaller extent [177]. The phenomenon of alloying element oxide formation has been observed at different temperatures and pressures; the oxygen concentration in the steam seems to have an effect as shown by [177].

2.4 Zirconium oxide and its properties

Zirconium dioxide (ZrO_2), also referred to as zirconia, is the main corrosion product of zirconium alloys and the naturally occurring oxide of zirconium with monoclinic crystalline structure in a mineral called baddeleyite.

For the oxide layer formed on zirconium and its alloys, three different structures have been observed, monoclinic, tetragonal [98, 154, 158, 211] and maybe cubic [98, 149] zirconia (ZrO_2), for their crystallographic data see Table 2. The monoclinic and tetragonal polymorphs of zirconia were first described by Ruff and Ebert 1929 [212] and the cubic one by Smith and Cline 1962 [213]. The temperature regions of stability for those three zirconia polymorphs are at ambient pressure the following: cubic structure between 2680 °C and 2370 °C, tetragonal below 2370 °C and above 950 °C (on cooling) and 1150 °C (on heating) and below those temperatures monoclinic (Figure 3) [214-216]. This temperature dependence of the polymorphs explains the presence of mainly monoclinic oxide in the temperature region of interest to our studies. At room temperature, at which most observations have been made, and at the typical oxidation temperatures, the monoclinic polymorph is the thermodynamically stable form if no other factors such as alloying elements, small grain size or mechanical stresses are present. The stabilisation of the tetragonal phase by pressure in the temperature range of interest can be observed in the phase diagram in Figure 4.

Table 2: Crystallographic data of the cubic, tetragonal and monoclinic zirconia polymorphs of pure zirconia extrapolated to room temperature [217] and references herein.

polymorph	a / Å	b / Å	c / Å	β / °	V / Å ³	Space group
cubic	5.135	5.135	5.135	90.0	135.4	Fm3m
tetragonal	5.099	5.099	5.179	90.0	134.7	P4 ₂ /nmc
monoclinic	5.148	5.200	5.322	99.2	140.6	P2 ₁ /c

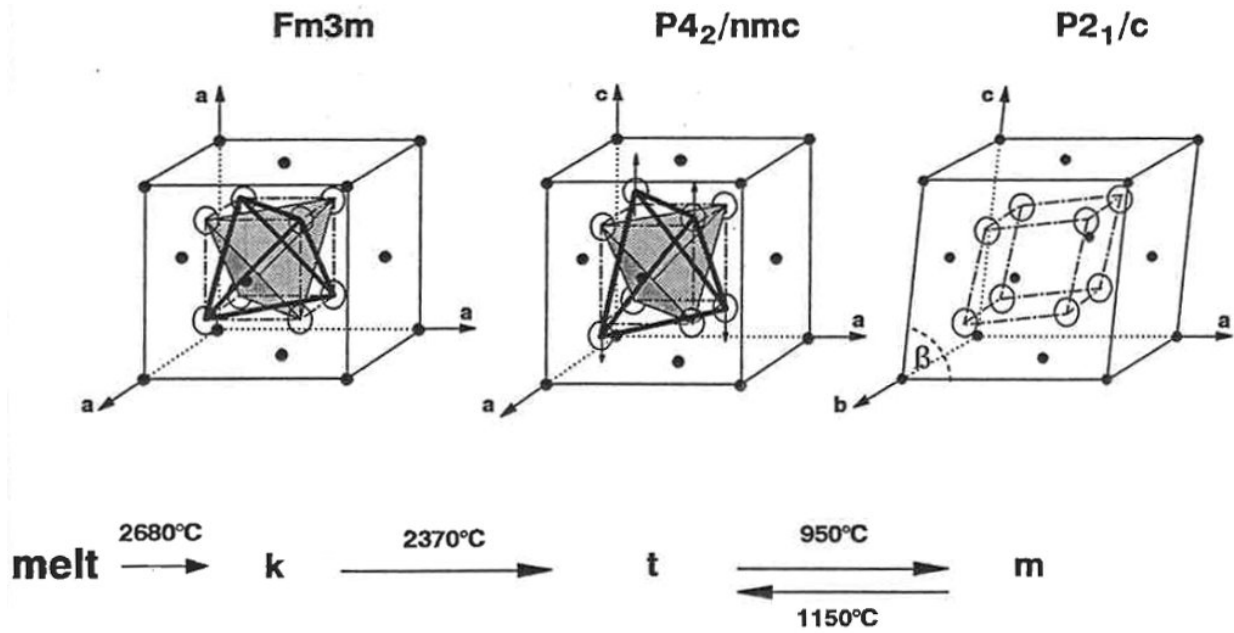


Figure 3: Zirconia polymorphs and their transformation temperatures from [216].

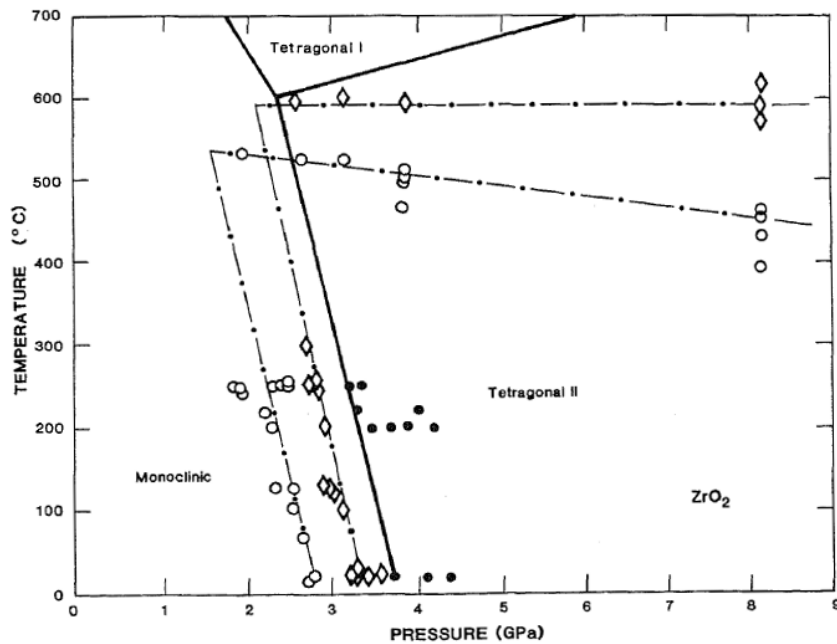


Figure 4: Temperature-pressure phase diagram of zirconia showing the stability domains of the monoclinic and tetragonal polymorphs from [218]. Solid lines data from [219], dash-dotted lines [218], full circles fresh monoclinic crystal, diamonds represent transition on increasing pressure/temperature during cycling and open circles represent transformation upon decreasing pressure or temperature [218].

When comparing the three polymorphs (Figure 3), it should be noted that the c-axis of the monoclinic polymorph is parallel to the one of the tetragonal polymorph. The transformation between both structures is a shear movement parallel to the a-b-plane. This martensitic transformation from tetragonal to monoclinic results in a volume increase for the monoclinic structure of 4.7% at room temperature [214].

The cubic and tetragonal structure can both be stabilized to room temperature by adding nitrogen or different oxides containing Y, Mg or Ca [214, 215].

Besides the pressure [218, 220] and the alloying elements e.g. [183, 221, 222] the tetragonal zirconia phase is also stabilized by the grain size [156, 214]. In the oxide they have to be below 30 nm in diameter to be stable [156] and in powder form zirconia grains have to be smaller than 10 nm [156] to stabilize the tetragonal structure at room temperature. Due to very large anisotropy in thermal expansion coefficient, in partially stabilized zirconia (PSZ) the metastable tetragonal structure can be retained in particles with up to 90 nm diameter due to compressive pressure from the surrounding matrix [220]. A pressure release can result in the transformation of the tetragonal grains to the monoclinic structure, the associated volume expansion was found to oppose crack propagation by generation of compressive stresses in the matrix [223]. Of the two high temperature polymorphs the tetragonal has been frequently shown to exist in oxide scales by different groups using Raman spectroscopy [154, 158] and XRD [211]. The observation of cubic zirconia using Raman spectroscopy has been reported by [98, 149]. The lower the symmetry of the polymorph, the higher is the anisotropy of thermo-mechanical properties, one order of magnitude difference in the thermal expansion coefficient for different lattice direction has been observed for the monoclinic polymorph and only a factor of 1.5 for the two extremes in the tetragonal polymorph [224].

2.4.1 Mechanical aspects of the oxidation of zirconium alloys

Oxidation processes usually involve a stress build-up at the metal-oxide interface, as the formed oxide has a different volume compared to the metal. The ratio of formed oxide volume and the consumed metal volume has been first compared for different systems by Pilling and Bedworth in 1923 and is called today Pilling-Bedworth ratio (P-B ratio or also PBR) [225]. According to their classification a P-B ratio of less than 1 does lead to a discontinuous oxide layer and a P-B ratio above 1 to a compact and continuous oxide layer, which can be protective. Experiments have shown that for a P-B-ratio exceeding 2 the oxide scale spalls and is not protective.

In the case of zirconium, the oxide formed (ZrO_2) has approximately 150% of the volume of the oxidised metal; therefore a protective oxide scale is expected according to the P-B ratio of 1.52 [226], 1.55 [225] or 1.56 (for example [224])(own calculations resulted in a P-B ratio of 1.51 with crystallographic data provided in Table 17 on page 137). Stresses are present, as the expansion is not only perpendicular to the oxidising surface, which would result in no stresses in the ideal case of an oxidising plate. In the case of real fuel cladding, which has tube shape, already unidirectional expansion during oxidation will cause compressive stresses in the oxide and tensile stresses in the metal.

Stresses occurring in the oxide scale of corroding zirconium alloys have been measured in order to understand the correlation of stresses and corrosion resistance of the alloys. It has been found that the compressive stresses in the oxide decrease from the metal-oxide interface towards the surface [224, 227]. Parallel to the decrease of the compressive stresses in the oxide scale is the decrease of the tetragonal zirconia content in the oxide ([228]).

Table 3: Stress measured in oxide of oxidised zirconium alloys.

method	compressive stress in oxide / MPa	material	conditions
x-ray [229]	180 to 1400	pure Zr Zircaloy-4 Zr-1NbO	400°C 10.3 MPa in steam
x-ray [72]	1500-2200	Zircaloy-4	350 °C 16.5 MPa in lithiated water
x-ray [157]	up to 1200	Zircaloy-4	steam 400°C
x-ray [230]	1500-2000	Zr2.5%Nb	300 /400 °C in steam
x-ray [231]	140-4800	pure Zr Zircaloy-2 Zr0.5Nb1Cr	550 / 400 °C in steam
in situ x-ray [224]	close to interface 200-500 close to interface 1800 outer oxide 500-600	Zircaloy-4, Zr1%NbO	470°C, measured at RT and 470°C in oxygen
Raman spectroscopy [227]	up to 1500	Zircaloy-4 Zr-1NbO	360 °C pure and lithiated water
bend strip [149]	up to 800	Zircaloy-4	400°C n steam
bend strip [232]	1100 1600	pure Zr Zircaloy-2	500°C in oxygen at 40 / 1013 mbar
bend strip [233]	1310 400	Zircaloy-2 pure Zr	500-700°C in dry oxygen

Taking the data provided in Table 3 into consideration, it must be said that the stress variation between water/steam and oxygen containing oxidation atmospheres does not indicate an influence of the environment on the determined stresses in the oxide. Comparing the stresses for different alloys from the same study [224, 229, 232, 233], the oxide on pure Zr seems to exhibit always lower stresses than on the Zr alloys, except for [231] who reported pure Zr to exhibit the highest initial stresses.

The overall variation between different studies is quite large, reported stresses in the oxide on Zircaloy-4 range from 200 MPa [224] to 2200 MPa [72], exceeding the generally reported difference between pure Zr and Zr alloys. The highest reported stress was 4800 MPa for pure Zr [231]. The high compressive stresses in the oxide scale at the initial stage should be seen under the following aspects: the thin oxide is brittle and the metal thickness is sufficient to counterbalance the expansion that would be necessary to obtain a stress free oxide. With increasing oxide thickness the mean stresses in the oxide decrease e.g. [224, 229, 231], as the stresses in the oxide relax in the outer part.

2.4.2 Mechanical properties of zirconia

So far the focus was on the mechanical properties of the metal-oxide interface, however, during the oxidation process the oxide forms cracks and even spalls in some cases. Therefore, the mechanical properties of zirconia, the stiffness (Young's modulus) and the critical stress are of interest, as these parameters can help to understand why the oxide fails. Due to lack of such mechanical data for the oxide formed on zirconium alloys, the Young's modulus found in the literature for different types of zirconia with different preparation and testing techniques are presented in Table 4.

Table 4: Young's modulus of different types of zirconia. The Young's modulus corrected to zero porosity was calculated for those data, for which the porosity was reported and less than 15% by using the following equation: $E_0 = E(\pi) / (1 - k\pi)$ where E represents the Young's modulus, π the porosity and k is a scaling factor around 2.5 for spherical cavities [234]. Abbreviations used: Yttria stabilized zirconia (YSZ). The thickness of a zirconia layer is stated where reported in the case of coatings.

type of ZrO ₂ (if provided)	preparation method	testing method (as stated)	Young's modulus (GPa)		Thickness of zirconia
			1. reported	2. extrapolated to 0% porosity	
		Brillouin scattering and ultrasonic wave velocity			
monoclinic [235]	single crystals		122-326	-	-
monoclinic [236]	pressed and sintered	impulse excitation method	190-199	-	-
monoclinic [237]	pressed and sintered	sonic resonance	244-247	-	-
monoclinic [238]	hot pressing	flexural bending	80-100	-	-
monoclinic [239]	single crystals	wave velocity	188-233	-	-
monoclinic [240]	atmospheric plasma-spraying technique	nanoindentation	108-197	-	-
monoclinic [241]	MOCVD	nanoindentation	216-225	-	380 μ m
tetragonal [241]	MOCVD	nanoindentation	240	-	-
tetragonal YSZ [242]		ultrasonic velocity	140	-	-
tetragonal YSZ [243]	electron beam PVD	nanoindentation	160	-	30-230 nm
cubic YSZ [244]		sonic resonance	220	-	-
cubic [245]	ion beam assisted deposition	nanoindentation	53-219	-	-
YSZ [246]	top-coat	microindentation	230-250	-	300 μ m
YSZ 0-10 mol% [247]	electron beam PVD	nanoindentation, Brillouin light scattering	170-223	-	-
YSZ 8 mol% [248]	atmospheric plasma-spraying	-	223-239	-	-
YSZ [249]	electron beam PVD	nanoindentation	65-180	-	250 μ m
			85-150	-	2-4 μ m
			35-100	-	600 μ m
			145	-	-
			126	-	-
			252	-	-

Several points are obvious: the reported Young's modulus for the polycrystalline zirconia is correlated to the type of zirconia and its preparation method. Monoclinic zirconia exhibits a lower Young's modulus in the polycrystalline state than tetragonal or cubic zirconia. Studies on single crystals of monoclinic zirconia showed that the crystal orientation with the highest Young's modulus is with 326 GPa [235] considerably above the highest reported Young's modulus of 250 GPa [243] for polycrystalline tetragonal zirconia. The second study on single crystals of monoclinic zirconia reported an average Young's modulus of 240 GPa [239].

The influence of porosity on Young's modulus of polycrystalline zirconia has been investigated by two studies [238, 242], see for example [242] in Table 4 where the lowest value of Young's modulus corresponds to 38% porosity of YSZ and the highest to full density. This demonstrates that only specimens with similar porosity and of the same zirconia polymorph are really comparable, as otherwise too many parameters are influencing the obtained Young's modulus. This is illustrated by the overall spread of the average Young's modulus ranging from 30 to 250 GPa, almost one order of magnitude.

Crack formation leads to a reduction of the Young's modulus [250]. The fracture toughness has been shown to increase with the formation of microcracks in brittle materials by energy dissipation and reduction of the local stress concentrations during crack propagation [251].

2.5 Open questions concerning corrosion of (binary) zirconium alloys

The overview provided on zirconium alloy corrosion illustrates that although many phenomena are known and at least understood on a phenomenological basis, still some open questions concerning the corrosion of the alloys remain. The open questions need to be identified and answered to be able to develop a better understanding.

This list of open questions is not intended to be exhaustive and is limited to topics being possible to address with the performed studies:

1. Is there a correlation between the oxidation behaviour of the precipitates in binary alloys and their composition?
2. Can the results obtained for precipitates in binary alloys be extrapolated to precipitates in more complex alloys?

Even though answers to these questions will help to understand more of the precipitate behaviour, maybe also in more complex commercial alloys, much will be left to do to understand all the parameters influencing the corrosion behaviour of zirconium alloys.

3 Materials and methods

The materials studied in the course of this project were selected with the aim to study the influence of different alloying elements on the oxidation of binary zirconium alloys for a comparison with commercial alloys. The samples were chosen to reflect the initial stage and the long-term corrosion behaviour. Different atmospheres such as water and air were used to be able to observe the influence of the presence of hydrogen on the oxidation.

The experiments described in this chapter have been performed at two different institutions: the Paul-Scherrer-Institut (PSI) and at the Swiss Centre for Electronics and Microtechnology (CSEM) in Neuchâtel. The respective institute where the experiments have been conducted is stated for each instrument. Environmental scanning electron microscopy was used to perform short time oxidation experiments with in situ observation of the surface. Atomic force microscopy and scanning electron microscopy have been applied to characterise the surface of the samples. Focused ion beam was used to prepare transverse sections and samples for transmission electron microscopy. Thin oxide films were prepared from oxidised samples by electrolytic polishing and by standard polishing to test their mechanical properties with the bulge test and nanoindentation.

3.1 Materials

The autoclaved binary alloys and pure zirconium as Zircaloy-4 have been provided by CEZUS, France. They were beta-quenched after forging, hot rolled and annealed at 640°C and three times cold rolled and annealed at 600°C [10]. The studied Zircaloy-2 is a standard commercial alloy within the specifications for this type of alloy. The results from the previous studies including the weight gains, electrochemical impedance spectrometry and potential sweeps and hydriding behaviour of these alloys are published in [10, 202] and used in this study.

3.1.1 Binary alloys

The autoclaved binary alloys containing 0.2 wt.% Fe and 1 wt.% of Cr, Fe and Ni and pure Zr investigated in this project have been provided by CEZUS, France. Experimental results for the previous study on these materials have been published in an ASTM special technical publication [10]. Their composition as provided by CEZUS is given in Table 5 together with the maximum possible precipitate volume, assuming all alloying element content to be present in the precipitates (also for β -Nb) and the precipitates having the stated composition.

The thermal treatment of the material used for the oxidation tests by CEZUS resulted in a cumulative annealing parameter of about $\Sigma A = 1.3 \cdot 10^{-10}$ h with $\Sigma A = \Sigma t \exp -40\,000/T$, where T is temperature in K and t the time in h. This was followed by a stay in the autoclave at 415°C [10] for either 3 days in air or steam at 0.1 MPa or for 110 days in steam at 10.5 MPa for the selected samples. Samples of a binary zirconium-niobium alloy containing 0.6 wt.% Nb oxidized for 40 days in steam and 55 days in air, also provided by CEZUS from another study, have been included to compare the oxidation behaviour of the binary Nb-containing alloys with the other binary alloys.

Table 5: Chemical analysis of the binary alloys (in ppm or wt.%) and precipitate data from Barberis et al. [10] for Zr1%Fe, Zr1%Ni and Zr1%Cr. Volume fraction of β -Nb is from own calculations.

alloy type	Cr / ppm	Fe / ppm	Ni / ppm	Nb	O / ppm	average metal grain size / μm	SPP type	SPP density / g/cm^3	SPP volume fraction / %
Zr0.2%Fe	45	0.22 wt.%	35	-	650	6.2	Zr ₃ Fe	6.81	1.13
Zr1%Fe	44	0.99 wt.%	28	-	720	3.1	Zr ₃ Fe	6.81	5.71
Zr1%Ni	46	205	1.17 wt.%	-	755	4.6	Zr ₂ Ni	7.20	3.70
Zr1%Cr	1.04 wt.%	247	37	-	760	5.2	ZrCr ₂	6.98	1.76
Zr0.6%Nb	-	-	-	0.6 wt.%			β -Nb (20%Zr)	8.49	0.57

The weight gain data from CEZUS [10] for the different oxidation tests performed were transformed into oxide thickness using the generally used conversion factor of 1 μm oxide corresponding to 15 mg / dm^2 .

The oxide scale on the samples obtained from the autoclave oxidation, containing 1 wt.% of alloying element, has been examined by electrochemical impedance spectrometry [10, 252], metallography, AFM and SEM/EDS in previous studies [10, 252]. Their average oxide thickness for the different testing conditions calculated from weight gain reported in [10] is provided in Table 7.

3.1.2 Pure zirconium, Zircaloy-2 and Zircaloy-4

Pure zirconium and the commercial alloys Zircaloy-2 and Zircaloy-4 were included for selected conditions to allow the comparison of their behaviour with the binary alloys. The matrix oxidation of the binary alloys is to be compared with pure zirconium to evaluate if there is an influence of the precipitates. The commercial Zircaloy-2 and -4 are included to compare the oxidation of binary intermetallic precipitates in model alloys with those present in the commercial alloys which contain two alloying elements (ternary intermetallics) and also contain tin in the Zr matrix.

Table 6: Chemical analysis of pure Zr and Zircaloy-2 and -4 (in ppm or wt.%).

Alloy type	Cr / ppm	Fe / ppm	Ni / ppm	Sn / wt.%	O / ppm
pure Zr [202]		150	-		300
Zircaloy-2	within ASTM specifications, see Table 1 Chapter 1				
Zircaloy-4 [202]	1040	2200		1.3	1150

3.1.3 Overview of available samples

In Table 7 an overview of the samples being studied in the course of this PhD research is provided. The samples provided by CEZUS are presented in the first three columns, their average oxide thickness was calculated from the provided weight gain. Samples oxidised for 1 hour at 415 and 700°C at 130 Pa in an environmental scanning electron microscope (ESEM) are shown in column 4 and 5 and short time autoclave tests at PSI for 1 hour to 72 hours at 10.5 MPa to complement the time and pressure range are also presented, their average oxide

thickness was determined from FIB sections, as their sample size did not allow precise oxide thickness determination from weight gain data.

The conditions were selected in order to cover the following parameters having possibly an influence on the oxidation of the alloys and the precipitates:

- oxidation atmosphere (air / steam)
- pressure of oxidation atmosphere
- oxidation time

Table 7: Overview of all available samples with their oxide thickness given in μm . The oxide thickness of samples provided by CEZUS [10] (column 1-3 shadowed) was determined from weight gain, for all other samples oxidized during this PhD project, from FIB sections.

Alloy	Average oxide thickness (μm)							
	air oxidation	steam oxidation		In situ ESEM at		steam oxidation at PSI		
	CEZUS	CEZUS		CSEM, Neuchatel		Limbo 350 autoclave		
	3 days 415°C 0.1 MPa	3 days 415°C 0.1 MPa	110 days 415°C 10.5 MPa	1 hour 415°C 130 Pa	1 hour 700°C 130 Pa	1 hour 415°C 10.5 MPa	1 day 415°C 10.5 MPa	3 days 415°C 10.5 MPa
Zr0.2%Fe	0.67	1.61	4.19	—	—	0.42	1.08	—
Zr1%Fe	1.01	1.37	5.00	0.32	3.2	0.62	1.14	1.53
Zr1%Cr	0.79	1.08	4.23	0.35	2.7	0.52	0.94	1.28
Zr1%Ni	0.93	1.26	4.15	0.41	2.8	0.49	—	—
Zr0.6%Nb	6.02 (55 days)	2.58 (40 days)	—	0.34	3.2	0.40	—	—
Pure Zr	0.63	4.12	—	0.27	2.4	0.62	0.88	—
Zry-2	—	—	—	—	—	0.40	1.15	—
Zry-4	—	—	6.36	—	—	—	—	—

For oxidation in air at 415°C (Table 7) the low weight gain of pure zirconium in comparison to alloys reported in the literature is also observed. Oxidation in steam at ambient pressure and 415°C (Table 7) showed the lower resistance of pure zirconium to water containing oxidation environments compared to the binary alloys.

3.2 Oxidation experiments

In the course of the PhD research additional oxidation experiments were carried out to obtain samples with different oxidation conditions than those supplied by CEZUS. The oxidation experiments were performed in (a) an ESEM, (b) an autoclave in water containing environments and (c) in furnaces in air.

3.2.1 In situ oxidation campaigns

The in situ oxidation experiments were designed to provide as many details as possible about the samples before and after in situ oxidation in the ESEM. The surface topography and composition were analysed before and after the oxidation and TEM samples were prepared to observe the changes taking place during oxidation from the metal-oxide interface to the outer surface. Non-destructive methods were applied before destructive methods to minimize the chances to create and observe artefacts.

The characterisation procedures and the experimental steps applied to all samples were the following:

1. Atomic force microscopy (polished surface)
2. Scanning electron microscopy (polished surface)
3. ESEM in situ oxidation experiment at 415 / 700°C
4. SEM (oxidised surface)
5. AFM (oxidised surface)
6. further SEM/EDS and focused ion beam (FIB) characterisation of surface and transverse sections (oxidised surface)
7. Transmission electron microscopy on specimens prepared by FIB

A gas secondary electron (GSE) detector was used for the high temperature observations. At 415°C the energy dispersive x-ray spectrometer could not be used for chemical analysis due to the high temperature and the cover of the heating stage (Figure 6) would have absorbed most x-rays even if it would have been possible to use the detector. The chemical analysis of the surface was therefore performed subsequent to the in situ oxidation experiment after cooling the sample and changing to the normal specimen holder. The cover of the heating stage for shielding the microscope from excessive heat from the stage required also a somewhat larger working distance to avoid contact of the cover and the GSE detector.

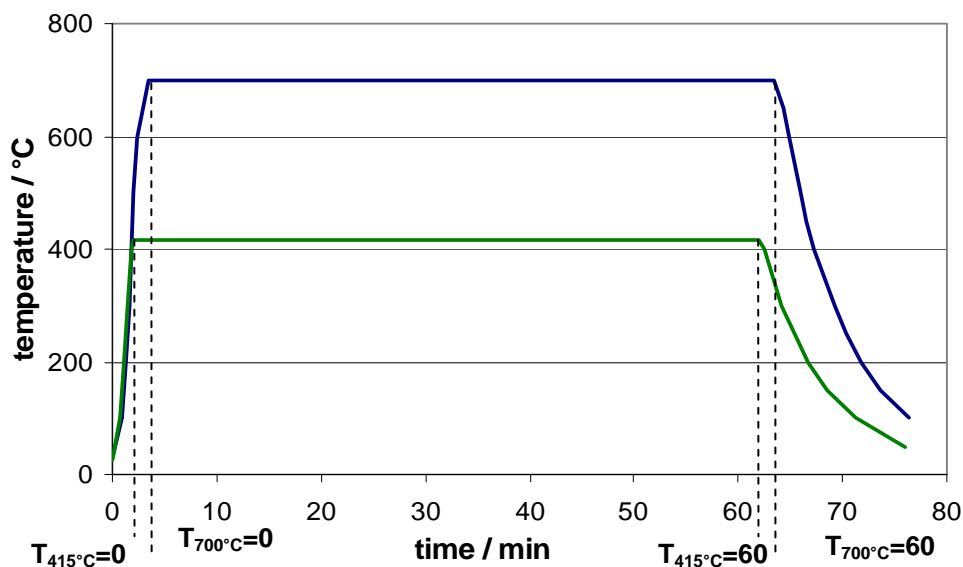


Figure 5: Temperature versus time curves for the in situ oxidation experiments performed at 415 and 700°C.

During the in situ oxidation the surface was continuously observed and images were acquired every 5 minutes on each specific area of the sample.

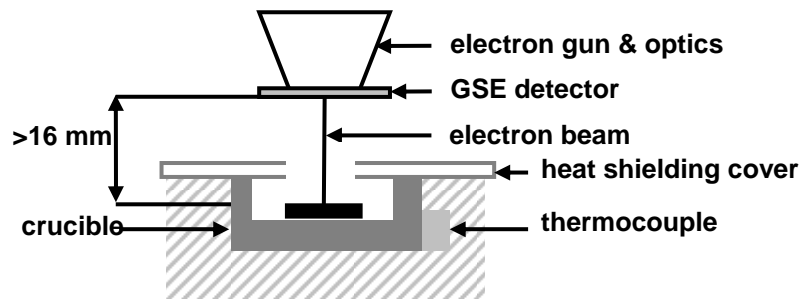


Figure 6: Schematic sketch of sample position in the heating stage used for in situ oxidation experiments.

For the in situ oxidation the instrument was operated in ESEM mode and the water vapour pressure was held at 1.3 mbar in the specimen chamber. The sample was heated on a water cooled heating stage in a platinum crucible. The heating current of the stage was automatically adjusted according to the temperature measured by the thermocouple and the programmed target temperature. The maximum possible heating rate was 3.9 °C/s, allowing to reach 415 °C in 2 minutes and 700 °C in just above 3 minutes. The observations started when this temperature was reached ($t=0$). Before the oxidation temperature was reached, the focus had to be adjusted due to the thermal expansion of the sample and the holder; also adjustments of the electron optics were required to compensate for the changes in the electron optics induced by the heat from the heating stage. The material was held for 60 minutes at 415/700 °C and subsequently cooled to ambient temperature. The initial cooling rate of the specimen was about 0.8 °C/s from 415 °C and 1.2 °C/s from 700 °C.

3.2.2 Autoclave oxidation

The autoclave oxidation of small test specimens was performed in a Limbo 350 autoclave from BüchiGlasUster [253] at PSI. The autoclave vessel made of stainless steel was fitted with a hook holder enclosed in a zirconia tube for fixation of specimens (Figure 7), a thermocouple for the automated temperature control via a “TC 450” type controller, a digital manometer from WIKA (DG-10-S, 0-600 bar) and a pressure valve for manual pressure release and a safety pressure valve. The heating of the autoclave vessel was achieved by an electrical heating with a maximum power of 2000 W. The temperature range specified for safe operation was -10 to +450°C and a maximum pressure of 350 bars at 350°C.

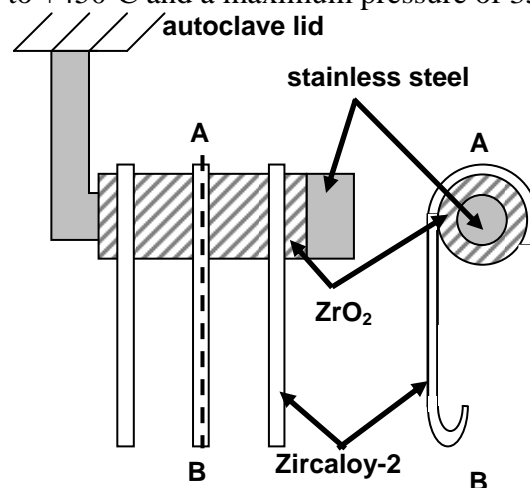


Figure 7: Specimen holder used for the autoclave oxidation experiments at PSI.

The samples were fixed to the zirconia holder with hooks made of Zircaloy-2, which were regularly replaced. Before closing the autoclave all sealing parts were cleaned and the autoclave was filled with 50 ml of deionised water (0.05-0.1 μS). The temperature controller was programmed to 450°C for the experiment start to allow heating at the maximum possible heating rate close to the target temperature of 415°C. The pressure was regularly reduced manually to 100 bars within the 100-110 bar range before exceeding 110 bars. At 400°C the target temperature of the automated temperature control was set to 415°C and the pressure regulated to be between 100 and 105 bars at 415°C. After the planned time at the oxidation conditions (1 h, 24 h and 72 h) the heating was switched off and the autoclave left to cool down to room temperature without external cooling (Figure 8).

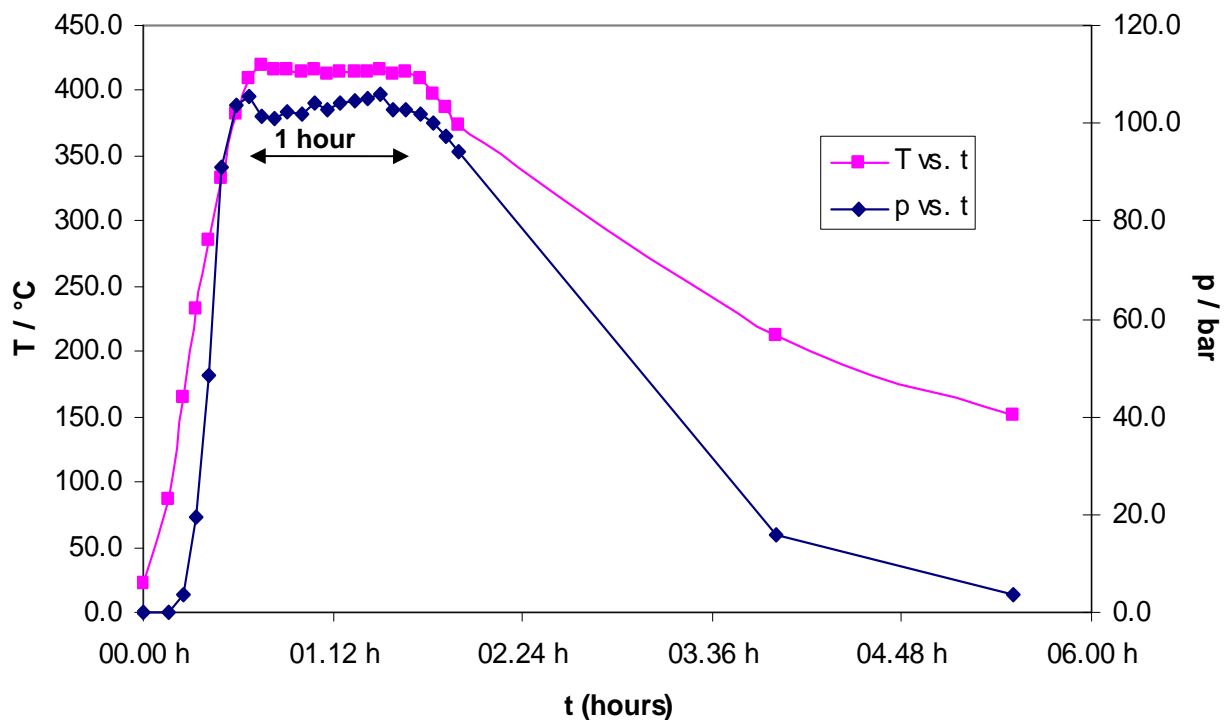


Figure 8: Temperature and pressure profile for a typical autoclave run for 1 hour at 415°C and 100 bar nominal pressure. The temperature readings are presented by squares (left y-scale) and the pressure reading by diamonds (right y-scale).

3.2.3 Furnace oxidation in air

The additional furnace oxidation experiments were performed in air at ambient pressure and $\sim 415^\circ\text{C}$. This was done in order to be able to verify the presence of alloying element oxide on the surface, in the absence of an external contamination on the surface such as those possible in an autoclave with water. The furnace oxidation in air was performed in two different furnaces: in the retort furnace CP 1050-3-P2 by Borel [254] the sample temperature is quite well controlled within $\pm 5^\circ\text{C}$ of the set temperature of 415°C (taking into account the T gradients inside the furnace), while for the other furnace used for short time oxidation (MR 170 E by Heraeus) the sample temperature can only be estimated to be within a certain temperature range around $415 \pm 25^\circ\text{C}$.

3.3 Sample preparation

3.3.1 Sample cutting and surface polishing

The samples were cut from the oxidised coupons using a wire saw (wire diameter 0.17 mm) with lateral dimensions of up to 15x15 mm. For autoclave samples a 0.3 mm hole for the sample fixation was drilled at one corner for suspension. Depending on the sample size, the samples were fixed to the disk grinder from GATAN (max. 6x6 mm) or a larger copper block for the grinding and polishing, the disk grinder has the advantage that flat surfaces without excessive edge rounding can be obtained. All samples were ground with 1000, 2000 and 4000 SiC paper and then polished with diamond suspensions containing diamonds of 6 μm , 3 μm and 1 μm size to remove the mechanical damage of the previous grinding and polishing steps. Some samples were polished with a basic slurry (pH 9.5) containing 60 nm Silica particles in the vibratory polisher (VibroMet 2 from Buehler [255]), as this resulted in a smoother surface finish compared to the only diamond polished surface.

After the last polishing step glued samples were first rinsed in acetone to remove the samples from the holder and remaining glue. All samples were ultrasonically cleaned in ethanol to reduce the amount of surface contamination.

3.3.2 Mechanical preparation of transverse sections

The transverse sections for mechanical testing and SEM observations were prepared by embedding the samples in epoxy resin in a 1 inch diameter cylindrical form, the sample oriented perpendicular to the flat faces of the cylinder. For imaging in the SEM conductive silver paint was applied after polishing to electrically connect the metallic part of the sample to the SEM holder to reduce the charging.

3.3.3 In situ oxidation experiment samples

For each sample, a piece (3 mm x 3.5 mm) was cut from the material oxidised in air by CEZUS, the dimensions were chosen to be close to the maximum size fitting in crucible of the heating stage. One corner of the sample was removed by polishing to have a macroscopic reference feature for orientation of the specimen. The surface was polished as described in 3.3.1 above with the 1 μm diamond polish as last step (two in addition with vibratory polisher). Three micro-hardness indents were produced on the surface, in order to have reference points for the accurate observation of the same region at different stages of the study.

3.3.4 Electropolished TEM samples

To determine microstructural details of the alloys, such as their precipitate size distribution, metallic 3 mm discs with 200-300 μm thickness were prepared from the oxidised samples with the oxide being removed. These discs were jet electro-polished with a jet electro-polishing instrument from Struers [256] (Tenupol-5) at PSI. The electro-polishing solution used contained 10vol.% perchloric acid in methanol maintained at -20-25°C and the flow rate was kept at 10 (internal standard) and the voltage at 20.5 V. The polishing voltage

was determined by an automated procedure for each material by a voltage scan from 0-40 V, suggesting used 20.5 V for optimal polishing conditions. The electrolyte temperature and flow rate were adjusted to obtain well polished samples with sufficiently large electron-transparent regions around the hole created by the polishing process.

3.3.5 Focused ion beam

Focused ion beam (FIB) instrument uses an ion source, from which a focused ion beam is formed and accelerated to the surface of the sample [257] similar as in an SEM. The current in a modern FIB can reach several tens of nanoamperes, which can be used to sputter and micro-machine the surface. Low ion currents are used to image the sample surface with a spot size in the range of a few nanometres. The amount of sputtered material depends on the ion current; it should be kept in mind, that sputtering takes always place, the extent being dependent on the ion current. Beside the sputtering and imaging, the ion beam can also be used to deposit (e.g. Pt or C) via ion beam induced chemical vapour deposition by decomposing precursor gas on the sample.

The focused ion beam (FIB) used was the NVision 40 workstation at PSI from Zeiss equipped with an INCA EDS system, a Kleindiek micromanipulator and a gas injection system for platinum and carbon deposition. This FIB works with a liquid gallium source, from which gallium ions are accelerated with an acceleration voltage of 30 kV and focused onto the sample surface, where they sputter a small amount of material. The NVision 40 workstation was used to prepare transverse sections of the oxide scale and TEM-samples with the lift-out technique. The angle between the SEM column and the FIB column is 54° for the used instrument. The sample orientation during milling is shown with respect to SEM and FIB column in Figure 9. The x-axis of the images is undistorted, because the tilt axis of the sample stage is along the x-axis. Distances in the y-direction on the images obtained are to be multiplied by $1/\sin(54^\circ)$ to obtain the real length, which is due to the geometry of SEM, FIB and sample to each other (Figure 9).

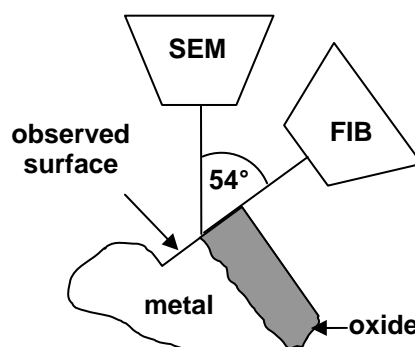


Figure 9: Geometry of SEM and FIB column in the NVision 40 workstation from Zeiss. The sample orientation is shown for polishing of transverse sections.

Increasing the beam current to several nA increases the amount of material removed per second, however the damage caused by the impinging ion beam is also increased [257].

3.3.5.1 FIB transverse sections

The FIB technique allows preparing transverse sections of the oxide at specific sites. This permits the direct correlation of features in the section with features on the surface. The sections were made perpendicular to the oxide surface. From those transverse sections the oxide thickness and variation of the oxide thickness were determined by milling sections at different positions on the samples and polishing the studied face. The large size of the sections obtained and their high number allows having a good statistics for the observations.

The FIB preparation method was used for the transverse sections instead of the standard mechanical polishing procedure, which caused damage to the oxide scale and provided less observable details in the sections compared to the FIB made sections. Sections were made perpendicular to the sample surface (Figure 9) with a 6 nA beam current, decreasing the beam current down to 150 pA for the final polish of the transverse sections.

3.3.5.2 TEM lamella preparation with the lift-out technique

TEM lamellas of oxidised samples were prepared using the lift-out technique. For this preparation technique first a region of interest is selected in SEM mode to avoid damage of the sample by ion irradiation and implantation. The preparation procedure is shown at several stages in Figure 10, starting with the deposited protective layer and finishing with the electron-transparent specimen.

The region of interest is protected with a strip of platinum by electron beam assisted deposition of a precursor gas from a gas injection system. Then the sample is tilted with its surface perpendicular to the ion beam. The protective strip is thickened to a total platinum thickness of 1 μm by ion beam assisted deposition, for which the ion current should not exceed 4 $\text{pA}/\mu\text{m}^2$ and a pixel fill factor of 50% (corresponding to a 50% coverage of the sputtered area with Ga ions). The strip is then thickened to approximately 3 μm by deposition of carbon on top of the platinum (Figure 10a).

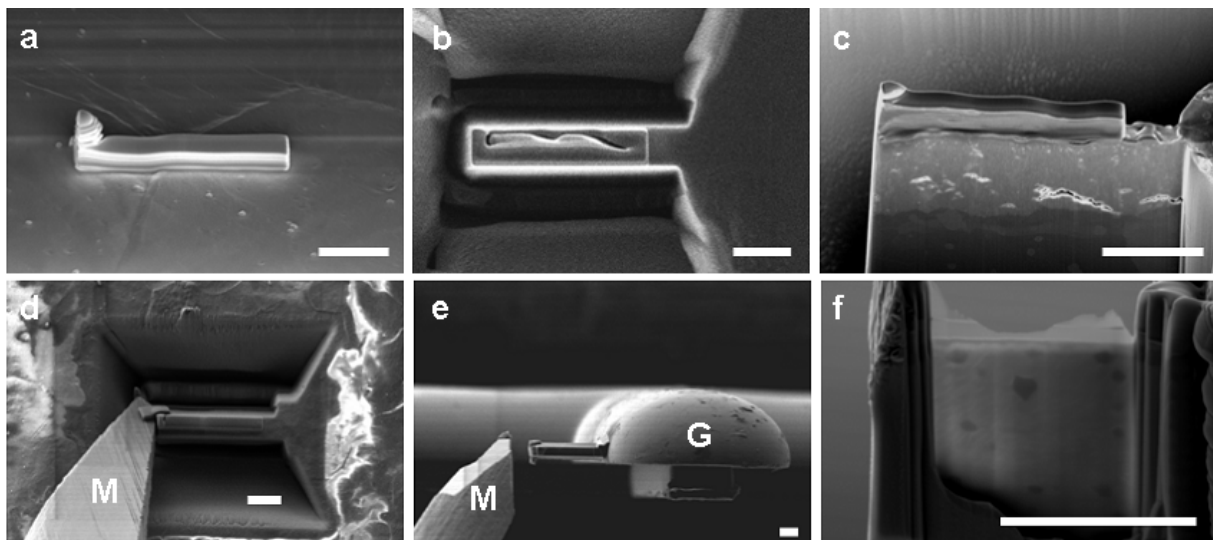


Figure 10: TEM lamella preparation by lift-out technique. Steps from platinum/carbon strip deposition, milling trenches, welding to micromanipulator and TEM grid and thinning to electron transparency are shown. M marks the micromanipulator and G the post on TEM grid. Scale bars represent 5 μm .

Trenches were milled on three sides of the TEM specimen, starting with 6.5 nA (only for very large samples 13 nA for the coarse trenches were used) and reducing the current to 1.5 nA close to the deposited strip (remaining thickness 2-3 μm) (Figure 10b). After tilting the sample surface perpendicular to the electron beam, the bottom of the TEM specimen is milled free with an approximately 0.5 μm wide rectangular pattern with an ion beam of 1.5 nA (Figure 10c – milling position indicated by two white arrows). The trenches parallel to the TEM specimen should be wide enough to allow good access to the bottom of the specimen for the cut underneath the lift-out specimen. The removal of the material underneath should be confirmed by tilting and observation before the lift-out procedure, otherwise the weld to the micromanipulator can break and the specimen is irretrievable. The micromanipulator (Kleindiek) is brought close to the specimen and welded to it by carbon deposition on the side of the specimen and the touching micromanipulator (Figure 10d) (40/80 pA with a deposition area of at least $2 \times 3 \mu\text{m}$). The last side of the lift-out specimen connected to the sample is milled free (1.5 nA ion beam current) and the specimen is transferred to a pole of the TEM-grid, to which it is welded by carbon deposition. The specimen is milled free from the micromanipulator (Figure 10e) and the opposite side is also welded to the TEM-grid to assure good adhesion.

The TEM specimen is thinned from both sides to electron transparency (Figure 10f) by milling with ion beam currents from 750 pA down to 80 pA with the specimen tilted up to 2° off the ion beam direction to obtain as parallel sides as possible, and thus avoid a wedge shaped specimen with a strong thickness increase from the top to the bottom of the TEM lamella (Figure 11). Depending on the height of the final TEM lamella, its tilt off the ion beam direction needs to be adjusted (for thick oxides 1.5° off can be already sufficient. It is important to avoid milling holes in the sample, especially close to the metal-oxide interface, as this region is of interest and the metal is milled faster than the oxide.

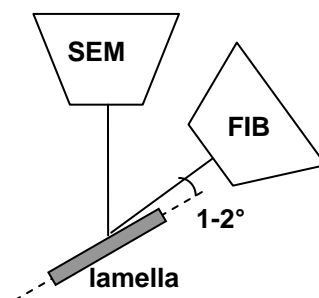


Figure 11: Sample orientation to 2° off the ion beam during thinning to electron transparency to obtain parallel sides (angle is exaggerated!).

The final polish of TEM lamella was done by tilting the lamella 6° off the ion beam direction and milling with a broad ion beam at 2 kV acceleration voltage and 60 pA beam current on the thinned region to remove the amorphous layer formed by the higher energy ion milling.

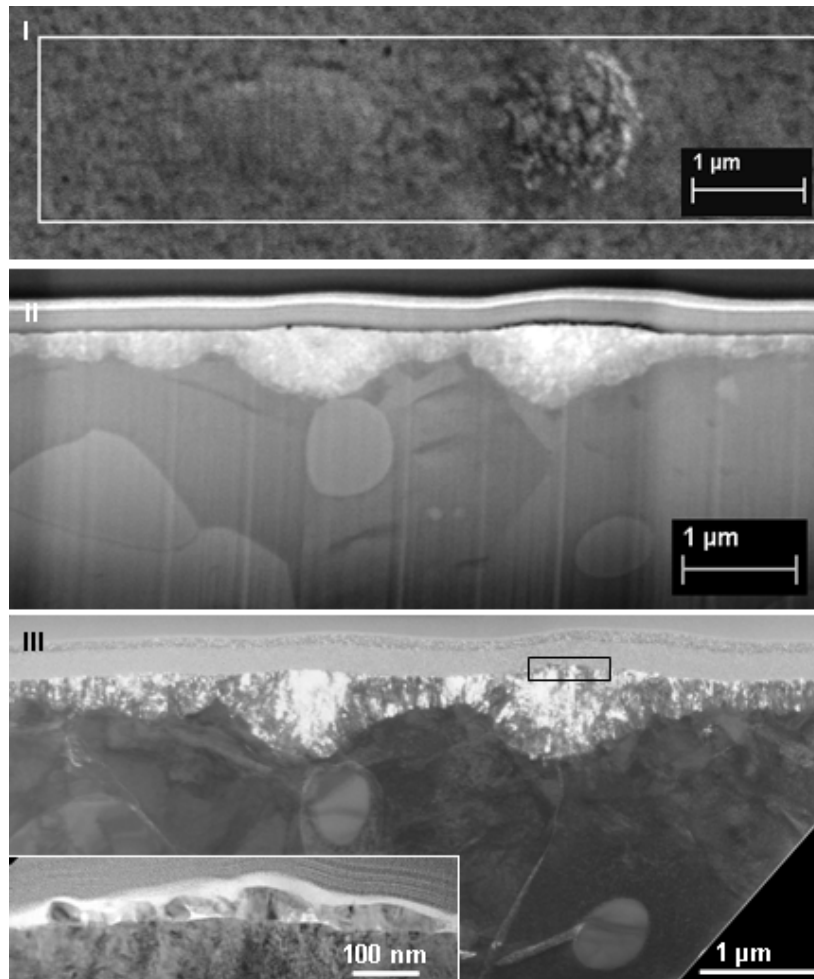


Figure 12: Stages of FIB TEM sample preparation and characterization for Zr1%Fe oxidized in situ: I Selection in SEM and protection with platinum (white frame marks region for deposition), II SEM image of FIB thinned TEM specimen and III dark field contrast of finished TEM lamella in TEM. The black frame marks the position of the inset.

The difference in information obtained by SEM and TEM is exemplified in Figure 12, in which the SEM image of the surface, the TEM lamella in SEM and finally in TEM micrograph are presented. Although the particles on the surface are visible in both instruments, only the TEM is able to clearly show the microstructure, composition and height of the iron oxide particles. The analysis of the structure by electron diffraction as well as EDS for composition and EELS for oxidation state is also performed in TEM.

3.3.6 Preparation of freestanding oxide membranes

To test the mechanical bulk properties of the formed oxide scales with the so called bulge test (see section 3.4.8 on page 52), the preparation of freestanding oxide membranes was required. The freestanding zirconia membrane was prepared by electrolytic polishing from one side to remove the metal in a circular region. The oxide side was protected by a transparent paraffin film (Parafilm® “M” from American National Can™), which allowed the use of the automated optical end point detection system. The electrolyte used was a 40% HNO₃ 5% HF solution cooled to approximately -22 to -23°C. The light stop value of the end point detection system was set to a high stop threshold (200 instead of 20 for TEM sample preparation) to obtain large freestanding membranes. This was possible as the oxide

films in the thickness range of not more than few microns are still transparent for the infrared light used for the end point detection system.

However, this preparation technique has some drawbacks: the holes are not perfectly circular, the metal support at the membrane fringe is thin, and so the mechanical boundary of membrane is not well defined. A possible mechanical damage of the oxide by the electrolyte jet cannot be excluded and the membrane does not have a homogeneous thickness, since the oxide is thinner in the centre of the film.

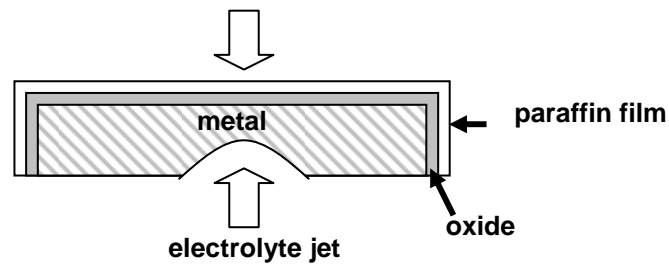


Figure 13: Sample preparation for bulge test by electrolytic polishing with oxide side protected by transparent paraffin film.

3.4 Characterisation methods

The applied experimental methods allow the characterisation of a variety of properties of the studied oxidised alloys. The different employed experimental methods will be described shortly together with the applied characterisation procedures. Details are provided for non-standard techniques and parameters specific for the studied material system.

3.4.1 Atomic force microscopy

Atomic force microscopy (AFM) is applied for surface topography analysis [258]. A tip with a radius of curvature in the order of nanometres is scanned over the surface and the surface height is recorded, providing data about surface roughness and height differences.

Atomic force measurements of the surface were performed on a Digital Instrument Nanoscope IIIa at CSEM in Neuchâtel. For the surface topography scans a silicon tip was used in tapping mode at ambient temperature. The scanning speed for recorded scans was chosen to result in less than 1 nm deviation of the height profiles between forward and backward scan. The scanning resolution of points of interest was 254x254 points, for selecting regions of interest a scanning resolution of 128x128 pixels and a higher scan rate were used. The size of the scanned area ranged from 700x700 nm to 80x80 μm , covering the local and general surface topography of the investigated samples.

3.4.2 Scanning electron microscopy

In the scanning electron microscope (SEM) a focused electron beam is scanned over the surface of the sample [259]. The signals generated are recorded with respect to the beam position and contain compositional and topographical information. The effective acceleration voltage applied to the electrons can be tuned from few hundred Volts to 30 kV. Depending on the acceleration voltage and the selected detector, the recorded signal is generated very close to the surface (low acceleration voltage) or from a region in the range of up to some micrometers in depth from the surface at 30 kV.

The SEM installed on the NVision 40 (Gemini column from Zeiss) at PSI equipped with the INCA EDS system from Oxford Instruments was used for imaging the sample surface and transverse sections and local chemical analysis. The applied acceleration voltage was usually 5 kV for minimised charging and optimal surface sensitivity. For EDS analysis this acceleration voltage is sufficient if no quantitative analysis is intended. The point analysis was used to verify the presence of precipitates in areas intended to be examined in FIB transverse sections and for TEM sample preparation.

3.4.3 Environmental scanning electron microscopy

The Environmental Scanning Electron Microscope (ESEM) is a specially adapted SEM with pressure limiting apertures, which allow to vary the pressure in the specimen chamber considerably above the vacuum levels required in normal SEMs [260, 261]. Using the ESEM in combination with a heating stage allows the study of corrosion processes at higher temperatures. The purged gas (e.g. water vapour) can together with heating stage be used to study high temperature corrosion processes. The in situ oxidation experiments were

performed in the Philips XL30 ESEM-FEG equipped with an EDAX micro-analyzer (energy dispersive x-ray analysis system) at CSEM.

3.4.4 Transmission electron microscopy

In the transmission electron microscope (TEM) [262] information about the investigated material is obtained from electrons transmitted through a thin specimen (less than ca. 150 nm), interacting with the specimen as they pass through. The transmitted electrons are used for imaging, diffraction analysis and chemical analysis, EDS and electron energy loss spectroscopy (EELS). The power of the TEM is in its resolution down to the sub-nanometre level together with structural and chemical information.

The TEM characterisation was performed on the JEOL 2010 at PSI operated with an acceleration voltage of 200 keV. The TEM is equipped with a LaB₆ filament, an INCA EDS system by Oxford Instruments and a post column electron energy loss spectrometer (EELS). Three different image recording devices are available: negatives, a STEM detector and a CCD camera with 4008 x 2672 pixel resolution (Orius from GATAN [263]). The energy resolution of the EDS detector is 132 eV. The tilt range along the specimen holder axis is $\pm 30^\circ$. The TEM specimen holders used were either single tilt or a low background Be double-tilt sample holder in case EDS measurements were performed. Except the beryllium holder, all other available sample holders resulted in a background signal containing iron and chromium, being therefore not used when experiments for quantitative results of iron and chromium were planned. In the following the characterisation procedures is described for precipitate analysis on electro-polished samples and of oxide scales containing precipitates.

3.4.4.1 Precipitate analysis on electro-polished samples

For the precipitate size analysis of the different alloys a number of negatives was acquired at 40k magnification. The scanned images were then analysed in the image treatment software LINCEN [264], with the precipitate diameter being measured in two orthogonal directions (Figure 14). From these data the corresponding circular diameter was calculated and the resulting size distributions plotted as histogram. The size range represented by one bar in the histogram was chosen according to the overall precipitate size range for the material of interest (e.g. 10 nm for Zr1%Cr and 50 nm for Zr1%Ni).

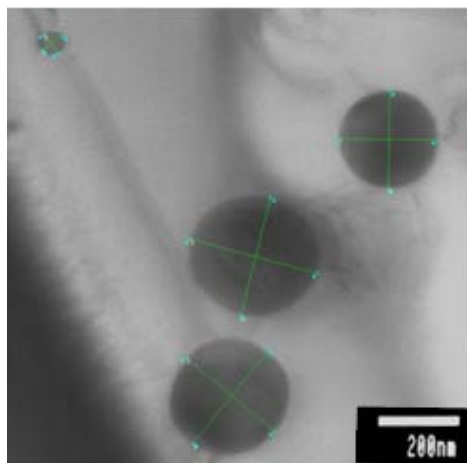


Figure 14: Example of Zr1%Ni for the precipitate size determination from TEM micrographs.

3.4.4.2 Characterisation of oxide scale and precipitates

Detailed characterisation of precipitate structure and oxygen content was performed by TEM using imaging, diffraction and chemical analysis (EDS). The location of the larger precipitates in TEM specimens prepared with the FIB is already known from the preparation (Figure 12), so that the features of interest (oxidised precipitates, precipitates at the metal-oxide interface, etc.) can be directly located and investigated. For the large precipitates the local microstructure in the precipitate and its surrounding is of interest, using electron diffraction and EDS, the metal-oxide interface is localised and the precipitate analysed on both sides of the interface.

Smaller precipitates in the oxide scale can be difficult to observe, as their size is similar to the matrix oxide grain size. For these precipitates tilting can improve the contrast, their presence needs to be validated by EDS point analysis, as the microstructural features observed often cannot be unambiguously identified as precipitates without additional information and electron diffraction on such small objects without matrix contribution is very difficult.

The change of the oxygen content of the material at the metal-oxide interface is investigated by performing chemical point analyses from the oxide to the metal. To obtain information about the lateral distribution of alloying elements for example at the metal-oxide interface and at the surface, EDS mapping is carried out. Additional to qualitative and quantitative information of points of interest EDS point analyses are also used to assess the level of gallium contamination from the FIB milling process to judge the validity of the findings. The milling direction in the FIB during sample preparation has to be considered to differentiate between milling induced artefacts and features originally present in the specimen.

3.4.5 Energy dispersive x-ray spectroscopy

Energy dispersive x-ray spectroscopy (EDS) is applied in both SEM [259] and TEM [262] for chemical analysis. Of interest for this analysis technique are the characteristic x-rays which have a specific energy for the element from which they are emitted. The characteristic x-ray lines can be used to map the distribution of different elements in the sample and to quantify the elements present.

The INCA EDS system from Oxford Instruments was installed on both SEM and TEM at PSI. On both microscopes point analysis, line scans and mapping of elemental distributions are possible. On the TEM the EDS software requires the specimen thickness and density as input for quantification. On the SEM measurements with known standards under the same conditions are necessary to allow quantitative analysis.

3.4.6 Microhardness

Indentation hardness testing is the most often applied method for hardness measurements. The basic principle of indentation hardness testing is the observation of the investigated material's ability to resist plastic deformation from a standardised indenter. The Vickers test can be used for all metals and many other materials and covers one the widest hardness range of all hardness tests.

For the microhardness test, performed with the MHT-4 microhardness tester mounted on the optical microscope (Jenaphot 2000 by Zeiss) in the hotlab of PSI, the following procedure was applied: the load was increased with 0.01 N/s until the final load of 0.1 N was reached and then the load was hold for 10 s at this level and then released. The indent diagonals were measured manually on a digital image recorded by the camera and converted into the corresponding Vickers hardness (HV).

3.4.7 Nanoindentation

The nanoindenter (Nano G200 by MTS Nano Instruments) can determine the hardness and other mechanical properties of samples such as Young's modulus [265]. Different indenters can be mounted, for the performed experiments a Vickers indenter was chosen. The Young's modulus is determined by the slope of the force versus indentation depth curve for the retraction of the indenter. Continuous Young's modulus versus indentation depth curves [266] can be obtained by superposition of the general applied indentation force with a small force oscillation, orders of magnitude below the indentation force. The experimental data were automatically acquired and processed by the MTS software according to the chosen test procedure.

3.4.8 Bulge test

The so-called bulge test is a method to determine the mechanical properties of a freestanding circular thin film supported on a substrate [267, 268]. The test principle is the following: on a freestanding circular thin film a uniform pressure is applied from the back side and the corresponding bulge height is measured.

In the set-up used the bulge height is determined by scans of the freestanding circular thin film and its surrounding with a laser interference microscope. Acquiring several pressure bulge height pairs and applying Equation 4 to a least-squares fit of the resulting curve, the modulus of elasticity (E) and the residual stress (σ_0) in the thin film can be obtained. The requirements for this equation to be valid is a real circularity of the freestanding membrane and that only the membrane deforms, otherwise the mechanical properties of the compound of thin film and substrate are analyzed. In Equation 4 p stands for pressure, ν for Poisson's ratio, E for modulus of elasticity, s_0 for the residual stress, t_0 for the initial membrane thickness, r for membrane radius and z for bulge height.

$$p = \frac{8(1-0.24\nu)Et_0z^3}{3(1-\nu)(r^2+z^2)^2} + \frac{4\sigma_0t_0r^2z}{(r^2+z^2)^2}$$

Equation 4: Relationship between applied pressure and parameters of the tested membrane . [269]

To obtain reliable data with this experimental method, the surface should be as smooth as possible and the film should exhibit a well defined thickness beside the above mentioned requirements.

For the bulge test the sample is clamped with the freestanding membrane centred in a specimen holder with a pressure inlet on the bottom of the sample. The surface at the freestanding membrane and around the membrane is scanned with an optical interferometer

(Wyko NT1100 Optical Profiling System by Veeco [270]) using a tungsten halogen lamp. The diameter of the circular freestanding membrane should be maximum 1 mm to have coverage of a sufficiently large region around the membrane for the height measurement. The height of the bulge on the surface is measured by tuning the focal depth and acquiring interference images with the microscope mounted above the specimen (Figure 15).

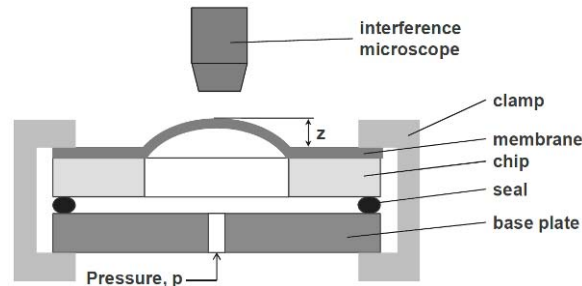


Figure 15: Experimental set-up for bulge test with z being the bulge height – courtesy [269].

Those images are converted by the Wyko Vision software [270] into 3D height profiles of the surface for each scan. The pressure supply is regulated by a pressure gauge, allowing the application of a controlled overpressure, with respect to atmospheric pressure. Starting from ambient pressure, the pressure is raised in steps of few millibars, after each pressure change a height profile of the surface is acquired with the interference microscope, resulting in overpressure versus bulge height data sets (Figure 16).

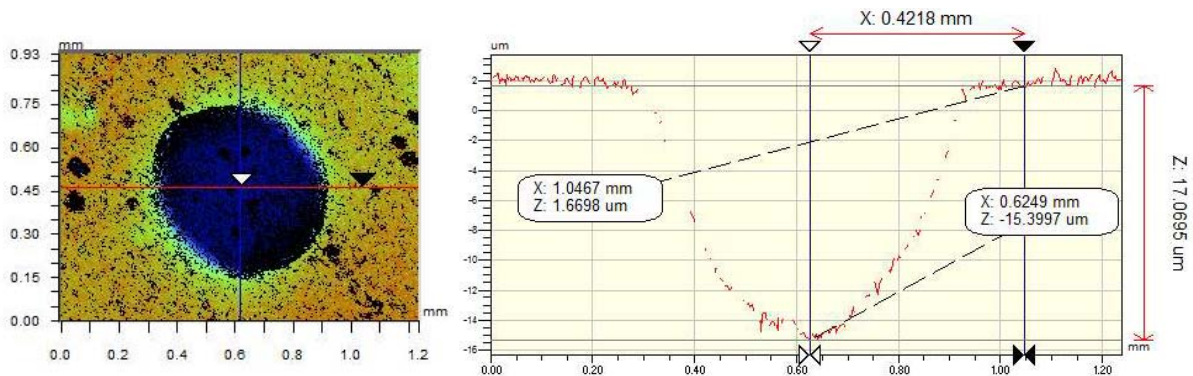


Figure 16: Height profile as obtained from interference microscope and corresponding section in x -direction as obtained by the Veeco Vision software [270].

4 Characterisation of as received material and oxidation experiments

4.1 Characterisation of precipitates in as received material

In this chapter the experimental results obtained using the different methods described in the previous chapter will be presented. The results are classified into microstructural findings concerning the precipitate oxidation and mechanical properties of the formed zirconia. The microstructural information is presented for the oxidation conditions for the analysed materials, to allow a better overview of the obtained results. Within each section the results are presented for each alloy and then compared with each other, with a short discussion of the reliability of the results for each section.

4.1.1 Precipitate size

Precipitate sizes for the investigated materials have been reported in the paper of Barberis et al. [10]. A precipitate size analysis on electro-polished TEM samples was performed. Materials oxidised in air were used for this analysis. In Table 8 the results for the precipitate size distribution are presented.

Table 8: Precipitate size from electro-polished TEM samples. Metal grain size data except for Zr0.6%Nb from [10].

	Zr1%Fe	Zr1%Ni	Zr1%Cr	annealed Zr1%Cr	Zr0.6%Nb
average precipitate diameter / nm	261	252	35	89	47
standard deviation / nm	229	120	17	40	24
median / nm	167	240	30	80	43
minimum diameter / nm	23	31	9	23	10
maximum diameter / nm	861	597	126	282	145
number of measured precipitates	111	109	624	293	286
average metal grain size / μm	3.1	4.6	5.2	-	4.4
standard deviation / μm	1.0	2.2	2.9	-	1.6
number of measured grains	-	-	-	-	55

Comparing them with the data provided by Barberis et al. [10], the data matched well for Zr1%Ni, 252 nm from our analysis to 249 nm. For Zr1%Fe (261 nm / 395 nm) and Zr1%Cr (35 nm / 56 nm) they deviated from the given values. For Zr1%Fe the results on the electro-polished TEM sample showed a peak of the precipitate size around 100 nm diameter with an asymmetric distribution exhibiting a tail towards large precipitate diameters (Figure 17), while for Zr1%Ni with a similar average precipitate diameter the overall size range is not as broad and the median diameter is close to the average diameter. For the precipitates in Zr1%Cr the difference in average diameter of 56 nm (our value was 35 nm) is most probably due to the different methods for their precipitate size analysis (SEM [10] and not TEM), the detection limit (see [271]) was reported to be ~ 50 nm, which explains the reported average diameter. For Zr0.6%Nb no information was provided by CEZUS for the precipitate size and type, the analysis showed a peak of the precipitate size distribution around 40 nm with an

asymmetric tail towards larger precipitate diameters.

Plots of the precipitate size distribution for Zr1%Fe and Zr1%Ni are provided in Figure 17, showing the broader size range of the Zr₃Fe precipitates compared to the Zr₂Ni precipitates.

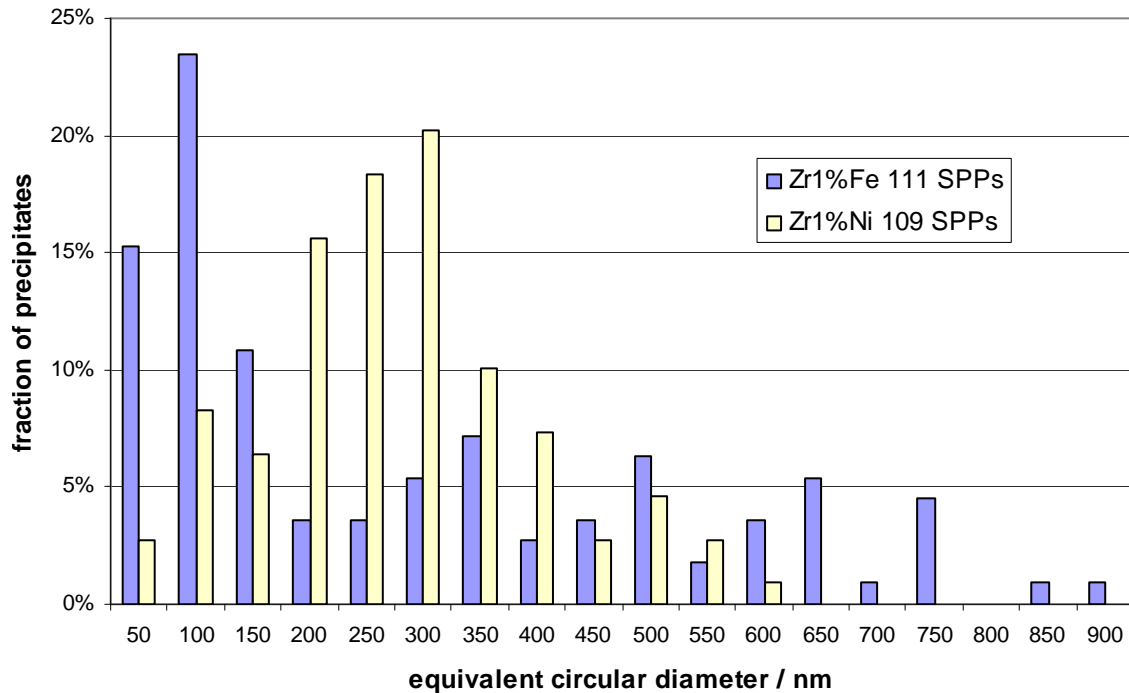


Figure 17: Precipitate size distribution for Zr1%Fe and Zr1%Ni. Fraction of precipitate falling in a certain size range (50 nm) is plotted against the equivalent circular diameter.

In Figure 18 the corresponding plots are shown for ZrCr₂ and β -Nb precipitates. The ZrCr₂ precipitates exhibit a higher fraction of small precipitates than the β -Nb precipitates, whose size distribution is also broader, being reflected by the larger standard deviation of the precipitate size (Table 8).

To be able to study the oxidation behaviour of the precipitates in Zr1%Cr in the oxide and at the surface, larger precipitates than those present in the provided material were required, as the small precipitates could not be unambiguously identified at the surface and no distinction of oxidised and unoxidized precipitate parts was possible. Therefore an annealing treatment at 730°C for 48 hours was performed under argon atmosphere in a retort furnace (CP 1050-3-P2 by Borel [254]), which led to a significant increase in precipitate size (Table 8), allowing the study of precipitate oxidation close to the outer surface and the influence of precipitate size on the oxidation behaviour.

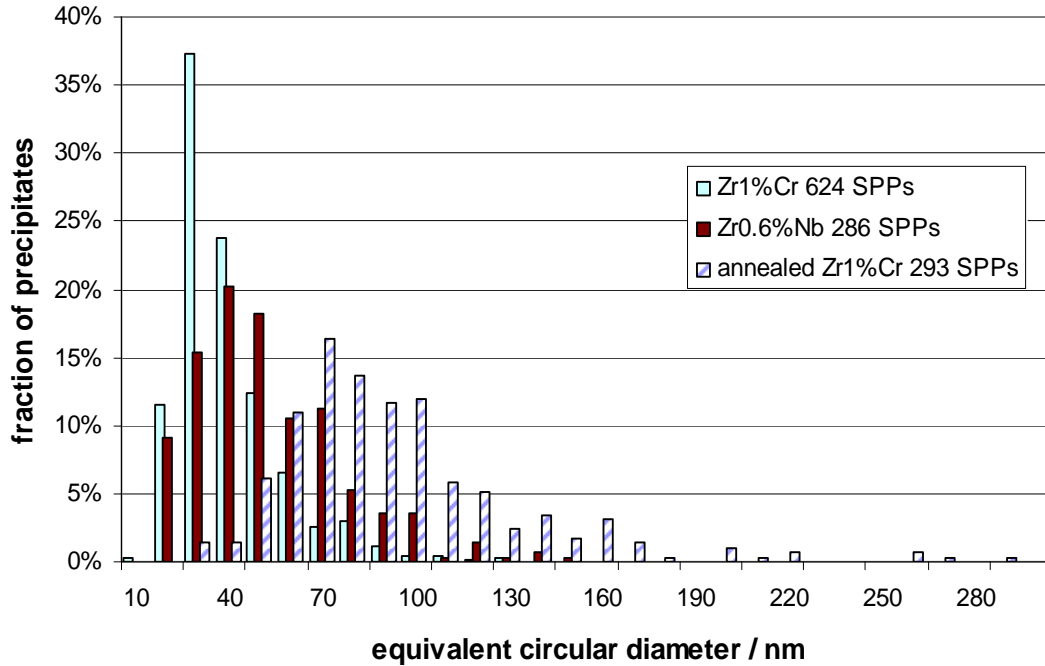


Figure 18: Precipitate size distribution for Zr1%Cr and Zr0.6%Nb. Fraction of precipitate falling in a certain size range (10 nm) is plotted against the equivalent circular diameter.

4.1.2 Precipitate composition

The precipitate composition was evaluated on different types of TEM samples, as different preparation methods can produce different artefacts. The preparation procedures used for those samples on which precipitate composition was checked with EDS were electro-polished samples and focussed ion beam milled samples.

The criteria by which precipitates were selected for this analysis were a) large size and b) as far as possible in thin regions of the TEM thin foil sample. Only large precipitates were selected for TEM studies to assure full presence of the precipitate in the TEM thin foil, therefore in the case of Zr1%Cr the annealed sample was taken, for the other alloys the as received material.

Table 9: Ratio of zirconium to alloying element content in precipitates, as determined by EDS measurements on electro-polished and FIB samples. Quantification performed using default line selection of the INCA software (Fe, Cr and Ni K-line and Zr and Nb L-line). Precipitate type was identified by electron diffraction by Cezus [10]. In Table 10 the ratio of zirconium to alloying element content in precipitates is shown for quantification with Zr-K and alloying element K-line.

alloy	precipitate type	crystal structure	alloying element at%	Zr at. %	Zr/alloying element ratio
Zr1%Fe	Zr ₃ Fe	orthorhombic	14.2	57.5	4.0
Zr1%Ni	Zr ₂ Ni	tetragonal	23.8	57.8	2.4
Zr1%Cr	ZrCr ₂	cubic	57.1	38.7	0.68
Zr0.6%Nb	β-Nb	bcc	50.2	12.7	0.25

The quantification with the Zr L-line and the K-lines of the alloying elements Fe, Cr and Ni leads to considerably sub-stoichiometric precipitate compositions for these alloying elements, when comparing the obtained precipitate compositions with the ones generally assumed for the intermetallic phases. These alloying elements have considerably lower

energies when their x-ray lines originating from the same shell are compared with the x-ray lines of Zr.

Only for Nb the quantification yields results matching the expected Zr/Nb ratio. Zr and Nb have similar line energies and therefore the default selection of x-ray lines for quantification does not seem to cause problems, as the L-lines of both elements are used. Therefore only for the Nb containing precipitates the quantitative information is reliable with the limitation inferred by the precipitate size (excess Zr signal from surrounding matrix for small precipitates. The presence of β -Nb precipitates can be assumed, although other precipitates with lower Nb contents cannot be excluded due to the small size. The Zr/Nb ratio of 0.25 (Table 9) agrees quite well with β -Nb with approximately 80 at.%Nb and 20 at.%Zr. This was the most Nb rich single measurement, other measurements gave considerably lower Nb contents.

Table 10: Ratio of zirconium to alloying element content in precipitates as determined by EDS measurements on electro-polished and FIB samples with quantification using Zr-K and alloying element K-line (average of several precipitates).

alloy	Precipitate type	alloying element at%	Zr at. %	Zr/alloying element
Zr1%Fe	Zr ₃ Fe	18.1	48.7	2.7
Zr1%Ni	Zr ₂ Ni	29.5	54.7	1.9
Zr1%Cr	ZrCr ₂	65.3	30.1	0.46

Taking the obtained zirconium to alloying element ratios from EDS measurements with the K-lines of both zirconium and the alloying elements (Fe, Cr and Ni) for quantification into account, it can be stated that for electro-polished and FIB samples (Table 10):

- in the Fe containing alloy the precipitates have a zirconium to alloying element ratio around 2.7, which corresponds quite well to the reported intermetallic Zr₃Fe, also for this type of precipitates no interference of the matrix.
- in the Ni containing alloy the precipitates have a zirconium to alloying element ratio around 1.9, which corresponds quite well to the reported Zr₂Ni phase beside pure Zr in the composition range of interest. As large precipitates were analysed, the precipitate composition is considered to correspond to a signal purely from the precipitate.
- in the Cr containing alloy the precipitates have a zirconium to alloying element ratio around 0.46, which corresponds quite well to the reported intermetallic ZrCr₂, also for this type of precipitates no contribution of the matrix to the measured signal was expected (for annealed Zr1%Cr sample).

4.2 Oxidation experiments

The samples supplied by CEZUS [10], see column 1-3 in Table 11, cover oxidation in air and steam at 415°C and in the case of steam two different pressures. As the early stages of oxidation were of interest and no data were available, the oxidation in the environmental scanning electron microscope (ESEM) was selected for in situ experiments at low pressure and for short times (column 4&5 in Table 11), because this type of experiments enables the observation of the surface during the oxidation, so that the evolution of the surface with time is obtained. In addition to this oxidation experiments in steam at 10.5 MPa for times between 1 hour and 3 days (column 6-8 in Table 11) were performed in a small autoclave at PSI [272].

The in situ experiments in the ESEM enabled the observation of the surface during the oxidation and with oxidation pressures much lower than those accessible under normal autoclave conditions. The short time autoclave tests were performed in order to obtain data on the oxide formation during early stages of oxidation at high pressures.

In addition to the binary alloys and pure zirconium additionally Zircaloy-2 was included for some oxidation conditions so as to compare the precipitate oxidation behaviour of this commercial alloy with that of the binary alloys.

Table 11: Overview of all available samples with their oxide thickness given in μm . The oxide thickness of samples provided by CEZUS [10] (column 1-3 in grey) was determined from weight gain. The other samples were obtained from in situ experiments at CSEM (4-5) and autoclave oxidation experiments at PSI (6-8) and their oxide thickness has been measured on transverse sections (FIB or mechanically polished). This table is identical to Table 7 on page 39.

Alloy	Average oxide thickness / μm							
	air oxidation CEZUS			In situ ESEM in Neuchatel		steam oxidation at PSI Limbo 350 autoclave		
	3 days 415°C 0.1 MPa	steam oxidation CEZUS		1 hour 415°C 130 Pa	1 hour 700°C 130 Pa	1 hour 415°C 10.5 MPa	1 day 415°C 10.5 MPa	3 days 415°C 10.5 MPa
		3 days 415°C 0.1 MPa	110 days 415°C 10.5 MPa					
Zr0.2%Fe	0.67	1.61	4.19	—	—	0.42	1.08	—
Zr1%Fe	1.01	1.37	5.00	0.32	3.2	0.62	1.14	1.53
Zr1%Cr	0.79	1.08	4.23	0.35	2.7	0.52	0.94	1.28
Zr1%Ni	0.93	1.26	4.15	0.41	2.8	0.49	—	—
Zr0.6%Nb	6.02 (55 days)	2.58 (40 days)	—	0.34	3.2	0.40	—	—
Pure Zr	0.63	4.12	—	0.27	2.4	0.62	0.88	—
Zry-2	—	—	—	—	—	0.40	1.15	—
Zry-4	—	—	6.36	—	—	—	—	—

4.2.1 In situ oxidation in ESEM

In the frame of the in situ oxidation experiments oxide thickness and the roughness of the oxide surface were measured and features of interest on the surface characterised. The results of the different characterisation techniques are presented in chapter 5, summarised in Table 12 on page 86.

4.2.2 Autoclave oxidation

The autoclave oxidation of small test specimens was performed in a Limbo 350 autoclave from BüchiGlasUster [253] at PSI. The temperature was raised as fast as possible to the desired oxidation temperature, with the pressure being regulated to remain within the 100-110 bar range. After the planned time at the oxidation conditions (1 h, 24 h and 72 h) the heating was switched off and the autoclave left to cool down to room temperature without external cooling, which took several hours (Figure 8). The results of these autoclave oxidation experiments were reported in more details in the master thesis report of Bhadri N.L. Srinivas [272]. Micrographs of $Zr_2(Fe,Ni)$ precipitates at the metal-oxide interface and in the oxide from these experiments are presented in section 8.2.1.

4.2.3 Furnace oxidation in air

The furnace oxidation in air at 415°C was applied to Zr1%Cr (annealed) and Zr1%Ni for 1 hour and to Zr1%Cr (annealed) and Zr1%Fe for 24 hours. The aim of these oxidation experiments was in the case of Zr1%Cr and Zr1%Ni to observe the different oxidation behaviour of samples with neutral diamond slurry polish as last polishing step and samples polished with a basic solution in the Vibratory polisher . The 24 hour oxidation experiments were performed to judge if a formation of alloying element oxide at the surface takes place without water vapour in the atmosphere and if the amount of alloying element oxide was increased with respect to shorter oxidation times. The observations of the surface and the microstructure for these samples are presented in section 8.1.2.

5 Microstructure of in situ oxidised alloys

5.1 *In situ oxidation at 415°C*

The in situ oxidation experiments at 415°C were performed to obtain experimental insight into the early stage of oxidation for the same temperature at which the autoclave experiments were conducted and observe the surface evolution and possible crack formation. The observation of the oxidation process in the ESEM allowed also determining the time scale of processes taking place, which is otherwise impossible for corrosion experiments and very short oxidation times. In the following the results will be presented for each type of alloy. The images acquired during the in situ experiments are presented for all cases except for Zr1%Cr as received.

5.1.1 Zr1%Fe

5.1.1.1 *In situ oxidation*

Before the oxidation some precipitates were already visible with the GSE detector (Figure 19a), showing that these precipitates are in contact with the outer surface. Those precipitates being visible before the oxidation experiment exhibited a much brighter contrast and were therefore well distinguishable on the oxidising sample (Figure 19b) during the first minutes of the experiment. The evolution of the surface concerning these features is almost complete after 14 minutes at 415°C (Figure 19b), with only few more precipitates appearing after that time (Figure 19b-c). After this oxidation time the evolution of small particles showing a bright contrast on the larger features can be observed to develop with oxidation time, which can be confirmed by the comparison of images taken after 14 and 54 minutes of in situ oxidation (Figure 19b-c); two such particles are marked on the inset of Figure 19c with arrows. The subsequent cooling process does not lead to significant surface changes (Figure 19d). It should be noted that the size of the large features remained relatively constant throughout the oxidation process and only their visibility increased with time. The size of the small particles on top of the features increased with oxidation time and they were not observed at the beginning of the experiment. The presence of cracks was not observed during the in situ oxidation and during cooling to room temperature.

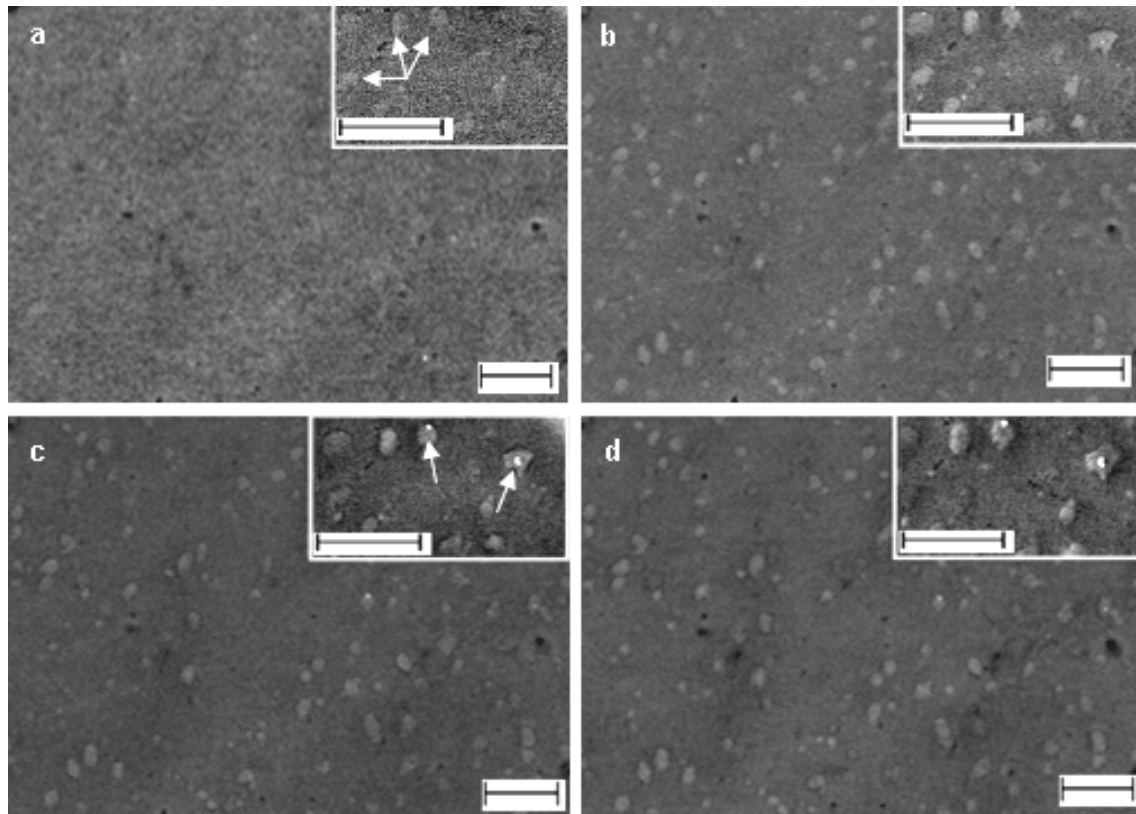


Figure 19: The GSE images of Zr1%Fe oxidised at 415 °C show the surface (a) as observed before oxidation, (b) in situ after 14 minutes, (c) in situ after 54 minutes, (d) after cooling down to room temperature. Insets show regions imaged at higher magnification. All scale bars correspond to 5 μm .

5.1.1.2 Atomic force microscopy

To quantify the changes taking place on the surface, the surface roughness of the oxidised surface was compared with the roughness of the polished surface as obtained by AFM surface profiles. This comparison confirmed a surface roughening during the oxidation process, as the roughness mean square of the surface increased from 3.9 nm before to 21.2 nm after oxidation (Figure 20). The local change in surface topography before and after oxidation is presented in Figure 20 for Zr1%Fe. The features observed in AFM before oxidation, two being marked with arrows in Figure 20a, cannot be linked to the presence of precipitates (i.e. black arrows in Figure 20a and same positions in Figure 20b). This can be concluded from the direct comparison of AFM profiles acquired from the same region of the polished and oxidised surface.

The sections of the surface profiles on Zr1%Fe presented in Figure 20c&d reveals the drastical change in surface topography during the first hour of oxidation, the location of the sections is indicated in Figure 20a&b. Before oxidation at 415°C, no protrusions higher than 4 nm are present in this section: after oxidation the two observed protrusions have been measured to be 70 nm high. A saturation is assumed, as no distinct change of the features is observed in the ESEM after some time (Figure 20b&c). The average height of the protrusions after oxidation for 1 hour has been measured on 10 AFM profiles to be ~68 nm (Table 12). Sufficient statistics cannot be obtained from this number of profiles and the reported height is to be compared to the results obtained for the other materials under similar conditions.

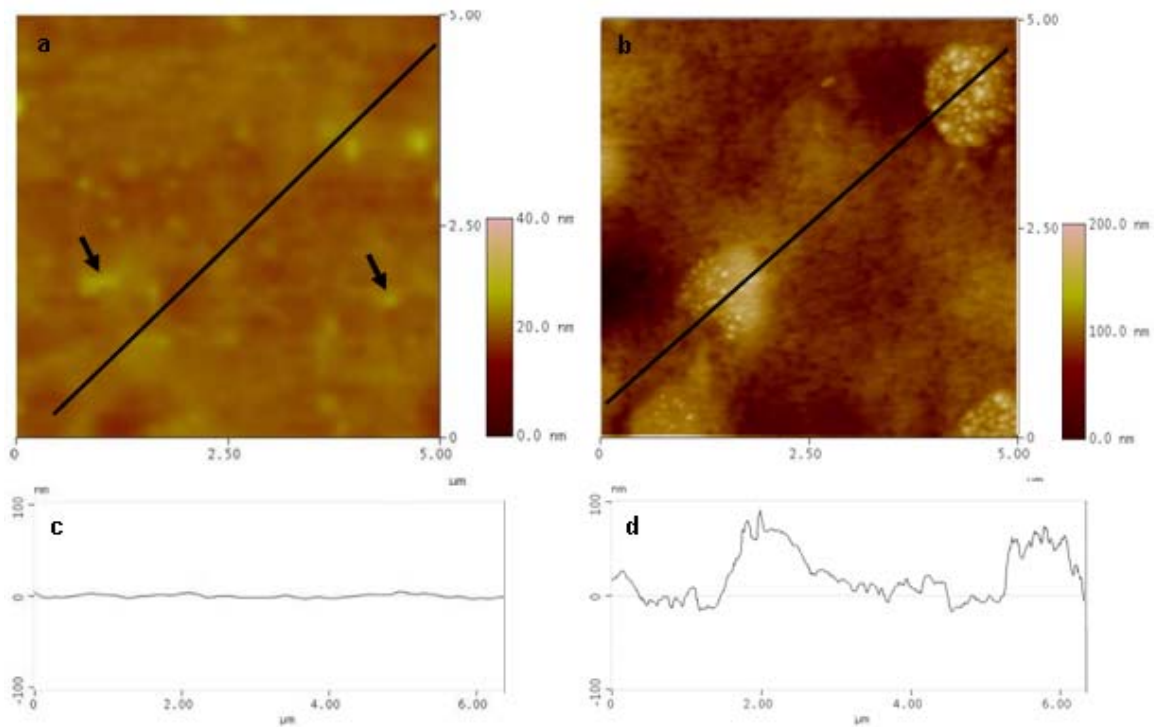


Figure 20: AFM surface profile on Zr1%Fe (a) polished surface at room temperature (lower resolution than (b)), (b) same region after oxidation and cooling to room temperature. The AFM line profiles (c) and (d) represent the sections marked on the surface profiles (a) and (b) respectively.

5.1.1.3 SEM and EDS after oxidation

The mean diameter of the features on the surface was determined to be $\sim 1 \mu\text{m}$, the largest observed being $1.8 \mu\text{m}$. Because the features observed are not perfectly circular, the given diameters are average diameters for corresponding circular features.

In Figure 21 an example for the characterisation of the features developed during oxidation on the surface of Zr1%Fe is shown. EDS point analyses after cooling confirmed the presence of Fe at the positions of features on the surface, while beside them no Fe was detected. The majority of protrusions exhibit only some small particles (Figure 21a and Figure 20b); while some are densely covered with crystals of up to 100 nm in diameter (Figure 21b). The EDS analysis of these crystals shows a higher Fe signal in comparison with protrusions without crystals. The presence of features appearing during the in situ oxidation at the surface was subsequently linked to precipitates for Zr1%Fe using EDS point analyses and EDS mapping.

Comparing Figure 20 and Figure 21 showing the same position on the sample surface, it can be concluded that the features observed in SEM correspond to the protrusions observed in AFM.

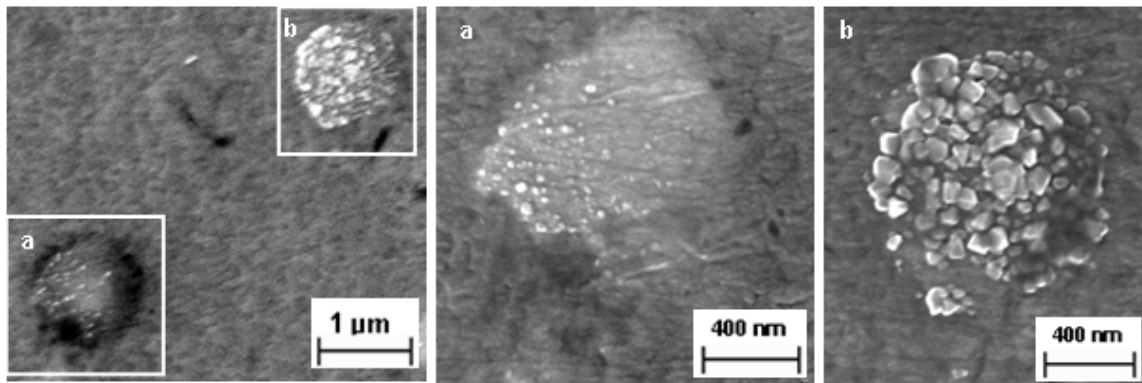


Figure 21: SEM micrographs of features on the oxidised surface of Zr1%Fe as observed with SE detector. The regions marked (a & b) are presented at higher magnification in (a) and (b) respectively.

The regions with presence of iron on the EDS map (Figure 22) were well correlated to the presence of features on the surface observed on the SEM image. However, some regions in which the presence of iron was observed did not exhibit features visible on the surface. To check the information depth of the EDS signal obtained at 20 kV acceleration voltage, simulations of the electron trajectories in the material were made using CASINO V2.42 [273]. CASINO is a Monte Carlo simulation software for the electron trajectories and generated X-rays in matter. The penetration depth of 20 keV electrons into Zr was calculated to be up to 1 µm, electrons having 4% of the original energy in that depth, and the X-ray from the K-line of Fe, Cr and Ni will escape from a maximum depth of 730 nm (90% of overall signal). The oxide thickness on Zr1%Fe is ~ 320 nm (Table 12) and the oxide density (5.6 g/cm³) is lower than the density of zirconium metal (6.5 g/cm³), so the escape depth is higher than the values given above. The detected EDS signal can therefore originate from precipitates underneath the oxide layer, which will not be observable at the outer surface but on the EDS map.

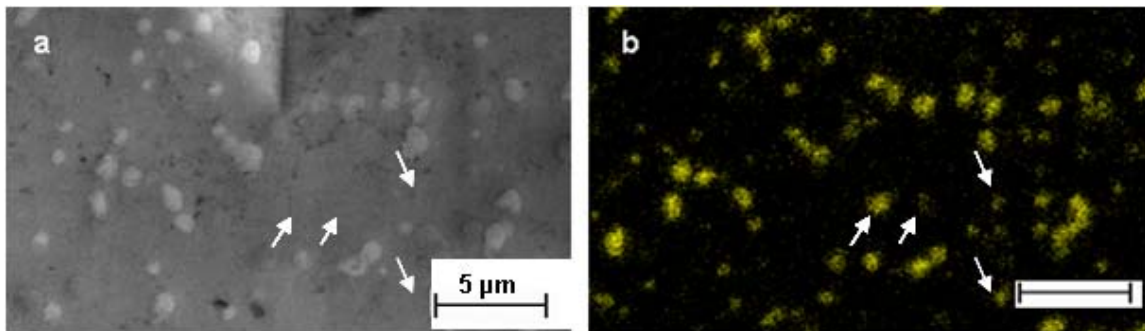


Figure 22: Zr1%Fe oxidised for 1 hour at 415 °C (a) SE image (b) EDS map of Fe K-edge. Arrows indicate regions with iron signal with no feature at the surface.

5.1.1.4 FIB transverse sections

The protrusions on the surface correspond to the underlying precipitates as shown by EDS, which can also be confirmed on FIB transverse sections, on which positions with protrusions on the surface are always connected to regions underneath identified as precipitates, which is shown in Figure 23 by the black arrow in the FIB transverse section (precipitate) and the white arrow on the oxide surface (protrusion). The bright contrast of the edge is due to the

FIB milling and the edge effect and can be minimised by the use of low milling currents. The oxide thickness appears to be homogeneous throughout the whole sample, a similar oxide thickness was observed at different locations on the oxide. The metal-oxide interface is undulated and the amplitude of the undulation is often higher at the sites of oxidised precipitates.

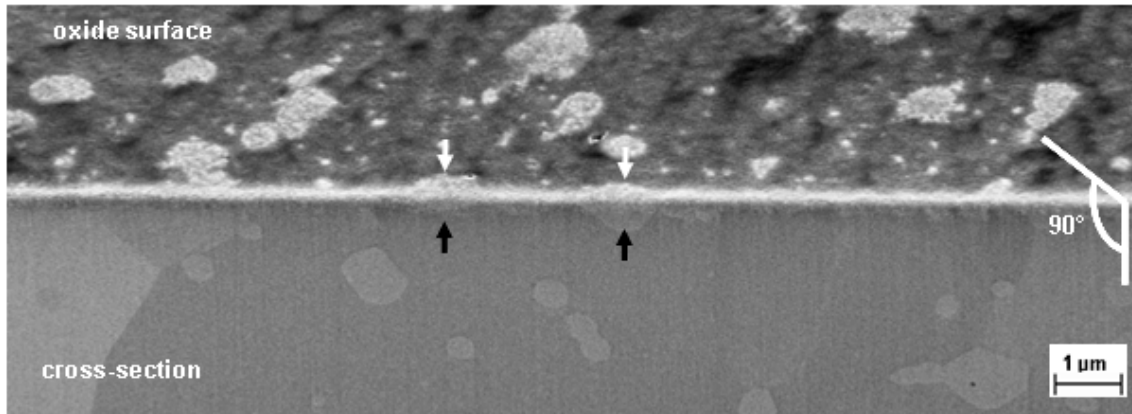


Figure 23: FIB transverse section of Zr1%Fe sample. In this section features on the surface (white arrows) can be directly linked to the underlying precipitates (black arrows).

5.1.1.5 Transmission electron microscopy

Further characterisation of the metal-oxide interface and the precipitates was performed by TEM to obtain microstructural and chemical information at higher resolution than in the SEM.

A TEM transverse section of oxidised Zr1%Fe is presented in Figure 24. The oxide layer on the matrix and the thicker oxide at oxidised precipitates in contact with the outer surface can be well distinguished in the dark field contrast of the oxide; arrows depict the metal-oxide interface. A closer examination of the oxide microstructure at the oxidised precipitate revealed a fine-grained, equiaxed oxide. The pure zirconia formed on the zirconium matrix has a columnar grain structure.

The nature of crystals formed on the surface at the protrusions (as shown in Figure 20b and Figure 21c) has been examined on a TEM sample prepared with special care to protect the outer surface on the site of the crystals. Figure 24a shows this TEM sample and Figure 24b the crystals with heights between 25 and 55 nm present at the surface above an oxidised precipitate. The electron diffraction pattern of the iron oxide crystal (Figure 24 I) marked with an D in Figure 24b exhibits a well defined pattern which could be identified as a [0-22] zone-axis of a cubic structure (magnetite $a = 0.83950$ nm [274] / maghemite $a = 0.8347$ nm [275]) with 111, 200 and 113 spots present, quite different to the diffraction obtained from the underlying oxidised precipitate (Figure 24 II).

For precipitates underneath the outer surface (Figure 25) the observed oxidation is similar to the surrounding zirconium matrix, the oxidised part exhibits a similar small grained equiaxed oxide microstructure as observed also for those precipitates in contact with the original surface.

Two types of oxidation behaviour can be observed for the precipitate oxidation in Zr1%Fe:

1. For precipitates in contact with the outer surface the oxide thickness is greater than on the matrix and the precipitates are oxidised to a larger extent than the matrix (Figure 24a).
2. For precipitates underneath the original surface observations show an oxidation more or less similar to the zirconium matrix (Figure 25).

For the precipitates in category 1 iron diffusion to the outer surface and the formation of iron oxide crystals can be observed for some precipitates. The extent of iron diffusion and oxide formation is different from one precipitate to another; the parameters being responsible for this could not be identified. For precipitates falling in category 2 it cannot be excluded that in their case a certain amount of diffusion takes place also from the precipitates below the outer surface. Observations clarifying this point have not been made, as all iron oxide crystals were observed on the aforementioned protrusions, which are related to the precipitates in contact with the surface. Metallic bcc iron in the oxide at the interface of oxidised precipitate and zirconia, as reported e.g. by Pecheur et al. [179], has not been observed.

The two categories of precipitate oxidation are also confirmed by the FIB observation of several tens of precipitates, which showed a thicker oxide if initially in contact with the outer surface, leading to the formation of oxide undulations at the metal-oxide interface and similar oxidation similar to the surrounding matrix if not in contact with the surface.

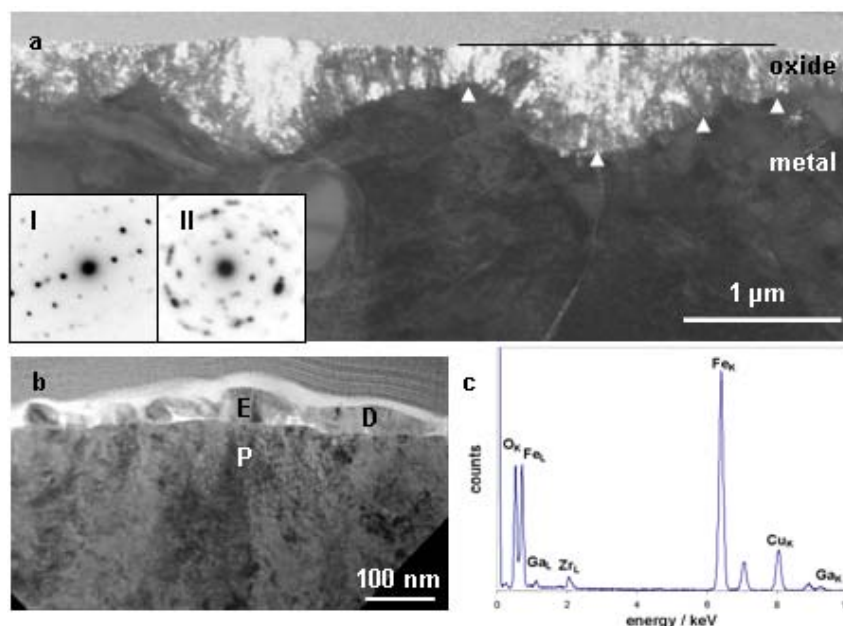


Figure 24: (a) Dark field contrast of Zr1%Fe. Oxide interface undulations and surface protrusions can be observed at the precipitate in contact with the surface (black line as reference for flat surface). The white arrowheads mark the metal-oxide interface. (b) Bright field contrast showing iron oxide crystals formed on the oxide surface. (c) EDS spectrum of crystal in (Figure 24b) at position marked by E. The Cu signal is from the FIB-TEM grid and the gallium signal from implantation during TEM sample preparation. At E the composition is 63.5 at% O, 34 at% Fe and 2 at% Zr and at P 69 at% O, 3.5 at% Fe and 27 at% Zr. The two insets in (a) show the electron diffraction pattern of a iron oxide crystal (I) at position D and the oxidized precipitate underneath (II) at position P.

The height of protrusions on the surface caused by oxidised precipitates can be measured on TEM micrographs, for example in Figure 24a the height of the protrusion is ~ 95 nm measured on the precipitate with a black line inserted as reference for a flat surface. Height measurements for precipitates in another region gave a height of ~ 60 nm for the protrusion (Figure 24b) and additional 55 nm for the thickest iron oxide crystal. These results are in the same range as the values obtained by AFM for the protrusions (Figure 20d). A comparison of the two methods shows that in TEM a separation of the protrusion height and the iron oxide layer above is possible, while in AFM only the total height can be measured and the lateral extension of the surface oxide protrusions has to be estimated (half of maximum height was chosen, as this is clearly observable).

The EDS analysis of the TEM samples provided the following information:

The crystals formed at the surface consist of almost pure iron oxide. Only small amounts of zirconium and gallium have been detected (Figure 24c) for the crystal marked with E in Figure 24b, the first being due to the width of the electron beam during EDS measurements and the latter due to contamination from the TEM sample preparation process by FIB.

For precipitates in the oxide, iron and oxygen EDS signals indicated that the precipitates are oxidised (Fe: 10-15 at.%, O: 60 at.%, Zr 25-30 at.%), electron diffraction confirmed this observation. Therefore in the case of Zr1%Fe, no metallic precipitate was observed in the oxide. The precipitate underneath the iron oxide crystals at the surface are depleted in iron, 3.5 at% Fe and 27 at% Zr were detected there.

Precipitates in the underlying metal near the metal-oxide interface showed an oxygen concentration similar to the surrounding matrix (Fe: 20-30 at.%, O: 10-20 at.%, Zr 50-60 at.% at precipitate and oxygen in matrix in a similar range at same distance to the metal-oxide interface). In other words the EDS point line scans in the metallic precipitates showed no oxygen enrichment with respect to the zirconium matrix.

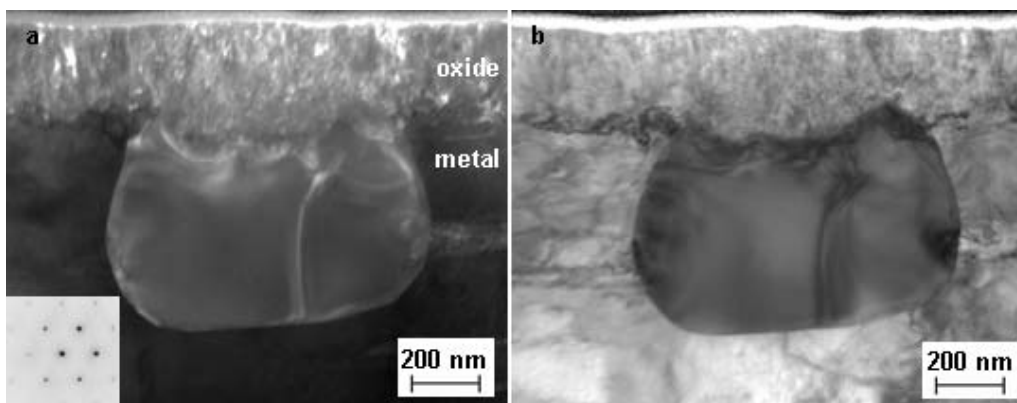


Figure 25: (a) Dark field contrast and (b) bright field contrast of partially oxidized precipitate at the metal-oxide interface of Zr1%Fe. Diffraction pattern from the metallic precipitate shows a $[6\ 2\ -4]$ zone axis of orthorhombic Zr_3Fe part.

5.1.2 Zr1%Ni with diamond finish

For Zr1%Ni several in situ oxidation experiments were performed for 1 and 2 hours of oxidation time and also with slightly modified surface preparation. The reason for the higher number experiments compared to the other materials was the uncertainty about the behaviour

of Ni in precipitates close to the surface, which was not as obvious as in the case of Zr1%Fe. Two of the three experiments performed at 415°C were with the same surface preparation as for Zr1%Fe for 1 and 2 hours oxidation time; the longer oxidation time was chosen in order to allow more time in case the processes observed on Zr1%Fe were slower on Zr1%Ni.

The third experiment was performed on a sample with an additional finishing with Vibratory polisher finishing with a slurry (pH 9.5), which resulted in a smoother surface finish compared to the only diamond polished surface.

As the results of the three experiments are similar for those with similar surface preparation, the results for the 2 hour oxidation are only presented for additional information in the part with the results for the 1 hour oxidation with diamond polishing as finish.

5.1.2.1 *In situ oxidation*

For Zr1%Ni the features visible before oxidation in SEM are precipitates at the outer surface (Figure 26a). Comparing the images acquired before (Figure 26a) and during the in situ oxidation (Figure 26b-c), it can be concluded that these precipitates still remain visible, but their contrast with respect to the matrix decreases and the changes of the surface during oxidation are mainly due to the oxidising zirconium matrix. No evolution of the surface can be observed after the first 13 minutes to 54 minutes of oxidation (Figure 26b-c). The cooling process did not lead to significant changes on the surface and no crack formation was observed (Figure 26d).

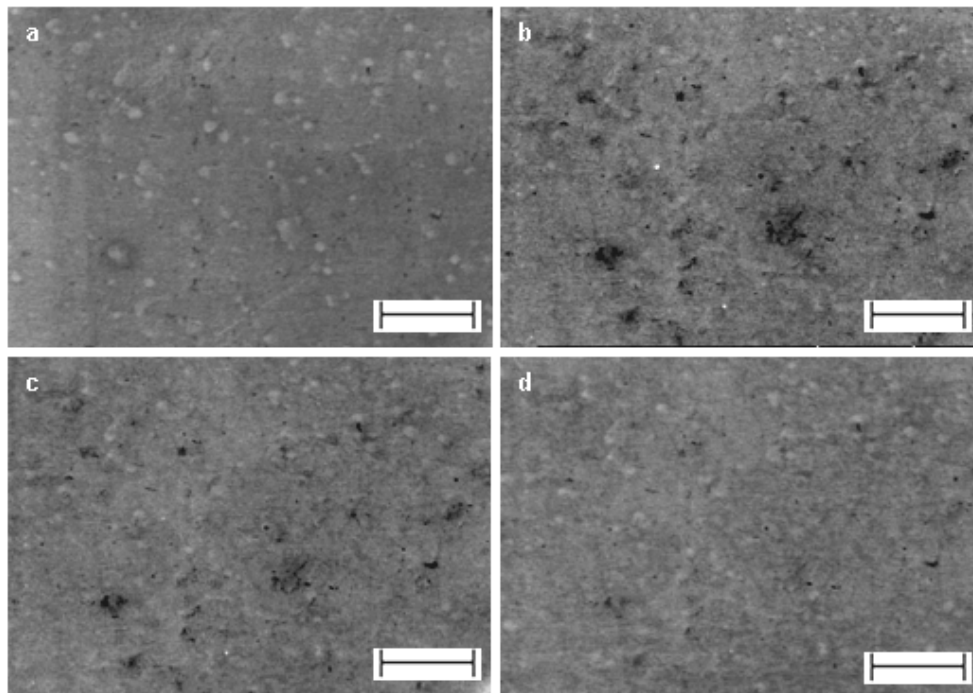


Figure 26: The images of Zr1%Ni (diamond polish) oxidised at 415 °C show the surface a) as observed before oxidation (SE detector), after (b) 13 and (c) 54 minutes in situ oxidation and (d) after cooling, as observed in SEM with the GSE detector. The scale bars correspond to 5 μm.

Most changes observed occurred during the first minutes after the start of the oxidation, on the precipitates no specific changes could be detected. The size distribution of the observed features remained relatively constant throughout the oxidation process.

A second oxidation experiment was performed for 2 hours to check if the protrusions would show small crystals on the surface above oxidised precipitates. For protrusions, in particular the larger ones, cracking of the surface could be observed, which was not the case after 1 hour of oxidation in the ESEM.

5.1.2.2 Atomic force microscopy

AFM scans revealed protrusions on the oxidised surface of Zr1%Ni. The average height of these protrusions is 20 nm (Table 12), as shown in Figure 27a. The height variation is presented (Figure 27b) for a section of the surface topography marked by a line in Figure 27a. The aspect of the surface oxide between the protrusions is rather flat with small undulations of the surface. The surface roughness increased after oxidation to twice its original value on the oxidised Zr1%Ni sample (Table 12), with the roughness mean square increasing from 5.2 nm before to 10.3 nm after oxidation.

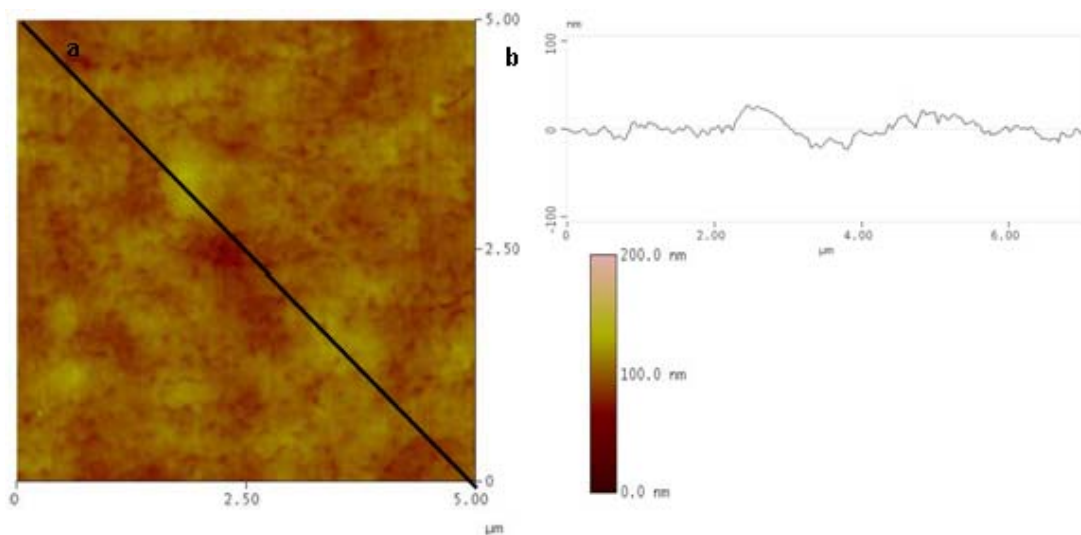


Figure 27: AFM surface profile (a) of oxidised Zr1%Ni exhibiting protrusions on the surface sticking out ~20 nm. (b) AFM line profile on Zr1%Ni with RMS of 14 nm, see black line for the position.

5.1.2.3 SEM and EDS after oxidation

Comparison of SEM images with visible protrusions at the surface and EDS signals showed for Zr1%Ni a correlation of the Ni rich points with the observed protrusions. Not all Ni rich regions on the EDS map correspond to a clearly observable protrusion. This could be either because some protrusions might not be recognisable, or because the information depth of the x-rays is deeper than the oxide thickness, showing the presence of precipitates not in contact with the outer surface.

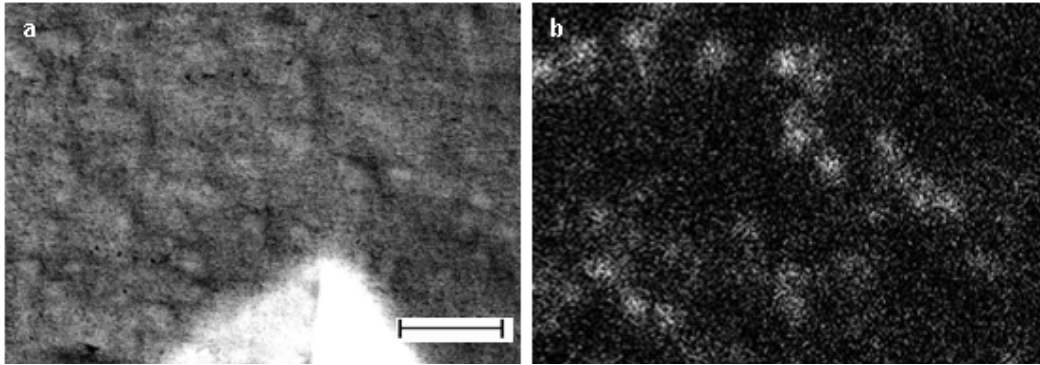


Figure 28: Zr1%Ni oxidised for 1 hour at 415 °C (a) SE image (b) EDS map of Ni K-edge. The scale bar corresponds to 3 μm .

On the protrusions above oxidised Ni-containing precipitates no nickel was observed after 1 and 2 hours of oxidation. The oxide on protrusions after oxidation for 2 hours showed in some cases cracks, as shown in Figure 29. The protrusions exhibiting cracks at the oxide surface are also the largest protrusions visible, smaller protrusions have been less frequently observed to exhibit a cracked oxide surface.

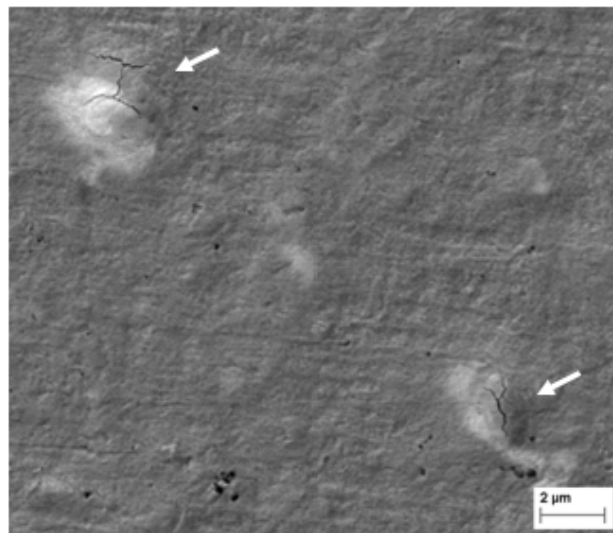


Figure 29: SEM micrograph with cracked oxide on some protrusions on Zr1%Ni (marked with white arrows) after oxidation in ESEM for 2 hours.

5.1.2.4 FIB transverse sections

For Zr1%Ni higher amplitude of undulation of the metal-oxide interface has been observed at precipitates in contact with the outer surface. Precipitates not in contact with the outer surface exhibit an oxide thickness similar to the surrounding matrix at the metal-oxide interface, in other words, they are not preferentially oxidised. The contrast of the interface implied a metallic nature on the metal side and an oxidised on the oxide side. For both observations unambiguous proof can only be obtained in TEM. No specific features on the surface were correlated to precipitates in contact with the surface on the FIB transverse sections.

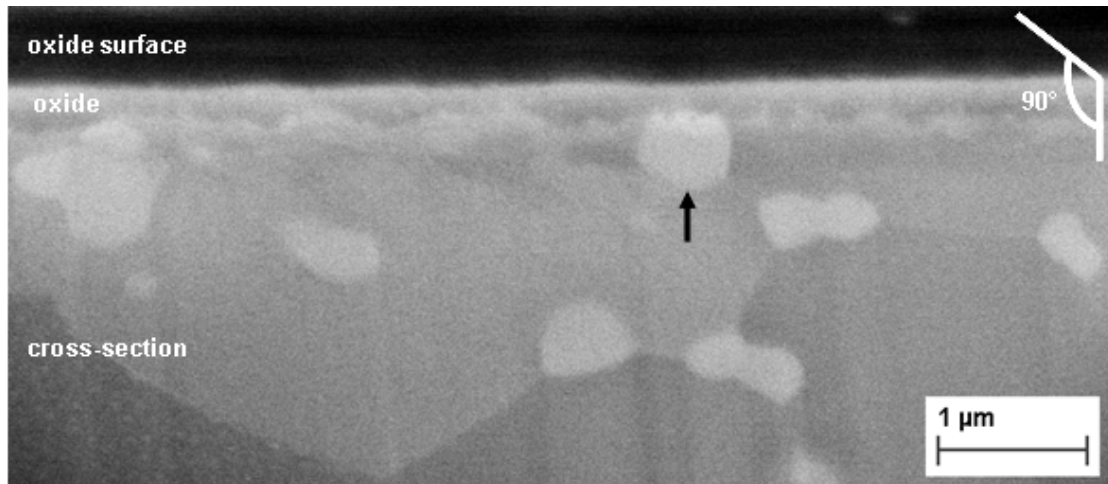


Figure 30: FIB transverse sections of oxide scale formed on Zr1%Ni. Precipitates at the metal-oxide interface (black arrow) were not found to be preferentially oxidised.

5.1.2.5 Transmission electron microscopy

A TEM transverse section of oxidised Zr1%Ni is presented in Figure 31. The precipitate at the metal-oxide interface can be well distinguished in the dark field contrast (Figure 31a), as well as the other precipitates present in the metal. A closer examination reveals that the precipitate at the metal-oxide interface (Figure 31b) is not oxidised in those parts in contact with the metal and the metal-oxide interface shape seems not to be influenced by the presence of the precipitate. The oxide at the oxidised precipitate is coarse-grained and equiaxed and the grain size is in the same range as the width of the columnar oxide grains on the matrix. The oxide layer is columnar and exhibits an undulation of the metal-oxide interface.

The EDS analysis of the TEM samples provided the following information:

Precipitates in the oxide showed nickel and oxygen signals indicating that the precipitates are oxidised (Ni: 10 at.%, O: 60 at.%, Zr 30 at.%). In the case of Zr1%Ni, no metallic precipitate was observed in the oxide.

The precipitates in the underlying metal showed an oxygen concentration similar to the surrounding matrix (Ni: 25 at.%, O: 10 at.%, Zr 65 at.%). In other words the EDS point line scans in the metallic precipitates showed no oxygen enrichment with respect to the zirconium matrix.

In the case of Zr1%Ni, no Ni diffusion to the outer surface and formation of pure nickel oxide could be detected. This implies if any such phenomenon exists, that the diffusion is much slower than in the case of the Zr-Fe alloy. Another reason could be that evidence for the presence of Ni at the surface has been missed during the surface examination. The last point is unlikely, as the TEM samples were prepared at a sufficient distance from the FIB transverse sections and the surface was protected with platinum by electron assisted deposition.

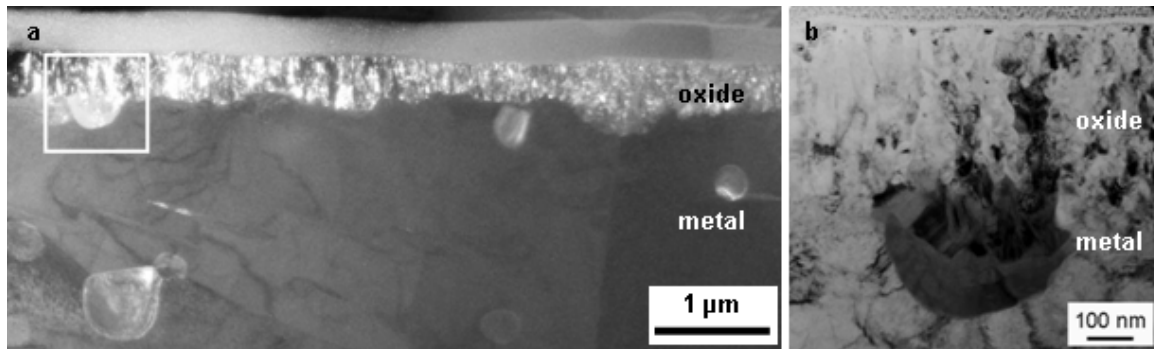


Figure 31: Dark field contrast (a) of Zr1%Ni. The precipitate at the metal-oxide interface is partially oxidised. (b) Bright field contrast of oxide and matrix, showing the unoxidized part of the Ni containing precipitate present at the metal-oxide interface in dark contrast.

5.1.3 Zr1%Ni with Vibratory polisher finish

The Vibratory polisher was used for the final polishing step of an additional test specimen, as it results in a smoother surface finish in comparison with the standard polishing method. However, the basic polishing solution of the Vibratory polisher was found to modify the surface and attack the precipitates preferentially, in some cases. Thus a difference in behaviour during oxidation can be observed and it exemplifies the influence of the final surface treatment before oxidation on the oxidation behaviour of the precipitates close to the surface.

5.1.3.1 In situ oxidation

For Zr1%Ni polished with the basic silica particles containing solution in the Vibratory polisher the features visible before oxidation in SEM are precipitates at the outer surface (Figure 32a). Comparing the images acquired before (Figure 32a) and during the in situ oxidation (Figure 32b-c), it can be concluded that these precipitates still remain visible, but their contrast with respect to the matrix decreases.

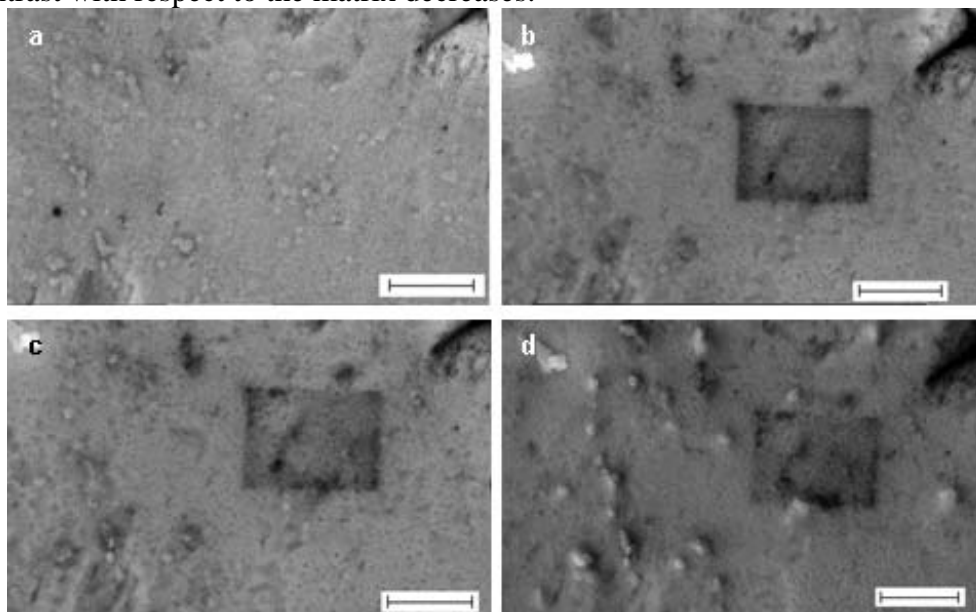


Figure 32: The images of Zr1%Ni (Vibratory polisher finish) oxidised at 415 °C show the surface a) as observed before oxidation (Se detector), after (b) 5 and (c) 15 minutes in situ oxidation (GSE detector) and (d) after cooling, as observed in SEM with the SE detector. The scale bars correspond to 5 µm.

As the oxidation time increases those precipitates become more prominent forming protrusions on the surface. On some of these small oxide crystals appear in the first 15 minutes of oxidation. After 15 minutes no evolution can be observed changing the surface appearance significantly, which was checked by comparing the images acquired up to 60 minutes and after cooling (Figure 32c-d). The image after oxidation (SE detector) does not have the same contrast as the GSE detector. During the observation with GSE detector, the surface did not show any change from high temperature to room temperature and during the cooling. The cooling process did not lead to significant changes on the surface and no crack formation was observed in situ due to cooling.

The significant changes were observed during the first minutes after the start of the oxidation, the reason why some precipitates formed crystals on the surface and the composition of these crystals could not be clarified during the in situ experiment.

5.1.3.2 Atomic force microscopy

AFM scans revealed protrusions on the oxidised surface of Zr1%Ni. For an example of such protrusions see Figure 33a and Figure 33c for an overview scan. The height variation at a protrusion is presented (Figure 33b) for a section of the surface topography marked by a line in Figure 33a. The aspect of the surface oxide between the protrusions is rather flat with small undulations of the surface. The vibratory polisher finishing reduces the surface roughness of the polished surface from 5.2 to 3.0 nm, but the roughness of the oxidised surface is with 12.2 nm higher than for the diamond polished surface (10.2 nm) (Table 12)

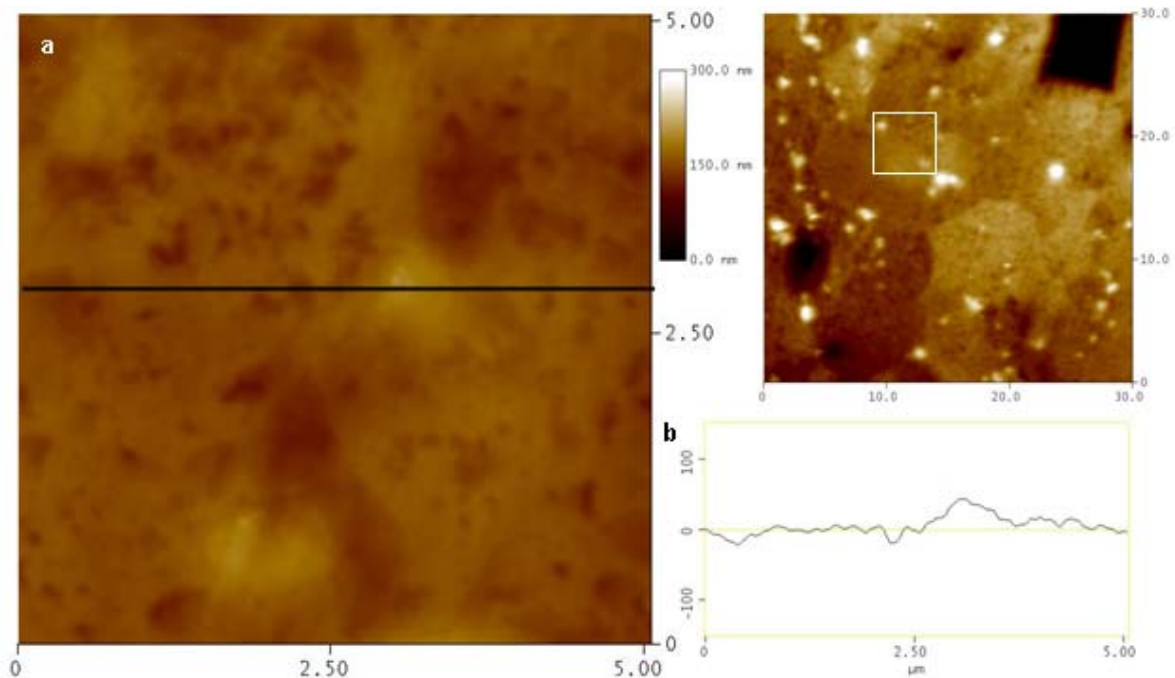


Figure 33: AFM surface profile (a) of oxidised Zr1%Ni (vibratory polisher finish) exhibiting protrusions on the surface sticking out ~40 nm from the surface. (b) AFM line profile on Zr1%Ni with RMS of 13 nm, see black line for the position. (c) Overview scan showing a microindent and the position of the presented scan.

5.1.3.3 SEM and EDS after oxidation

The surface of the sample polished with the basic silica solution in the Vibratory polisher exhibited small crystals on protrusions observed in SEM (Figure 34) and cracks in the vicinity of the protrusions. The small crystals are observed on many but not all protrusions.

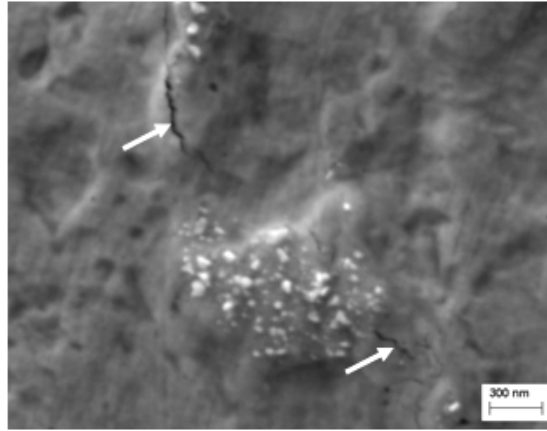


Figure 34: SEM micrograph of Zr1%Ni (Vibratory polisher finish) with small crystals observable on the protrusions and cracks in the vicinity and on protrusions.

5.1.3.4 FIB transverse sections

For Zr1%Ni with the last polishing with Vibratory polisher a higher amplitude of undulation of the metal-oxide interface has been observed at precipitates in contact with the outer surface (Figure 35). Precipitates not in contact with the outer surface exhibit an oxide thickness similar to the surrounding matrix at the metal-oxide interface, they are not preferentially oxidised.

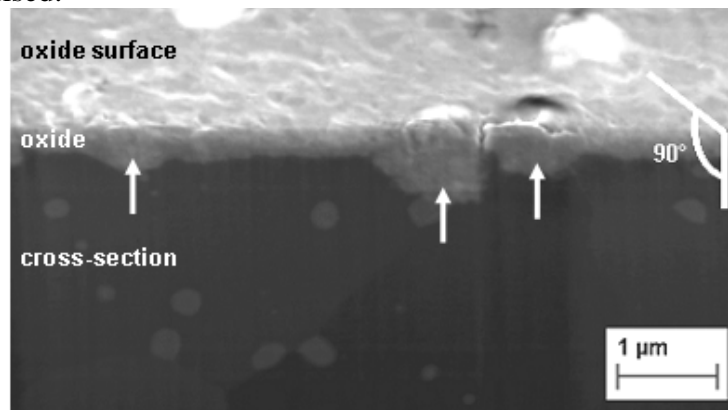


Figure 35: FIB transverse sections of oxide scale formed on Zr1%Ni polished with Vibratory polisher. Precipitates in contact with the surface (white arrows) were found to be preferentially oxidised.

5.1.3.5 Transmission electron microscopy

A TEM transverse section of oxidised Zr1%Ni (Vibratory polisher finished surface) is presented in Figure 38a. Thicker oxide than in the surrounding can be observed at the precipitate in contact with the outer surface. On the surface of the precipitates small crystals are visible (Figure 38b), consisting of iron oxide as shown by EDS analysis (spectrum in Figure 38). This iron oxide formation could be caused by a sensitisation to iron diffusion to the surface from the basic Vibratory polisher finishing. A typical Zr₂Ni precipitate exhibits an average Ni to Fe ratio of 40, corresponding to approximately 0.8 at% Fe in the precipitates (for a oxygen free precipitate).

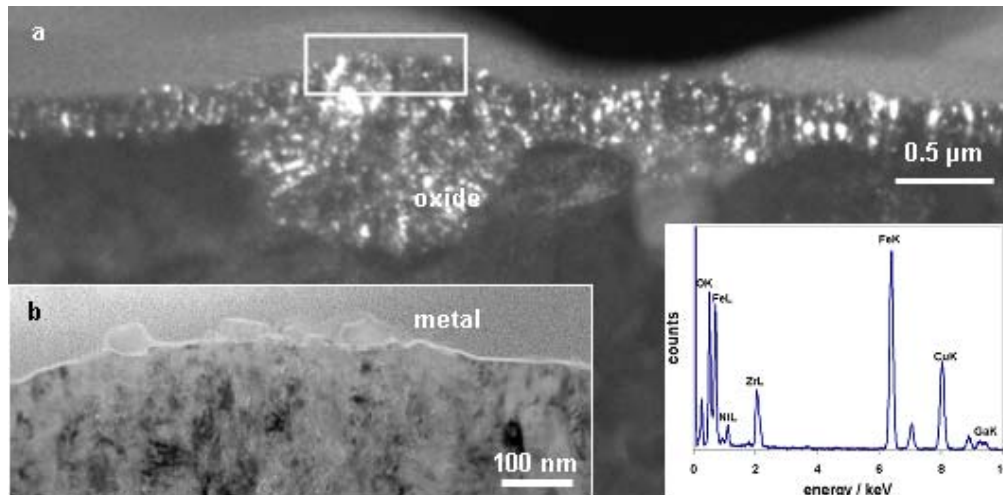


Figure 36: (a) Dark field contrast of oxidized transverse section of Zr1%Ni polished with the Vibratory polisher. The thicker oxide at the oxidized precipitate can be observed. (b) Bright field contrast of the iron oxide crystals on the surface of the oxidized precipitate, shown to consist of iron oxide. The position of (b) is marked in (a). EDS spectrum of crystals shows small Zr and Ni signals.

5.1.4 Zr1%Cr – as received

5.1.4.1 In situ oxidation

For Zr1%Cr precipitates were not observed on the surface before oxidation. During the in situ oxidation no changes on the surface other than those typical for the oxidation of the matrix also observed for the other binary alloys could be observed. In the ESEM the surface oxide exhibited a coarse-grained aspect with no specific protrusions or cracks, which could be linked to the presence of precipitates.

5.1.4.2 Atomic force microscopy

The surface of oxidised Zr1%Cr analysed by AFM exhibits no large protrusions, only many small grains are observed (Figure 37a). The small grains which show a higher height at the surface could be oxidised precipitates (Figure 37b). One of these is marked by arrows in the section and on the height profile. However, as no analytical method is available in AFM to prove this and also in SEM no verification is possible, this has to be checked on a sample with larger precipitates, which allows the correlation of protrusions and the presence of chromium. The height differences between surface oxide grains are not larger than those for Zr1%Fe and Zr1%Ni, although in the absence of larger protrusions this gives the impression of a rough surface. In numbers the roughness of the surface was doubled after oxidation (Table 12), increasing from 3.8 nm before to 8.3 nm after oxidation (Table 12).

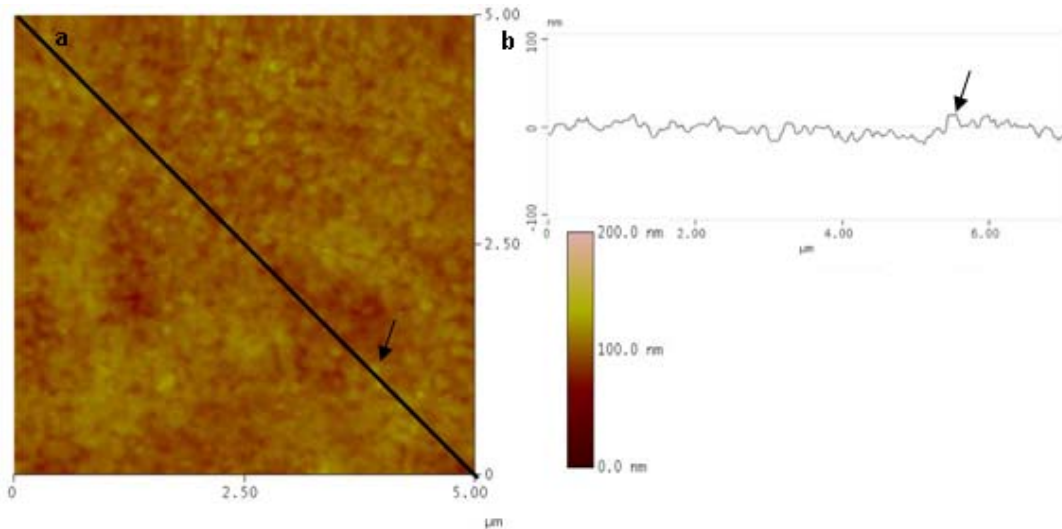


Figure 37: AFM surface profile (a) of oxidised Zr1%Cr. A coarse-grained surface is observed on Zr1%Cr without protrusions. (b) AFM line profile Zr1%Cr with a RMS of 7 nm for the oxidised surface, for the positions see the black line in (a). A small protrusion and its position on the height profile are marked by arrows.

5.1.4.3 SEM and EDS after oxidation

For Zr1%Cr the precipitate size is a problem for EDS analysis in SEM after oxidation, as shown for example by the size of the features on the surface in Figure 38. On Secondary electron detector and Inlens detector, features probably corresponding to precipitates can be observed on the outer surface (some marked with white arrows for clarity) using low acceleration voltage (700 V) to increase the surface sensitivity. In the first case due to a topographical contrast and in the second due to a different composition contrast. Also for backscattered electron images the same features can be observed with a different composition contrast (not shown). However, due to the large volume probed with the electron beam no analysis of only those small spots of interest is possible, as the volume from which the information originates will always be significantly larger than the precipitates even at low acceleration voltages so that the information of interest is too diluted to be useful.

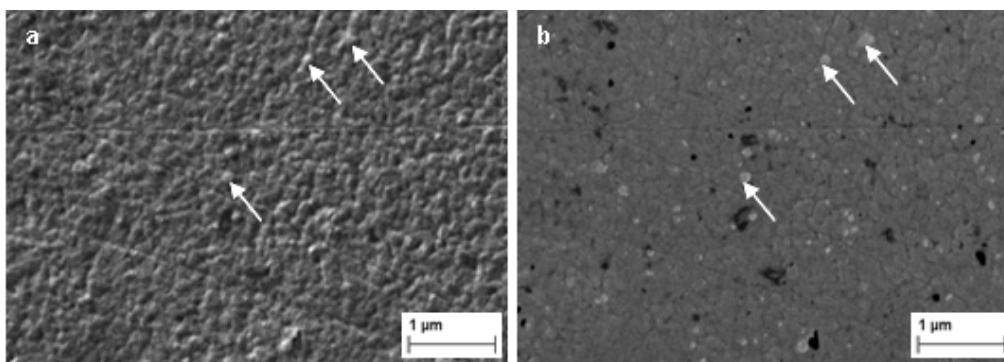


Figure 38: SE (a) and Inlens (b) micrograph of same position on Zr1%Cr after 1 hour in situ oxidation at 415°C. White arrows mark protrusions at the surface showing also composition contrast not related to contamination (dark). Images were acquired at very low acceleration voltage (700 V).

5.1.4.4 Transmission electron microscopy

The TEM transverse section of oxidised Zr1%Cr is presented in Figure 39. In the case of this material in an area of approximately $0.15 \mu\text{m}^2$ four unoxidized precipitates (marked with white arrows) can be observed in the oxide. They exhibit crescent shaped cracks at the precipitate-oxide interface towards the outer surface (marked with black arrows). The size of the crescent shaped cracks increases with increasing precipitate size. The matrix oxide has a columnar grain structure. The undulated metal-oxide interface can be seen in Figure 39a. Figure 39b presents an oxidised precipitate close to the outer surface, exhibiting a fine grained microstructure.

Using the integrated EDS signal from EDS spectra, it could be shown that at the position of the crescents the signal dropped significantly, indicating that the crescents are real cracks in the oxide.

The EDS analysis of the precipitates in the oxide provided the following information, taking the correction method explained in Appendix I on page 183 into account:

1. Many precipitates in the oxide exhibit too low oxygen contents to be fully oxidised (0-20 at.% oxygen with Zr L-line and Cr K-line), while the surrounding matrix was found to be fully oxidised. Precipitates within $\sim 150 \text{ nm}$ distance of the metal-oxide interface were usually low in oxygen; see for example precipitate most distant to interface in Figure 39.
2. Close to the outer surface the precipitate oxygen content was observed to be around 60 at.% oxygen, indicating fully oxidised precipitates, e.g. Figure 39b.

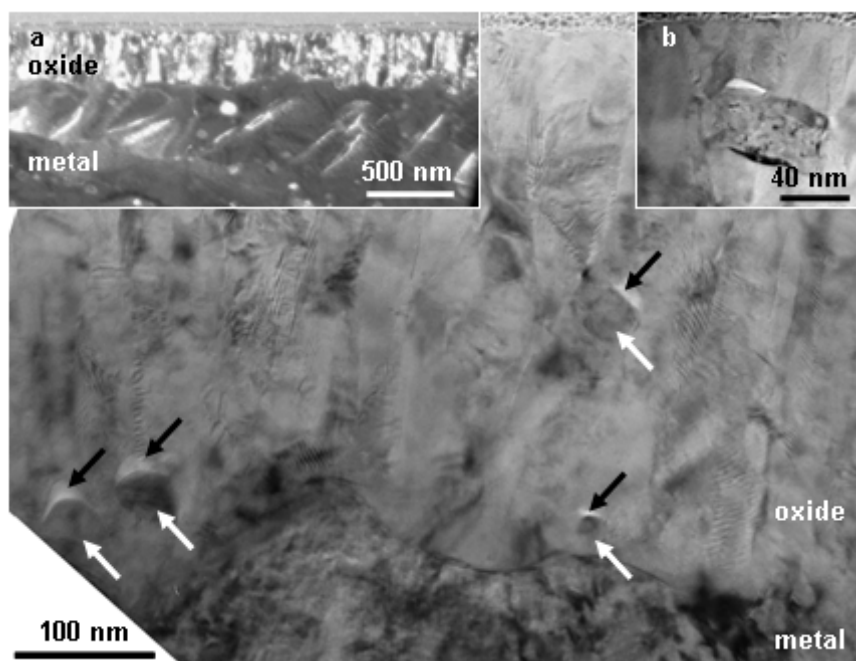


Figure 39: Bright field contrast of Zr1%Cr showing unoxidized precipitates in the oxide (white arrows) and the cracks associated with them (black arrows). Inset I presents an overview of the undulated metal-oxide interface. Inset II provides an example for oxidised precipitates.

5.1.5 Zr1%Cr – annealed 48 hours at 730°C

Some of the Zr1%Cr material was heat treated for 48 hours at 730°C to obtain larger precipitates in order to be able to study the precipitate oxidation behaviour in the oxide and at the outer surface in more detail.

5.1.5.1 *In situ oxidation*

Before oxidation some precipitates were already visible with the SE detector (not shown). Those precipitates visible at the surface became darker in their appearance during the first minutes of the experiment and therefore well observable on the oxidising sample (Figure 40a&b). The evolution of the surface concerning the appearance of the precipitates is almost complete after 6 minutes at 415°C (Figure 40a), as no real changes are observable after that time (Figure 40b-c), one feature on the surface identified as precipitate has been marked at each stage in Figure 40 with a circle. The subsequent cooling process does not lead to significant surface changes (not shown). It should be noted that the large features identified as precipitates changed their contrast somewhat with oxidation time, but remained the same in size and shape. At the interface of precipitate and oxide cracks were observed at the surface after cooling. During oxidation the topography around the precipitates at the surface was similar, the cracks were not possible to distinguish in situ (micrographs are blurred and no further adjustment was successful and therefore reduced visibility of small features like cracks), so the time of formation cannot be determined.

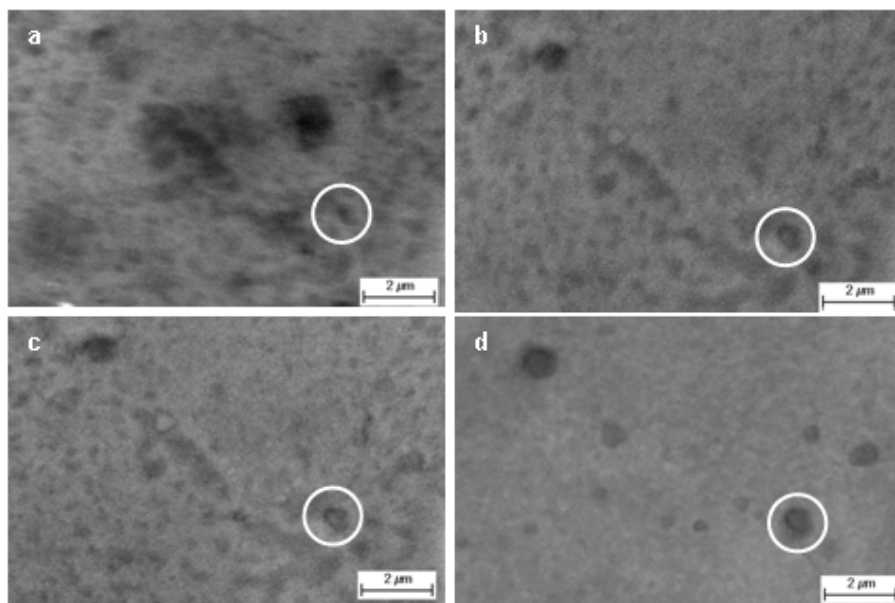


Figure 40: The images of Zr1%Cr oxidised at 415 °C show the surface in situ (a) after 6 minutes, (b) 29 minutes and (c) 58 minutes of oxidation as observed in ESEM with the GSE detector and (d) with BSE detector after cooling. The same precipitate is marked with a circle at all stages.

5.1.5.2 *Atomic force microscopy*

The AFM surface scans of Zr1%Cr with large precipitates showed shallow recesses at precipitates before oxidation (Figure 41a), being 5-10 nm deep. After oxidation the analysis of the same regions as before oxidation showed the precipitates to protrude with respect to their

surroundings (Figure 41b), their height being between 10 and 60 nm. In numbers the roughness of the surface after oxidation was four times higher than the roughness before oxidation, increasing from 3.0 nm before to 12.3 nm after oxidation (Table 12). The AFM scans before oxidation revealed a preferential attack of the precipitates from the polishing with recesses at precipitate positions (see P in Figure 41a). The height of the protrusions might therefore not be directly comparable to those protrusions detected on Zr1%Fe and Zr1%Ni. The presence of recesses at precipitate sites was not observed for diamond polished samples. The likely cause is the basic silica solution used for Vibratory polisher finishing.

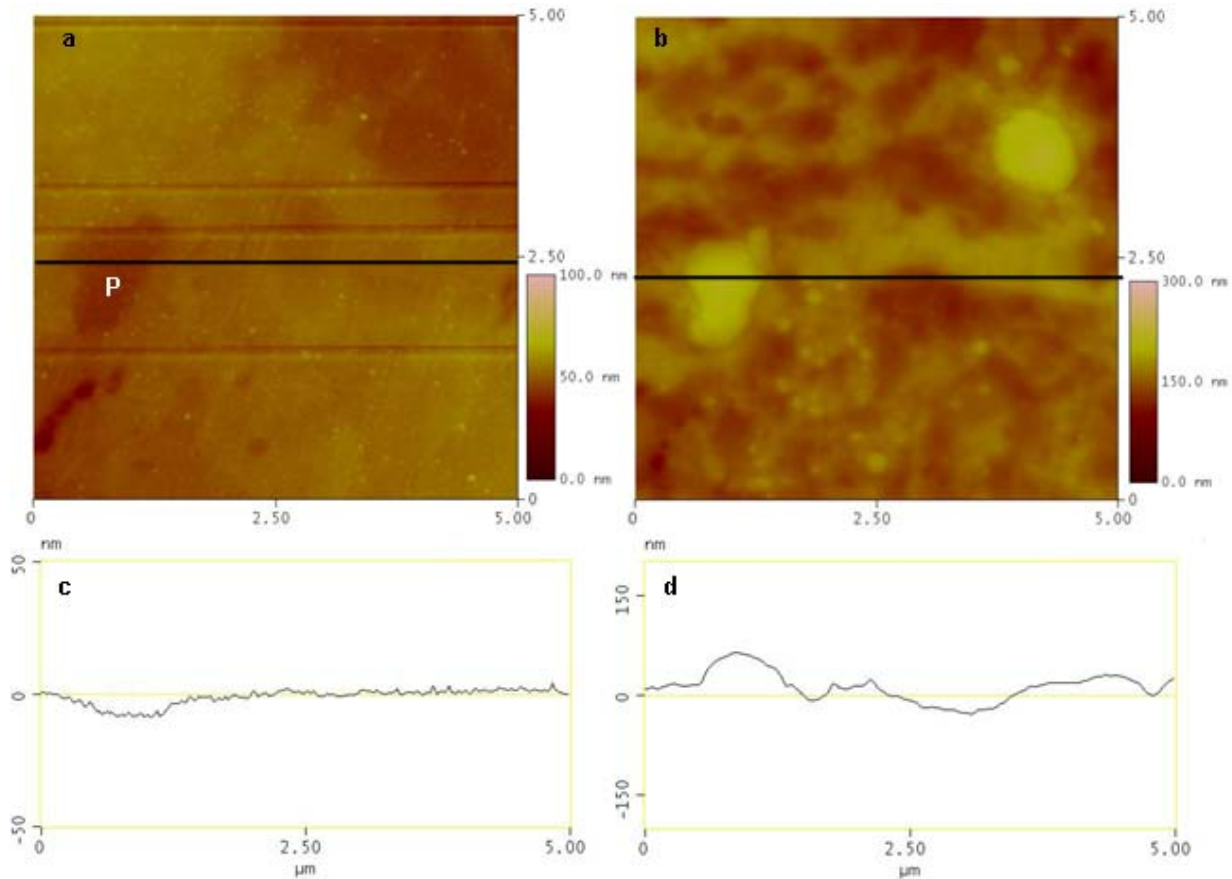


Figure 41: AFM surface profiles of (a) polished and (b) oxidised Zr1%Cr. Before oxidation shallow recesses are observed at precipitates, after oxidation protrusions are observed at the same positions. The AFM line profiles c and d represent the sections marked on the surface profiles in (a) and (b) respectively. The P in (a) marks the recession at a precipitate site, see (b) for comparison.

5.1.5.3 SEM and EDS after oxidation

The observation of the outer surface revealed a smooth surface at precipitates in contact with the outer surface, surrounded by cracks in the oxide scale at the precipitate-oxide interface (Figure 42). The matrix oxide is also flat; however, the small scale roughness is considerably higher than on the precipitates in contact with the outer surface. EDS measurements showed around 55 at.% of oxygen in the matrix oxide and around 40 at.% oxygen at precipitate sites, which is an indication for delayed oxidation of the precipitates with some oxide on the precipitate surface.

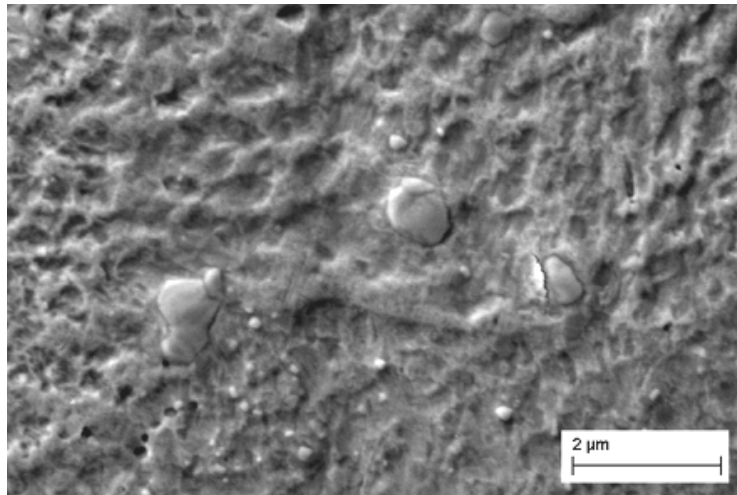


Figure 42: SEM micrograph of surface of Zr1%Cr with large precipitates showing the precipitates at the surface and the cracks at the precipitate-oxide interface.

5.1.5.4 FIB transverse sections

Transverse sections of the precipitates reveal a different contrast at the precipitates than on the oxidized matrix on micrographs acquired with the Inlens detector (Figure 43a&b). The comparison with the contrast of precipitates in the oxide of the other alloys leads to the conclusion that also the large precipitates in Zr1%Cr remain unoxidized. At the small surface of the precipitates a layer with a different contrast can be observed but not analysed with EDS due to the interaction volume. Cracks at the precipitate-oxide interface can be observed at the precipitates and the crescent shaped crack on precipitates in the oxide, not in contact with the outer surface can be observed in (Figure 43a marked with black arrow). EDS point analysis (at 5 kV) on the precipitate in top view and on the cross-sections shows lower oxygen contents than in the surrounding matrix (numbers similar to those mentioned in the section before), which is also an indication of delayed oxidation with respect to the matrix. The oxidation induced changes at the surface of the precipitates cannot be investigated on FIB transverse sections, as the resolution of EDS point analysis is not sufficient.

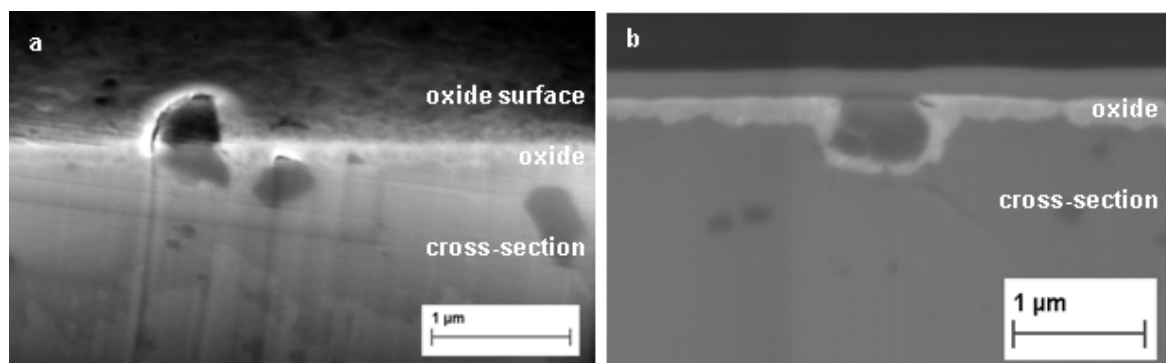


Figure 43: SEM micrographs of FIB sections of Zr1%Cr oxidized in situ with large precipitates. (a) Inlens micrograph of section and surface, showing a precipitate on the surface and in the section. (b) Inlens micrograph of other precipitate at the surface surrounded by oxide and covered with platinum.

5.1.5.5 Transmission electron microscopy

The bright field TEM contrast presented in Figure 44 shows a large precipitate in annealed Zr1%Cr oxidized in situ. The precipitate is partially oxidized and the respective parts (o - oxide and m - metallic) are marked for clarity on the micrograph. The precipitate is completely surrounded by oxide, which is partly cracked. EDS measurements at the precipitate showed, that the oxidized part exhibits oxygen contents around 55 at.% and the metallic part only 9 at.%. The Cr to Zr ratio was very close to 2 in the metal and in the oxide. Only at the very surface Cr to Zr ratios up to 5 were obtained, which could indicate a starting segregation of Cr to the surface and formation of pure chromia.

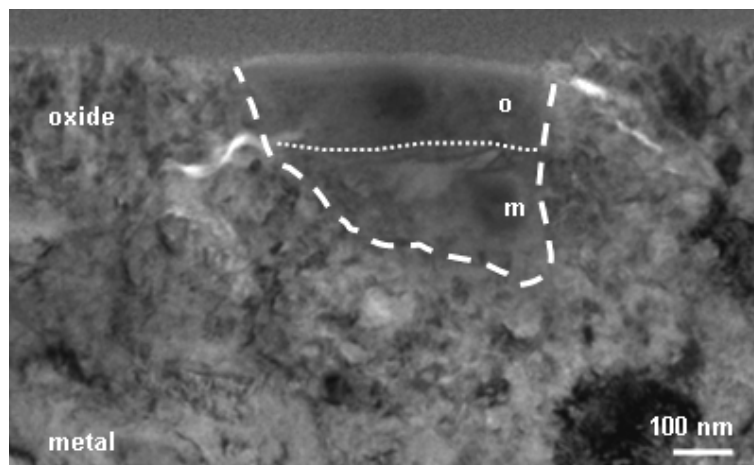


Figure 44: Bright field contrast of Zr1%Cr with large precipitates. A partially oxidized precipitate in contact with the outer surface is presented, being surrounded by oxide. The oxidized (o) and metallic (m) precipitate parts are marked for clarity.

5.1.6 Zr0.6%Nb

5.1.6.1 In situ oxidation

For Zr0.6%Nb precipitates were not observed on the surface before oxidation. During the in situ oxidation no changes were observed on the surface other than those typical for the oxidation of the matrix also observed for the other binary alloys. In the ESEM the surface oxide exhibited a coarse-grained aspect with no specific protrusions or cracks, which could be linked to the presence of precipitates.

5.1.6.2 Atomic force microscopy

The surface of Zr0.6%Nb analysed by AFM exhibits no large protrusions: only many small grains are observed (Figure 45a). Some of these could be oxidised precipitates, but, as mentioned before no analytical method is available to prove this. The surface roughness and aspect are similar to Zr1%Cr. The increase in surface roughness of the oxidised Zr0.6%Nb sample leads to a change from 5.3 nm before to 9.3 nm after oxidation (Table 12).

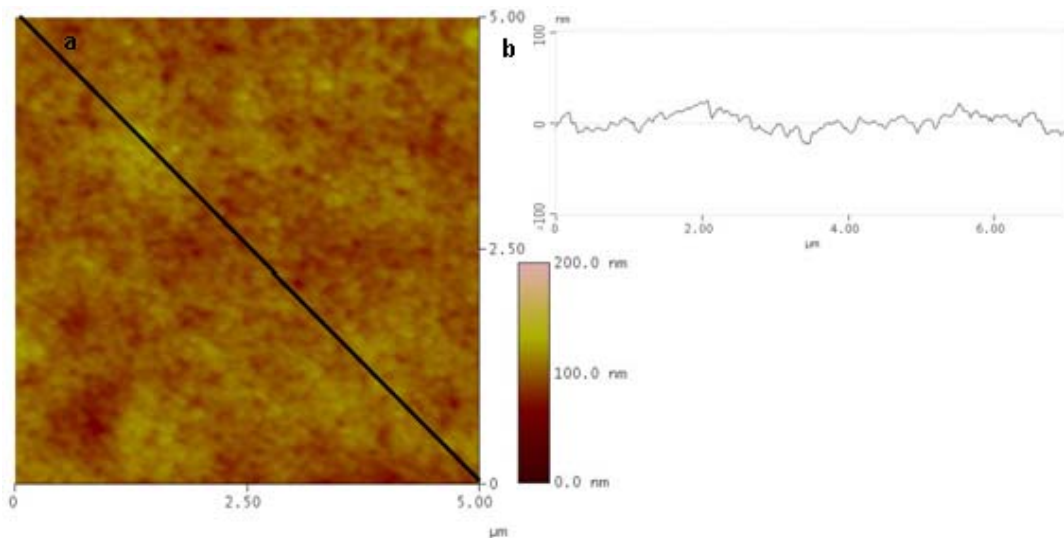


Figure 45: AFM surface profile (a) of oxidised Zr0.6%Nb. A coarse-grained surface is observed without protrusions. (b) AFM line profile with a RMS of 8.8 nm for the oxidised surface, for the position refer to the black line in (a).

5.1.6.3 Transmission electron microscopy

TEM analysis of Zr0.6%Nb showed precipitates in the oxide exhibiting crescent shaped cracks at the precipitate-oxide interface towards the outer surface (Figure 46b-d). The metal-oxide interface is undulated (Figure 46) and the matrix oxide has a columnar grain structure. The size of the crescent shaped cracks at the precipitates is correlated to the precipitate size (Figure 46b-d). In Figure 46b&c the small grained oxide microstructure of precipitates further away from the metal-oxide interface can be observed.

For niobium containing precipitates several possible compositions exist (e.g. β -Zr and β -Nb) and thicker TEM samples will always result in lower measured niobium contents due to the increasing matrix contribution and the precipitate size, as more zirconium will be present in the analysed volume. From the EDS measurements it could be concluded that the measured Zr to Nb ratio was around 1:1 for large precipitates (80-100 nm) in the metal, which indicates β -Nb precipitates with a contribution of the matrix to the Zr signal. The overall oxygen concentration measured at precipitate positions ranged between 55-60 at.% oxygen. Applying the estimation for the oxygen content of the precipitates described in Appendix I on page 183 and using an Nb to Zr ratio of 4 for β -Nb (20% Zr), the oxygen content of the precipitates was higher with increasing distance from the metal-oxide interface (~33 at.% O in precipitate 40 nm from the outer surface).

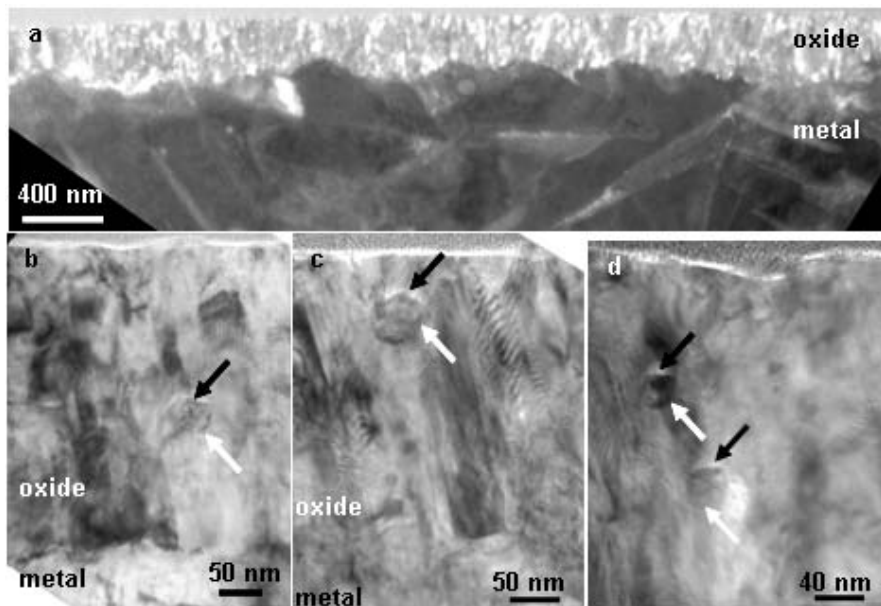


Figure 46: Micrographs of oxidised Zr0.6%Nb. (a) Dark Field contrast of oxide, showing the undulated metal-oxide interface. (b-d) Bright field contrast of precipitates in the oxide marked with white arrows.

5.1.7 Pure zirconium

The surface of pure zirconium has been investigated to observe the oxidation of the matrix to be able to evaluate the influence of the alloying elements on the oxidation behaviour of zirconium.

5.1.7.1 *In situ* oxidation

For pure zirconium no changes on the surface were observed during the in situ oxidation other than those also observed for the other binary alloys typical for the oxidation of the matrix (Figure 47). The surface oxide exhibited after 1 hour of oxidation a coarse-grained aspect with no specific protrusions or cracks (Figure 47d).

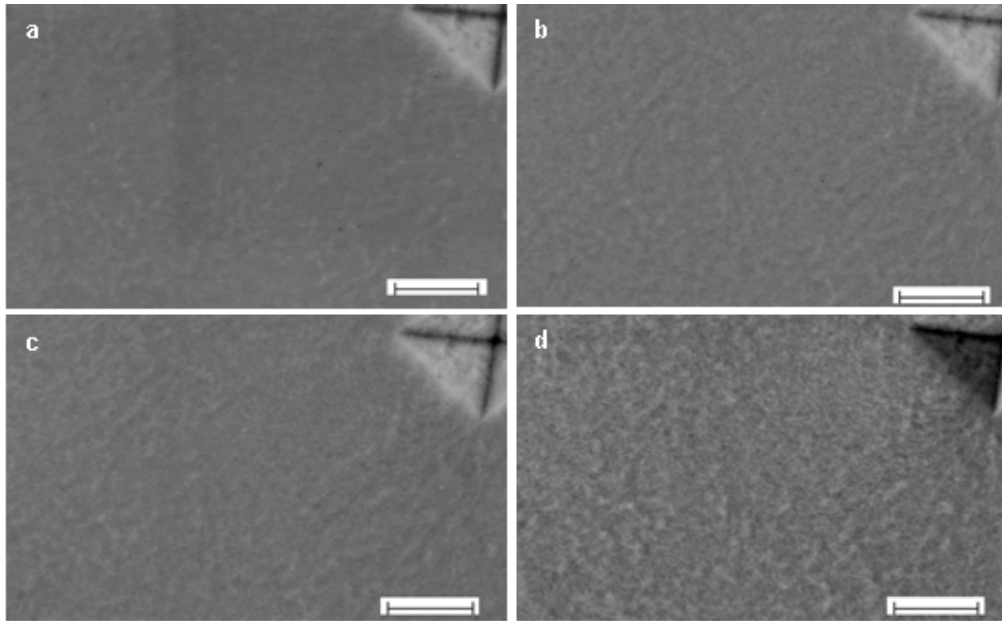


Figure 47: The micrographs of pure zirconium oxidised at 415 °C show (a) the polished surface, (b) in situ after 5 minutes, (c) 58 minutes (all GSE detector) and (d) after cooling with the SE detector. The micro indent is presented for orientation and the scale bars correspond to 5 μm .

5.1.7.2 Atomic force microscopy

The surface of pure zirconium analysed by AFM exhibits no large protrusions but many small grains (Figure 48a). The increase in surface roughness of the oxidised pure zirconium sample led to increase in surface roughness from 3.8 nm before to 11.2 nm after oxidation (Table 12).

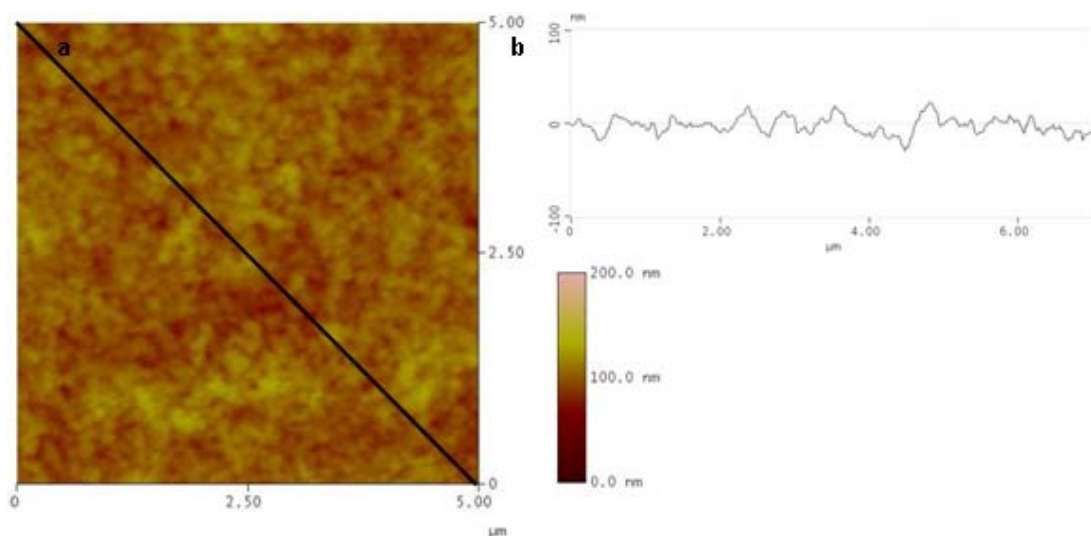


Figure 48: AFM surface profile (a) of oxidised pure Zr. A coarse-grained surface is observed without protrusions. (b) AFM line profile with a RMS of 8.8 nm for the oxidised surface, for the positions see the black line in (a).

5.1.7.3 Transmission electron microscopy

In TEM the metal-oxide interface was observed to be undulated for pure zirconium (Figure 49), which contains only very few Fe bearing precipitates due to the iron impurity present (one was observed on this TEM sample). The oxide structure consists mainly of columnar grains (inset of Figure 49). Some hydrides can be observed in the metal.

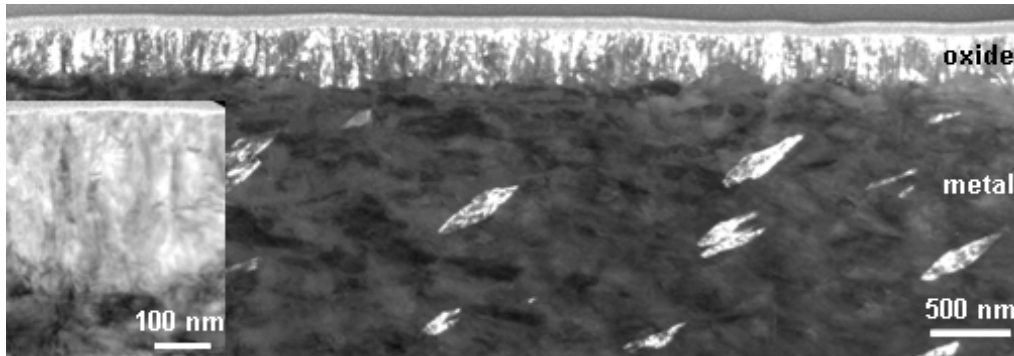


Figure 49: TEM dark field contrast of oxidised pure Zr. Overview of oxide scale, showing the undulated metal-oxide interface and hydrides in the metal. Inset at higher magnification showing the columnar oxide in more details.

5.2 Summary of in situ oxidation results at 415°C

For the in situ oxidation at 415°C the observations allow to make the following distinctions between the different tested materials.

AFM results showed the formation of protrusions on the surface on precipitates in contact with the original surface for Zr1%Fe and Zr1%Ni, their diameter was in the range of several hundred nanometres. Beside these protrusions the matrix was covered by small oxide grains, which were found to exhibit height differences in the nanometre range. The correlation of the large protrusions with precipitates was confirmed by EDS maps of the surface, FIB transverse sections and in the case of Zr1%Fe also on TEM samples. The average height of the protrusions as measured in AFM is ~70 nm on Zr1%Fe and ~20 nm on Zr1%Ni. In the case of Zr1%Fe small iron oxide crystals of different size were observed on the surface of several precipitates (Figure 21b&c and Figure 24b). Cracking of the oxide surface is observed on some protrusions for Zr1%Ni after 2 hours of oxidation. The influence of these oxide crystals on the overall protrusion height was not evaluated, as in AFM only the total height of protrusions can be measured and no separation is possible as in TEM samples, on which the height of both can be quantified.

On Zr1%Cr and Zr0.6%Nb the size of the oxide grains at the surface is similar to those observed on Zr1%Fe and Zr1%Ni and no large protrusions could be observed in AFM and SEM. On Zr1%Cr some grains at the surface protrude and protrusions observed in SEM exhibit a different z contrast being not similar to carbon containing contamination. However, due to the small precipitate size no correlation of these features to the presence of precipitates is possible with EDS measurements in SEM. Analysis of larger precipitates containing Cr is required to confirm a correlation between protrusions and precipitates. Therefore Zr1%Cr was annealed for 48 hours at 730°C and a sample with larger precipitates tested, for comparison

the acquired data are presented for information in a separate line at the bottom of Table 12. The precipitates Zr1%Cr also form protrusions on the surface, however, only a thin layer in contact with the surface oxidises and the rest of the precipitates remains metallic at this stage. As no thicker oxide scales were investigated, it cannot be concluded from these results about the distance from the metal-oxide interface required for oxidation of these precipitates.

Table 12: parameters of the samples oxidised in situ at 415°C for 1 hour

Alloy	Average oxide thickness / μm ϕ		RMS polished (5x5 μm) / nm	RMS oxidised (5x5 μm) / nm	Average height of protrusions / nm *		Average diameter of protrusions / μm *	
Zr1%Fe	0.32	\pm 0.11	3.9	21.2 †	68	\pm 15	1.1	\pm 0.3
Zr1%Ni	0.41	\pm 0.11	5.2	10.3 †	19	\pm 6	0.7	\pm 0.5
Zr1%Cr	0.35	\pm 0.07	3.8	8.3	Not detectable			
Zr0.6%Nb	0.34	\pm 0.09	5.3	9.3				
Pure Zr	0.27	\pm 0.05	3.8	11.2	Not detectable			
Zr1%Ni °	0.24	\pm 0.17	3.0	12.2	80	\pm 38		
Zr1%Cr ° annealed	0.28	\pm 0.17	2.7	16.2	53	\pm 16		

ϕ average from FIB transverse sections, † including specific protrusions, RMS: root mean square of roughness, * from 10 sections in AFM profiles, ° Vibratory polisher finishing

A summary of the average oxide thickness, the surface roughness before and after oxidation and the height of protrusions on the surface is summarised in Table 12. In the case of Zr1%Fe and Zr1%Ni alloys the average surface roughness after oxidation is in fact the average roughness of surface protrusions and matrix oxide. To separate these two factors, smaller areas (700x700 nm) were scanned on the matrix oxide only and resulted in the data presented in Table 13. The overall roughness decreased (influence of scanned surface area), the roughness of the matrix oxide on Zr1%Fe and Zr1%Ni is similar to Zr1%Cr and lower than on Zr0.6%Nb, pure zirconium exhibits the roughest surface. All alloys form an oxide scale with an average thickness in the range of 200-410 nm, as measured on FIB transverse sections. Zr1%Ni exhibited the thickest and pure Zr the thinnest average oxide thickness. For Zr1%Fe and Zr1%Ni a thicker oxide was observed at the precipitates and in their direct vicinity in case they were in contact with the outer surface (undulation of the metal-oxide interface). A first impression of the oxidation behaviour of the precipitate at the metal-oxide interface can be obtained on the FIB transverse sections for Zr1%Fe and Zr1%Ni. For Zr1%Cr and Zr0.6%Nb this is not possible due to the small average precipitate size.

Table 13: surface roughness for matrix oxide of in situ samples oxidised at 415°C

Alloy	RMS matrix oxide (700x700 nm) / nm
Zr1%Fe	4.5*
Zr1%Ni	4.5
Zr1%Cr	4.5
Zr0.6%Nb	5.1
Pure Zr	5.8

* From zoomed 5x5 μm scans

To be able to study the precipitate oxidation behaviour in detail, TEM is required for sufficient resolution for imaging and analysis of oxygen content and crystal structure. In the TEM the oxidation behaviour observed for the precipitates in different alloys differed for the different alloying elements:

Precipitates in Zr1%Fe and Zr1%Ni oxidised similar to the Zr-matrix, if not in contact with the outer surface. Those precipitates that were in contact with the outer surface exhibited higher oxide thickness than the surrounding matrix. In the case of Zr1%Fe the formation of iron oxide crystals was observed above precipitates being oxidised at or close to the outer surface.

A delayed precipitate oxidation was observed with respect to the surrounding matrix for precipitates in Zr1%Cr and Zr0.6%Nb with oxygen levels being much lower than in oxidised precipitates. Precipitates in both alloys showed crescent shaped cracks on the precipitate side facing the outer surface in the oxide scale. The observability of the cracks depends on the local sample thickness, the thinner the sample, the better they can be observed. The overall oxygen content measured depends on the local sample thickness, as at thin positions the contribution of the oxidised matrix is lower than in thicker regions.

The matrix oxide was observed to be columnar for all materials, with the oxide grains oriented in the oxide growth direction. No distinct difference between the columnar grains was observed for the different materials. The oxide structure was small grained and equiaxed for oxidised precipitates in Zr1%Fe, Zr1%Cr and Zr0.6%Nb, as can be observed on the respective micrographs. For Zr1%Ni due to the lack of clear observations of fully oxidised precipitates in the oxide, it cannot be stated what the oxide microstructure looks like for this material at the initial stage. A comparison of the oxygen profiles for the different materials showed a change from the oxidised state to metal within approximately 150 nm. The oxygen level in the metal has been measured to be usually above 10 at.%, which can be due to the oxidation of the TEM sample surface after preparation, as no storage is possible at oxygen partial pressures being low enough to avoid oxidation of zirconium.

Some differences in the observations are clearly connected to the average precipitate size, which is ~250 nm for Zr1%Fe and Zr1%Ni and 35 and 47 nm for Zr1%Cr and Zr0.6%Nb. The precipitate volume is much smaller and also the change of volume per precipitate is much lower for alloys with small precipitates. Estimation of the volume change and the associated height of protrusions using typical Pilling-Bedworth ratio for small precipitates revealed, that the possible height is in a similar range as the observed surface roughness.

The observation of alloying element oxide formation at the outer surface is also dependent on precipitate size. Small precipitates will result in small oxide quantities which cannot be easily observed and analysed. A targeted preparation of TEM samples is much more difficult for features being below 100 nm in size and the chances of having such features by chance within a prepared TEM sample are not high.

6 Microstructure of alloys oxidised in autoclave

The samples which were oxidised in autoclave were obtained from CEZUS/Areva. The sample surface was pickled before oxidation, as described in the ASTM G2 procedure [83], resulting in an increased surface roughness. The samples were tested in air and steam at ambient pressure for 3 days and at 10.5 MPa for 110 days. These selected environments show the influence of air and steam as well as pressure and oxidation time; however, for the available samples several parameters are changed simultaneously, so that they cannot be used to identify the particular influence of a certain parameter.

6.1 Oxidation for 3 days in air at ambient pressure

6.1.1 Zr1%Fe

6.1.1.1 SEM of surface and FIB sections

The SEM and EDS investigation of the surface of Zr1%Fe revealed for this environment the presence of iron oxide in form of agglomerates of small crystals on the surface (Figure 50). The surface density of the observed iron agglomerates is less than 1 per 100 μm^2 . The agglomerate size is in the range of several hundred nanometres to 1 μm in diameter with the individual particles being in the range of up to 100 nm. The observations showed many cracks on the surface with a length of up to several micrometers. These cracks on the surface are often present at pickling craters.

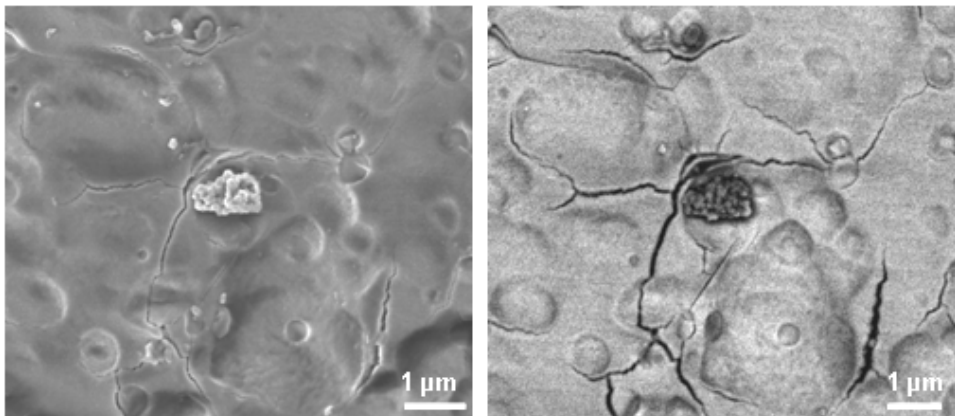


Figure 50: SEM micrograph of surface of Zr1%Fe oxidized 3 days in air showing iron oxide agglomerate at the surface and cracks in the oxide scale. The observed topography is caused by the pickling process prior to oxidation. The SE micrograph in (a) shows the topography of the surface together with cracks penetrating the surface, while the Inlens micrograph in (b) shows the topography and the chemical contrast between zirconia and iron oxide superimposed.

The roughness of the surface due to the pickling craters can be also observed on FIB transverse sections (Figure 51). The metal-oxide interface is undulated and the oxide thickness varies between 0.5 and 1.5 μm in the presented section. A large crack oriented parallel to the surface can be observed on the transverse section (white arrow).

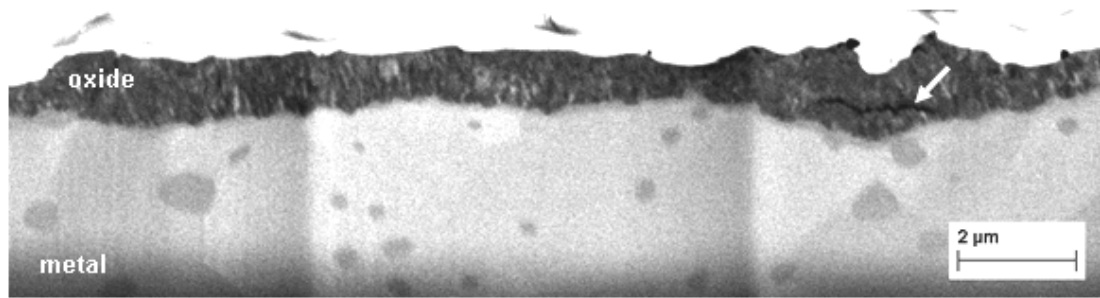


Figure 51: FIB transverse section of Zr1%Fe oxidized 3 days in air. The undulated metal-oxide interface and the rough surface can be observed on the section.

6.1.1.2 Transmission electron microscopy

The presented TEM micrographs were acquired on a sample which was prepared at the position of iron oxide agglomerates at the surface. The micrograph in Figure 52 shows the whole formed oxide scale with the metal-oxide interface, the agglomerate of iron oxide crystals at the surface (white arrow) and the hole under the oxide crystal. A partially oxidised precipitate at the metal-oxide interface can be seen in Figure 53.

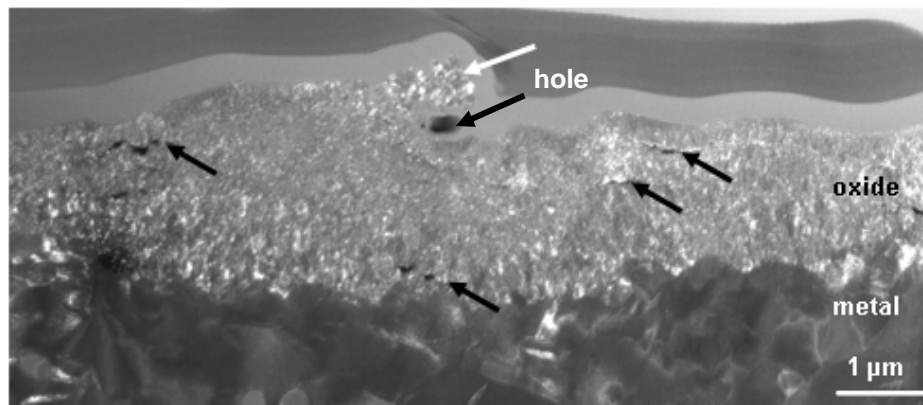


Figure 52: Dark field contrast of the oxide formed on Zr1%Fe oxidised for 3 days in air with iron oxide particles on the surface (white arrow). Large cracks in the oxide are marked with black arrows.

Cracks can be observed oriented parallel to the surface in the dark field contrast (black arrows) and the undulated metal-oxide interface is visible (Figure 52). The oxide thickness varies between 1 and 2 μm . Precipitates at the metal-oxide interface are found to exhibit a similar oxidation front as the surrounding matrix (Figure 53b); the oxidised part exhibits a small grained oxide in contrast to the surrounding columnar matrix and a crack has formed at the interface between the oxidised matrix and the oxidised precipitate. The small iron oxide particles present at the outer surface are 50-100 nm in diameter and the total height of the agglomerate is locally more than 500 nm (Figure 53a). The oxidised precipitates show an equiaxed oxide, while the matrix oxide is columnar and oriented parallel to the oxide growth direction. The cracks at the surface have not been observed to propagate deeper than 200 nm into the oxide - see for example the small crack in Figure 53a (white arrow). Underneath the iron oxide particles, the oxide shows cracks parallel to the outer surface.

EDS point analysis of the particles at the surface showed pure iron oxide with the copper signal originating from the TEM grid. In the EDS maps presented (Figure 53), it is clearly

observable that no significant amount of zirconium is present in these particles. The precipitates in the oxide showed oxygen signals indicating that the precipitates are oxidised. Therefore it can be concluded that for Zr1%Fe oxidised for 3 days in air, no metallic precipitate was observed in the oxide.

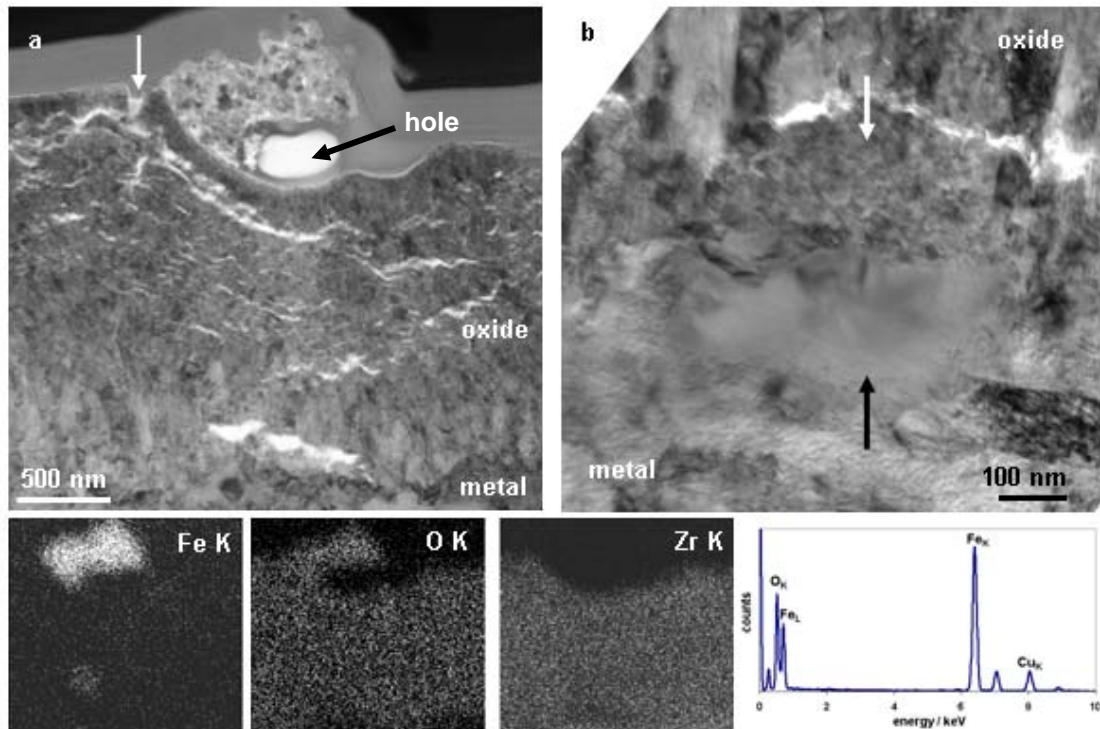


Figure 53: (a) Bright field contrast of the iron oxide particles at the surface of sample presented also in Figure 52, The corresponding EDS maps demonstrate that the particles at the surface are pure iron oxide (the map has a slight rotation with respect to the BF micrograph). The EDS point analysis showed pure iron oxide with only copper from the TEM grid being present beside iron and oxygen. (b) Bright field contrast presenting a partially oxidised precipitate at the metal-oxide interface, oxidised part (white arrow) and metallic part (black arrow).

6.1.2 Zr1%Ni

6.1.2.1 SEM of surface

The SEM and EDS investigation of the surface of Zr1%Ni revealed for this environment no presence of nickel oxide on the surface (Figure 54). On the surface precipitates and matrix can be distinguished from the topography caused by the pickling process in SE and BSE micrographs, which is correlated to the presence of precipitates and metal grain boundaries. Other features beside contamination (e.g. black spot at bottom left in b) which could be linked to the presence of nickel oxide were not observed.

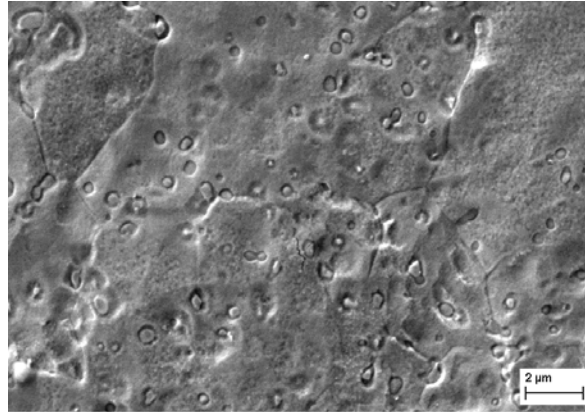


Figure 54: SEM micrograph (SE image) of surface of Zr1%Ni oxidized in air for 3 days showing the oxide formed on matrix and precipitates with mainly topographical contrast .

6.1.2.2 Transmission electron microscopy

The presented TEM micrographs show the whole oxide scale from the metal-oxide interface to the outer surface and a precipitate at the metal-oxide interface (Figure 55). The precipitate at the metal-oxide interface exhibits a similar oxidation front as the surrounding matrix. Cracks can be observed oriented parallel to the surface in the outer 200 nm of the oxide scale. The metal-oxide interface is undulated and the matrix oxide structure is mainly columnar. The oxide thickness ranges from 750 to 900 nm in the presented micrograph.

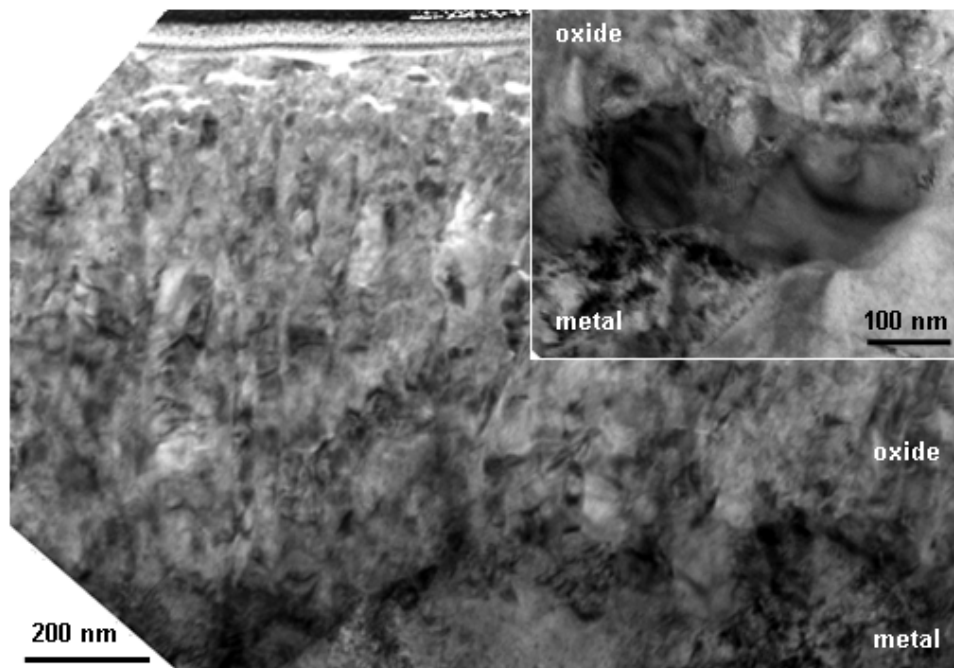


Figure 55: Bright field contrast of metal oxide interface of Zr1%Ni oxidized in air for 3 days. The inset shows a precipitate at the metal-oxide interface.

6.1.3 Zr1%Cr

6.1.3.1 SEM of surface

The SEM observations did not reveal an observable influence of chromium containing precipitates on the surface of Zr1%Cr oxidized for 3 days in air. The metal-oxide interface and the oxidation behaviour of the precipitates were therefore studied on a TEM sample.

6.1.3.2 Transmission electron microscopy

The dark field contrast (Figure 56) shows an oxide scale with a columnar matrix and an undulated metal-oxide interface. The oxide thickness is quite homogeneous between 0.7 and 0.9 μm . The chromium bearing precipitates (marked by white arrows in the inset of Figure 56) show delayed oxidation with low oxygen contents in the precipitates. The cracks typical for unoxidized precipitates can be observed at the precipitate-oxide interface towards the outer surface (marked by black arrows in the inset of Figure 56). The oxygen content measured at the precipitates was between 44 and 55 at.% oxygen without applying the correction procedure (Appendix I on page 183), which corresponded after subtracting the contribution from the oxidised matrix to 0-30 at.% oxygen within the precipitates.

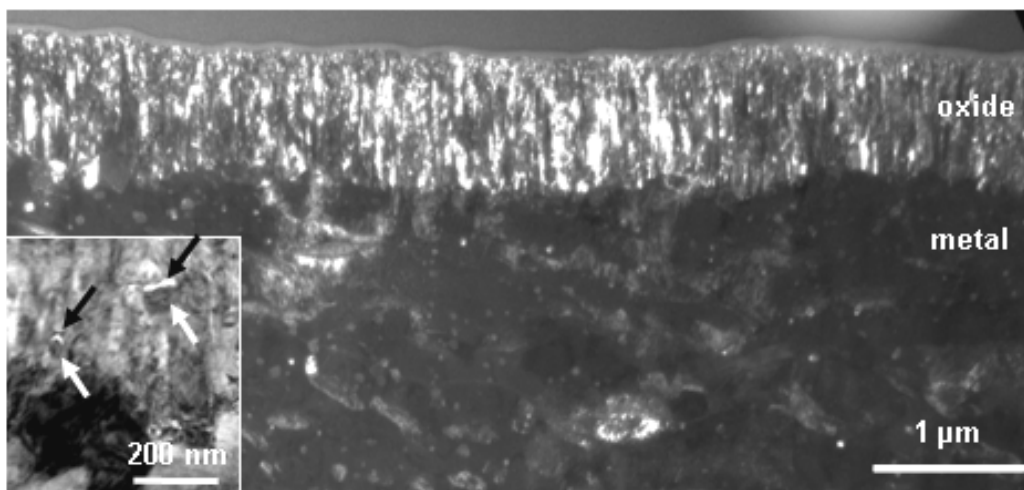


Figure 56: TEM dark field contrast of the oxide formed on Zr1%Cr after oxidation for 3 days in air. In the inset two unoxidised precipitates (white arrows) in the oxide are visible together with the typical cracks (black arrows).

6.1.4 Zr0.6%Nb oxidised for 55 days in air

For Zr0.6%Nb CEZUS could not supply a sample oxidised for 3 days under the same conditions as for the other binary alloys, therefore the available sample with 55 days oxidation time was chosen.

6.1.4.1 SEM of surface and FIB sections

The SEM observations did not reveal an observable influence of the niobium containing precipitates on the surface of Zr0.6%Nb oxidized for 55 days in air. FIB transverse sections showed an oxide with larger cracks oriented parallel to the surface and an undulated metal-oxide interface (Figure 57). The outer surface was not completely flat, the surface on different metal grains exhibited different heights, which could be either due to different etching during pickling or different oxidation kinetics of the metal grains with different orientation. More

details could not be extracted from the FIB transverse sections and the oxidation behaviour of the precipitates was therefore studied on a TEM sample.

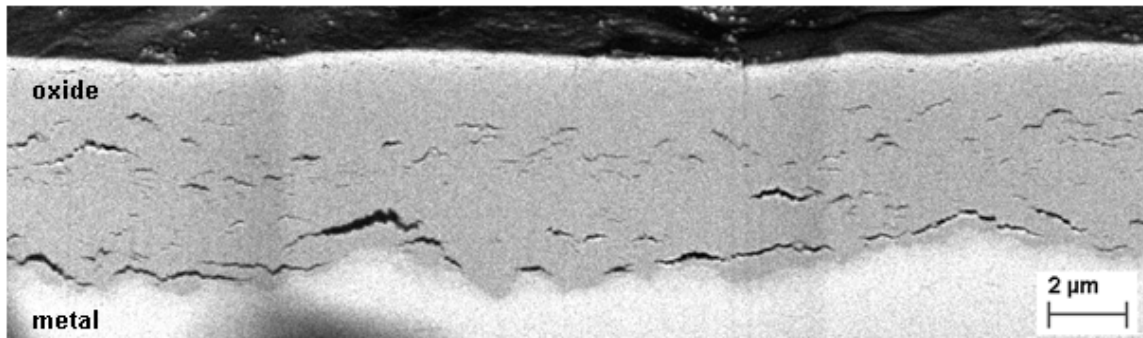


Figure 57: FIB transverse section of Zr0.6%Nb oxidized for 55 days in air. The metal-oxide interface, the cracks in the oxide and the outer surface can be observed.

6.1.4.2 Transmission electron microscopy

The dark field contrast (Figure 58) shows an oxide scale with a columnar matrix and an undulated metal-oxide interface. The oxide thickness in this sample is between 4.6 and 6.0 μm, differing between the two metal grains. At the step on the outer surface a crack in the oxide can be observed, extending about 1 μm down into the oxide. The niobium bearing precipitates (marked by white arrows in Figure 58a&b) show delayed oxidation with low oxygen contents in the precipitates. The crack typical for unoxidized precipitates can be observed at the precipitate-oxide interface towards the outer surface, marked by a black arrow in Figure 58a. One of the observed precipitates was present at a larger crack. The oxygen content measured at the precipitates was between 35 and 45 at.% oxygen without applying the correction procedure (Appendix I on page 183), which corresponded after subtracting the oxidised matrix contribution to 0-20 at.% oxygen within the precipitates. Inset I in Figure 58 shows an oxidised precipitate on the surface. This observation can be explained by the pickling treatment before oxidation, which obviously did not attack the precipitates. As several small particles were observed in SEM in this very region on the surface, being most probably identical with such precipitates, it is possible that a locally insufficient rinsing after pickling could cause the high number of precipitates on the surface. This type of precipitates on the surface was observed only on this sample. In inset II in Figure 58 an oxidised precipitate is presented without the typical crack of unoxidized precipitates.

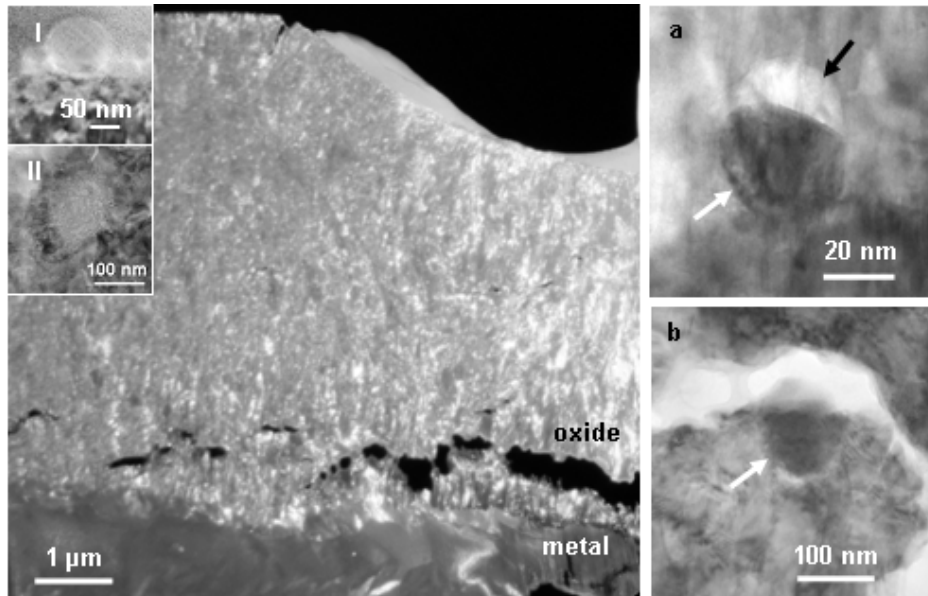


Figure 58: TEM dark field contrast of the oxide formed on Zr0.6%Nb after oxidation for 55 days in air. The oxide thickness variation and the resulting surface topography can be observed. In (a) an unoxidised precipitate in the oxide is visible, in (b) a similar precipitate situated at a larger crack. Inset I shows a precipitate on the surface and inset II an oxidised precipitate.

6.1.5 Pure zirconium

6.1.5.1 SEM of surface and FIB sections

The metal grains influence the surface topography of pure zirconium oxidised in air for 3 days (Figure 59).

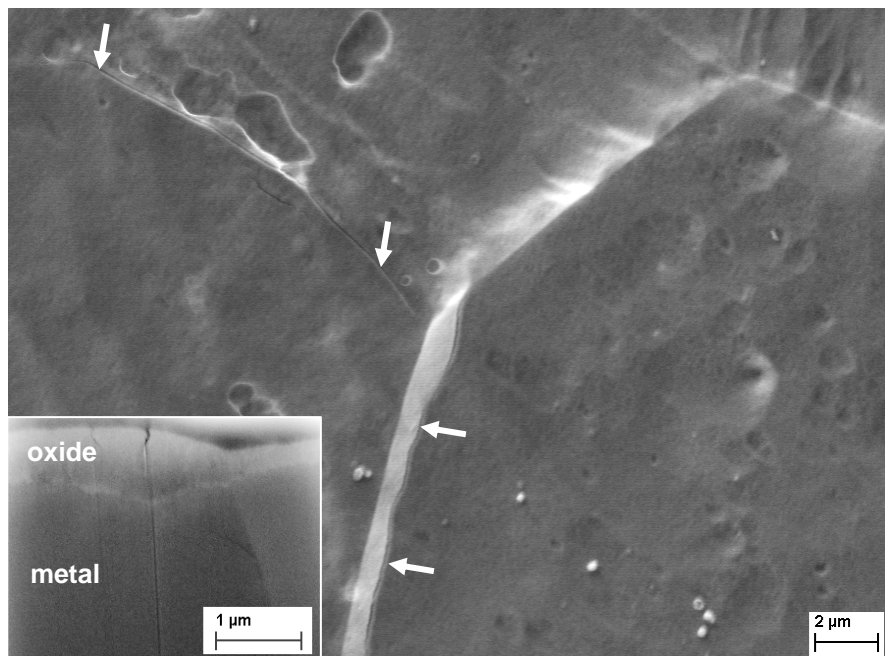


Figure 59: SEM micrograph of pure zirconium oxidised for 3 days in air. Cracks formed along steps at the surface above metal-grain boundaries can be observed (white arrows). The inset shows a FIB transverse section of a metal grain boundary and the formed oxide.

Different metal grain orientations lead to different oxide thickness and steps can be observed at the surface at grain boundaries of the underlying metal grains (white arrows in Figure 59). The orientation relationship of the metal grains and the formed oxide has not been investigated in this project, information about this can be found in the paper by David et al. [276]. It is not possible to judge the influence of different etching rates during the pickling process on the surface topography before oxidation, as the samples were only available in the oxidised form. In FIB transverse sections the oxide thickness variation between different metal grains can be observed (inset in Figure 59). The crack extending from the outer surface into the oxide can be observed as well.

6.1.5.2 Transmission electron microscopy

Figure 60 presents a TEM dark field contrast, showing the oxide scale and the metal-oxide interface of pure zirconium oxidised for 3 days in air. The oxide thickness varies between the two metal-grains, in the left grain the oxide thickness is around $0.7\ \mu\text{m}$ and in the right between 0.7 and $1\ \mu\text{m}$ with the maximum thickness close to the metal-grain boundary. The columnar oxide is oriented parallel to the oxide growth direction and the cracks in the oxide are oriented parallel to the surface. A crack perpendicular to the outer surface is presented in the inset of Figure 60, penetrating the oxide from the surface $400\ \text{nm}$ deep into the oxide scale above the metal-grain boundary. The contrast of metal and oxide is different on both sides of the grain boundary, showing that the oxide texture is related to the oxidised metal grains, as can be seen in the dark field contrast in Figure 60. The metal-oxide interface exhibits some undulation of up to $300\ \text{nm}$.

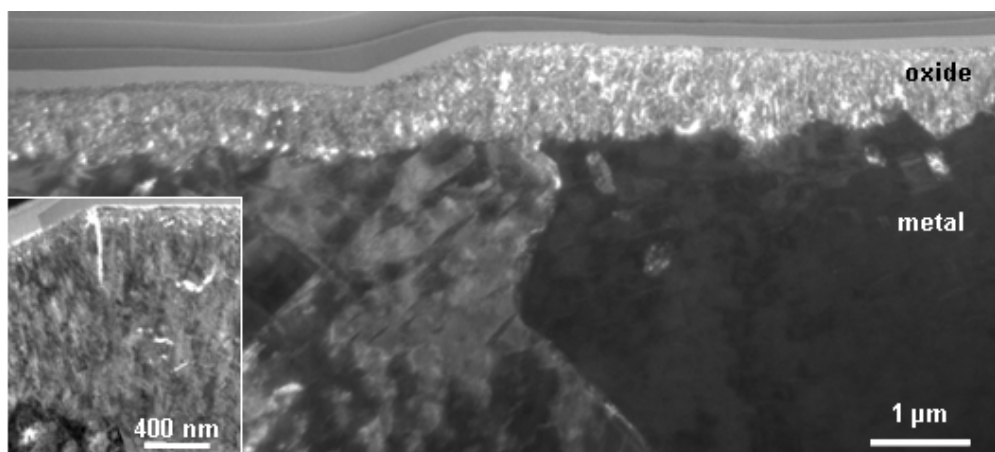


Figure 60: TEM dark field contrast of the oxide formed on pure zirconium in air. The different oxide thickness on different metal grains and the resulting steps on the surface can be observed. The bright field contrast in the inset shows the crack at the step on the surface.

6.2 Oxidation for 3 days in steam at ambient pressure

6.2.1 Zr1%Fe

6.2.1.1 SEM of surface

The surface was investigated with SEM and EDS, which revealed the presence of iron oxide in form of agglomerates of small crystals on the surface (Figure 61) on the surface of

Zr1%Fe oxidised for 3 days in steam. The surface density of these agglomerates is approximately 1.5 in an area of $100 \mu\text{m}^2$, ranging from 1-2 observable agglomerates on average for different regions on the surface. The size of the agglomerates is in the range of several hundred nanometres to one micrometer. The small oxide crystals are visible using the secondary electron (SE) detector, which is, however, only possible at higher magnification. On backscatter electron (BSE) images the contrast of the agglomerates to the matrix oxide is dark grey, being an indication for the lower average z of the crystals in the agglomerates compared to zirconia. In few cases also larger crystals with iron oxide can be found with a size of some hundred nanometres.

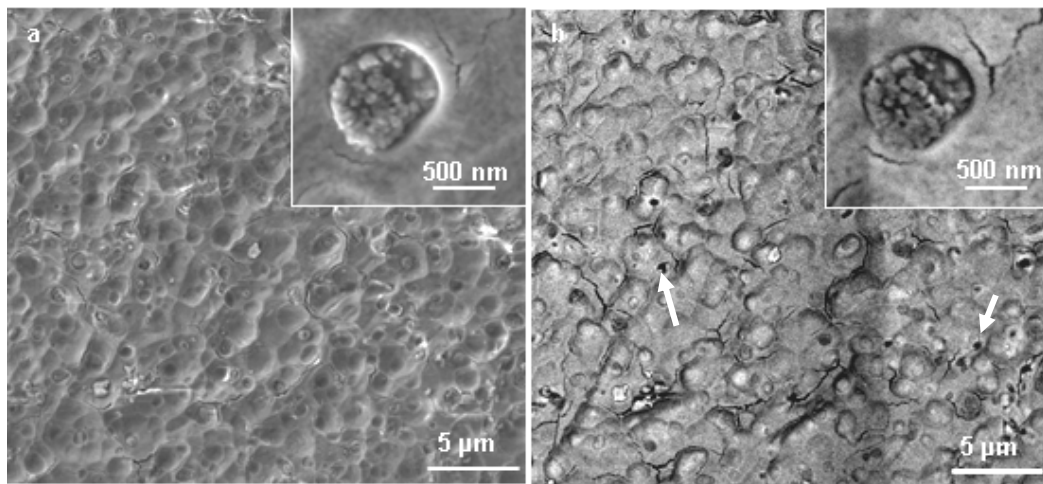


Figure 61: Surface of Zr1%Fe showing the crystals on the surface. (a) SE image, (b) BSE image of the same region. The dark grey regions in b) are iron oxide crystals and the black regions contaminations (some marked by white arrows for clarity) from handling and storage. The insets show an iron oxide crystal agglomerate at higher magnification. Cracks can be observed on the surface.

6.2.1.2 FIB transverse sections

FIB transverse sections show a varying oxide thickness and larger cracks in the oxide oriented parallel to the surface (Figure 62). Precipitates located at the metal-oxide interface did not show preferential oxidation. Two precipitates are present in the oxide scale just above the large cracks being indicated by the white arrows. The oxide thickness varies in the presented section between 0.5 and 1.5 μm.

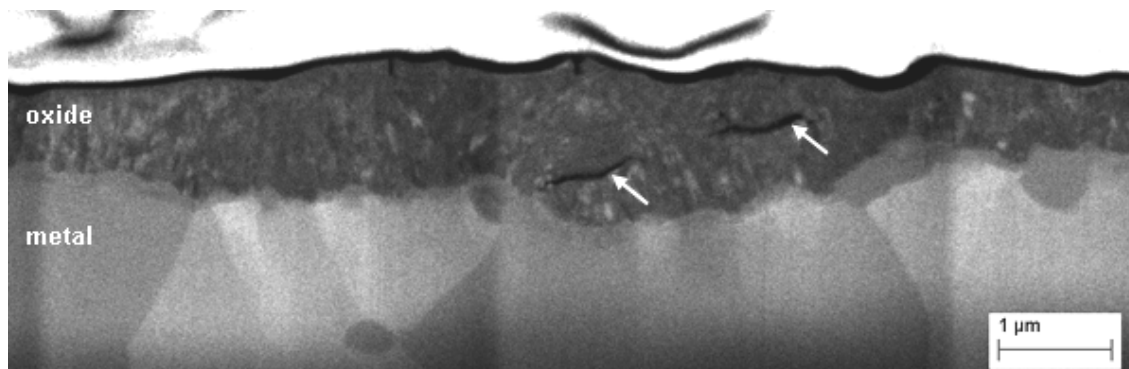


Figure 62: FIB transverse section of Zr1%Fe oxidized for 3 days in steam. Large cracks in the oxide scale are marked by white arrows.

6.2.1.3 Transmission electron microscopy

A TEM micrograph showing the oxide crystals at the surface and the metal-oxide interface of oxidised Zr1%Fe is presented in Figure 63. An approximately 200 nm thick layer of small iron oxide crystals is present above an oxidised precipitate, visible in the EDS map of Fe (indicated with a black arrow). Cracks can be observed within the oxidised precipitate (white arrow). The precipitate at the metal-oxide interface (Figure 63b) exhibited a similar oxidation behaviour as the surrounding zirconium matrix. The matrix oxide is columnar and oriented parallel to the oxide growth direction. In the oxidised precipitate a small crack oriented perpendicular to the oxide growth direction can be observed. The oxide grains underneath the oxidised precipitate are not oriented perpendicular to the outer surface and they are oriented towards the oxidised precipitate and not perpendicular to the outer surface. The outer surface is very rough as a consequence of the pickling treatment.

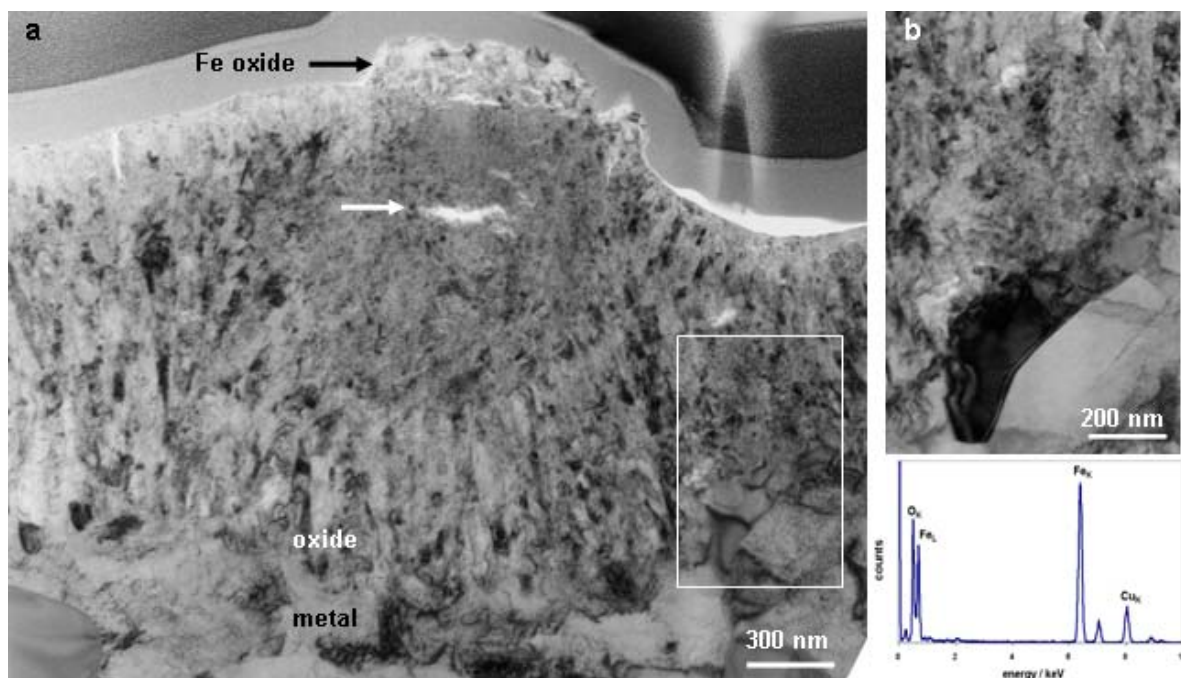


Figure 63: (a) TEM bright field contrast of Zr1%Fe oxidised for 3 days in steam showing pure iron oxide particles at the surface and the columnar matrix. (b) Bright field contrast showing the pure iron oxide particles on the surface. (c) Bright field contrast of a partially oxidised precipitate at the metal-oxide interface, the position is indicated with a white frame in (a). EDS spectrum is from iron oxide particles at the surface.

The EDS analysis in the TEM provided the following information: The crystals at the surface (Figure 63b) consist of almost pure iron oxide (EDS spectrum in Figure 63). EDS mapping (Figure 64 and Figure 65) and point analysis showed the depletion in iron of the precipitate underneath the iron oxide particles on the surface. The precipitates far from the outer surface did not show any Fe depletion; see the oxidised and metallic part of the precipitate at the metal-oxide interface (Figure 63b). Precipitates in the oxide showed oxygen signals indicating that the precipitates are oxidised. Therefore in the case of Zr1%Fe oxidised for 3 days in steam, no metallic precipitate was observed in the oxide.

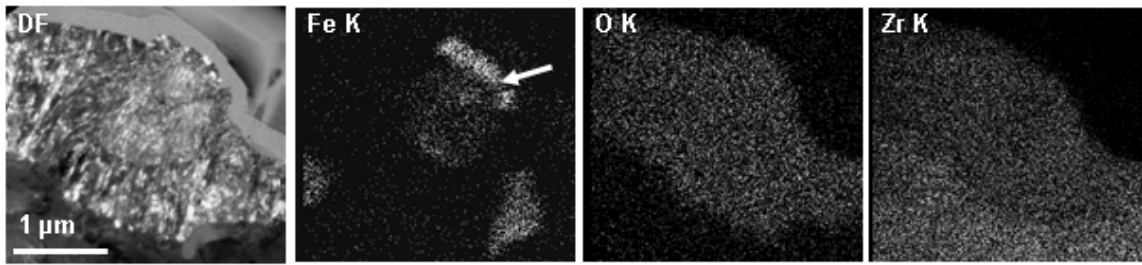


Figure 64: Dark field contrast and corresponding EDS maps showing the pure iron oxide at the surface (white arrow) and the iron depleted precipitate underneath.

In the case of crystals present at the outer surface (Figure 65), the situation is similar. The oxide of the oxidised precipitate is equiaxed and the columnar matrix oxide oriented parallel to the oxide growth direction. An oxidised precipitate is found in the oxide directly underneath the iron oxide crystal at the surface, being visible in the micrograph as region with equiaxed oxide. The oxide exhibits a small crack oriented perpendicular to the oxide growth direction close to the oxidised precipitate.

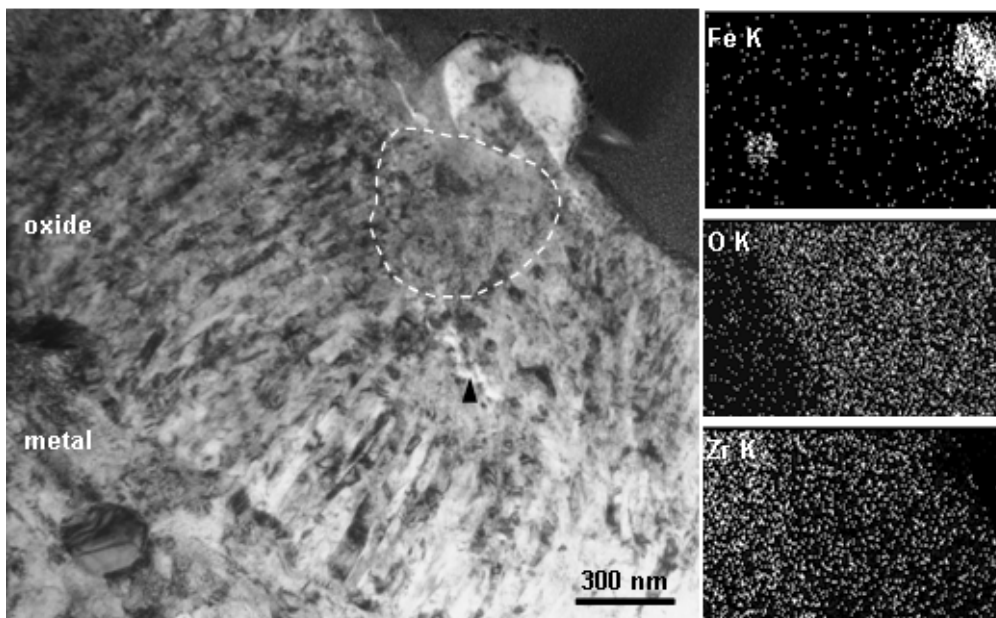


Figure 65: TEM Bright Field contrast of Zr1%Fe oxidised for 3 days in steam showing a pure iron oxide crystal at the surface and the columnar matrix. At the oxidised precipitate the oxide is equiaxed (white broken line). The EDS maps to the right show the Fe, O and Zr distribution (20° tilt with respect to presented micrograph!). A crack can be observed in the oxide scale (black arrowhead).

6.2.2 Zr1%Ni

6.2.2.1 SEM of surface

The surface was investigated with SEM and EDS. On most precipitates in contact with the outer surface, cracks can be observed in the oxide scale (Figure 66). On some precipitates small particles approximately 50 nm in size can be observed on the surface (Figure 66), EDS point analysis revealed the presence of nickel oxide at these positions with a weak Zr signal from the underlying precipitate or the matrix being detected beside the carbon being a contamination. There are usually less than 5 particles on one precipitate. The small oxide particles are visible on secondary electron (SE) images, however, they cannot be distinguished from contamination. Only on backscattered electron (BSE) images the contrast of the agglomerates to the matrix oxide helps to distinguish these from other features on the surface, as they exhibit a dark grey colour (and not black as carbon containing contamination), being an indication for the lower average Z of the crystals in the agglomerates compared to zirconia. EDS point analysis shows a high Ni signal, but an identification of the oxidation state of Ni is not possible in SEM from those spectra, but in the prepared TEM sample (Figure 68).

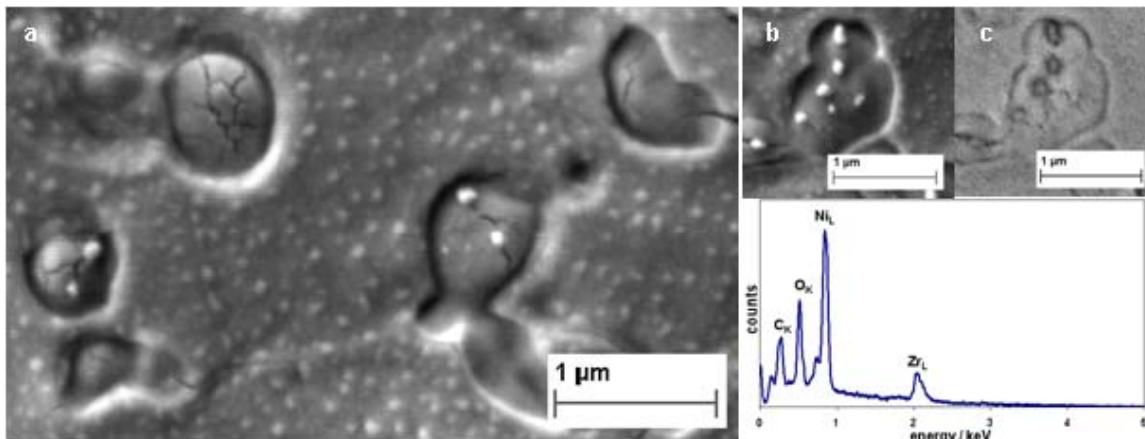


Figure 66: SEM micrographs of surface of Zr1%Ni oxidized for 3 days in steam. a) The oxide on precipitates at the surface is often observed to be cracked. The small insets show an oxidized precipitate with small particles (b) SE and (c) BSE signal. The small particles resulted in a high Ni signal with EDS point analysis at 5 kV as shown in the presented EDS spectrum.

6.2.2.2 Transmission electron microscopy

A TEM sample revealed that on Zr1%Ni the oxide thickness is significantly increased at positions of precipitates close to or at the outer surface (Figure 67). The matrix oxide is columnar and at oxidised precipitates it is equiaxed. The small crystals (marked with C) can be observed in the region of the oxidised precipitate.

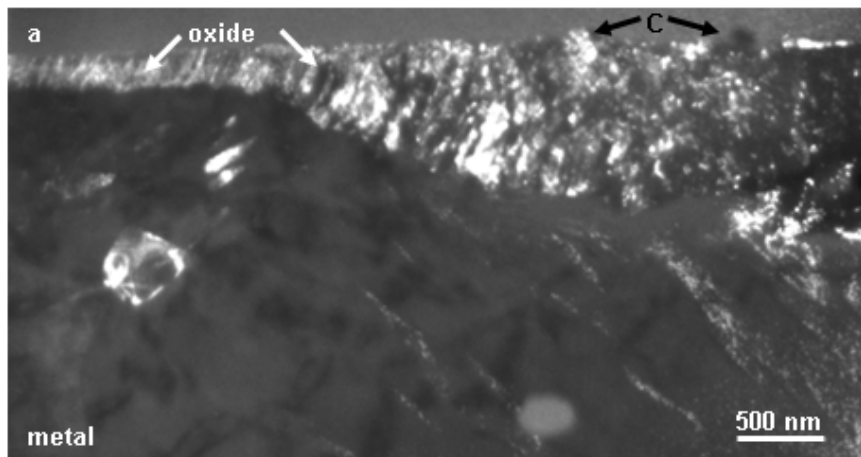


Figure 67: TEM dark field contrast of oxide scale on Zr1%Ni oxidised for 3 days in steam. The oxide is thicker in the part containing oxidized Ni containing precipitates on which the Ni rich crystals (C) can be found.

A more detailed study of the crystals at the outer surface revealed that they are single crystals, with the diffraction pattern being identified as [100]-zone axis (Figure 68) of nickel with 200 (0.172 nm) and 220 (0.120 nm) reflections (unit cell parameter metallic nickel $a = 0.35238$ nm [277]). The chemical analysis with EDS point analysis showed almost pure nickel (94 at.%) with a very small oxygen and small zirconium and copper peaks. Oxygen and zirconium could be a contribution from the underlying zirconia, due to the small size of the crystals it is not possible to avoid contributions from either the underlying zirconia or the deposited platinum. The copper signal originates from the TEM grid.

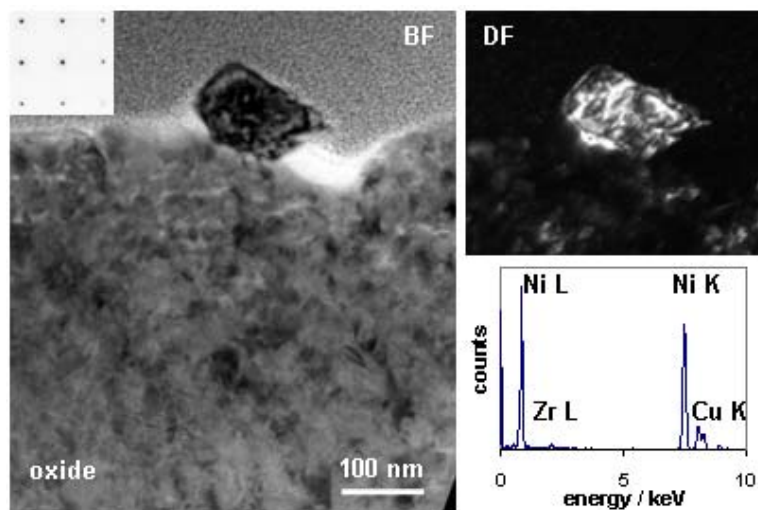


Figure 68: a) Bright field (BF) and dark field (DF) contrast of pure nickel found at the surface together with electron diffraction pattern of [100] zone axis and EDS spectrum of the crystal.

6.2.3 Pure zirconium

6.2.3.1 SEM of surface and FIB sections

The surface of pure zirconium oxidised in steam for 3 days exhibits a clear influence of the underlying metal grains on the formed oxide scale (Figure 69a). Different metal grains exhibit different surface aspects and at grain boundaries of the underlying metal steps can be

observed at the surface (inset (b) in Figure 69). The size of the metal grains is in the range of tens of micrometers for pure zirconium. In the oxide scale cracks parallel to the metal-oxide interface are present (inset (c) in Figure 69) being mainly in the sub-micrometer range.

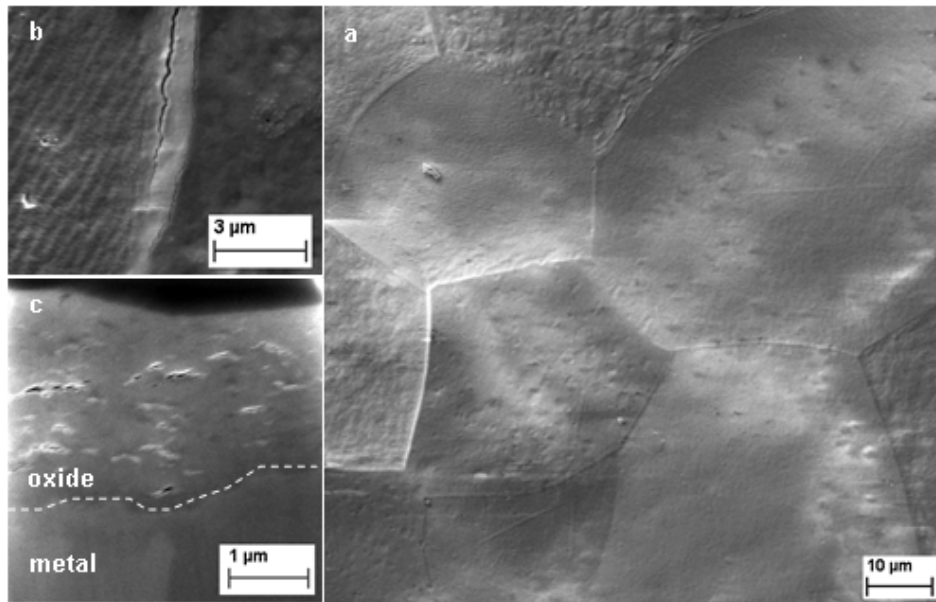


Figure 69: a) SEM micrograph of surface of pure zirconium oxidised for 3 days in steam. The inset (b) shows cracks formed along steps at the surface above metal-grain boundaries and inset (c) the cracks in the oxide scale on a FIB transverse section.

6.2.3.2 Transmission electron microscopy

A TEM dark field contrast showing the oxide scale and the metal-oxide interface of oxidised pure zirconium is presented in Figure 70a. The oxide thickness varies between the two metal-grains, in the left grain the oxide thickness is around 2.3 μm and in the right around 3 μm and up to 3.2 μm at the grain metal boundary.

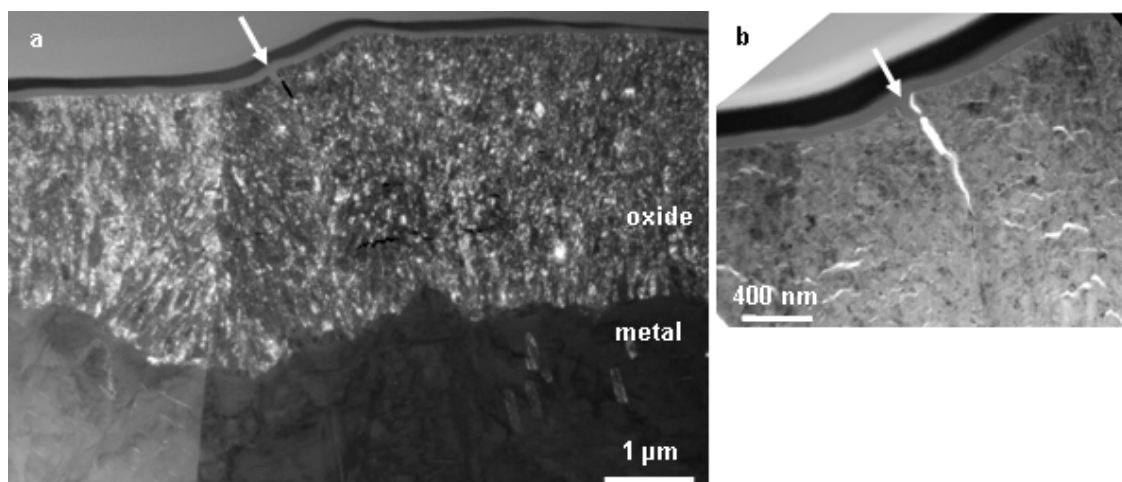


Figure 70: (a) TEM dark field contrast of pure zirconium oxidised for 3 days in steam. The step on the surface caused by different oxidation kinetics of neighbouring metal grains can be observed. (b) Bright field contrast of the crack at the step with same orientation as (a), but higher magnification.

The oxide is columnar and oriented parallel to the oxide growth direction while the cracks in the oxide are oriented parallel to the metal-oxide interface. An 800 nm deep crack perpendicular to the outer surface is present (Figure 70a&b white arrows) in the step at the surface above the metal-grain boundary, at some distance to the position of the metal-grain boundary at the outer surface. The dark field contrast in Figure 70a shows, that the oxide texture is related to the oxidised metal grains, the position of the metal-grain boundary can be traced from the metal to the outer surface, with the contrast of metal and oxide being different on both sides of the interface.

6.3 Oxidation for 110 days in steam at 10.5 MPa

6.3.1 Zr1%Fe

6.3.1.1 SEM of surface and FIB transverse sections

On the surface of Zr1%Fe oxidised for 110 days in autoclave the presence of the iron oxide in form of crystals on the surface has been confirmed with SEM (Figure 71) and EDS. Their surface density is approximately 2-3 crystals per 100 μm^2 . The larger crystals, being more than 1 μm in diameter, show usually well defined facets, which are clearly visible also on secondary electron (SE) images. The smaller crystals can be only clearly observed on backscattered electron (BSE) images, as their dark grey contrast makes it possible to separate them from other features on the surface like carbon containing contamination, which appears black. The cracks present at the surface have a length of up to several micrometers on the surface are often present at pickling craters.

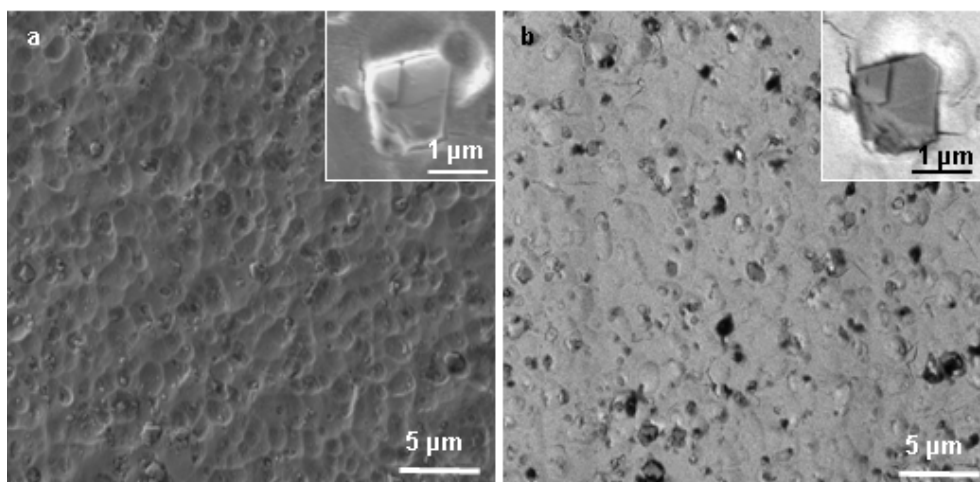


Figure 71: Surface of Zr1%Fe oxidised for 110 days in steam showing iron oxide crystals on the surface. (a) SE image, (b) BSE image of the same region. The dark grey regions in (b) are iron oxide crystals and the black regions contaminations from handling and storage. The insets show a larger iron oxide crystal at higher magnification. Cracks can be observed on the surface.

The oxide thickness, the undulation of the metal-oxide interface, the roughness of the outer surface and cracks in the oxide scale can be observed on the FIB section (Figure 72). To reduce the curtaining effect from the surface roughness, carbon was deposited on the surface to smoothen the surface topography; however, some curtaining is still observed.

Iron oxide crystals can be observed on the surface of the section in Figure 72, being clearly situated on the surface. Oxidised precipitates are visible in the oxide due to their brighter contrast compared to the oxide matrix (inset of Figure 72). The cracks in the oxide are oriented perpendicular to the oxide growth direction and are present in the whole oxide scale. The undulation of the metal-oxide interface is correlated to the presence of large cracks in the oxide, the oxide thickness is often reduced with respect to regions without large cracks close to the metal-oxide interface.

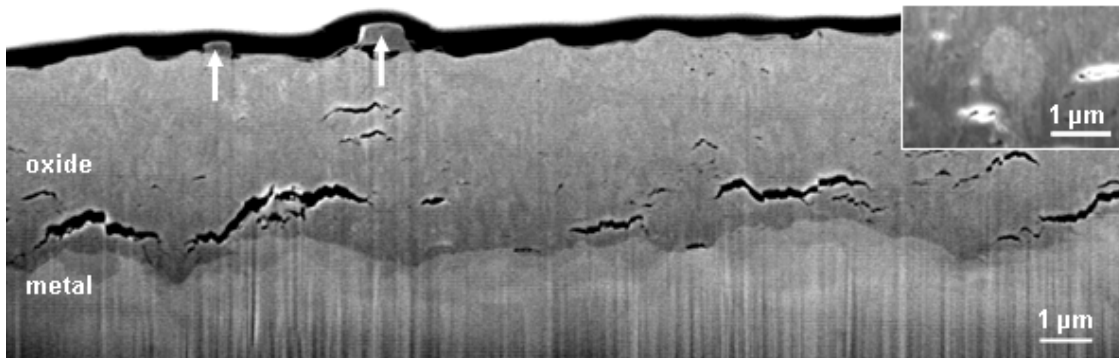


Figure 72: FIB section of Zr1%Fe oxidised for 110 days in steam showing the thick oxide and the undulated metal-oxide interface. Two Fe-oxide crystals on the surface (white arrowheads) can be observed. Precipitates in the oxide have a brighter contrast than the zirconia matrix (inset), the columnar structure of the matrix oxide being also observable.

6.3.1.2 X-ray diffraction of surface

The Zr1%Fe sample oxidised for 110 days in autoclave was characterised with X-ray diffraction of the surface to obtain more information about the iron oxide phase present at the outer surface. The diffractogram was acquired in the range of $15^\circ < 2\theta < 90^\circ$ using a step size of 0.019° and Cu_α radiation ($\lambda=0.154$ nm).

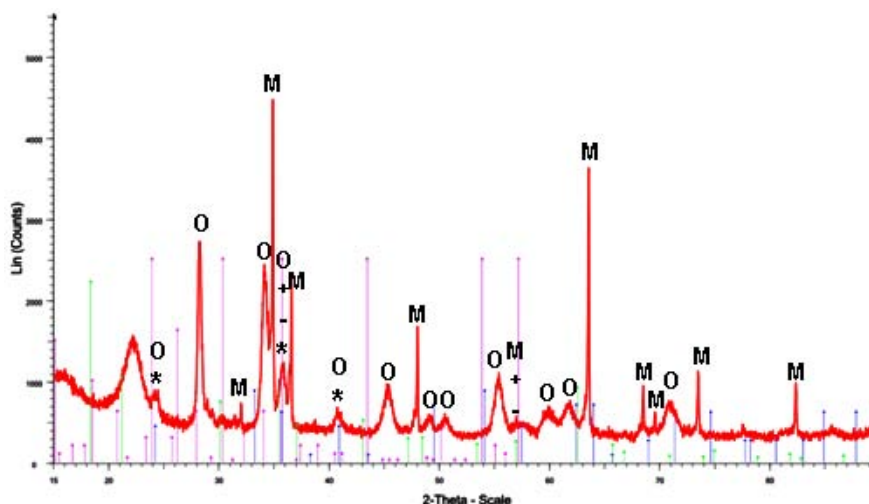


Figure 73: X-ray diffractogram of the surface of Zr1%Fe oxidised for 110 days in steam. The measured intensities are presented together with markers indicating possible phases contributing to the observed reflection (O zirconia, M zirconium, + magnetite, - maghemite, * hematite).

Only textured monoclinic zirconia could be identified unambiguously beside the underlying zirconium matrix, the possible reflections of iron oxide phases cannot be used to exclude the possible phases hematite, maghemite or magnetite as also the reflection intensities are low with some possible reflections of each phase not being observable at all and others not exactly where they are expected (Figure 73).

6.3.1.3 Transmission electron microscopy

A TEM micrograph of the oxide showing complete oxide scale from the metal-oxide interface to the outer surface of oxidised Zr1%Fe is presented in Figure 74. At the outer surface a crystal is observed. The equiaxed oxide of oxidised precipitates is visible and the columnar matrix oxide is oriented parallel to the oxide growth direction. The oxide exhibits large cracks oriented perpendicular to the oxide growth direction, the largest crack extends for more than 2 μm . Just below the outer surface the oxide contains many small cracks in a band of around 1 μm width.

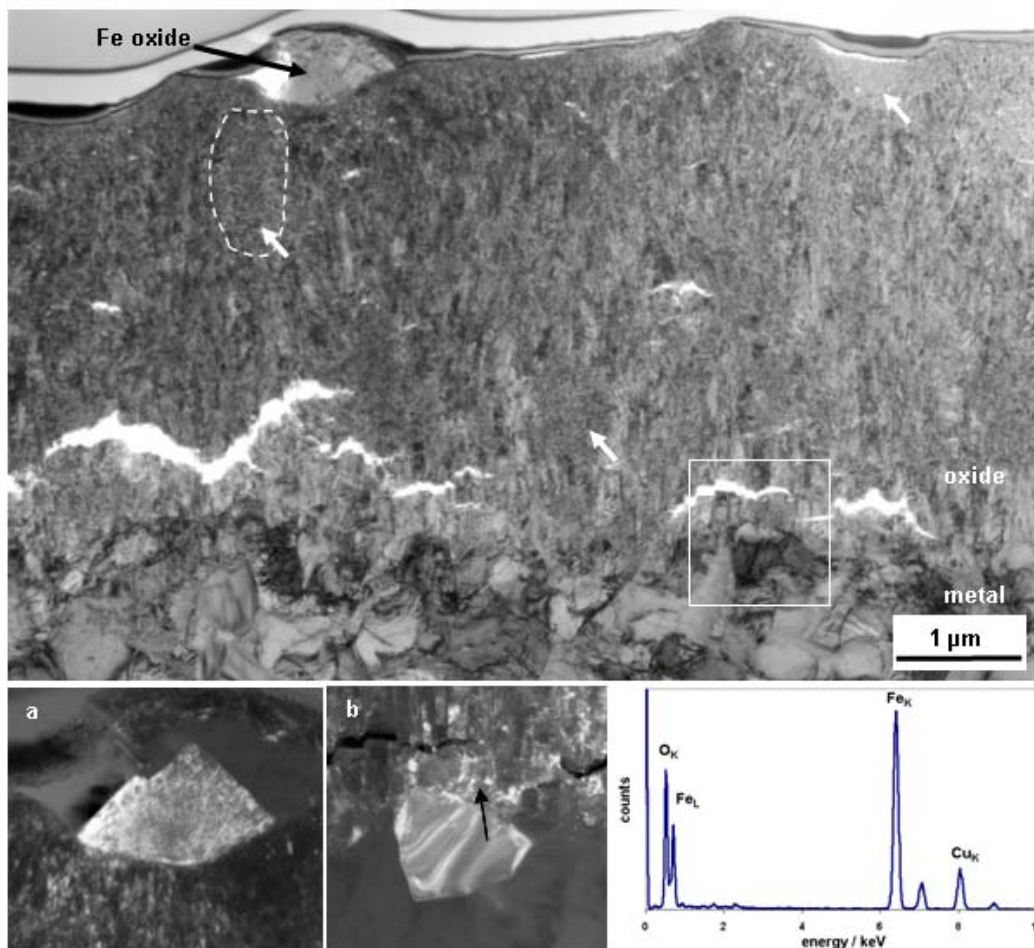


Figure 74 Bright field contrast of Zr1%Fe oxidised for 110 days in steam, showing a pure iron oxide crystal at the surface (black arrow), the thick columnar matrix oxide and the undulated metal-oxide interface. The precipitates show an equiaxed oxide (white arrows mark some for clarity). (a) Shows the dark field contrast of the single crystalline part of the iron oxide at the surface. (b) A partially oxidised precipitate at the metal-oxide interface is marked by the white frame. The EDS spectrum is from the iron oxide crystal at the surface.

A part of the crystal at the surface is a large single crystal (Figure 74a), being 565 nm wide and 450 nm high; the interface of the crystal and the matrix oxide is well defined. At the metal-oxide interface precipitates are observed to exhibit a similar oxidation front as the surrounding matrix, see also Figure 74b.

The EDS analysis of the TEM samples provided the following information: The EDS point analyses of the crystal observed at the outer surface show that it consists of pure iron oxide, EDS maps (Figure 75) confirm this; no zirconium can be observed in the region where iron and oxygen are present. No distinguishable trace of iron can be observed in the precipitate in the oxide underneath the crystal (Figure 74) visible as equiaxed oxide region marked with a broken line in Figure 74, point analysis resulted in a measured iron concentration below 1 at.% but above the slight iron background from the holder used for that measurement. Precipitates in the oxide showed iron and oxygen signals indicating that they are oxidised; so no metallic precipitate was observed in the oxide in the case of Zr1%Fe. EDS point analysis of oxidised precipitates resulted in iron concentrations which could be up to 8 at.%, which is quite close to the expected value for Zr_3Fe precipitates (8-9 at.% for pure oxidised precipitate signal without matrix oxide contribution).

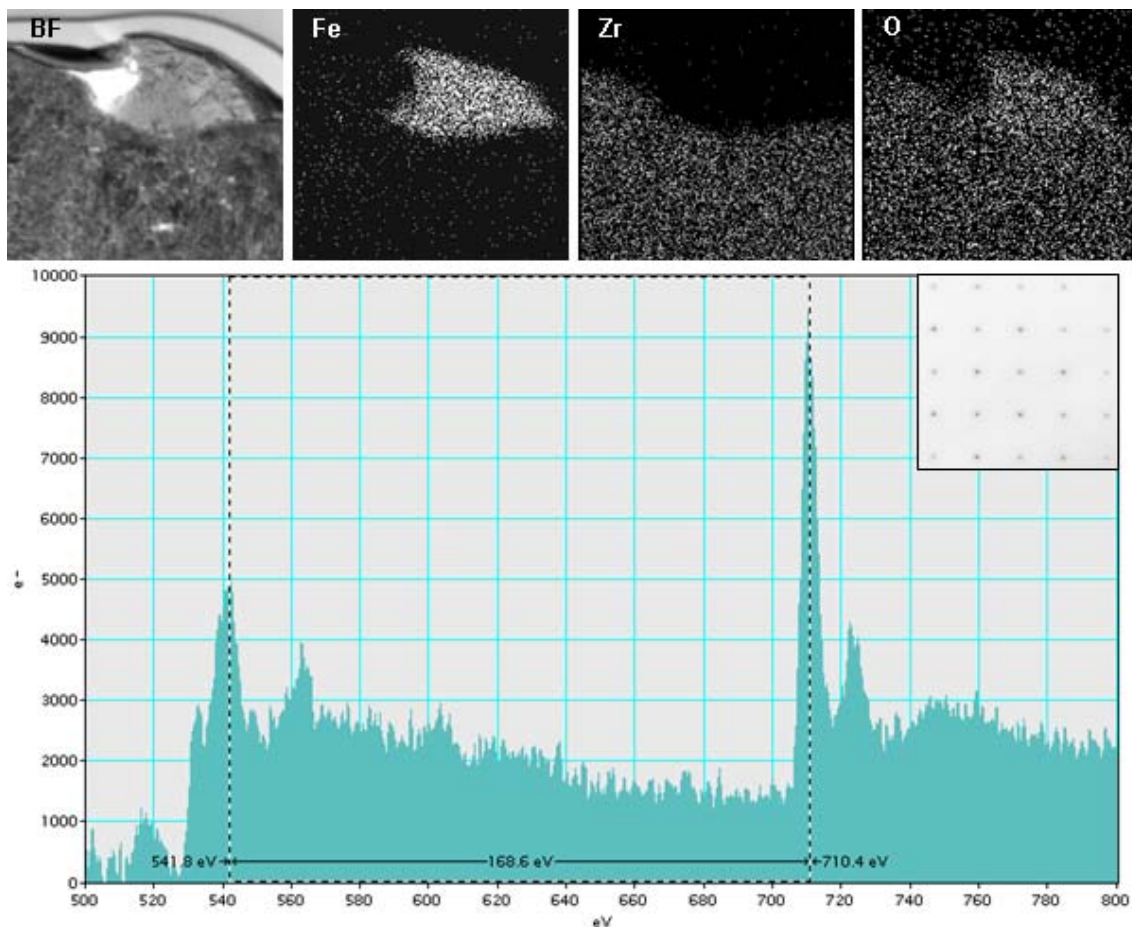


Figure 75: EDS maps are presented for iron oxide crystal formed at the surface, revealing no considerable presence of Zr in the crystal. The extracted EELS signal shows the Fe- $L_{2,3}$ and the O-K edge for the iron oxide crystal at the surface and the diffraction pattern a $[100]$ zone axis pattern of a cubic lattice ($a \approx 0.82$ nm).

Electron energy loss spectra (EELS) acquired from the iron oxide showed a spacing of 168.6 eV of the oxygen K-edge and the iron $L_{2,3}$ -edge (Figure 75), which is closer to the edge spacing of hematite and magnetite than that of wustite [278]. From the edge shape no unambiguous identification of either hematite or magnetite can be made comparing the extracted and smoothed signal with the spectra provided in [278]. The spectrum was corrected for the energy shift by acquiring a zero loss spectrum directly before and after the acquisition of the core loss spectrum. The peak positions (for oxygen K-edge 541.8 eV instead of 540 eV as in hematite and magnetite [278]) are shifted to slightly higher energies losses than in the reference, which is most probably due to the not exactly known energy shift during acquisition. The total energy shift for the zero loss peak after the core loss spectrum acquisition was -4.1 eV with respect to the zero loss peak before the core loss spectrum acquisition. The electron diffraction pattern presented in Figure 75 shows a diffraction pattern corresponding to the [100] zone axis of a cubic lattice with (200) and (220) directions present. The measured diffraction spots correspond quite well to the 220 (0.2967 nm) and 400 (0.2098 nm) directions of either magnetite ($a = 0.83950$ nm [274]) or maghemite ($a = 0.8347$ nm [275]), which are difficult to distinguish in electron diffraction due to their small difference in lattice spacing.

6.3.2 Zr1%Ni

6.3.2.1 SEM of surface and FIB transverse sections

On the surface of Zr1%Ni oxidised for 110 days in autoclave the grain boundaries of the metal grains before oxidation and the oxidised precipitates in contact with the outer surface can be observed in SEM. The precipitates show often cracks of the formed surface oxide.

On the FIB section in Figure 76 the oxide thickness, the undulation of the metal-oxide interface and cracks in the oxide scale can be observed. Oxidised precipitates cannot be easily distinguished from the matrix oxide on the transverse section shown. However, regions with a brighter contrast, corresponding to a more equiaxed grain structure, can be correlated to the presence of Ni in the oxide. The cracks in the oxide are oriented perpendicular to the oxide growth direction, being present in the whole oxide scale.

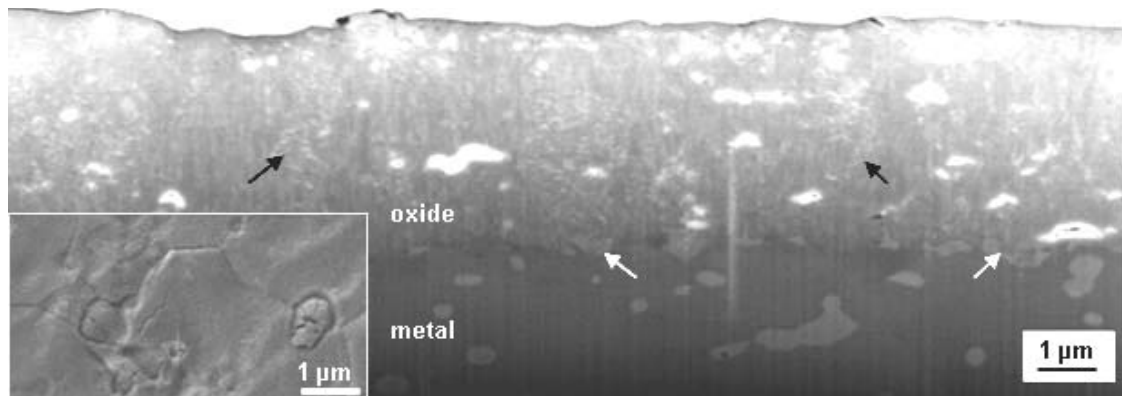


Figure 76: FIB section of Zr1%Ni showing the thick oxide and the undulated metal-oxide interface. Precipitates at the metal-oxide interface are marked with white arrows and two in the oxide with black arrows. The columnar matrix oxide structure can be observed locally. The inset shows two features looking like oxidised precipitates at the surface.

6.3.2.2 Transmission electron microscopy

A TEM bright field contrast of the complete oxide scale of oxidised Zr1%Ni is presented in Figure 77, the oxide can be observed from the metal-oxide interface to the outer surface. At features having the appearance of precipitates at the outer, surface cracks can be found. As an example for this, the feature at the surface in Figure 77 is the same as the right feature in the inset of Figure 76. Precipitates have exhibited a similar oxidation front as the surrounding matrix at the metal-oxide interface, as shown in Figure 77a. The zirconia matrix has a columnar structure oriented parallel to the oxide growth direction; oxidised precipitates have an equiaxed structure (Figure 77b). The cracks present in the oxide are oriented perpendicular to the oxide growth direction.

EDS point analysis of oxidised precipitates well surrounded by oxide resulted usually in nickel concentrations below 2 at.%, which is far below the expected value for Zr_2Ni precipitates (12-13 at.% for pure oxidised precipitate signal without matrix oxide contribution).

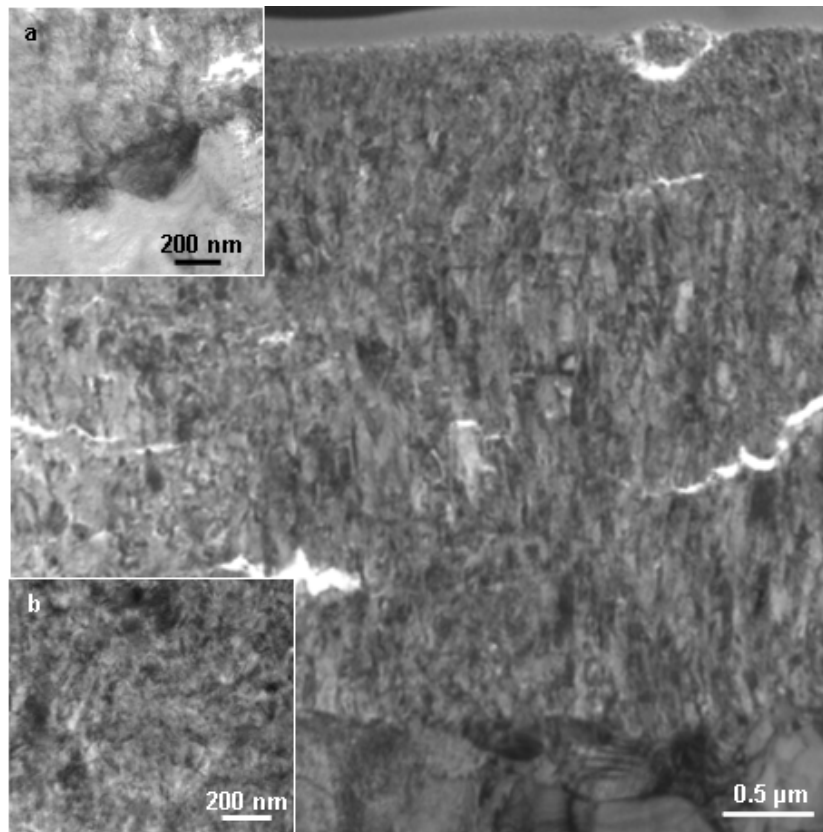


Figure 77: TEM Bright field contrast of Zr1%Ni showing the thick oxide and the undulated metal-oxide interface. In (a) at higher magnification details of a partially oxidised precipitate at the metal-oxide interface are presented and in (b) an oxidized precipitate in the oxide.

6.3.3 Zr1%Cr

6.3.3.1 SEM of surface and FIB transverse sections

On the surface of Zr1%Cr oxidised for 110 days in autoclave the cracks have a length of up to several micrometers (Figure 78). The surface is quite smooth, as the small precipitate size does not result in preferential pickling leading to larger craters. The precipitates are not observable at the oxide surface.

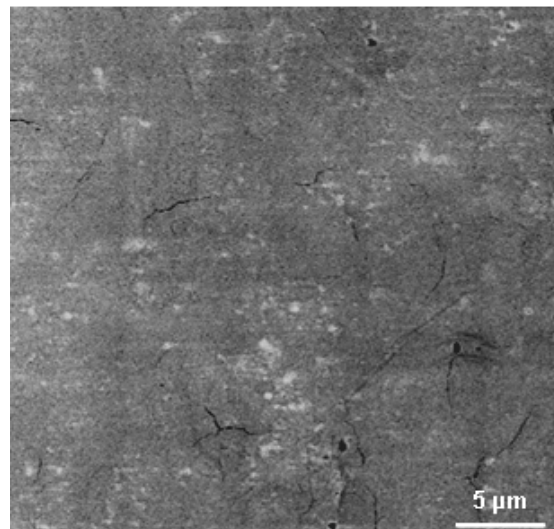


Figure 78: Surface of Zr1%Cr showing the cracks on the surface, some of them are interconnected (BSE image). The black regions are contaminations from handling and storage.

On the FIB sections the oxide thickness, the undulation of the metal-oxide interface and cracks in the oxide can be observed (Figure 79). The outer surface is almost flat. Precipitates in the oxide can be observed because of their darker contrast compared to the oxide matrix. However, due to their size no further characterisation is possible in SEM. The cracks in the oxide are oriented perpendicular to the oxide growth direction and they are present over the whole thickness of the oxide. The maximum size of the cracks observed in the oxide is approximately 1 μm in the presented section.

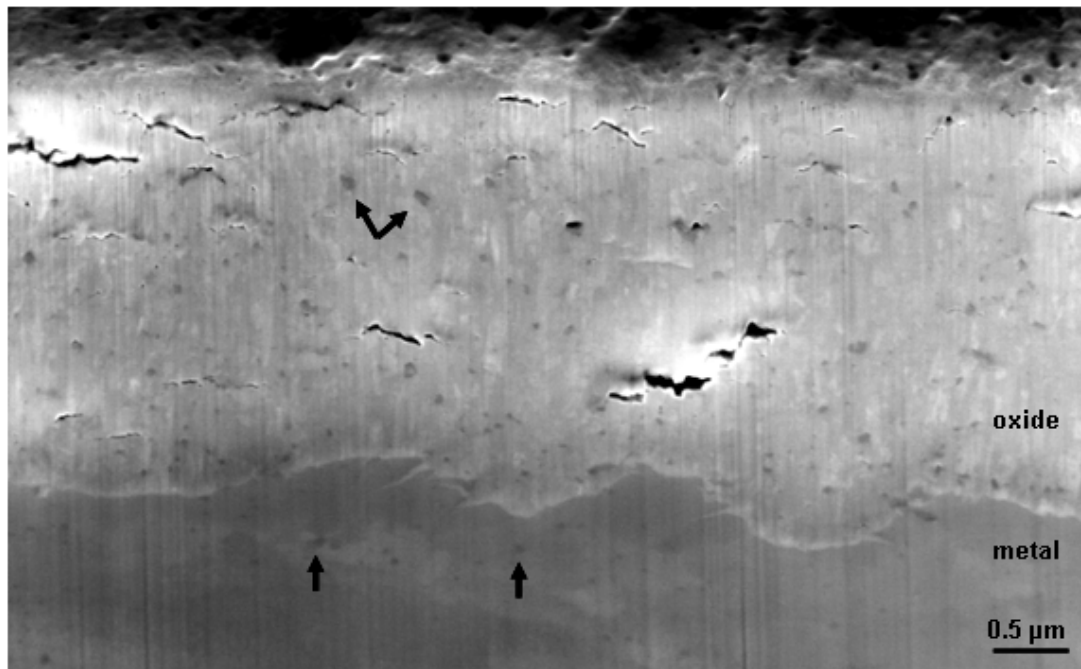


Figure 79: FIB cross-section of Zr1%Cr showing the thick oxide and the undulated metal-oxide interface. The precipitates show a dark contrast in the oxide and in the metal (arrows).

6.3.3.2 Transmission electron microscopy

A TEM micrograph of oxidised Zr1%Cr is presented in Figure 80, showing the oxide from the metal-oxide interface to the outer surface. The oxide crystals are columnar and exhibit cracks oriented perpendicular to the oxide growth direction. The innermost oxide shows a lower crack density compared to the rest of the oxide. Each precipitate observed in the oxide had a crescent shaped crack positioned at the top of the precipitate looking from the outer oxide surface (inset of Figure 80).

For the EDS measurements of the precipitate in the oxide, due to the small size of the precipitates, a significant contribution of the matrix is included in the signal. Therefore the oxygen content in the precipitate was determined by separating the contribution of the zirconia matrix using the known stoichiometry of the precipitate and considering the matrix to be fully oxidised, following the procedure described in Appendix I on page 183.

The EDS analysis of the precipitates in the oxide provided the following information:

1. Many precipitates in the oxide exhibit too low oxygen contents to be fully oxidised with 45-60 at.% oxygen at the precipitate and compared to 66 at.% oxygen in the surrounding oxide matrix. This corresponds to approximately 0-30 at.% oxygen in

the precipitate using the previously described method for subtracting the matrix contribution to the oxygen signal, using the Zr L-line and the Cr K-line for quantification. Precipitates showed delayed oxidation near the metal-oxide interface and up to a maximum distance of $\sim 1.5 \mu\text{m}$ from the metal-oxide interface.

2. Precipitates near the outer oxide surface were observed to have an oxygen content of approximately 60 at.%, indicating fully oxidised precipitates.

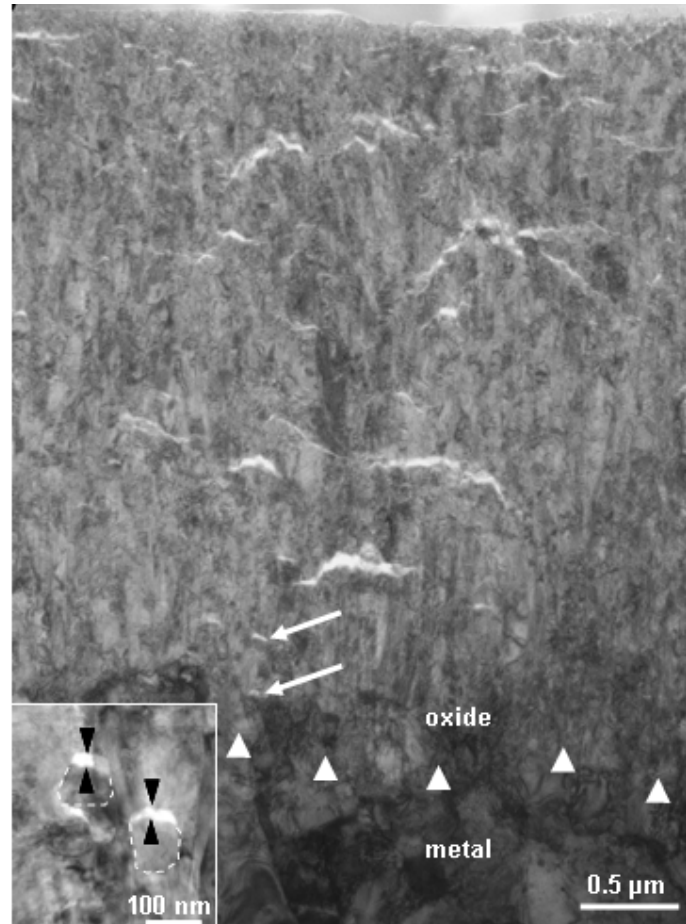


Figure 80: TEM bright field contrast of Zr1%Cr showing the oxide layer from the metal-oxide interface (arrow heads) to the outer surface. Cracks caused by unoxidised precipitates are visible in the oxide (white arrowheads). Inset at higher magnification shows unoxidized precipitates with the crescent shaped cracks (black arrowheads) in detail.

6.3.4 Zr0.6%Nb (for 40 days)

6.3.4.1 SEM of surface and FIB transverse sections

Similar to the Zr1%Cr, this alloy contained small precipitates, the topography of the surface was similar and the respective micrographs are therefore not shown. On Zr0.6%Nb oxidised for 40 days in autoclave cracks on the surface having a length of up to several micrometers were observed. They followed often the underlying metal grain boundaries.

On the FIB transverse sections precipitates in the metal and in the oxide (with maximum $1 \mu\text{m}$ distance from the metal-oxide interface) could be observed; however, due to their size no further characterisation is possible in SEM. On large precipitates in the oxide cracks could be observed on the side facing the outer surface. The cracks in the oxide were oriented perpendicular to the oxide growth direction and they were present in the whole oxide scale.

On Zr0.6%Nb oxidised for 40 days in autoclave cracks on the surface having a length of up to several micrometers can be observed (not shown here). They follow often the underlying metal grain boundaries, as the different oxidation kinetics of the metal grain orientations leads to steps at the surface, along which the oxide sometimes cracks close to the surface.

On the FIB section precipitates in the metal and in the oxide (not more than 1 μm apart from the metal-oxide interface) can be observed (Figure 81); however, due to their size no further characterisation is possible in SEM. On large precipitates in the oxide cracks can be observed on the precipitate side facing the outer surface (inset of Figure 81), which can be only resolved in the TEM for precipitates having the average precipitate size. The steps on the outer surface mark also regions of locally different oxide thickness with a variation of several hundred nanometres, which are also visible in the top view images in SEM. The cracks in the oxide are oriented perpendicular to the oxide growth direction and they are present in the whole oxide scale. The large cracks in the oxide close to the metal-oxide interface can be correlated to regions with somewhat thinner oxide, or alternatively delayed oxidation of the matrix.

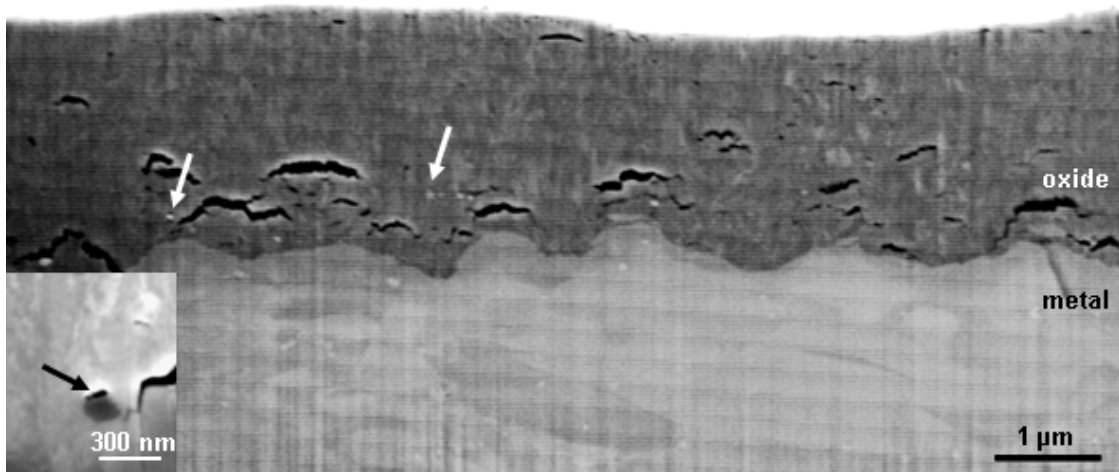


Figure 81: FIB section of Zr0.6%Nb Nb oxidised for 40 days in steam showing the thick oxide, the undulated metal-oxide interface and the columnar matrix oxide. The precipitate can be observed (two marked with white arrows for clarity), however, are too small to be further characterised. The inset shows a Nb containing precipitate with a crack (black arrow).

6.3.4.2 Transmission electron microscopy

A dark field contrast of Zr0.6%Nb, showing the oxide from the metal-oxide interface to the surface of oxidised Zr0.6%Nb is presented in Figure 82. The oxide layer is columnar and exhibits large cracks oriented perpendicular to the oxide growth direction close to the metal-oxide interface. The different oxide thickness on the two metal grains in Figure 82 can be clearly observed together with the step on the outer surface. For Zr0.6%Nb the precipitates observed in the oxide showed crescent shaped crack towards the outer surface (inset of Figure 82). The oxide grains of the matrix show a columnar structure.

The EDS analysis of the precipitates in the oxide provided the following information (considering the correction with the subtraction of the matrix contribution in Appendix I on page 183):

1. Many precipitates in the oxide exhibit low oxygen contents; measured oxygen signal being 35-50 at.%, thus oxygen in the precipitate will be between 25-50 at.% using the same procedure described above, with a niobium to zirconium ratio of 4 (β -Nb precipitates). The Nb content of the precipitates in the metal was the reference value for this calculation, the ratio of Nb to Zr in the metal being close to 4. The matrix surrounding the precipitates was found to be fully oxidised.
2. Precipitates in the oxide further away from the metal-oxide interface are found to be oxidised

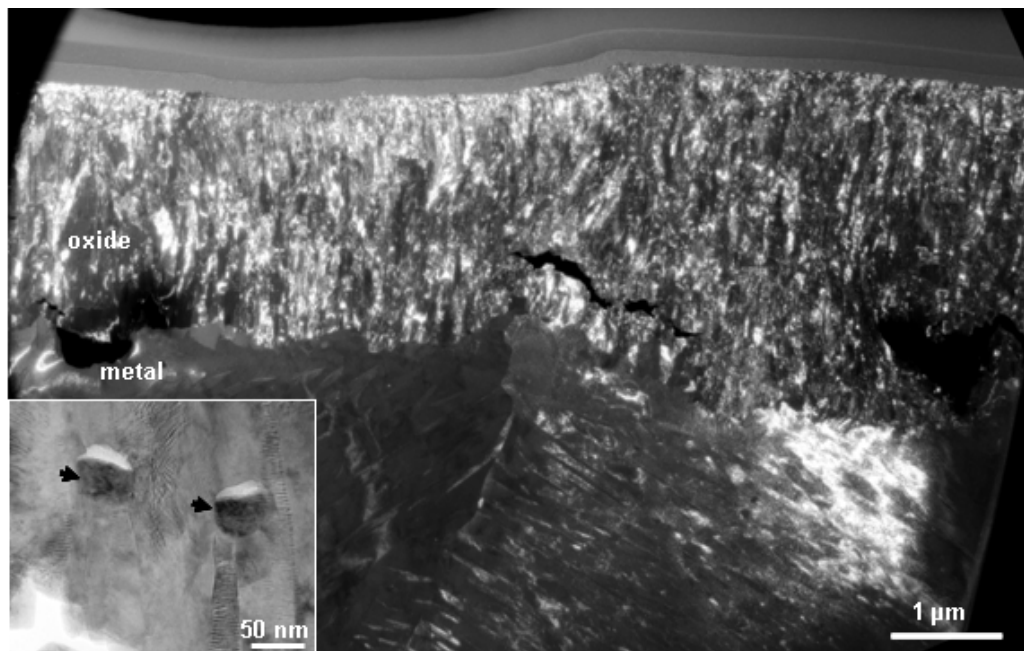


Figure 82: TEM dark field contrast of Zr0.6%Nb oxidised for 40 days in steam showing the oxide layer from the metal-oxide interface to the outer surface. Inset at higher magnification presents precipitates in the oxide (arrows) with the crescent shaped cracks.

6.4 Oxygen diffusion zone in the metal as a function of the oxidation time

To be able to compare the oxygen diffusion zone below the oxide scale, EDS point line scans were acquired at the metal-oxide interface in the oxide and the metal. The position of the individual EDS points with respect to the metal-oxide interface was determined by short exposures of the EDS spot on a negative which was exposed before the measurements to the bright field contrast of the interface region, see the example for pure zirconium in air in Figure 83. The position of the interface was determined on the micrograph in the region of the spots closest to the interface. In case it was not possible to localise the interface without doubt, a band is marked for the possible position. The same is done for STEM-EDS line scans, for which the STEM image had not sufficiently good contrast to allow unambiguous identification of the interface. The acquisition time used was 100 lifetime seconds (lifetime = (1 - percentage dead time of detector)), to minimise the impact of possible sample drift on the position of the spots and contamination of the sample at the measured spots. For the integrated zirconium signal more than 10000 counts were usually acquired in the metal and in

the oxide (less than 1% error in detected x-ray signal), for oxygen this was only achieved for thicker samples in the oxide, however not in the metal, inferring a considerably higher possible error of the detected signal and therefore in the deduced oxygen content for the metal part of the measurements. Data that were acquired too close to the metal-oxide interface and did not contain information only from one of the phases were rejected and are not plotted.

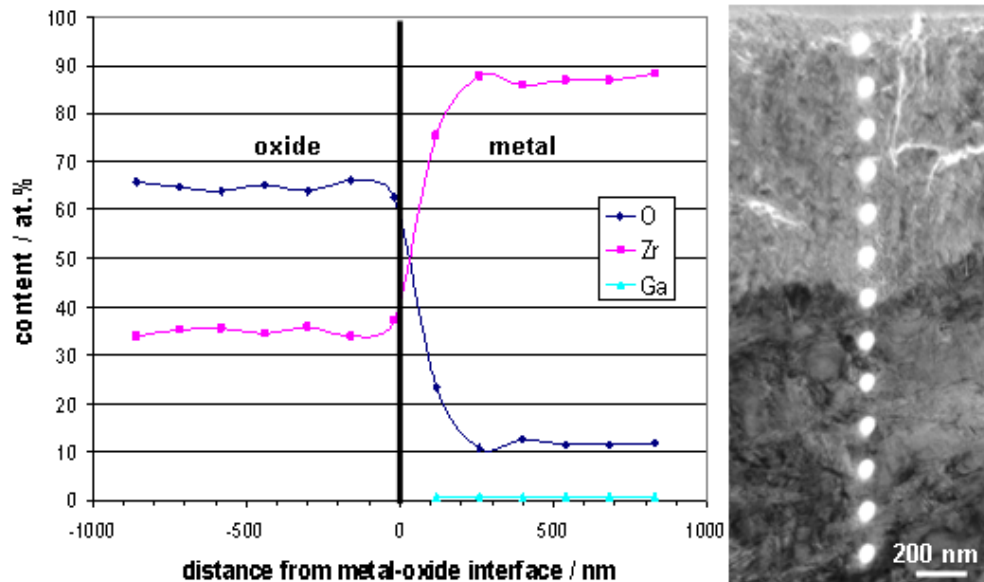


Figure 83: EDS point line scan over the metal-oxide interface on pure zirconium oxidized for 3 days in air. The bright field contrast shows the individual measurement points.

In the materials oxidised in the ESEM for 1 hour at 415°C the oxygen levels on the metal side do not reach a similar level at some distance of the metal-oxide interface (Figure 84). A diffusion zone and its upper limit cannot be extracted from the data, as no clear asymptotic shape is observed for the oxygen profiles of those point line scans for which data up to 200-300 nm into the metal are available. For pure zirconium and Zr1%Fe a levelling can be assumed around 150-200 nm, while for Zr1%Ni the oxygen level drops until 300 nm. For Zr0.6%Nb no asymptotic level is reached, as the points have been not acquired far enough into the metal and for Zr1%Cr very high oxygen levels have been measured in the metal with the oxygen level still dropping after 300 nm. In the case of Zr1%Ni also the total metal concentration curve is plotted to show that the overall metal concentration close to the metal-oxide interface is similar to pure zirconium oxidised under the same conditions.

The zirconium and oxygen profiles for the binary alloys oxidised in air at ambient pressure show a similar diffusion zone for all materials with the same oxidation time (Figure 84). After 3 days in air the diffusion zone is in the range of 200-300 nm and after 55 days in the case of Zr0.6%Nb 500-600 nm.

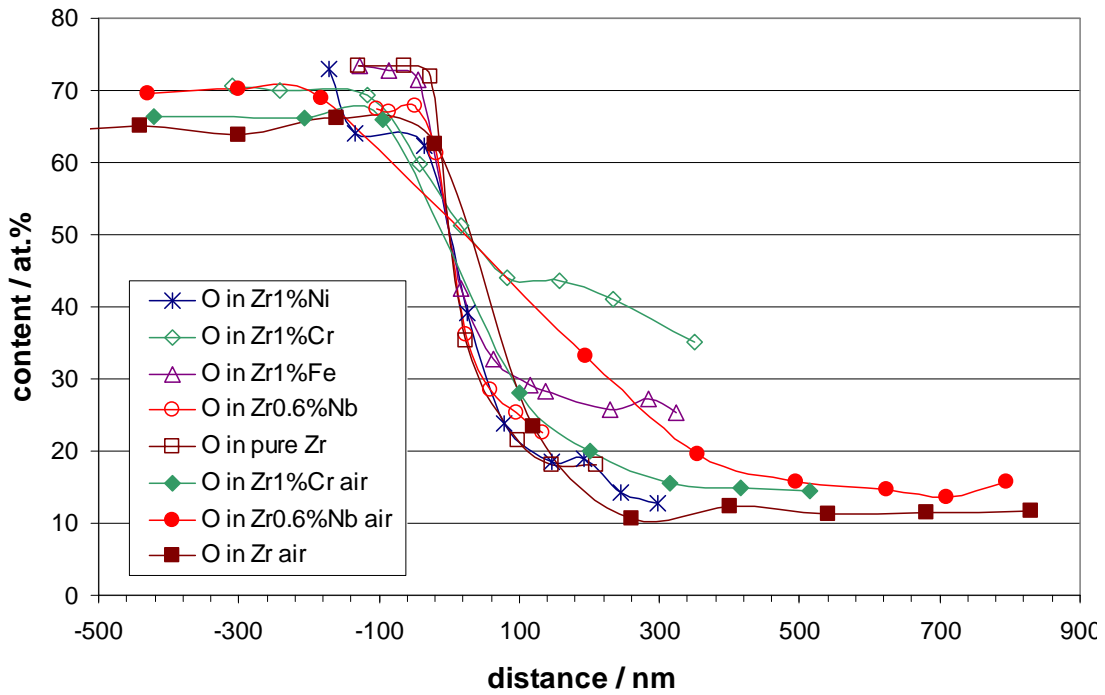


Figure 84: EDS point line scans for binary alloys and pure zirconium oxidised in 130 Pa vapour pressure for 1 hour in the ESEM and at ambient pressure for 3 days in air with the exception of Zr0.6%Nb, which was oxidised for 55 days in air at 415°C.

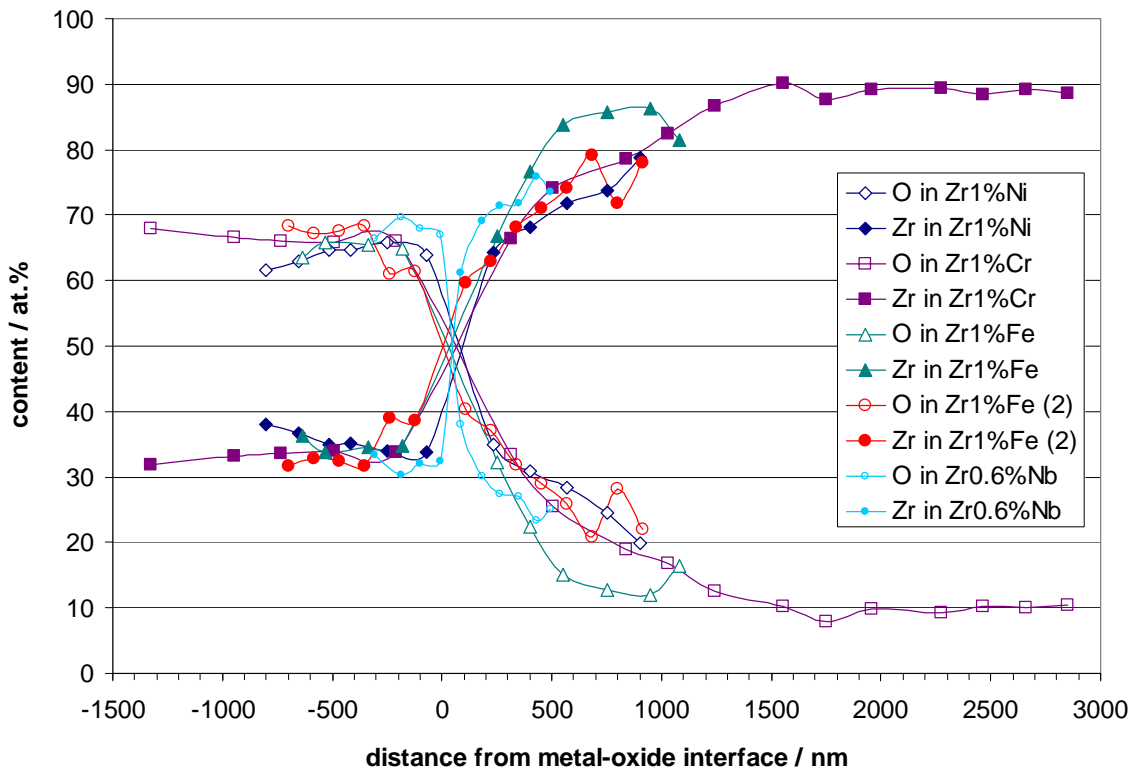


Figure 85: EDS point line scans for binary alloys oxidised for 110 days in steam at 415°C with the exception of Zr0.6%Nb, which was oxidised for 40 days in steam.

The zirconium and oxygen profiles for the binary alloys oxidised for 110 days in steam at 10.5 MPa show a similar diffusion zone for all binary alloys with the same oxidation time extending around 1500 nm from the metal-oxide interface (Figure 85). There is some scatter in the acquired data, which can be due to local variation in oxygen concentration (compare both profiles for Zr1%Fe) and the presence of alloying elements (small dip in Zr and O curve for Zr1%Cr). The oxygen gradient at the metal-oxide interface in Zr0.6%Nb oxidised for 40 days in steam is steeper, indicating a smaller diffusion zone than for the 110 day samples, due to the shorter oxidation time. Extrapolating to 110 days assuming a linear relationship of the diffusion profile shows that the oxygen profile in Zr0.6%Nb is similar to the other binary alloys.

In the plot presented in Figure 83 it can be observed that the gallium concentration detected is highest in the metal (always below 1 at.%) and below the detection limit in the oxide. This trend for higher gallium concentrations in the metal than in the oxide was observed for all TEM samples, regardless of whether they were prepared with the oxide on top or as transverse samples with the metal-oxide interface vertical in the sample. This observation indicates that the higher gallium content in the metal cannot be ascribed only to the preferential implantation in the lower part of the sample due to the milling geometry, as otherwise the gallium concentration in metal and oxide should be similar for transverse TEM samples.

7 Comparison of oxidation behaviour of binary alloys

A comparison of the SEM results on the different alloys showed the presence of iron oxide crystals on the surface of all iron containing alloys. The amount of iron oxide increased with oxidation time and the size of the crystals increased to more than 1 μm after 110 days. On the other alloys also some iron oxide could be observed, this was however much more rare than in the case of the Zr1%Fe alloy. For the Zr1%Ni alloys only for the oxidation for 3 days in steam small metallic nickel particles could be observed on oxidised precipitates in contact with the outer surface. On Zr1%Ni the oxidised precipitates in contact with the outer surface show after oxidation for at least 2 hours cracks of the oxide on the surface.

An influence of the precipitate oxidation on the surface topography could not be investigated for the autoclaved samples. The roughness from the pickling process rendered AFM scans of the surface not meaningful for evaluation of the influence of the precipitates on the outer surface of autoclaved samples, as the topography before oxidation could not be assumed to be flat.

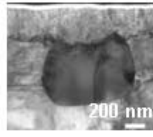
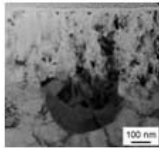
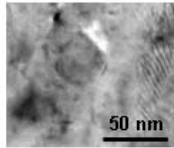
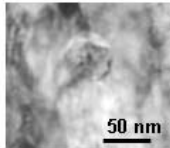
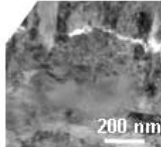
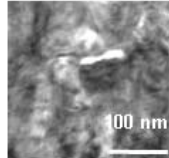
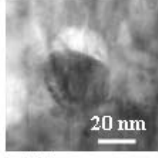

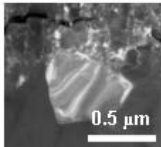
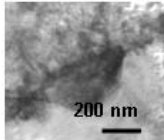
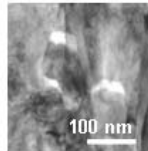
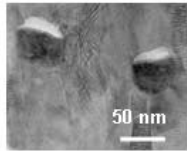
The oxidation behaviour of the precipitates is for the binary alloys clearly linked to the type of precipitate. The results obtained for the precipitate oxidation in the four binary alloys can be differentiated into two categories: delayed oxidation and oxidation similar to the surrounding matrix. These observations for the binary alloys were found to be independent of the oxidation time and pressure (Table 14), but correlated to the alloying element, as two alloying elements formed precipitates exhibiting the delayed oxidation and the two other oxidation behaviour similar to the matrix. The behaviour observed did not show a distinct difference between air and steam for the precipitate oxidation.

The delayed oxidation in the case of precipitates in Zr1%Cr and Zr0.6%Nb was for all different environments concluded from the same criteria as mentioned in the section dealing with the in situ results: lower oxygen contents than the surrounding oxide matrix and cracks at the precipitate oxide interface towards the outer surface.

The FIB sections did not reveal a correlation of the metal-oxide interface undulation and the presence of precipitates. For the presence of cracks and the metal-oxide interface undulation it can be stated, that large cracks seem to go along with a retarded oxidation front, however, this cannot be quantified further and also no conclusion is possible which of the two is the cause and which the consequence of the other.

For Zr1%Fe and Zr1%Ni a precipitate oxidation similar to the surrounding matrix was concluded from the observations of larger precipitates at the metal-oxide interface, which were oxidised on the oxide side and metallic on the metal side. For the precipitates in Zr1%Fe it could be shown with EELS that the oxidation state of Fe in the precipitates in the oxide and of pure iron oxide is the same, so reports of unoxidized iron in the oxide are not valid for the binary alloys investigated in this study. So from our results we have no proof for precipitates exhibiting a different oxidation state than the alloying element contained in them. For Zr₂Ni this has not been shown (no EELS measurements).

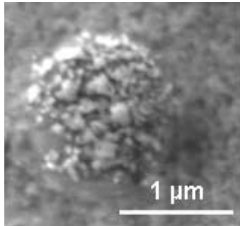
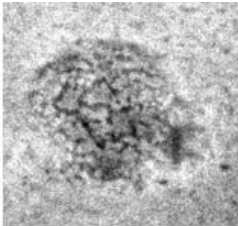
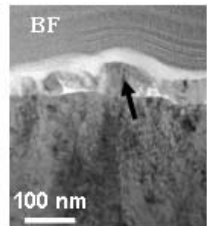
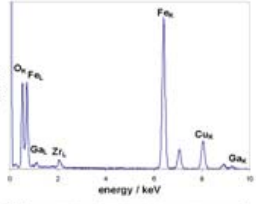
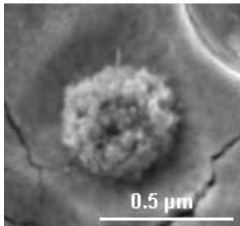
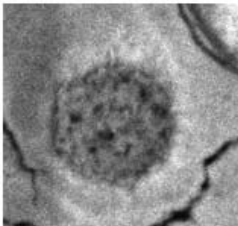
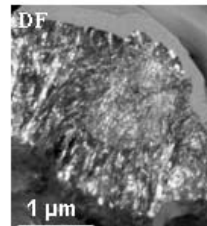
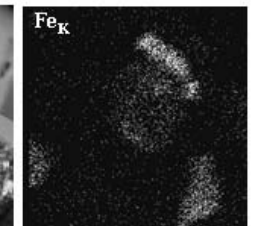
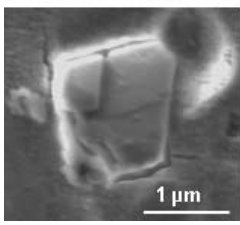
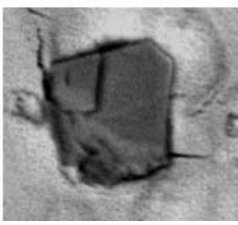
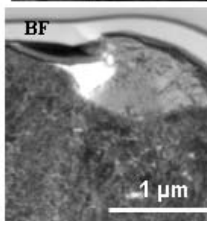
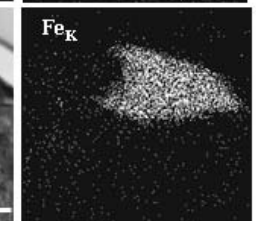
Table 14: Overview of precipitate oxidation behaviour at the metal-oxide interface showing similar behaviour in all oxidation consitions.

	Zr1%Fe	Zr1%Ni	Zr1%Cr	Zr0.6%Nb
in situ (ESEM) 130 Pa 1 hour vapour				
autoclave 0.1 MPa 3 days air				
autoclave 0.1 MPa 3 days steam				55 days
autoclave 10.5 MPa 110 days steam				

For all oxidation conditions the formation of iron oxide crystals was observed at the oxide surface of Zr1%Fe (Table 15). After 1 hour the oxide crystals were small, present over some oxidised precipitates in the oxide. For oxidation for 1 and 3 days the amount of iron oxide crystals over oxidised precipitates was larger than after 1 h and after 110 days large iron oxide crystals of up to few micrometers size had formed. Electron diffraction showed the presence of a cubic phase with diffraction spots and symmetry fitting well to the cubic structure reported for magnetite or maghemite. For the oxidised precipitates underneath the iron oxide on the surface a gradual depletion in iron was observed, which increased with the oxidation time. From the amount of iron oxide and the surface area covered by it, an effective diffusion coefficient for the transport to the surface could be estimated. The in situ and air oxidation on not pickled samples show that this phenomenon is not restricted to pickled surfaces or to steam environments.

The matrix oxide was observed to be columnar for all materials with the oxide grains oriented in the oxide growth direction. No distinct difference between the columnar grains was observed for the different materials. The longer the oxidation time, the more frequent cracks of large size were observed in the oxide scale. Small cracks were present especially in the outer part of the oxide close to the outer surface. The oxide structure was small grained and equiaxed for oxidised precipitates in Zr1%Fe, Zr1%Cr and Zr0.6%Nb, as can be observed on the respective micrographs. For Zr1%Ni due to the lack of clear observations of the oxidised part of precipitates it cannot be stated what the oxide microstructure looks.

Table 15: Overview of iron oxide presence at the surface and the connection to underlying Zr_3Fe precipitates.

	SE	BSE	TEM	EDS
in situ (ESEM) 130 Pa 1 hour vapour				
autoclave 0.1 MPa 3 days steam				
autoclave 10.5 MPa 110 days steam				

8 Other selected oxidations

8.1 Other selected oxidation conditions of the binary alloys

The oxidation behaviour in air of precipitates in contact with the outer surface was investigated in furnace exposures of polished samples for 1 and 24 hours at 415°C for selected alloys. This was done in order to have a flat surface, allowing the observation of surface topography changes and the study of precipitate behaviour at the outer surface, which is difficult on pickled samples, with the rough surface and preferential attack of the precipitates. Especially of interest was the behaviour of Zr1%Cr, which received an additional heat treatment at 730°C for 48 hours to increase the precipitate size considerably (average diameter before heat treatment: ~35 nm and after ~90 nm).

Samples from Zr1%Ni and Zr1%Cr were tested for 1 hour (comparable with in situ exposures) and from Zr1%Ni and Zr1%Cr for 24 hours.

8.1.1 Furnace oxidation for 1 hour in air

8.1.1.1 Zr1%Ni oxidized 1 hour in air

The surface of Zr1%Ni oxidised for 1 hour at 415°C is flat beside the protrusions (Figure 86a), which have formed on oxidised nickel containing precipitates in contact with the outer surface. At these oxidised precipitates in contact with the outer surface cracks can be observed in the oxide on the precipitates (Figure 86b). EDS analyses of the small crystals at 5 kV acceleration voltage results in up to 20 at.% Ni with 18.5 at.% Zr, which indicates that a migration of Ni to the surface (precipitate composition nominal Zr₂Ni), however, no confirmation with TEM was possible and no systematic observation of Ni rich regions was obtained.

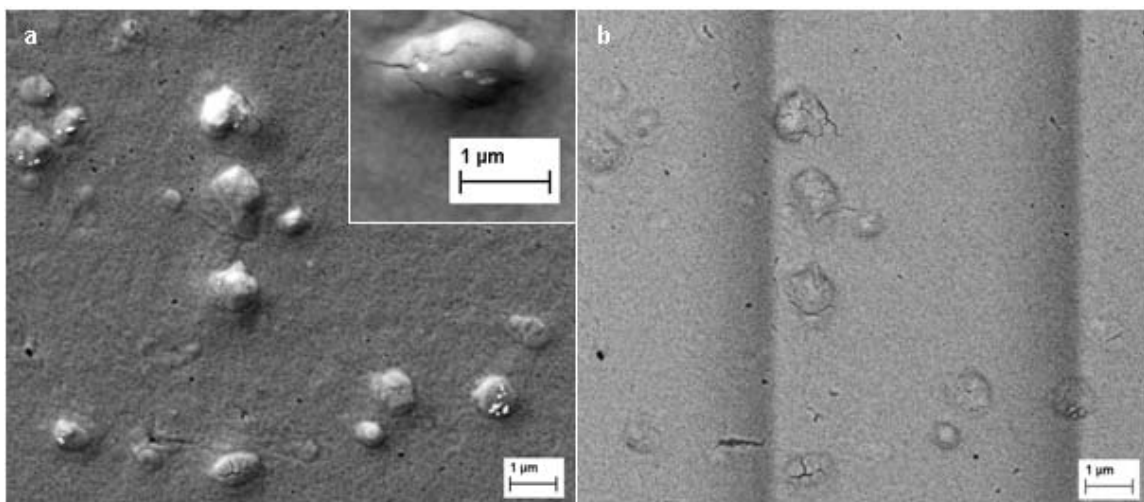


Figure 86: SEM micrographs of surface of Zr1%Ni oxidised for 1 hour at 415°C in air. The SE micrograph (a) shows the protrusions with cracks within the protrusions and small crystals on top, the also the inset at higher magnification, the BSE micrograph (b) shows there are cracks at most precipitates (same surface as (a)).

8.1.1.2 Zr1%Cr (annealed) oxidised 1 hour in air

The surface of the annealed Zr1%Cr oxidised for 1 hour at 415°C is flat beside the protrusions (Figure 87a&b), which have formed on chromium containing precipitates in contact with the outer surface. At these precipitates in contact with the outer surface cracks can be observed at the precipitate-oxide interface (Figure 87a-c). EDS analyses of the precipitates at 5 kV acceleration voltage resulted in much lower oxygen concentrations at the precipitates (<20 at.%) than on the oxide beside (>50 at.%) with the Cr to Zr ratio around 2 ($ZrCr_2$). The FIB transverse section of the surface (Figure 87c) at the precipitate in Figure 87a reveals, that the bulk of the precipitate (Figure 87c I) has a metallic appearance and the precipitate in contact with the metal-oxide interface (Figure 87c II) exhibits the same type of crack at the precipitate-oxide interface (black arrow) as for the smaller $ZrCr_2$ precipitates. In other sample the EDS analysis of the precipitates in the transverse section confirms the low oxygen content obtained from the surface measurements, the oxygen levels are below 5 at.% and the Cr to Zr ratio 2 and even higher, which could be caused by segregation of Cr and Zr close to the surface. This could be size dependent, as not observed for small precipitates; however no systematic observation of such a phenomenon was obtained.

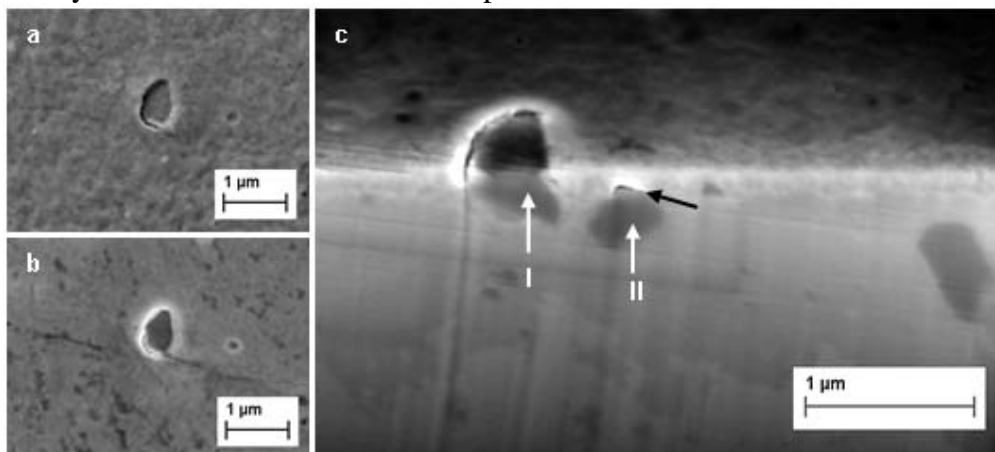


Figure 87: SEM micrographs of surface of Zr1%Cr oxidised for 1 hour at 415°C in air. The SE micrograph (a) and Inlens micrograph (b) show a Cr bearing precipitate at the surface with a cracked precipitate oxide interface. The Inlens micrograph of the FIB section (c) of the precipitate at the surface in a&b shows two precipitates (I and II marked with white arrows), one in contact with the surface and the other with the metal-oxide interface, crack at precipitate oxide interface marked with black arrow.

The TEM sample prepared from annealed Zr1%Cr oxidised for 1 hour in air shows a delayed oxidation of the precipitate with respect to the zirconium matrix (Figure 88). A thin region of oxidised precipitate with Cr to Zr ratios varying from 1 to 3 ($ZrCr_2$ precipitate) can be observed, as the protective platinum layer was milled away, the original thickness of this oxidised layer cannot be determined, on TEM micrographs an about 10 nm thick region with a different contrast can be observed. At a distance of 50 nm from the precipitate surface and more, maximum 5 at.% oxygen were detected; for the EDS spectrum at 50 nm distance from the surface see Figure 88. The Cr to Zr ratio in the metallic precipitate was about 2, as expected for $ZrCr_2$ precipitates and matched also with the composition obtained for a large precipitate in the metal.

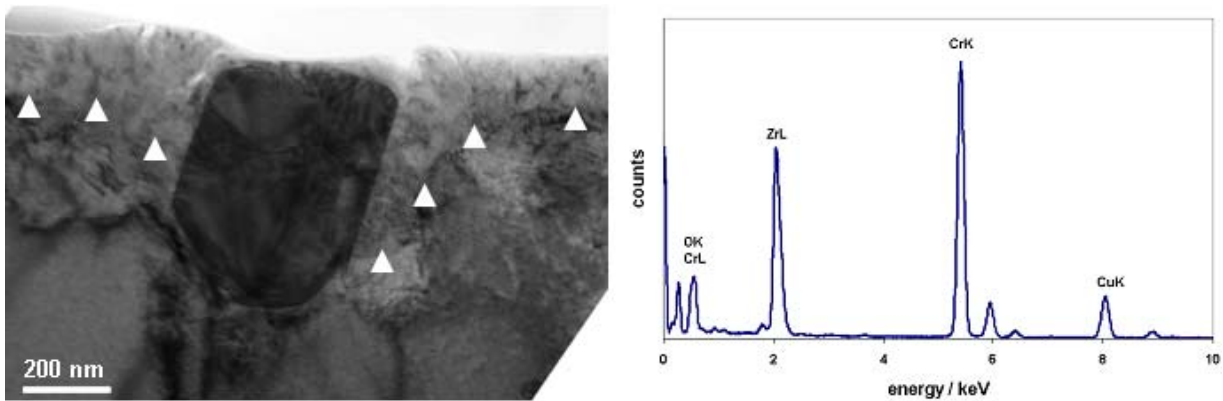


Figure 88: Bright field contrast of precipitate at surface of Zr1%Cr oxidised for 1 hour at 415°C in air. The precipitate is only oxidized at the surface in a very thin region. The metal-oxide interface beside the precipitate is marked by arrowheads. EDS spectrum from the precipitate 50 nm below the surface is presented, showing the low oxygen content.

8.1.2 Furnace oxidation for 24 hours in air

8.1.2.1 Zr1%Fe oxidized 24 hours in air

The oxidised surface of Zr1%Fe is flat beside the protrusions (Figure 89), which have formed on oxidised iron containing precipitates in contact with the outer surface. At the oxidised precipitates in contact with the outer surface some cracks can be observed. FIB transverse sections show the thicker oxide formed under these precipitates (inset in Figure 89). The cracks at the outer surface are not extending deep into the oxide with the width they have at the surface.

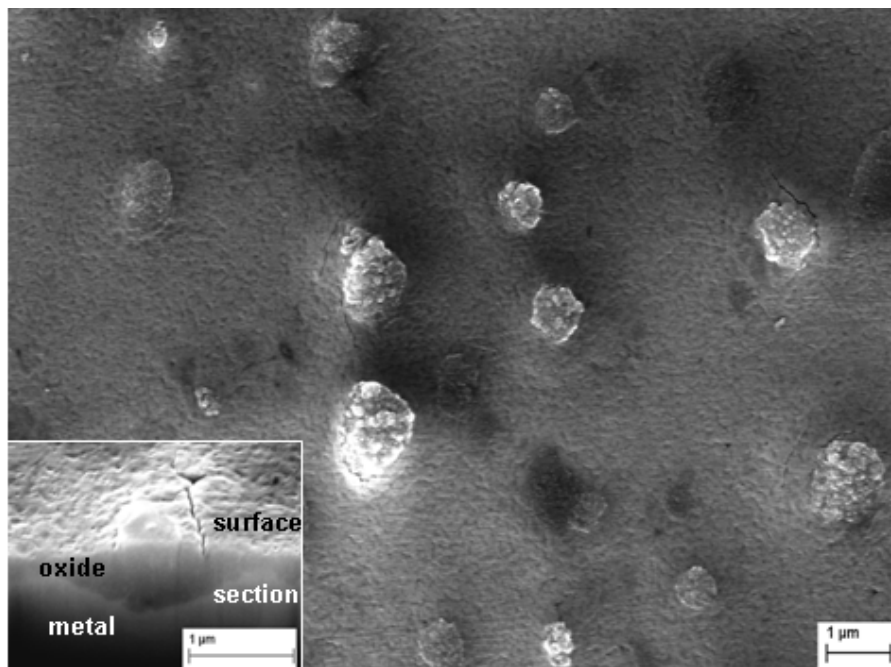


Figure 89: SEM micrographs of surface of Zr1%Fe oxidised for 24 hours at 415°C in air. The inset shows a FIB transverse section of a surface protrusion.

8.1.2.2 Zr1%Cr (annealed) oxidised 24 hours in air

The oxidised surface of the annealed Zr1%Cr sample exhibits some larger precipitates and beside these smaller protrusions, which could be oxide grains (Figure 90a&b). At the positions of the large precipitates (Figure 90b) chromium could be detected using an acceleration voltage of 10 kV, at 5 kV no chromium signal could be identified at the surface. Around the oxidised precipitates in contact with the outer surface some cracks can be observed. On the FIB transverse section (Figure 90c) it can be observed, that the oxide thickness is very much increased locally around the precipitate with cracks in the oxide. On the precipitate the protrusion is lower than beside, which could be an indication, that no expansion (as consequence of oxidation) has taken place. However, the question about the oxidation state of the precipitate cannot be answered in SEM, as the volume analysed with EDS contains always contributions from matrix and precipitate. No TEM sample has been prepared.

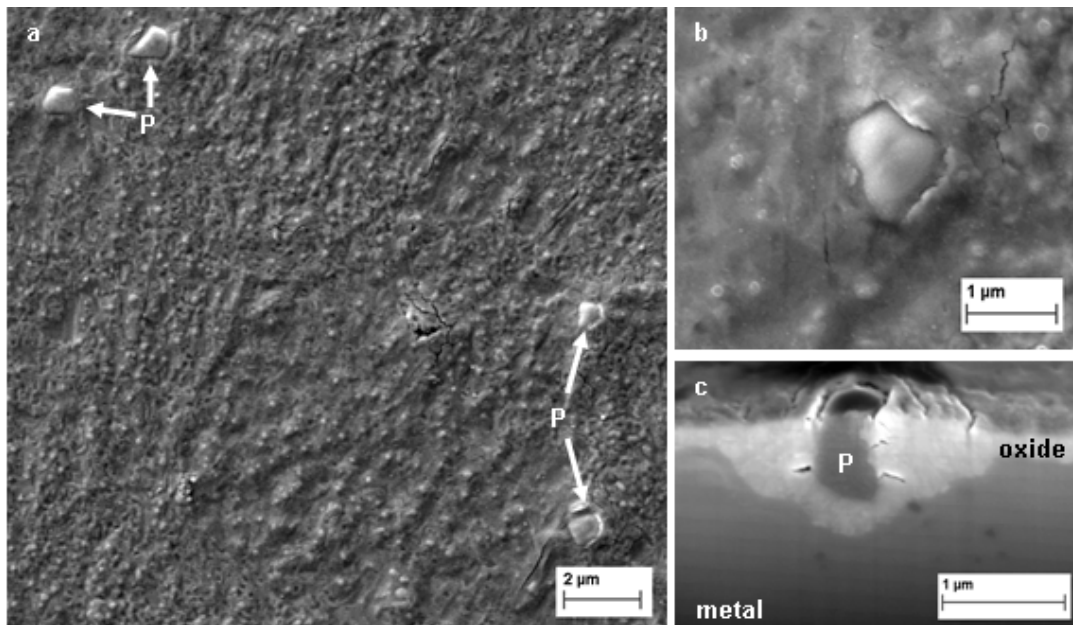


Figure 90: SEM micrographs of surface of Zr1%Cr oxidised for 24 hours at 415°C in air. (a) Overview micrograph showing the presence of few larger precipitates (P) being observable at the surface and cracks in the oxide. (b) Micrograph of one large precipitate at the surface at higher magnification. (c) FIB transverse section of a larger precipitate (P), showing the thicker oxide scale at the precipitate and some cracks in the oxide.

8.2 Autoclave oxidation of Zircalloys in steam at 415°C

8.2.1 Zr₂(Fe,Ni) precipitates

The oxidation behaviour of Zr₂(Fe,Ni) precipitates was studied on a Zircaloy-2 sample oxidised at 415°C for 1 day in steam at 10.5 MPa [272]. In Figure 91 TEM micrographs of one Zr₂(Fe,Ni) precipitate at the metal-oxide interface (a) and one fully in the oxide about 300 nm from the outer surface (b) can be observed. Both micrographs show precipitates in the range of 200-300 nm diameter. The precipitate at the metal-oxide interface (Figure 91a) is in large parts metallic, only small parts in contact with the surrounding oxide are oxidised. The

precipitate present in the oxide about 300 nm from the outer surface (Figure 91b) is fully oxidised and some smaller cracks can be observed at the oxide-precipitate interface. The oxide is equiaxed and small grained within the oxidised precipitate and for the oxidised matrix. No detectable formation of alloying element oxide was found at the outer surface above oxidised $Zr_2(Fe,Ni)$ precipitates.

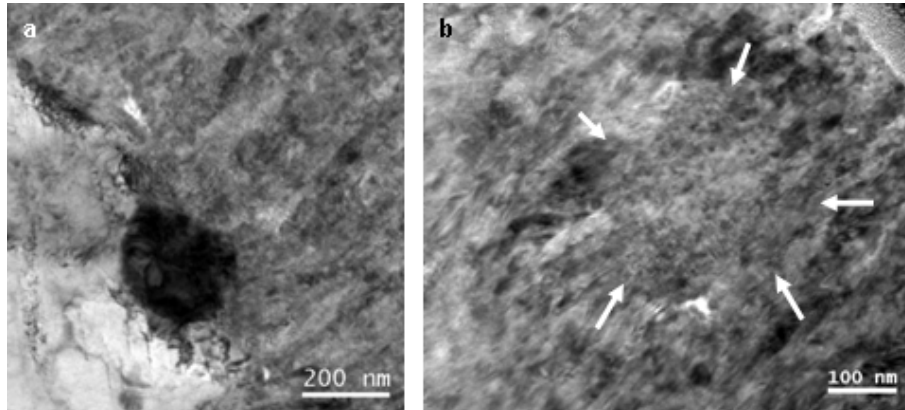


Figure 91: TEM micrographs of $Zr_2(Fe,Ni)$ precipitates (a) at the metal-oxide interface and (b) fully in the oxide (white arrows) on Zircaloy-2.

8.2.2 $Zr(Fe,Cr)_2$ precipitates

The oxidation behaviour of $Zr(Fe,Cr)_2$ precipitates was studied on a Zircaloy-2 sample oxidised at 415°C for 1 day in steam at 10.5 MPa [272] and a Zircaloy-4 sample oxidised for 110 days under similar conditions [10].

On the Zircaloy-2 sample $Zr(Fe,Cr)_2$ precipitates in the oxide less than 300 nm from the metal-oxide interface are found to be unoxidized in the oxide matrix (Figure 92a). The cracks at the precipitate-matrix interface are situated on the precipitate side facing the outer surface. At the surface a protrusion containing high contents of alloying elements was observed (Figure 92b). In the protrusion the chromium content was almost double the zirconium content and iron and nickel were also present at higher concentrations than found in the oxide underneath.

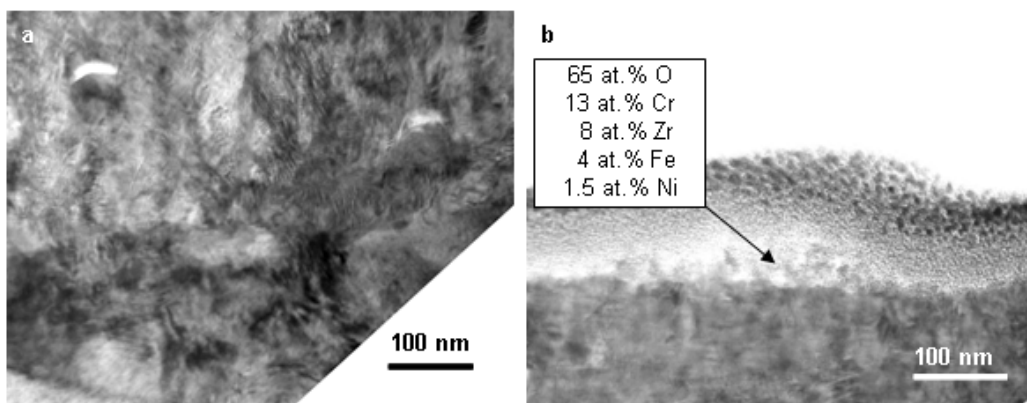


Figure 92: TEM micrographs of Unoxidised $Zr(Fe,Cr)_2$ precipitates in the oxide close to the metal-oxide interface (a) and region high in alloying elements close to the outer surface (b) on Zircaloy-2.

On a Zircaloy-4 sample $Zr(Fe,Cr)_2$ unoxidized precipitates could be observed in the oxide (Figure 93). Due to the thickness of the foil precipitates were difficult to observe and therefore no information is available up to which distance from the metal-oxide interface they remain unoxidized.

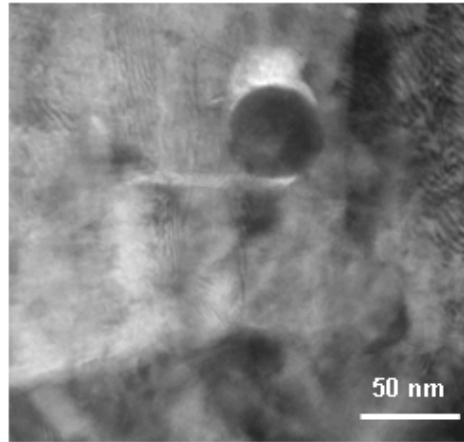


Figure 93: TEM micrograph of unoxidised $Zr(Fe,Cr)_2$ precipitate in the oxide formed on Zircaloy-4 close to the metal-oxide interface.

8.2.3 Comparison of binary zirconium alloys and Zircalloys

For the commercial alloys also both precipitate oxidation behaviours were observed. The precipitates containing more than two elements were found to exhibit delayed oxidation in the case of $Zr(Fe,Cr)_2$ and similar oxidation to the surrounding matrix in the case of $Zr_2(Fe,Ni)$. Interesting here are two aspects, precipitate composition and crystal structure. The $Zr_2(Fe,Ni)$ precipitates have the same structure as the Zr_2Ni precipitates and contain Fe and Ni beside zirconium, which both show in the binary alloys similar precipitate oxidation to the surrounding matrix. The $Zr(Fe,Cr)_2$ precipitates have the same structure as $ZrCr_2$ and contain both Fe and Cr beside zirconium, of which one element shows delayed oxidation (Cr) in the binary alloy and one similar oxidation as the surrounding matrix (Fe).

On oxidised $Zr(Fe,Cr)_2$ precipitates iron and chromium oxide were observed on the outer surface. The outer part of this oxide protrusion was rich in Cr and the overall thickness of this region was around 30-40 nm, but no crystals as in the case of iron were observable.

9 Mechanical properties of zirconia layers formed on binary alloys

Nanoindentation was applied to determine Young's modulus of formed oxide layers on different materials. The elastic response of the sample upon retraction of the Vickers indenter was used to determine the Young's modulus of the oxide layer. The results are presented in appendix III. The microhardness tests to determine the hardness of the material at the metal-oxide interface are presented below.

The microhardness tests performed close to the metal-oxide interface were done with an indentation force of 0.1 N, by loading the sample with 0.01 N/s until the preset load was reached and holding this load for 10 s. The indent positions were taken to be at the crossing of the diagonals, which was the point possible to determine with the highest accuracy.

A comparison of the measured hardness data for different binary alloys oxidised at 415°C in air and steam showed a sharp decrease of the hardness at the metal-oxide interface towards the metal (Figure 94). The average metal hardness for 0.1 N indentation force ranges between 150-180 HV and is reached for distances larger than 5 µm into the metal. The hardness drops from the oxide towards the metal and reaches around 5 µm from the interface into the metal the average metal hardness. The maximum hardness obtained for the oxide was in the range of 900-1000 HV. The precision in location with respect to the metal-oxide interface is 2-3 µm, being also due to the interface roughness.

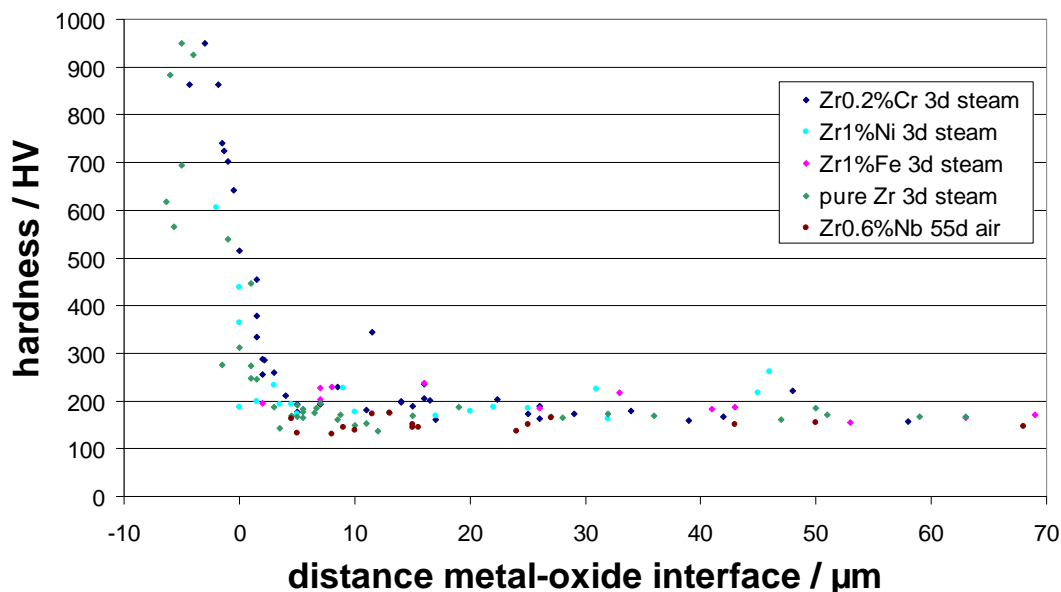


Figure 94: Hardness as determined with 0.1 N load at the metal-oxide interface and in the metal of different binary alloys and pure zirconium oxidized at 415°C.

For comparison with 415°C the hardness was measured for two binary alloys oxidised at 700°C in the environmental SEM (Figure 95). The hardness data show a sharp decrease of the hardness at the metal-oxide interface towards the metal. The hardness obtained for the metal ranges between 160 and 220 HV and is reached for distances larger than 10-15 µm into the metal. In the region between 0 and 15 µm the two hardness curves show a difference of about

150 HV, but are both showing a steep decrease in hardness down to 300/400 HV and then a less steep curve down to the metal hardness reached between 10 and 15 μm distance from the metal-oxide interface.

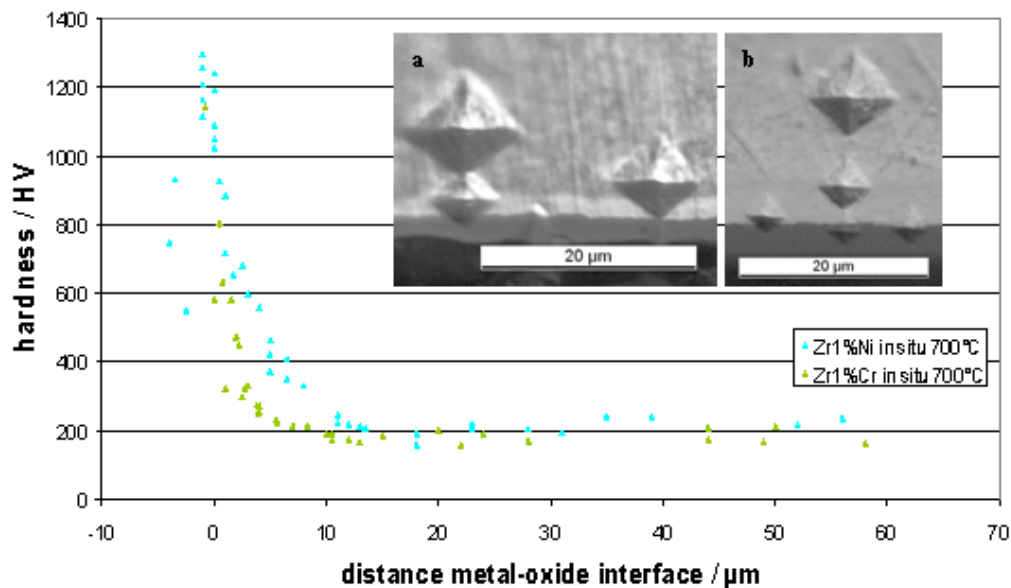


Figure 95: Hardness as determined with 0.1°N load at the metal-oxide interface and in the metal of different binary alloys oxidized at 700°C . Insets show optical micrographs of (a) $\text{Zr1}\%\text{Cr}$ and (b) $\text{Zr1}\%\text{Ni}$ with indents.

The scatter in hardness is quite large, which depends on several factors: inhomogeneities of the material (precipitates etc) and errors in the determination of the diagonals are to be mentioned. For the inhomogeneities the influence on the indents should decrease with indent size, as more volume is tested, which means that the data from the oxide and close to the oxide should exhibit more spread than in the metal at some distance to the oxide. The determination of diagonals is to be expected to exhibit a similar trend, as the same absolute error increases the deviation from the real hardness more for small indents than for large indents. The indents obtained also show the influence of a hardness gradient, which can be observed in the inset in Figure 95a for the asymmetric indents which are symmetric on the axis perpendicular to the interface but not parallel to the interface. The indent side facing the oxide is somewhat smaller than the side facing the metal, which results in a crossing of the diagonals off centre for the indents close to the oxide. Hardness testing is ideally not to be done in such a (steep) gradient; however, here it was intended to observe the gradient. However, the impact of this non-ideal conditions on the correctness of the obtained hardness should be not neglected. Problematic is the assignment of the indents being both in the metal and the oxide, as these contain information from both which cannot be quantified. Also those indents close to but not in contact with the oxide reflect already the influence of the mechanical properties of the oxide and the oxygen rich diffusion zone which can be observed as a band of brighter contrast at the metal-oxide interface (inset Figure 95a).

10 Discussion

10.1 Introduction

In this chapter the experimental results obtained with the different methods described in the previous chapter will be discussed with respect to their interpretation and their relevance to the oxidation process.

First the influence of experimental parameters as surface preparation and sample geometry is addressed. An influence of the surface preparation on the resulting oxide, especially at precipitate sites, has been observed, as well as the influence of the precipitate-sample geometry on EDS measurements and their reliability.

In the second part of the discussion chapter the experimental results obtained and their interpretation are in the focus. The experimental results are compared with thermodynamic calculations of the oxidation behaviour of different types of precipitates.

The origin of the surface protrusions observed with AFM is dealt with. The existence of two general precipitate oxidation behaviours is shown and the influence of different possible parameters on the precipitate oxidation behaviour is discussed. The two parameters being most probable, a zirconium to alloying element ratio in the precipitates and the calculated free energy of oxide formation of the different intermetallics, are compared with each other. Possible experiments to determine the more adequate criterion of the two to predict the precipitate oxidation behaviour are proposed.

10.2 Influence of surface preparation on results

The surface preparation has been observed to influence the precipitate oxidation behaviour at the outer surface. In this project samples with three different types of surface finishing were investigated:

1. Polished and pickled surface according to ASTM G2 [10] (as received samples).
2. Mechanically polished with last step being a neutral 1 μm diamond slurry polishing.
3. Mechanically polished with last step being a vibratory polisher finish with 60 nm large Silica particles at a pH of 9.5.

It was noticed that the polishing and pickling process removes all large precipitates in contact with the outer surface. The oxidation behaviour of the precipitates for samples prepared with this procedure can only be studied for precipitates not in contact with the surface after the pickling process. The surface is rough in the case of alloys with large precipitates, due to the preferential dissolution of larger precipitates, so that analysis of the topography in AFM can only be performed on small features like oxide grain size at the surface, as reported before in [252], and in this project this has not been done for samples with this surface preparation.

Samples prepared with neutral 1 μm diamond slurry in the last polishing step resulted in a smooth surface without a recognisable attack of precipitates at the surface.

Polishing with a solution containing 60 nm large Silica particles and a pH of 9.5 with the

vibratory polisher resulted in an optically smooth surface, however, in AFM depressions were observed at positions, which were identified in SEM to be the sites of precipitates. On the samples oxidised in situ at 415°C surfaces treated with this type of finishing the precipitates were exhibiting a thicker oxide than those on samples with diamond slurry polish. In SEM, EDS measurements of the oxygen content of ZrCr₂ precipitates showed higher oxygen content at precipitates at the surface compared to the only diamond slurry polished material (heat treated Zr1%Cr with larger precipitates). In TEM a 150 nm thick oxide layer was observed for the vibratory polisher finished material on ZrCr₂ precipitates, on the diamond slurry polished surface the oxide layer was significantly thinner than this. For Zr1%Ni, rapid formation of iron oxide on the surface was observed during in situ oxidation at 415°C for the vibratory polisher finished surface. The iron originates from the precipitates, where it is present as impurities and due to its low solubility in the Zr matrix. The Ni/Fe ratio is about 57 for the Zr1%Ni alloy, assuming that all Ni and Fe are present in the precipitates. The average of the measured Ni/Fe ratio was in this project around 42 in the Zr₂Ni precipitates in the metal. Thus, the Fe impurity content of the Zr1%Ni alloy is therefore mainly present in the precipitates. The basic polishing solution modifies Zr₂Ni precipitates in such a way, that the iron content rapidly forms iron oxide on the surface, which is not the case for the same oxidation conditions in situ on the surface of samples polished with the diamond slurry. This could be due to the removal of the mechanically deformed outer layer from polishing.

10.3 Quantitative EDS measurements

For quantitative EDS measurements in TEM some precautions have to be taken. The interaction volume of the beam with the primary electron beam is much smaller, than in the SEM, however, even here the analysed volume should be homogeneous in composition to allow correct quantification. As the interest for quantitative EDS measurements is mainly at precipitate sites, it is of interest how different precipitate-matrix geometries encountered in TEM samples have to be dealt with, to obtain optimal data from the reliability point of view. As there are different possible settings in EDS routines for quantification, suitable settings for different questions of interest are addressed. The influence of different sample parameters, as thickness and density, on the obtained quantification is discussed in this section with respect to their possible range and introduced errors.

10.3.1 Precipitate-matrix geometries in TEM specimens

For EDS measurements it is advisable to know the impact of the possible geometries on the results obtained. The possible precipitate-matrix geometries in TEM specimens can be categorised into specimens with uniform thickness at the precipitate location and of the matrix beside (1.1 to 1.3 in Figure 96) and specimens with different thickness at the precipitate location and of the matrix beside (2.1 to 2.3 in Figure 96).

In the case of configuration 1.1 the precipitate is the only phase present in the volume between both surfaces of the specimen, which is possible for precipitates exhibiting larger diameters than the specimen thickness at this position. This is the case for Zr1%Fe and Zr1%Ni from the materials studied and in the centre of the precipitates the contribution of the

matrix to the signal obtained is negligible. In the case of configuration 1.2 and 1.3 there is the precipitate and the matrix present in the analysed part of the specimen, either because the precipitate is only partially within the sample, although it has a diameter larger than the specimen thickness (1.2), or because it is smaller than the overall specimen thickness (1.3). These cases are all possible regardless of the specimen preparation technique if no preferential thinning takes place. In these two cases EDS measurements will always contain a contribution of the matrix, which is difficult to correct for without further measurements and calculations, as the exact extent of precipitate and matrix contribution to the signal obtained is not easily separated.

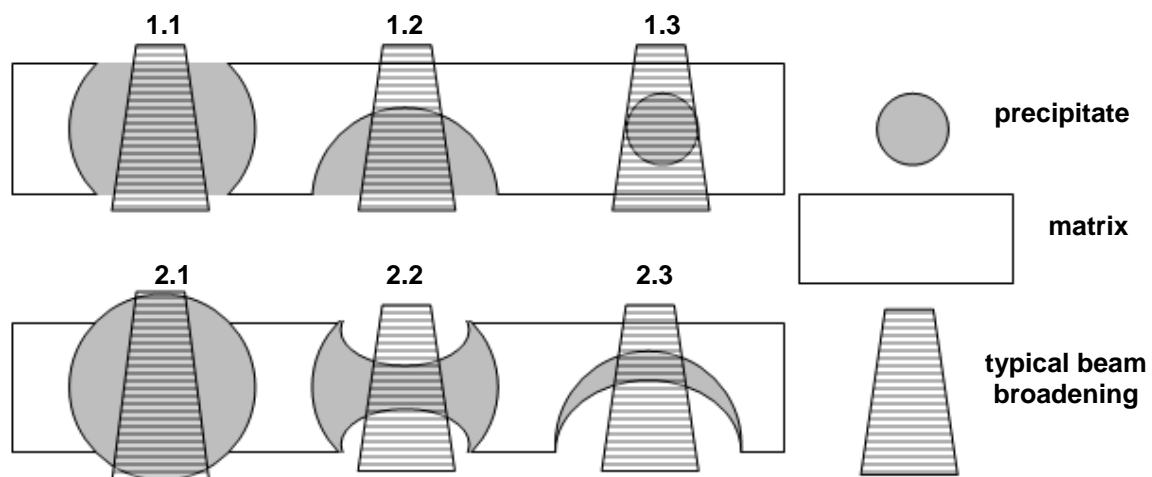


Figure 96: Examples of possible precipitate matrix configurations encountered in TEM samples. 1.1-1.3 present configurations with uniform and 2.1-2.3 configurations with non-uniform thinning of matrix and precipitates. The interaction volume with the electron beam is shown.

In case the sample thickness is not uniform on precipitates and the matrix, different configurations are possible (2.1-2.3 in Figure 96). These configurations are especially interesting in the case of large precipitates with a diameter larger than the sample thickness. Configuration 2.1 can be the result of a preferential attack of the matrix in an etchant or a higher resistance of the precipitate towards milling in the FIB. Configuration 2.2 and 2.3 can be caused by preferential etching of the precipitate with respect to the surrounding matrix, in configuration 2.3 the preferential attack of the precipitate is combined with configuration 1.2.

A good TEM specimen with optimal preparation should be represented by the configuration 1.1-1.3; however, due to non-uniform thinning during the preparation process, also configuration 2.1-2.3 are possible. Preferential attack of the matrix has not been observed for the electro-polished TEM specimens, for FIB prepared TEM specimens at least for Ni bearing precipitates a protrusion was detected at the precipitate site in an AFM scan of a TEM specimen. Preferential attack of the precipitates has been observed for electro-polished TEM samples, especially for Zr1%Fe and Zr1%Ni for the large precipitates.

10.3.2 Influence of precipitate-sample geometry in TEM on obtained results

The different precipitate-matrix geometries presented in Figure 96 have all an impact on the EDS signal obtained. Without any correction only configuration 1.1 allows the correct determination of the precipitate composition if obtained in the centre of the precipitate. In case of sufficiently large precipitates the signal originates from the precipitate only and results therefore in the correct ratio of the elements constituting the precipitate, which is possible for Zr1%Fe and Zr1%Ni from the studied materials. In this case the density of the intermetallic should be used for quantification of metallic precipitates; as will be discussed in 0. For configuration 1.2 with various degrees of matrix contribution, it is not possible to determine correctly the alloying element content of the precipitate, which is especially important in the oxide to evaluate the release of alloying elements from the oxidized precipitate into the surrounding oxide. Configuration 1.1 and 1.2 cannot be distinguished by other means than comparing the zirconium to alloying element ratio obtained for the precipitate with the nominal one for this type of precipitates, therefore the release of alloying element content from oxidised precipitates in the oxide is only unambiguously proven, if a corresponding increase in alloying element content of the surrounding oxide matrix is observed, as a lower alloying element to zirconium ratio is alone no unambiguous evidence.

In the case of small precipitates (configuration 1.3), as present in Zr1%Cr and Zr0.6%Nb, a separation routine has been applied, described in more detail in the respective section in the results chapter (5.1.4.4 on page 77). This routine allows an estimation of the precipitate oxidation state in the oxide with some assumptions. However, in the case of precipitate depletion this routine will not be applicable, as a fixed zirconium to alloying element ratio is one of the essential assumptions on which the routine is based.

The configurations presented in 2.1 and 2.2 can also be used to determine the precipitate composition, however, the local thickness at the measurement point is required for this. For Zr1%Ni configuration 2.1 has been found when a precipitate at the metal-oxide interface in a TEM sample was checked with AFM. The other configurations (1.2, 1.3 and 2.3) always contain a matrix contribution, which cannot be quantified and therefore these do not allow the correct determination of the precipitate composition. In TEM it is not straightforward to distinguish between the different cases (except for configuration 1.3), only AFM on precipitates for each preparation method can clarify if any preferential etching has taken place (either configuration 2.1 or 2.2 and 2.3).

Therefore for small precipitates (configuration 1.3) and partially included large precipitates (1.2 and 2.3) depletion of the precipitates in alloying elements is difficult to identify correctly and even more difficult to quantify.

The local difference in sample thickness (configuration 2.1-3) can also affect the quantification, if the sample thickness has been determined for the matrix, however, the influence of the thickness on the determined zirconium to alloying element ratio is low, the influence of a matrix contribution as in 2.3 is considerably higher.

10.3.3 Quantitative EDS results

The INCA EDS software of Oxford Instruments was used with the standardless automatic quantification unless stated otherwise. For this setting the software chooses the preset x-ray lines for quantification. In case EDS analyses on the SEM, no further input is required (unless the sample has been coated e.g. with carbon).

10.3.3.1 SEM/EDS

In SEM the provided quantitative information is only taken as indication of the approximate composition, as important requirements as homogeneity of the investigated volume and a sample surface perpendicular to the incoming electron beam are not fulfilled for some setups. To obtain unambiguous results, the penetration volume of the electron beam has to be smaller than the precipitate volume, for example at 5 kV acceleration voltage the generated zirconium signal originates from a maximum depth of 150 nm. This is small enough for large precipitates in Zr1%Fe and Zr1%Ni if the precipitate is analysed in the centre, otherwise some contribution of the surrounding zirconium matrix will contribute to the zirconium signal and dilute the alloying element signal contribution. At 20 kV acceleration voltage, as used for EDS mapping, the interaction volume is therefore more than 1 μm diameter larger than most precipitates and reaches deeper into the material than the oxide thickness present on the in situ samples. The EDS results can therefore be only considered as qualitative at this acceleration voltage in SEM. For FIB transverse sections also a tilt of the analysed surface with respect to the electron beam, spurious x-rays from the surrounding of the inclined surface and shadowing of the x-ray detector by the walls of the section are additional factors affecting the reliability of the quantification.

10.3.3.2 TEM/EDS

For quantitative EDS results in TEM the user has to provide additional input in form of sample thickness and density of the material to allow the quantification with the appropriate parameters. In TEM the standardless automatic quantification requires only sample thickness and density as user input. For TEM this procedure results in semi-quantitative results, unless the thickness is determined carefully at the spots of interest for example with EELS. The preset x-ray lines of the identified elements in the INCA software from Oxford Instruments are the K-line for O, Cr, Fe and Ni and L-line for Zr and Nb. These standardless settings had been found to provide the most accurate quantification results for zirconia standard samples with known stoichiometry and thickness [114].

For the intermetallic precipitates present in the materials investigated the quantification with L-line for Zr and K-Line for the alloying element resulted in too high Zr to alloying element ratios with respect to their nominal composition (e.g. Zr to Ni ~3:1) compared to the stated stoichiometry in the literature (Zr₂Ni [10]). Only if both Zr and alloying element were quantified using their respective K-lines, the nominal precipitate compositions (Zr₃Fe, Zr₂Ni, ZrCr₂) were obtained, see also Table 10 on page 58. With the sample thickness at a precipitate determined using EELS for Zr1%Fe and the appropriate density being entered into the EDS software, only the x-ray line chosen for quantification can be the cause for a different

quantification result. Therefore it must be assumed that the studies reporting those precipitate compositions used the Zr K-line and the alloying element K-line for quantification.

The EDAX-software on the TEM at CSEM had in their preset selection of x-ray lines for quantification the setting using the same line family (K-line) for both Zr and the alloying elements, which resulted in the nominal precipitate composition, proving that not a detection problem but rather the quantification procedure using x-ray lines of two different families (K and L) is at the origin of this quantification problem.

A problem arises therefore with the correct quantification of oxygen and the alloying elements in oxidised precipitates. Either the Zr to alloying element ratio is correct (both elements quantified with their K-lines), or the Zr to oxygen ratio is correct (zirconium L and oxygen K-line used for quantification). The suggested solution is to quantify the oxygen present using the Zr L-line and the alloying element with the Zr K-line and then correct the Zr to alloying element ratio using the K-line quantification without changing the oxygen quantification from the L-line quantification. The suggested procedure is:

1. Measure the point of interest
2. Set thickness and density
3. Quantify with L-line for Zr and keep oxygen content and fixed metal content (sum of Zr and alloying element(s))
4. Quantify with K-line for Zr and adjust Zr to alloying element ratio obtained in 3 (same metal content but corrected Zr to alloying element ratio).

Application of this procedure increases the alloying element content, compared with the quantification using only the Zr L-line (Table 16). To compare the impact of this change in the quantification result one oxidised and one metallic precipitates of $ZrCr_2$ are treated with both procedures, only Zr K-line, Zr L-line and Zr K and L-line, denoted as Zr K+L line in the Table.

Table 16: Impact of Zr x-ray line selected for EDS quantification on precipitate composition in the oxide for $ZrCr_2$ precipitates. Surplus Zr, O/surplus Zr and oxygen content in precipitate calculated according to Appendix I on page 183.

	Zr line used for quantification	O	Cr	Zr	surplus Zr at.% ($c(Zr)-0.5 \cdot c(Cr)$)	O/ surplus Zr	oxygen content SPP / at.%
metallic precipitate	K	24.6	45.9	28.0	5.1	4.8	17%
	L	22.8	40.7	35.2	14.8	1.5	0%
	K+L	22.8	47.1	28.7	5.2	4.4	15%
oxidised precipitate	K	64.5	16.2	18.6	10.5	6.1	64%
	L	61.0	14.4	24.0	16.8	3.6	56%
	K+L	61.0	17.9	20.6	11.6	5.3	58%

The increase of alloying element content can be as high as 6 at% in the case of $ZrCr_2$ precipitates between L-line and K+L-line procedure (Table 16). This increase in Cr content has an impact on the estimation of the oxygen content of the precipitates, for details of the routine see 5.1.4.4 on page 77, which is with the correction higher, up to 19 at.% oxygen more than with just the Zr L-line quantification, as the Zr/Cr ratio on which the estimation depends is changed. The 0% oxygen result for the metallic precipitate is not reliable, as even

for a large unoxidized ZrCr_2 precipitate, presented in Figure 88 (in contact with the outer surface), around 5 at.% oxygen in its centre were detected. This oxygen concentration of 5 at.% is still low, considering that even in the metal not close to the metal-oxide interface low but measurable oxygen content is detected, see for example Figure 84 to Figure 85 and [114]. The absence of oxygen in small precipitates in the oxide is therefore not realistic, as it is suggested by the matrix subtraction routine in 5.1.4.4.

Considering also the uncertainty of about 10% in EDS quantification results, it is not possible to judge, which of the two quantification procedures, Zr L-line or Zr K+L line, provides the data representing the real concentrations best.

10.3.3.3 Influence of density and sample thickness on quantification in TEM

The density used for the quantification procedure in the INCA EDS software of Oxford Instruments was usually set to be 5.8 g/cm^3 for the oxide or 6.5 g/cm^3 for the metal. These densities can be assumed to be valid for pure zirconia and the zirconium matrix. For larger precipitates in the metal the higher densities of the intermetallics should be used ($6.8\text{--}7.2 \text{ g/cm}^3$, see Table 5), for small precipitates the density of the surrounding matrix will be a good estimate. For the $\beta\text{-Nb}$ phase this should be even higher (8.57 g/cm^3). In case of the as received Zr1\%Cr and Zr0.6\%Nb material, this correction was not applied, as the precipitates were generally smaller than the TEM specimen thickness.

In the oxide the correct density of the oxidised precipitates is more difficult to estimate, as this depends on the oxidised phase formed and also the degree of oxidation. Therefore the density chosen for quantification is the density of zirconia, as this is the best approximation possible. The parameter mostly affected by a variation of the sample density was the oxygen quantity. This variation of the oxygen concentration is due to the absorption correction, which takes into account the attenuation of the oxygen signal by absorption from zirconium and the other elements for the quantification.

The sample thickness, being provided by the user for the quantification procedure in the INCA EDS software of Oxford Instruments, was estimated by assuming an oxygen to zirconium ratio of 2 in the outer oxide, in case no thickness measurement (e.g. with EELS) was performed. For Zr1\%Fe oxidised for 110 days in steam the thickness calibration with EELS was performed in the metal and the oxide, as there also the oxidation state of iron was investigated in detail. The thickness determined with EELS was around 140 nm, higher than first expected, which resulted in too low oxygen concentrations with the too small thickness value entered into the quantification routine.

The limits of the thickness range usually encountered are 50 and 200 nm, as thicker samples would not be suitable for TEM investigations. Varying the thickness in this ranges showed that also for this parameter oxygen is the most sensitive element.

It is therefore acceptable to use the EDS data for semi-quantitative composition information, however, information about the precipitate oxidation state cannot be directly obtained and only via relative comparison with the oxygen content of the surrounding matrix, assuming the same thickness, an estimation can be made for large deviations from the matrix oxygen content (routine applied for small precipitates in Zr1\%Cr and Zr0.6\%Nb).

10.4 Change of surface topography during oxidation

The AFM measurements of the surface topography before and after oxidation of polished surfaces revealed the formation of protrusions on some of the binary alloys. Here the observations will be discussed and possible explanations and a modelling approach of the phenomenon with ANSYS will be presented.

10.4.1 Protrusions on the surface

The protrusion height observed with AFM on large precipitates at the surface after oxidation of polished (not pickled) surfaces [279] can have different origins:

1. A higher Pilling-Bedworth ratio than the zirconium matrix,
2. Thicker oxide formed at precipitates in contact with the outer surface,
3. Diffusing species to the outer surface.

The height of the protrusions measured in AFM is therefore dependent on different contributing phenomena, which cannot be separated in AFM, as only the topography, but no chemical profile in depth can be acquired to provide an answer.

Factor 1 and 2 contribute for all precipitates which oxidise preferentially when in contact with the outer surface and cannot be separated by the experimental results presented, as the large precipitates of Zr1%Fe and Zr1%Ni both exhibit the behaviour described with metal-oxide interface undulations observed in SEM and TEM.

In the case of all alloys with formation of an alloying element oxide on the surface of oxidised precipitates, factor 3 contributes to the protrusions observed in AFM. The AFM will provide the overall surface topography, which means for the protrusions observed, the contribution from an alloying element oxide formation cannot be separated from the height of the underlying surface protrusion, so the measurements in AFM will always give the sum of both contributions. In case the alloying element oxide is present as small crystals with a sufficient spacing between the crystals (so that the tip can reach the bottom of the gap between the crystals); the AFM will be able to provide information about the actual protrusion height and the alloying element crystal thickness. However in TEM the separation of the different contributions can be done in all cases.

10.4.2 Pilling-Bedworth ratio of intermetallics

The protrusions observed on the surface of Zr1%Fe and Zr1%Ni were related to the presence of large precipitate underneath the surface. The increase in height at these locations could be due to the volume increase difference between the oxidised precipitate and oxidised matrix, or due to migration of alloying elements to the free surface and their subsequent oxidation [198]. Both aspects will be discussed below.

$$P - B \text{ ratio } (Zr_a M_b) = \frac{\left(\frac{N_{metal}(Zr)}{N_{oxide}(Zr)} \cdot V_{oxide}(Zr) \right) + \left(\frac{N_{metal}(M)}{N_{oxide}(M)} \cdot V_{oxide}(M) \right)}{V_{SPP}(Zr_a M_b)}$$

Equation 5: M stands for the alloying element, $n_{metal}(X)$ for the number of atoms of X in unit cell of precipitate, $N_{oxide}(X)$ for the number of atoms of X in the unit cell of the oxide formed by X and $V_{oxide}(X)$ for the volume of the unit cell of the respective oxide.

In order to quantify the effect of the expansion differences a hypothetical Pilling-Bedworth (P-B) ratio [225] was calculated for the intermetallics with an equation (Equation 5) derived from one proposed by Xu and Gao [280], assuming the formation of ZrO_2 and the respective alloying element oxide (Fe_2O_3/Fe_3O_4 , NiO and Cr_2O_3 in Table 17). This assumption is judged to be valid in the case of pure alloying element oxide formation, as the solubility of Fe_2O_3 and Cr_2O_3 in ZrO_2 was found to be 2 mol% or less [281] and 5 mol% for NiO [282] and the zirconia unit cell volume is decreased by addition of the transition elements of interest, as explained in the following:

In case the ions of the alloying elements are dissolved in zirconia, their solubility is: 50 mol% for Fe^{3+} [282] (ion size 0.645 Å for coordination number = 6 [283]) and 26 mol% for Cr^{3+} [282] (ion size 0.615 Å for coordination number = 6 [283]) and 5 mol% for Ni^{2+} [282]. However, in this case no higher P-B ratio than for the surrounding zirconia matrix would be observed, as the unit cell volume of zirconia containing for example the alloying element Ni is smaller than for the pure zirconia unit cell [282].

The P-B ratio gives the ratio between the volume of the formed oxide and the volume of metal consumed forming this oxide (Equation 5).

Table 17: Pilling-Bedworth ratio of the different metals in the binary zirconium alloys calculated with presented data.

oxide	PBR	V_{oxide} / nm^3	Z_{oxide} / V	m / Z_{oxide}	m / V_{oxide}	V_{metal} / nm^3	m / V_{metal}	oxide density / g/cm^3	oxide density (x-ray) / g/cm^3
m- ZrO_2	1.51	0.1408	4	1	4	0.0466	2	5.68	5.8
t- ZrO_2	1.44	0.0670	2	1	2	0.0466	2		6.10
c- ZrO_2	1.45	0.1349	4	1	4	0.0466	2		6.1
Fe_2O_3	2.09	0.3019	6	2	12	0.0240	2	5.20	5.3
Fe_3O_4	2.05	0.5921	8	3	24	0.0240	2	5.17	5.2
Cr_2O_3	2.00	0.2882	6	2	12	0.0240	2	5.23	5.0
NiO	1.65	0.0729	4	1	4	0.0442	4	6.60	6.8
NbO	1.37	0.0746	3	1	3	0.0363	2	7.26	7.3
NbO_2	1.92	1.1129	32	1	32	0.0363	2	5.96	6.0
Nb_2O_5	2.67	1.3584	14	2	28	0.0363	2	4.66	4.5

V unit cell volume, Z / V formula units per unit cell, m / Z metal atoms per formula, m / V metal atoms per unit cell.

It was considered, that the pure unconstrained oxide of each of the metals involved is formed (ZrO_2 , Cr_2O_3 , Fe_2O_3 , NiO , NbO , NbO_2 and Nb_2O_5). In other words mixed oxides are not considered in this calculation. With this assumption and the presented data for the respective oxides (Table 17), the P-B ratio of the precipitates is calculated (Table 18). The presented data are not a linear combination of the P-B ratios of the two metals involved.

Table 18: Pilling-Bedworth ratio calculated for precipitate phases assuming the formation of pure oxides of the alloying element and of zirconium (ZrO_2 & M_xO_y).

phase	$V_{\text{metal}} / \text{nm}^3$	Z / V_{metal}	a / Z_{metal}	Zr / Z_{metal}	M / Z_{metal}	Zr / V_{metal}	M / V_{metal}	P-B ratio
Zr	0.0465	2	1	1	0	2	0	1.51
Zr ₃ Fe	0.5580	8	4	3	1	24	8	1.87 ^a
Zr ₃ Fe	0.5580	8	4	3	1	24	8	1.87 ^b
Zr ₂ Ni	0.2230	4	3	2	1	8	4	1.59
ZrCr ₂	0.3730	8	3	1	2	8	16	1.78
β -Nb (20%Zr)	0.0363*	2	1	0.2	0.8	0.4	1.6	1.48 ^c
β -Nb (20%Zr)	0.0363*	2	1	0.2	0.8	0.4	1.6	1.92 ^d
β -Nb (20%Zr)	0.0363*	2	1	0.2	0.8	0.4	1.6	2.53 ^e

V: unit cell volume intermetallic, *Z/V* formula units per unit cell, *a/Z* atoms per formula unit, *Zr/Z* Zr atoms per formula unit, *M/Z* alloying atoms per formula unit, *Zr/V* atoms per unit cell, *M/V* alloying element atoms per unit cell. ^a Fe_2O_3 , ^b Fe_3O_4 , ^c NbO, ^d NbO_2 , ^e Nb_2O_5 , * unit cell of pure Nb was considered, consistent with [56, 284].

Of the different intermetallics Zr₃Fe has the highest P-B ratio with 1.87 for the identified magnetite, ZrCr₂ a lower one with 1.75 and Zr₂Ni the lowest with 1.59, compared to 1.51 for pure Zr forming monoclinic zirconia. For the β -Nb precipitates (with 20%Zr) either a similar (NbO) or much higher P-B ratio (NbO_2 , Nb_2O_5) than that of pure zirconium is calculated. However, as several oxides are possible and the one formed is not known, Nb bearing precipitates are not considered in the next section.

10.4.3 Cases modelled with ANSYS

The theoretical Pilling-Bedworth ratio values were used to calculate the average height of protrusions for each material for precipitates with different diameters (Table 19). The protrusion height was modelled in ANSYS for 3 different precipitate diameters (35, 250 and 500 nm) with the precipitates in contact with the outer surface and embedded in a 200 nm thick metal layer to be transformed into zirconia. This is a good approximation of the conditions present for the precipitates in the in situ samples, on which the AFM measurements of the topography were conducted. The model had a width of 2 μm and 3 μm thickness of the metal, the expansion was constricted in the x-direction (parallel to the surface), to take the restricted in plane expansion of the sheet samples into account. The oxide and the oxidised precipitates were modelled with a Young's modulus of 136 GPa and Poisson's ratio of 0.25, the metal with a Young's modulus of 71 GPa and Poisson's ratio of 0.3 (at 415°C). The expansion due to oxidation was modelled by using the thermal expansion and a linear thermal expansion coefficient for the precipitates and the zirconium matrix transformed to zirconia being set equal to the cubic root of the Pilling-Bedworth ratio in Table 18. This implies an isotropic expansion during oxidation, which is an assumption; however, to our knowledge no information about the actual expansion during oxidation in the direction of the surface normal has been published for the oxide on zirconium or zirconium alloys. The protrusion height on the oxidised surface was calculated by subtracting the matrix height 2 μm from the precipitate position from the change in y-direction, to set the matrix oxide surface as reference for the protrusion height, which is also done for the AFM profiles.

The height of protrusions caused by small precipitates (35 nm diameter) is in the same

range as the roughness of the matrix oxide, as detected by AFM. Therefore protrusions caused by small precipitates cannot be resolved at the surface by AFM, even if they are present.

Table 19: Maximum protrusion heights extracted from ANSYS models for different precipitate diameters in a 249.6 nm thick oxide layer formed from 200 nm metal and fully oxidised precipitates.

diameter / nm	oxidised phase			
	Zr ₃ Fe	Zr ₂ Ni	ZrCr ₂	pure Zr
35	2.5	0.6	1.9	0.0
250	27.1	7.9	21.6	2.4
500	79.7	42.0	68.9	31.2

The protrusion heights observed experimentally for the different binary alloys are in accordance with the data in Table 19, taking into account their average precipitate size and the observed formation of iron oxide crystals on Zr1%Fe. As the protrusions on the surface were identified manually, a bias towards well distinguishable protrusions on precipitates with above average diameters is expected and the Pilling-Bedworth ratio calculated is in any case only truly valid under the assumptions mentioned above. Calculations with almost uniform expansion during oxidation, the expansion coefficients $\varepsilon_{\perp \text{ surface}} = 0.54$ and $\varepsilon_{\parallel \text{ surface}} = 0.05$ as used by [160, 285], do also explain together with thickness variation of the oxide the observed protrusions. On the other hand the observed undulation at the metal oxide interface of pure Zr does not result in well defined protrusions on the surface. In the binary alloys the large protrusions are clearly linked to larger oxidised precipitates, the influence of precipitate size on the observed protrusion heights is in agreement with this. On Zr1%Cr and on Zr0.6%Nb no protrusions caused by precipitates can be observed, as the protrusions expected for precipitates with an average diameter below 100 nm without formation of an additional alloying element oxide layer of significant thickness, is not distinguishable from the surface roughness. For Zr1%Ni the observed protrusion height of about 19 nm is between the heights expected for precipitates between 250 nm and 500 nm diameter. For Zr1%Fe the observed protrusions had an average height of 68 nm, this is somewhat below the height expected for a Zr₃Fe precipitate of 500 nm, but considerably above the calculated height for 250 nm precipitates. This deviation to higher protrusion heights of Zr₃Fe has to be seen in the context of iron oxide crystal formation at the outer surface. The crystals observed in TEM have a thickness of 30-50 nm. Some of the observed protrusions are densely covered by small crystals, their individual height being not exactly measurable as they are too close to each other. Considering that some smaller protrusions might have been neglected due to the manual selection and the associated bias towards larger protrusions, the calculated protrusion height is in agreement with precipitates with iron oxide crystals on a number of them, increasing the measured precipitate height by few tens of nanometres. For pure Zr a protrusion is only present in case of a locally thicker oxide, 50 nm thicker oxide (250 nm diameter of Zr “precipitate”, Table 19) leads to a protrusion height of 2.4 nm. For the calculated cases only the 500 nm Zr “precipitate” being completely oxidised would result in a obvious protrusion on the surface of 31.2 nm height.

The contribution of the thicker oxide at precipitates will also contribute to the protrusion

height beside the higher Pilling-Bedworth ratio of the intermetallics compared to pure zirconium. To evaluate the influence of the thicker oxide at precipitate sites on the protrusion height (faster oxidation), the Pilling-Bedworth ratio of the precipitate was set to the value of Zr/ZrO_2 in the model and the protrusion formed for this case was compared to Zr_3Fe (highest Pilling-Bedworth ratio of intermetallics). For the model of a 200 nm thick metal region transformed to oxide with a precipitate with 500 nm diameter in contact with the outer surface a protrusion of 79.7 nm height was obtained for Zr_3Fe and one of 26 nm protrusion height for the intermetallic replaced by zirconium oxidised to zirconia (Figure 97). The influence of a higher Pilling-Bedworth ratio becomes even more pronounced, in case the fully oxidised region is reduced to a 250 nm diameter, which reduces the surface protrusion to 2.4 nm for pure zirconia, while a Zr_3Fe precipitate still causes a protrusion height of 27.1 nm.

The protrusion width extends beyond the precipitate diameter and the height beside the precipitate (in the model at 0.25 μm for a precipitate with 500 nm diameter) is reduced to 63% of the maximum height of the protrusion in the case of the oxidised Zr_3Fe precipitate, for pure zirconia with an equivalent diameter the decrease is only about 5% of the maximum height at the same distance from the maximum height of the protrusion. A higher Pilling-Bedworth ratio does therefore not only causes a higher absolute protrusion height, but also a steeper slope of the protrusion flanks.

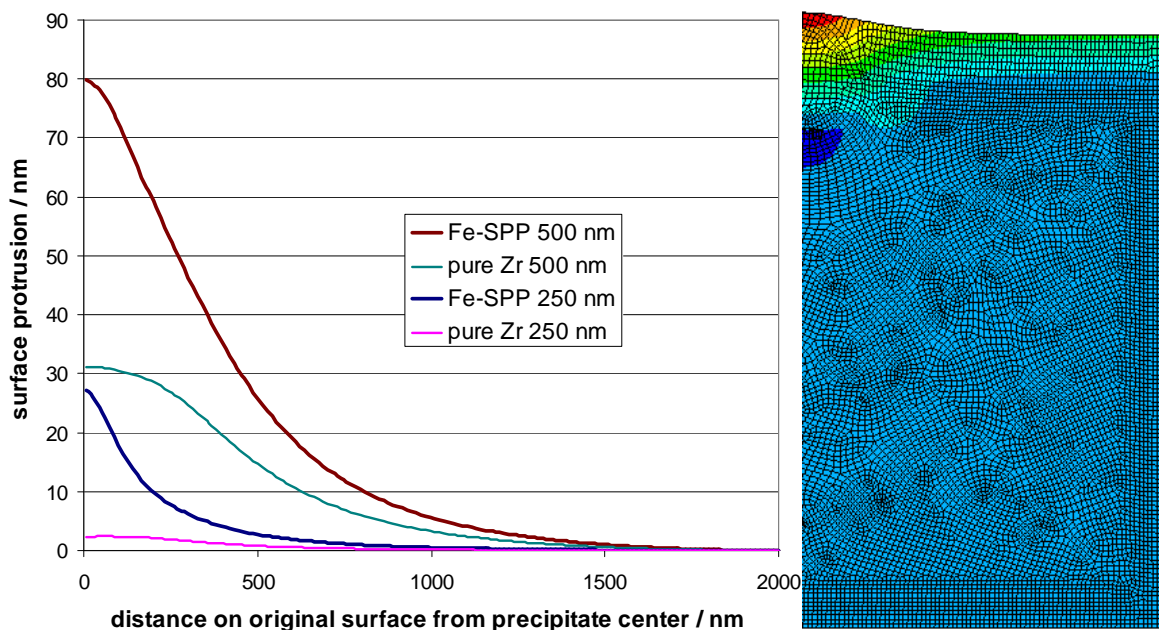


Figure 97: Comparison of the influence of a metal-oxide interface undulation of pure ZrO_2 and of a corresponding precipitate of Zr_3Fe type on the surface topography for 500 and 250 nm diameter. On the right the model is presented for the Zr_3Fe precipitate with 500 nm diameter.

10.5 Influence of oxidation conditions on precipitate oxidation

10.5.1 Influence of pressure

A comparison of the precipitate oxidation and microstructure formed during oxidation in situ (130 Pa) and in autoclave (0.1 and 10.5 MPa) did not reveal significant differences

between both environments. The precipitate oxidation as observed for samples oxidised in situ did not significantly differ from the one observed for autoclave oxidation at 0.1 and 10.5 MPa (Table 20).

Table 20: Influence of pressure on oxidation

lowest pressure / Pa	highest pressure / Pa	environment	material	influence
93	10 132	oxygen 375°C	zirconium	15% difference [92]
2 666	26 664	oxygen and water vapour 350-400°C	Zircaloy-2	20% difference [286]
4 000	101 325	oxygen 500°C	zirconium, Zircaloy-2	none [232]
1 300	8 000	water vapour 500-550°C	Zircaloy-4	none before transition [287]
133	53 329	oxygen 700°C	zirconium	none [288]
130	10 500 000	air / water vapour / steam 415°C	binary zirconium alloys	no significant (this study)

The pressure dependence of the oxidation kinetics has been addressed in earlier studies and in general no strong dependence of the oxidation kinetics on the pressure of the oxidation environment has been reported for pressures above 130 Pa [287]. Below that pressure the changes in oxidation kinetics become more pronounced [288]. It has been pointed out that the pressure dependence of the oxidation kinetics is pronounced after the kinetic transition [287]

Concerning the precipitate oxidation no large influence of pressure within the pressure range investigated has been observed for the conditions studied [92] and no study being published in the open literature does report this to our knowledge.

10.5.2 Influence of temperature

The temperature dependence of the oxidation behaviour of zirconium alloys is known [92]. Here only selected examples for the reported temperature dependence of the dissolution behaviour of the oxidised precipitates in the oxide will be discussed [197], the general tendency for dissolution of alloying elements was for all temperatures: iron > nickel > chromium, with iron already dissolving at 400°C (oxidised for 41 days), nickel at 500°C and chromium at 600°C (details in Table 21).

Table 21: Alloying element behaviour during precipitate oxidation at different temperatures [197]. Diffusion out of precipitates is marked by + and remaining in the precipitate by -. Alloying element oxide formation denoted with O.

oxidation time and temperature	reported alloying element behaviour		
	Fe	Ni	Cr
41 days / 400°C	+, O at SPP oxide interface	-	-
151 hours / 500°C	+, Fe rich oxide further away from SPP +, almost uniform	+/-, O in SPP / O at SPP oxide interface	+, O at SPP oxide interface
10 hours / 600°C	distribution in and around SPP	+, O at SPP oxide interface	+, 15 at.% remain in SPP, rest distributed around

A change of precipitate oxidation as function of oxidation temperature has so far not been reported, considering the experimental effort for microstructural observations required for such a study, this is not surprising.

10.6 Precipitate oxidation behaviour

10.6.1 Precipitate oxidation behaviour in the oxide of binary alloys

The observed oxidation tendency for precipitates not in contact with the outer surface is: $Zr_3Fe \approx Zr_2Ni \approx Zr$ matrix $> \beta$ -Nb $\approx ZrCr_2$, also shown schematically in Figure 98. Comparing the observed phenomena and the different precipitate types, a classification of the precipitate oxidation behaviour into the three following categories covers all microstructural observations from this study:

1. For the alloys Zr1%Fe and Zr1%Ni, precipitates in contact with the outer surface show an apparent faster oxidation rate with respect to the zirconium matrix resulting in an oxide protrusion at the surface and an undulated metal-oxide interface. This behaviour could be connected to the nucleation process of nodules. Precipitates not in contact with the outer surface oxidise at approximately the same rate as the surrounding zirconium matrix (Zr_3Fe & Zr_2Ni).
2. Alloying elements diffuse to the outer surface and form pure oxides ($Zr1\%Fe$).
3. For the alloys Zr1%Cr and Zr0.6%Nb, precipitates oxidise after the matrix and once fully surrounded by the oxide at a distance from the interface (β -Nb & $ZrCr_2$).

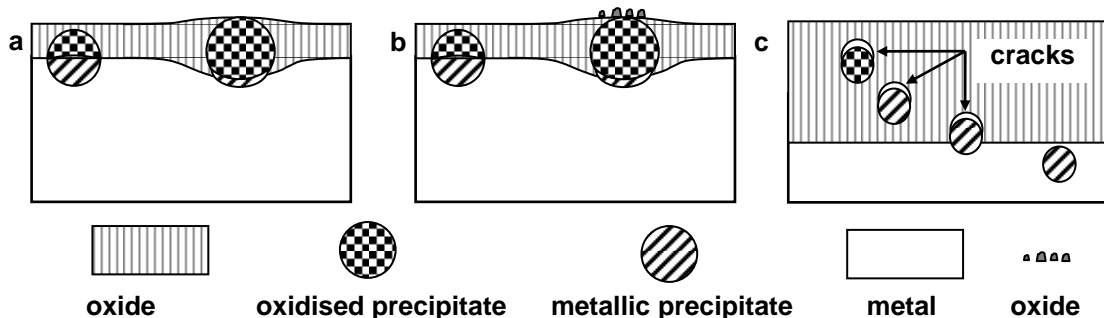


Figure 98: Schematic view of the metal-oxide interface and the oxidation state of the precipitate. (a) precipitate oxidation behaviour observed for Zr_3Fe & Zr_2Ni precipitate, (b) oxide crystal formation as observed for Zr_3Fe , (c) precipitate oxidation behaviour observed for $ZrCr_2$ and β -Nb precipitates.

The precipitates in Zr1%Cr and Zr0.6%Nb exhibited lower oxygen concentrations than the surrounding oxide matrix, owing to their small size, no confirmation of the metallic state of the precipitates with electron diffraction was successful. Crescent shaped cracks above the precipitate facing the outer surface are observed both in the Zr1%Cr and Zr0.6%Nb. It must be noted that these cracks were not observed in the case of Zr1%Fe and Zr1%Ni. These cracks are suggested to be the consequence of the delayed oxidation of the precipitates, as they were only observed for precipitates with comparatively low oxygen content in the oxide.

The oxidation of the precipitates in contact with the outer surface (also in contact with the metal-oxide interface for large precipitates for the in situ experiments) is faster than the oxidation of the surrounding matrix, but they are not oxidized completely within a short time, as a small part having remained metallic could be observed for most precipitates exhibiting this behaviour in the in situ samples.

Comparing the observed precipitate oxidation with results of previous authors, the following differences are observed:

For Zr_2Ni precipitate Ploc observed a delayed oxidation with respect to the Zr matrix [64] and an accelerated oxidation behaviour with respect to the Zr matrix for Zr_3Fe precipitate while we observed both to behave fairly similar; accelerated with respect to the matrix if in contact with the outer surface and similar with respect to the matrix if not in contact with the outer surface. From the presented results in the paper by Ploc [64] it cannot be concluded if one of the two types of precipitates was in contact with the outer surface and the other one not. For the $ZrCr_2$ precipitates no results are available in the paper by Ploc, as they were suggested to be below required size for analysis.

10.6.2 Precipitate oxidation behaviour in the oxide of commercial alloys

The same categories are also applicable to the ternary or more complex alloys used in reactors. Interesting in connection to the above categories shown schematically in Figure 98 is the fact, that apart from Zircaloy-2 containing also $Zr_2(Fe,Ni)$ precipitates, currently used alloys in nuclear power plants contain mainly precipitates exhibiting a delayed oxidation with respect to the zirconium matrix [54, 117, 138, 142, 179, 183, 184, 187, 188], with the exception of the $Zr_2(Fe,Ni)$ precipitates in Zircaloy-2, for which this behaviour has not been reported [187, 190]. A possible correlation between delayed oxidation and improved corrosion performance should be studied in detail, as all Zircaloys and the Nb containing alloys contain precipitates showing delayed oxidation.

For alloys used in nuclear reactors, commercial and test alloys, TEM observations of precipitates in the oxide of zirconium alloys and their oxidation state has been reported by different groups. An overview of precipitates types and alloys is provided in (Table 22). The criteria for including results in the presented list were apart from the precipitate type:

- Alloy type (different alloy, but same precipitate type),
- Precipitate size,
- Additional data regarding precipitates in oxide, e.g. EDS data.

For some of the precipitate types no crystal structure or nominal composition has been reported, so that they cannot be judged with the earlier discussed criteria (e.g. HANA-6 [54]).

Table 22: Overview of precipitate oxidation for different precipitates types and related parameters reported by different authors and results from this study.

alloy	precipitate type	ratio of alloying elements in SPPs	size (max. reported or measured in paper)	oxidation state in oxide at metal-oxide interface	EDS
Zr1%Nb [184]	β -Nb	-	80 nm	unoxidised	spectra
Zirlo™ [117]	β -Nb	-	80 nm	unoxidised	-
Zr-1Nb-O [138]	β -Nb	-	50 nm	unoxidised	-
Zr-1.5%Nb [193]	β -Nb	-	60 nm	unoxidised	-
Zircaloy-2 [187]	Zr(Fe,Cr) ₂	Fe/Cr \approx 0.7	800 nm	unoxidised	-
Zircaloy-2 [186]	Zr(Fe,Cr) ₂	-	100 nm	unoxidised	-
NDA [191] (Zry-4 with Ni and Nb)	Zr(Fe,Cr) ₂	-	< 80 nm	unoxidised	-
Zircaloy-4 [184]	Zr(Fe,Cr) ₂	Fe/Cr \approx 1.7	-	unoxidised	spectra
Zircaloy-4 [179]	Zr(Fe,Cr) ₂	Fe/Cr \approx 1.7	350 nm	unoxidised	-
Zircaloy-4 [155]	Zr(Fe,Cr) ₂	Fe/Cr \approx 1.7	200 nm	unoxidised	-
Zircaloy-2 [186]	Zr(Fe,Cr) ₂	-	-	unoxidised	-
Zr-0.5%Sn-0.6%Fe-0.3%V [184]	Zr(Fe,V) ₂	Fe:V \approx 1.9	200 nm	unoxidised	spectra
HANA-6 [54]	Zr(NbCu) ₂	Nb/Cu \approx 5	50 nm	unoxidised	spectra & data
HANA-4 [54]	Zr(Nb,Fe) ₂	-	100 nm	unoxidised	-
NDA [191] (Zry-4 with Ni and Nb)	Zr(Fe,Cr) ₂	-	200 nm	unoxidised	-
	Zr ₂ (Fe,Ni)	-	> 100 nm	oxidised	-
Zr-0.5Nb-0.3Fe and Zr-0.7Nb-0.1Fe [55] *	Zr(Nb,Fe) ₂	Nb/Fe \approx 1.3	300 nm	not obvious	spectra & data
	(Zr,Nb) ₂ Fe	Fe/Nb \approx 1.3	-	oxidised	-
Zircaloy-2 [186]	Zr ₂ (Fe,Ni)	-	-	oxidised	-
ZrSnNbFeCrNi [190]	Zr ₂ (Fe,Ni)	-	-	oxidised	spectra
HANA-6 [54]	Zr-Nb-Cr-Fe ‡	-	100 nm	oxidised	spectra & data
Zr-2.5Nb[192]	β -Zr	-	-	oxidised	spectra & EELS
Zr1%Fe °	Zr ₃ Fe	-	> 1 μ m	oxidised	-
Zr1%Ni °	Zr ₂ Ni	-	> 1 μ m	oxidised	-
Zr1%Cr °	ZrCr ₂	-	100 nm	unoxidised	-
Zr0.6%Nb °	β -Nb	-	145 nm	unoxidised	-

‡ no further information about precipitate type and structure, * no information which type of precipitate observed was before oxidation ((Zr,Nb)₂Fe or Zr(Nb, Fe)₂), ° this work

10.6.3 Cracks on precipitates exhibiting delayed oxidation

The presence of unoxidised [54, 142, 179, 187, 188] and partly oxidised [117] precipitates with the hexagonal / face centred cubic ZrCr₂ structure has also been reported for oxides formed on Zircaloy-4 and crescent shaped cracks at the precipitate-oxide interface facing the free oxidised surface can be observed on the micrographs presented in these papers [54, 117, 138, 142, 179, 184]. As the applied preparation methods are different between our study and the previous works, and the milling direction in FIB was perpendicular to the cracks, these crescent shaped cracks are unlikely to be an artefact of the preparation process.

Considering the Pilling-Bedworth ratio suggested for the intermetallics in 10.4.2, the crack height expected for a ZrCr₂ precipitate of a certain size has been calculated for three scenarios under the following assumptions:

1. The metallic precipitate is not significantly deformed by the expanding matrix.
2. The precipitate remains fixed to the matrix part facing the metal oxide interface.

The three scenarios are the following (situation is studied at 415°C and changes due to the different thermal expansion with cooling are not considered):

1. The expansion of the matrix during oxidation is isotropic (Figure 99-1). On the sides the expansion of the matrix closes the hypothetical crack, so that only on the front side a crack is observed.
2. The expansion of the matrix during oxidation is uniform unidirectional (similar crack height over the precipitate) (Figure 99-2).
3. The expansion of the matrix during oxidation is unidirectional (Figure 99-3) and the precipitate expands isotropic upon oxidation.

$$(1) \quad \Delta h = 2 \cdot r_{SPP} \left[\left(P - B \cdot \text{ratio}_{matrix} \right)^{\frac{1}{3}} - 1 \right]$$

$$(2) \quad \Delta h = \frac{4}{3} \pi \cdot r_{SPP}^3 \left(P - B \cdot \text{ratio}_{matrix} - 1 \right) / \left(2\pi \cdot r_{SPP}^2 \right)$$

$$(3) \quad \Delta h = \frac{4}{3} \pi \cdot r_{SPP}^3 \left(P - B \cdot \text{ratio}_{matrix} - 1 \right) / \left(2\pi \cdot r_{SPP}^2 \right) - 2 \cdot r_{SPP} \cdot P - B \cdot \text{ratio}_{SPP}^{\frac{1}{3}}$$

Equation 6: Calculation of the crack height for the different scenarios: (1) isotropic expansion during oxidation, (2) uniform unidirectional expansion during oxidation (uniform crack height) and (3) uniform unidirectional during oxidation and later isotropic expansion of precipitate during oxidation. r_{SPP} designates the precipitate radius, and Δh the crack height.

Common to the different scenarios is that the crack height is approximated as the difference between the precipitate diameter and the diameter an equivalent volume of zirconium would occupy (assuming different expansion regimes and a P-B ratio of 1.51 for zirconium/zirconia). Due to the expansion of the surrounding matrix the precipitate side facing the surface a crack will form when the oxidation front passes the precipitate (dynamic process), as the precipitate-oxide interface fails (top of precipitate) and the precipitate metal interface does not fail (bottom of precipitate) (as observed for large $ZrCr_2$ precipitate in FIB transverse sections of the annealed Zr1%Cr (Figure 43 on page 80), for illustration see Figure 99b. On the sides, the expansion of the surrounding matrix will close the possible small crack, as the overall expansion in the horizontal direction is constrained. The crack height expected under these conditions after the oxidation front has passed the precipitate completely, is directly proportional to the original precipitate diameter.



Figure 99: (a) The three sketches show the crack scenarios for different matrix expansion behaviours during oxidation. (1) uniform matrix expansion during oxidation (definition of crack height shown), (2) uniform unidirectional matrix expansion during oxidation and (3) uniform unidirectional matrix expansion during oxidation with isotropic precipitate expansion. (b) The crack height evolution upon incorporation of the precipitate in the oxide is presented. Changes due to different thermal expansion coefficients are not considered.

To test if the isotropic expansion of the oxide best explains the observed crack heights, the experimentally observed crack heights are plotted versus the observed precipitate diameter for Zr1%Cr (Figure 100) and Zr0.6Nb (Figure 101) and the theoretical lines for crack heights in case of isotropic oxide expansion, uniform unidirectional oxide expansion (crack height is uniform and oxide expands just towards the outer surface) and unidirectional expansion (crack height is 0.51 x precipitate dimension at a given position).

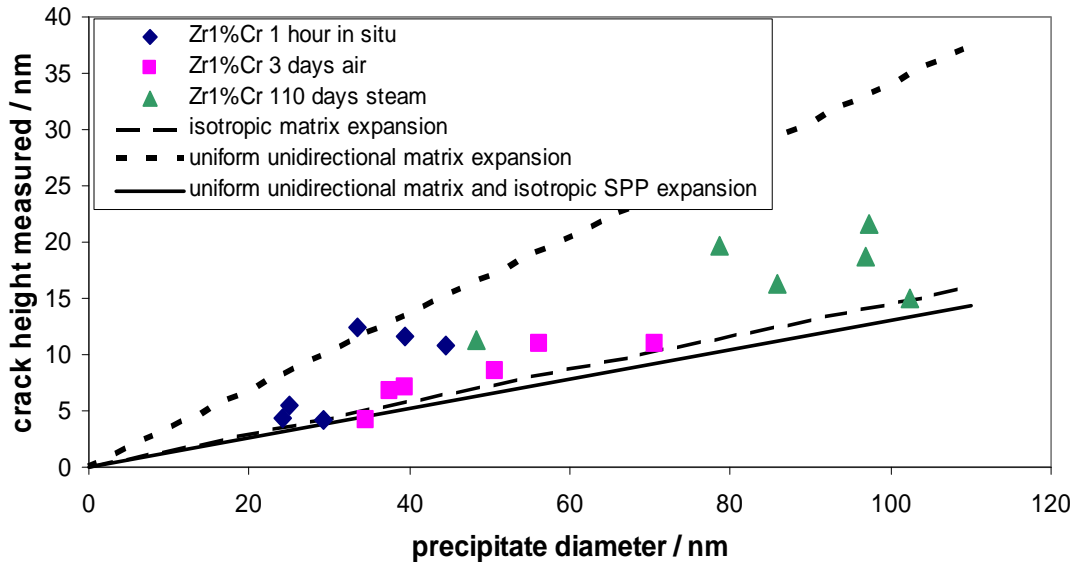


Figure 100: Crack heights on precipitates observed in TEM for Zr1%Cr with the calculated crack heights for (1) isotropic, (2) uniform unidirectional and (3) uniform unidirectional matrix expansion with isotropic precipitate expansion.

The observed crack heights fall between the two postulated models which assume isotropic expansion during oxidation and uniform unidirectional expansion (Figure 100 and Figure 101). In the case of Zr1%Cr oxidised in air there is the tendency for smaller crack heights than the two other oxidation environments (Figure 100).

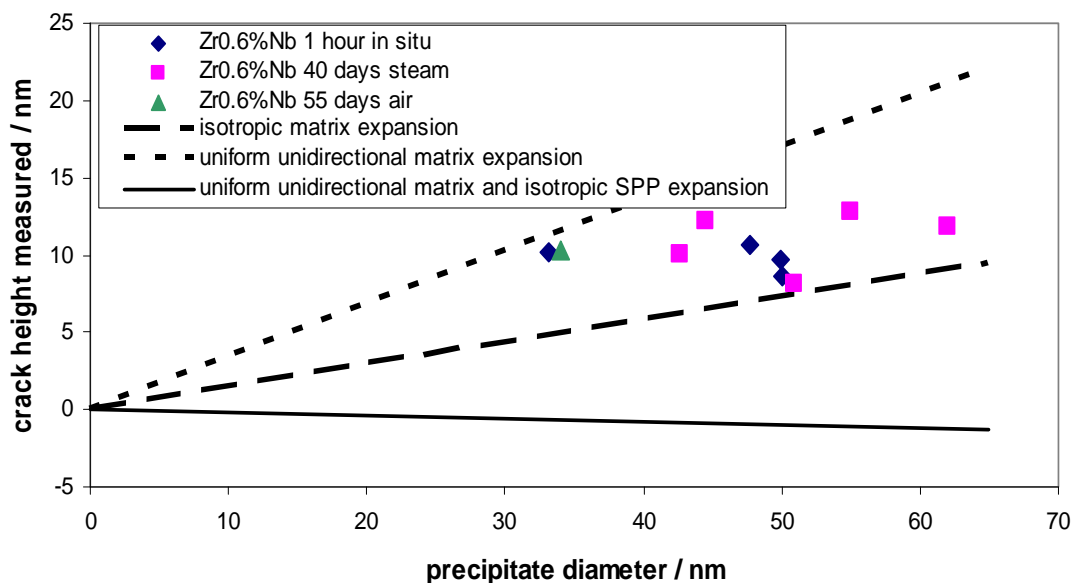


Figure 101: Crack heights on precipitates observed in TEM for Zr0.6Nb with the calculated crack heights for (1) isotropic, (2) uniform unidirectional and (3) uniform unidirectional matrix expansion with isotropic precipitate expansion (assuming formation of NbO_2).

For larger precipitates also the relaxation of the surrounding zirconia should be taken into account (which will also lead to some expansion towards the crack), which will lead to smaller crack heights than could be expected even for the scenario predicting the smallest crack heights. For isotropic expansion during oxidation for a 20 nm precipitate a crack height of about 2.9 nm is expected and for a 300 nm precipitate one of 44 nm, such large crack heights have not been observed experimentally for large precipitates and for the other scenarios even larger crack heights would be expected. Pecheur et al. have observed a large precipitate in the oxide with a crack in Figure 3a of reference (precipitate diameter ~350 nm and crack height ~35 nm), which according to the model with isotropic expansion during oxidation would exhibit a crack height of 51 nm, the difference is assumed to be caused by the relaxation of the surrounding zirconia, reducing the crack height especially for large precipitates. The scenario considering the unidirectional matrix expansion with consecutive isotropic precipitate expansion leads also to crack heights not observed in experiments. The drawback of this last scenario is that real isotropic expansion during precipitate oxidation is not possible, as the matrix will fit the lateral dimension of the precipitate; only towards the free surface an unconstrained isotropic expansion is possible.

The reason for the experimentally found crack height being mostly between the scenarios with isotropic and uniform unidirectional expansion could be, that the expansion during oxidation is between isotropic and unidirectional, which does not explain why for larger precipitates the crack heights are found to be close or even below the values predicted for the isotropic matrix expansion scenario. A possible further opening of the cracks by the FIB milling during preparation is not accounted for in the scenarios, but cannot be excluded to take place. Unfortunately no other data are available which could help to clarify this issue, the question how the oxide expansion is distributed in the different directions has already been raised by Petigny et al. [224], an answer is as far as we know not yet available.

The systematic presence of cracks at the interfaces of precipitate within the oxide, on the free surface side, induced by the different P-B ratios and delayed oxidation, could be expected to be one of the possible nucleation sites for the larger cracks reported often in TEM observations [54, 117, 138].

In the case of oxidised β -Nb precipitates the absence of cracks is frequently observed [117, 184, 192]. This provides us with the information, that the oxidised precipitates exhibit a Pilling-Bedworth ratio of at least 1.51 (zirconium/zirconia, see Table 17 on page 137). Consequently only NbO_2 and Nb_2O_5 beside ZrO_2 are possible, considering the formation of the alloying element oxide and zirconia (Table 18 on page 138). From the EELS results by Lin and Woo [192] it could be expected, that Nb_2O_5 is the probable oxide phase formed at β -Nb precipitates. For the metastable β -Zr Lin and Woo [192] stated the oxide composition at precipitates as $\text{Nb}_2\text{Zr}_{x-2}\text{O}_{2x+1}$ which was found to be structurally different from zirconia and could accommodate varying Nb contents. This indicates NbO (for the Nb part of the oxide), which is not in agreement with what could be concluded from the absence of the cracks.

10.6.4 Possible parameters affecting precipitate oxidation behaviour

The only studies which to our knowledge address the issue of alloying elements and oxidation of precipitates in the oxide to some extent are the ones by Pecheur et al. [179, 183] and Cox and Sheikh [197]. Pecheur et al. [183] explained the presence of pure metallic iron in the surrounding of oxidised $Zr(Fe,Cr)_2$ precipitates by the different free energies of formation of the oxides of Cr, Fe and Zr and the respective oxygen partial pressures required for their oxidation at 400°C. They had studied this type of precipitates in Zircaloy-4 and found metallic Fe at the precipitate-matrix interface. From the observations it was suggested that the size of the precipitates is of importance for the precipitate oxidation state, as only precipitates smaller than 350 nm were observed unoxidized in the oxide close to the metal-oxide interface. Cox and Sheikh [197] studied Zircaloy-2. They did not report pure metallic iron, but almost pure iron oxide at the precipitate-matrix interface and presented a similar scheme as Pecheur et al. [183] and included also the oxidation pressures for the oxidation of Ni and of Fe_3O_4 to Fe_2O_3 in their schematic diagram, as they were studying Zircaloy-2. However, none of them provides an explanation for the precipitate oxidation behaviour and addresses the influence of the precipitate composition and thermodynamic properties on the precipitate oxidation. Following the scheme presented by Cox and Sheikh [197], it is clear that Ni and Fe have both a lower oxidation tendency than Cr, however, all studies report the $Zr(Fe,Cr)_2$ precipitates to exhibit delayed oxidation and the $Zr_2(Fe,Ni)$ precipitates oxidise when incorporated into the oxide. Also they [197] show only the $Zr(Fe,Cr)_2$ precipitates to be metallic in the oxide close to the metal-oxide interface.

Therefore possible parameters influencing the precipitate oxidation behaviour will be discussed in the light of the own results for precipitates in binary alloys and those published for more complex alloys. The parameters already suggested [55, 179] are presented together with two which were developed in the course of this project:

1. Precipitate size determines oxidation behaviour as already suggested by Pecheur et al. [179], the precipitates observed to exhibit delayed oxidation were never exceeding 100 nm for the binary alloys studied in the as received condition,
2. Different crystal structure of the precipitate could be at the origin of the differences, for example proposed by [55],
3. Also could be considered the ratio of zirconium to alloying element atoms in the precipitate (this study),
4. Thermodynamics properties for oxidation of the elements constituting the precipitates could lead to different oxidation tendency of the precipitates (this study).

10.6.4.1 Precipitate size

In case the precipitate size is the main parameter influencing the oxidation behaviour, there should be a limiting size above which no delayed oxidation should be observable. This limiting size could be somewhat depending on the precipitate type, should however, in any case be in a similar range. A possible influence of the precipitate size on the precipitate oxidation behaviour was proposed by Pecheur [179] for $Zr(Fe,Cr)_2$ precipitates in Zircaloy-4,

precipitates in the whole size range were found oxidised and only precipitates up to 350 nm were found unoxidized. The $Zr(Fe,Cr)_2$ precipitates of the same type as studied by Pecheur also in Zircaloy-4 have been found unoxidized up to 800 nm size by Kubo and Uno [187]. For other precipitate types the maximum size of unoxidized precipitates presented in the literature is up to 200 nm (Table 22). However, it should be noted that these are just the largest ones presented and except for [179] in no other study a comment regarding a size dependence of the precipitate oxidation state can be found. The different precipitate sizes for those alloys are depended on the heat treatment the alloys received and it should be considered that for some studies the precipitate size was on purpose increased for facilitating their study and others used material as produced for application in the reactor with the requirement of a specific size range.

For the precipitates from the binary alloys in this study it should be noted, that no small precipitates of Zr_2Ni and Zr_3Fe type (identified by electron diffraction by CEZUS and confirmed by EDS in this project) were observed unoxidized and the larger ones were shown to be oxidised upon incorporation into the oxide. The precipitates which had remained unoxidised should have been observed due to the crack associated with them if they were present, which was not the case during thorough scanning of the oxide in this study. From these observations is concluded that the precipitate size is not a factor determining if delayed precipitate oxidation can be observed. The test of Zr1%Cr with large precipitates (>500 nm) confirmed this, as no change in precipitate oxidation behaviour could be observed.

10.6.4.2 Precipitate crystal structure

In case the crystal structure of the precipitates would be a parameter influencing the oxidation behaviour (proposed by [55]), the precipitates exhibiting delayed oxidation should all have a structural feature in common, being not present for the other precipitates. The $Zr(Fe,Cr)_2$ precipitates can already exhibit the hexagonal and the face centred cubic structure, being both close packed structures. The $ZrCr_2$, $Zr(Fe,V)_2$ [54] and $Zr(Fe,Nb)_2$ [289, 290] exhibiting delayed oxidation all have also either the hexagonal or the face centred cubic structure. Only the β -Nb precipitates have the body centred cubic structure. The fact that the zirconium matrix exhibits a hexagonal close packed structure and $(Zr,Nb)_2Fe$ with the face centred cubic structure [55] oxidises similar to matrix renders the direct influence of the crystal structure unlikely, as two different oxidation behaviours can be observed for two close packed crystal structures.

10.6.4.3 Zirconium to alloying element atom ratio in precipitate

In case the atomic ratio of zirconium to alloying element atoms in the precipitate determines the oxidation behaviour, all precipitates with the same zirconium to alloying element atom ratio should exhibit the same oxidation behaviour. The more alloying element content is present in the precipitate, the more the environment is changed from the pure zirconium environment to an environment dominated by the properties of the alloying elements (which all have a lower oxidation tendency than zirconium). For those precipitates with the same atomic ratio of zirconium to the alloying elements, for which observations of precipitates in the oxide are available, this reasoning is consistent with experimental

observations available. ZrM_2 representative for $ZrCr_2$, $Zr(Fe,Cr)_2$, $Zr(Fe,V)_2$ and $Zr(Fe,Nb)_2$ exhibit all a ratio of 0.5 (the alloying element content is twice the zirconium content) and have been observed unoxidized in the oxide close to the metal-oxide interface, and β -Nb (20%Zr) with a ratio of 0.25 also has been observed unoxidized under these conditions. For Zr_2M (ratio is 2, for example the case for Zr_2Ni , $Zr_2(Fe,Ni)$ and $(Zr,Nb)_2Fe$) and higher Zr contents in the precipitates (Zr_3Fe) (the zirconium content is at least twice the alloying element content) oxidation similar to the surrounding zirconium matrix has been observed.

10.6.4.4 Thermodynamic properties of the elements constituting the precipitates

In case the thermodynamic properties of the elements constituting the precipitates determine the oxidation behaviour, it should be possible to predict the precipitate oxidation behaviour when the limit for the change from delayed oxidation to similar oxidation is known beside the precipitate composition. The free energy values used for the calculations are provided in Table 23 and the dataset closest to 415°C was taken.

Table 23: Free energy of oxide formation of zirconium and selected alloying elements at ca. 415°C from different references [291-294]. Only data with more than 5 kJ/mol deviation are stated separately. For the calculations the oxides marked with * were considered (highest stated value). The column with the total free energy of oxidation up to the stated oxide has been calculated taken the stoichiometry of the different reactions into account.

element	oxide (product)	oxidised phase (educt)	O ₂ / metal atom	free energy of oxide formation (from metal to this oxide) / kJ/(mol of oxygen)	free energy of oxide formation (this reaction) / kJ/(mol of oxygen)	p(O ₂) / Pa
Cr	Cr ₂ O ₃ *	Cr	0.75	-628	-628 [294]	2·10 ⁻⁴³
Ni	NiO *	Ni	0.5	-354	-354 [291-294]	1·10 ⁻²²
Nb	NbO	Nb	0.5	-707	-707 [293]	2·10 ⁻⁵⁴
	NbO ₂	NbO	1.0	-688	-669 [293]	2·10 ⁻⁵¹
Fe	Nb ₂ O ₅ *	NbO ₂	1.25	-678	-640 [293]	4·10 ⁻⁴⁴
	FeO	Fe	0.5	-444	-444 [291, 292]	1·10 ⁻³³
	Fe ₃ O ₄	FeO	0.67	-446	-452 [294] / -444 [293]	4·10 ⁻³⁵
	Fe ₃ O ₄ *	Fe	0.67	-444	-444 [292]	3·10 ⁻²⁴
Zr	Fe ₂ O ₃	Fe ₃ O ₄	0.75	-417	-305 [294] / -284 [293]	4·10 ⁻²⁸
	ZrO ₂ *	Zr	1	-965	-965 [293, 294]	8·10 ⁻⁶⁹
V	VO	V	0.5	-739	-739 [293]	8·10 ⁻⁵⁷
	V ₂ O ₃ *	VO	0.75	-724	-693 [293]	3·10 ⁻⁴⁸
	VO ₂	V ₂ O ₃	1.0	-639	-599 [293]	3·10 ⁻⁴⁶
Cu	Cu ₂ O *	Cu	0.25	-239	-238 [292, 293] / -233 [294]	6·10 ⁻¹⁵
	CuO	Cu ₂ O	0.5	-214	-187 [293] / -137 [294]	7·10 ⁻¹⁹
Mo	MoO ₂ *	Mo	1	-464	-464 [294]	8·10 ⁻³¹
	MoO ₃	MoO ₂	1.5	-435	-380 [293] / -212 [294]	8·10 ⁻¹⁷

The oxidation tendency of the intermetallic phases present in zirconium alloys, was calculated from the value of the free energy of oxide formation of the constituting elements from Table 23 using several assumptions:

1. same free energy of oxide formation for an alloying element atom in the intermetallic and in the pure metal.
2. a linear dependence on the element properties according to the ratio of the elements present in the intermetallic of interest (ideal solution),
3. a 1:1 ratio of intermetallics containing two alloying elements

For the calculation Hess' law (e.g. [295]) was applied to obtain the free energy of formation of the oxide of the different intermetallic phases. This involves separating the intermetallic into the pure isolated elements in their standard states (enthalpy of formation) and then the formation of the respective oxide for the metals constituting the intermetallic. This approach is illustrated for the example of Zr_2Ni in Figure 102. As the enthalpy of formation was reported in the literature, this was used to calculate the dissipation of the intermetallic into its elemental constituents.

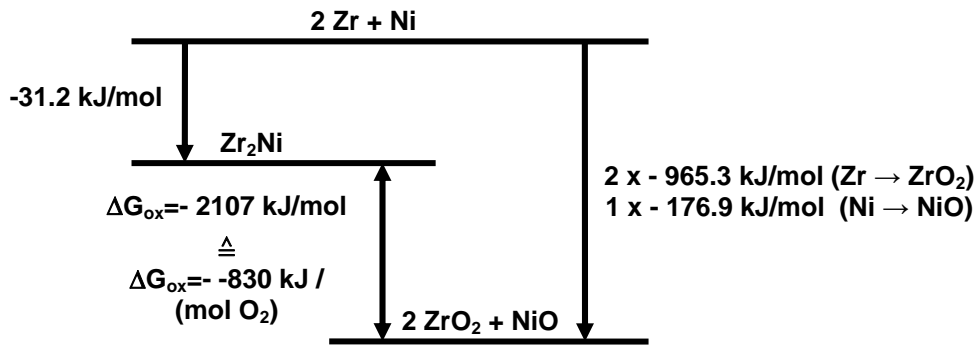


Figure 102: Schematic presenting the application of Hess' law to the oxidation of the intermetallic phases constituting the precipitates. The free energy of oxide formation is then stated per metal atom in the intermetallic to allow a comparison between the different intermetallics.

$$\Delta G_{ox} (Zr_x M_y) = \frac{-\Delta H_{formation} (Zr_x M_y) + x \cdot \Delta G_{ox} (Zr) + y \cdot \Delta G_{ox} (M)}{x \cdot n_{O_2} (ZrO_2) + y \cdot n_{O_2} (M_a O_b)}$$

Equation 7: Calculation of free energy of oxide formation for intermetallics applying Hess' law and normalisation per mol of oxygen in the oxidised intermetallic. $\Delta G_{ox} (A)$ refers to the free energy of oxide formation of substance A. $\Delta H_{formation}$ is the formation enthalpy of the intermetallic compound from the elements. n_{O_2} is the number of oxygen molecules required to oxidise one metal atom to the stated oxide.

The results of the calculation of the free energy of oxide formation using these assumptions are presented in Table 24 for the intermetallics investigated in this project and reported in the literature with microstructural information about their oxidation behaviour (Table 22). For those binary intermetallics for which the formation enthalpy was known from experiments or has been calculated, this had been taken into account for the calculation (Table 24). This will of course render direct comparison of all intermetallics difficult, as some are corrected for the formation enthalpy of the intermetallics and some not, however, as those of interest are in the energy range in which the oxidation behaviour changes and those for which no correction has been applied are more than 50 kJ/(mol oxygen) away from this energy range, so that the shift to lower free energy of oxide formation will not change their order concerning their free energy. The free energy of oxide formation was normalised with respect to the number of metal atoms in the precipitate to be comparable for different precipitate stoichiometry. Some studies reporting microstructural results of intermetallics in zirconium alloys after oxidation are listed in Table 22.

Table 24: Calculated free energy of oxide formation for phases encountered in zirconium alloys normalised to number of metal atoms in intermetallic. For details concerning the calculation see the text.

Phase	ratio Zr / alloying element		$\Delta G_{ox} / \text{kJ}/(\text{mol O}_2) \circ$		$\Delta H_{formation} / \text{kJ}/\text{mol intermetallic}$		precipitate oxidation state observed in oxide
	(1)	(2)	(1)	(2)	different sources	Zircobase [296]	
Zr-matrix	1	0	-965	-965	-	-	-
Zr ₃ Fe	3	1	-867	-869	-13.5 [297] t	-3.1	oxidised
Zr ₂ Ni	2	1	-830	-833	-31.2 [298] e	-24.2	oxidised
ZrCr ₂	1	2	-757	-755	-14.5 [299] e	-18.7	delayed oxidation
β -Nb (20%Zr)	1	4	-727	-728	3-4 [300] t	10.6 *	delayed oxidation
β -Zr (20%Nb)	4	1	-891	-891	3-4 [300] t	-	oxidised
Zr(Fe,Cr) ₂	1	2	-717	-704	-	-31.6	delayed oxidation
Zr ₂ (Fe,Ni)	2	1	-839	-833	-	-15.2	oxidised
Zr(Fe,V) ₂	1	2	-746	-746	-	-	delayed oxidation
Zr(Fe,Nb) ₂	1	2	-703	-702	-	-3.4	delayed oxidation
(Zr,Nb) ₂ Fe	2	1	-826	-825	-	-4.7	oxidised
ZrV ₂	1	2	-818	-824	-5.0 [300] t	9.1 *	not available
Zr ₂ Cu	2	1	-805	-815	-25.0 [300] t	-	not available
ZrMo ₂	1	2	-628	-630	-8.0 [300] t	-	not available

* denotes positive formation enthalpies for metastable phases from Zircobase [296], which are present due to thermodynamic constraints. Formation enthalpy: e denotes experimental values and t theoretical values. (1) denotes free energy of oxide formation values derived using different sources for the formation enthalpy and (2) formation enthalpies at 415°C from Zircobase [296]. \circ normalised per metal atom in formula unit of intermetallic.

The energy range in which the change from delayed precipitate oxidation to similar oxidation as the zirconium matrix takes place is between -760 and -830 kJ/(mol oxygen) (Figure 103). All intermetallics with a free energy of oxide formation above -830 kJ/(mol oxygen) exhibit the oxidation similar to the zirconium matrix and all below -730 kJ/(mol oxygen) the delayed oxidation with respect to the zirconium matrix. The formation enthalpy of the compound leads to a small shift of the free energy of oxidation; however, as the value is divided by the number of mols oxygen required for oxidation of one mol of the compound, the change is usually below 10 kJ/mol. Therefore the values of the free energy of oxide formation do not deviate strongly for the two different sets of formation enthalpies used for the calculation. The different behaviour of precipitates containing the same alloying element can also be explained with this approach. The Zr₂(Fe,Ni) precipitates contained in Zircaloy-2 not reported to be unoxidized in the oxide [187] have with ca. -830 kJ/(mol oxygen) a distinctly higher oxidation tendency than the Zr(Fe,Cr)₂ precipitates present in Zircaloy-2 and Zircaloy-4 with -703 kJ/(mol oxygen), the formation enthalpy of the respective ternary intermetallics has not been taken into account. As the oxidation tendency of iron and nickel is lower than the one of chromium, this illustrates quite well the fact that there is also a critical limit of alloying element content which needs to be exceeded to obtain precipitates with a free energy of oxide formation below -760 kJ/(mol oxygen). The zirconium to alloying element ratio is for the first precipitate type 0.5 and for the later 2. The Fe/Cr ratio in the Zr(Fe,Cr)₂ precipitates varies between 0.7 to 1.7, which corresponds to a free energy of oxide formation of -713 and -687 kJ/(mol oxygen) respectively, indicating that

the $Zr(Fe,Cr)_2$ precipitates in typical Zircaloy-4 [155, 179, 184] should be slightly more oxidation resistant than those in Zircaloy-2 [187] because of their higher Fe/Cr ratio.

For the Nb bearing precipitates $Zr(Fe,Nb)_2$ and $(Zr,Nb)_2Fe$ a similar trend is observed, the $Zr(Fe,Nb)_2$ has a free energy of oxide formation of -707 kJ/(mol oxygen) and $(Zr,Nb)_2Fe$ one of -838 kJ/(mol oxygen) and the same zirconium to alloying element ratio as in the case of the two precipitate types in the Zircalloys.

10.6.4.5 Comparison of different probable parameters for precipitate oxidation behaviour

With the precipitate size and crystal structure excluded as parameters influencing the precipitate oxidation behaviour, the two other parameters remain for discussion. For all precipitates for which microstructural observations are available, the calculation of the thermodynamic driving force (free energy of oxidation) and the zirconium to alloying element ratio in the precipitate are in agreement with each other.

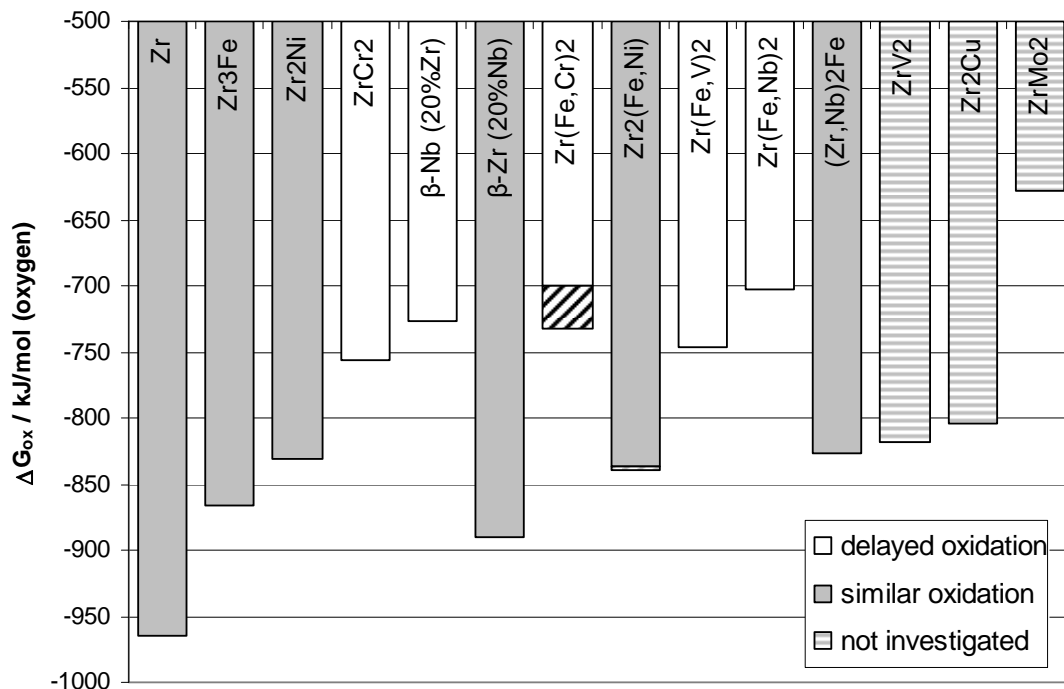


Figure 103: Free energy of oxide formation for the different phases encountered in precipitates of zirconium alloys normalized to the number of mols of oxygen in the oxidised precipitate from Table 24. The plotted data are from the left free energy column of Table 24.

All precipitates observed to exhibit delayed oxidation exhibit a free energy of oxide formation of maximum -760 kJ/(mol oxygen) and a zirconium to alloying element ratio of 0.5 or below and all those with similar oxidation to the zirconium matrix a free energy of oxide formation of minimum -830 kJ/(mol oxygen) and a zirconium to alloying element ratio of 2 or above. The appropriate criterion of the two for prediction of the precipitate oxidation behaviour cannot be decided with only the available results (Figure 103). At least one type of precipitate falling into different groups for both criteria has to be analysed to determine the correct criterion.

10.6.4.6 Identification of probable parameters for precipitate oxidation behaviour

The two precipitates which do not fit into this scheme are the precipitates expected for binary zirconium alloys containing Cu or V. The binary intermetallics with the highest zirconium content formed by these two alloying elements (Zr_2Cu and ZrV_2) would be useful to elucidate the question if either the alloying element to zirconium ratio or thermodynamics are a factor that can be considered to determine the precipitate oxidation state in the oxide close to the metal-oxide interface, as they fall for each criterion into a different group.

According to the calculations performed Zr_2Cu and ZrV_2 should exhibit the same oxidation behaviour (-800 kJ/(mol oxygen)) while the alloying element to zirconium ratio would be once 0.5 (Zr_2Cu) and once 2 (ZrV_2).

Testing either one or even both binary alloys would therefore allow to clarify, which of the two criteria (ratio of zirconium to alloying element content in the precipitates or the thermodynamic properties for oxidation of the constituents in their elemental state) is responsible for the observed oxidation behaviour. The two binary alloys in question have already been tested ($Zr_{0.8\%}Cu$ [54], $Zr_{1\%}Cu$ [301] and $Zr_{1\%}V$ [184]), however, no microstructural observations of precipitates in the oxide close to the metal-oxide interface are available.

An indication for the influence of the oxidation tendency of the elements constituting the precipitate on precipitate oxidation behaviour is a study, in which the intermetallics as encountered in the Zircalloys were tested with Nb additions in autoclave [191]. For $Zr(Fe,Cr)_2$ with Nb substituting 1 out of 4 Zr atoms a lower oxidation tendency was observed for the precipitates in the oxide [191] compared to pure $Zr(Fe,Cr)_2$. The observation of the reduced oxidation tendency of the $Zr(Fe,Cr)_2$ precipitates in the alloys with Nb additions agrees with both proposed explanations for the oxidation tendency, the Nb additions reduce the zirconium content of the precipitate (higher alloying element to zirconium ratio) and because of the lower free energy of oxide formation of Nb also the free energy of oxide formation of the intermetallic is reduced. They found however a contradicting oxidation behaviour for bulk intermetallics, with higher oxidation tendency for the intermetallic with Nb additions (XRD showed only oxide phases in case of the bulk intermetallics with Nb additions). The faster oxidation behaviour of the intermetallic with Nb additions is also observed for the bulk $Zr_2(Fe,Ni)$ intermetallic with Nb additions compared to the bulk intermetallic without Nb. For the precipitates in the oxide scale no information about a deviating oxidation tendency has been provided. Unfortunately Anada et al. [191] did not present further data for the oxides formed on the bulk intermetallics (e.g. weight gain), which renders it impossible to reach a conclusive answer explaining the observed behaviour. Comparing the oxidation behaviour of the two types of bulk intermetallics with Nb additions with each other, it was found that $Zr(Fe,Cr)_2$ with Nb additions oxidized faster than the respective $Zr_2(Fe,Ni)$ compound containing Nb. As the precipitates in zirconium alloys are always in contact with the zirconium or zirconia matrix, the oxidation behaviour of the bulk intermetallics cannot be taken as reference for the precipitate oxidation behaviour.

10.7 Precipitate oxidation at the surface

For the precipitates in contact with the outer surface the oxidation behaviour observed was different to their behaviour below the surface in the oxide. This change in behaviour was even enhanced due to the modification of the surface by the preparation method; the details are discussed in section 10.2. However, in the case of the neutral diamond slurry finish, which is assumed to induce no significant surface modification, the precipitates still behave different with respect to their oxidation behaviour at sub-surface positions. They exhibit a faster oxidation than the surrounding zirconium matrix with locally thicker oxide (Figure 98), resulting in protrusions on the surface (10.4.1). For oxide scales formed during the in situ experiments an increased metal-oxide interface undulation is observed, as a consequence of the faster precipitate oxidation. The anodic protection provided by the galvanic couple of the intermetallic precipitates and the zirconium matrix was shown by Isobe et al. [21] for large couples. Considering the observed precipitate oxidation behaviour of Zr_3Fe and Zr_2Ni precipitates (Figure 98), the anodic protection of the zirconium matrix by the precipitates can be safely assumed for those precipitates in contact with the outer surface, where the precipitate also exhibit preferential oxidation. The anodic protection of the zirconium matrix by the precipitates not in contact with the surface seems more unlikely in the light of the observed precipitate oxidation behaviour at the metal-oxide interface, the precipitates of Zr_3Fe and Zr_2Ni type oxidise similarly to the surrounding matrix and the $ZrCr_2$ and $\beta-Nb$ precipitates exhibit even delayed oxidation, remaining metallic in the oxide scale.

As the microstructural information from this study does not provide a clear answer, additional information from electrochemical properties measured in other studies is considered to reach further conclusions about the precipitate influence. The thermodynamic considerations in 10.6.4.4 do not explain the precipitate oxidation behaviour at the surface. Of interest for comparison are those studies having investigated binary intermetallics which are also present in the binary alloys [59, 202, 208, 209, 271, 302].

The same material as the studied has been characterised by Barberis et al. [202] with cathodic oxidation and Simic and Ahlberg [271, 302] with anodic oxidation. The findings of Barberis et al. [202] were: the rest potential increases from pure Zr over Zr_3Fe , $Zr(FeCr)_2$ and $ZrCr_2$ to Zr_2Ni . This was also found by Weidinger et al. [59] who also studied different intermetallics and found the same order with the $Zr_2(Fe,Ni)$ exhibiting the highest rest potential. When they compared the weight gain of the different intermetallics, they found the iron bearing intermetallics to exhibit higher weight gains than those containing no iron for an oxidation in an autoclave purged with argon to remove the oxygen. The enhanced oxidation of iron bearing alloys in oxygen containing oxidation environments was reported by Shirvington [177], however for deoxygenated environments this deleterious influence of iron was not observed.

High cathodic currents were observed for $ZrCr_2$ and Zr_2Ni , which were associated with hydride formation, for Zr_3Fe and pure Zr the cathodic currents were more than two orders of magnitude lower [202].

Galvanic couples of intermetallics with pure zirconium tested by Weidinger et al. [59]. The couples showed that the efficiency for shifting the rest potential to more noble values increased from $Zr(FeCr)_2$ over $Zr_2(Fe,Ni)$ to Zr_2Fe . The differences between different tested materials were significantly reduced for oxidation at $250^\circ C$ ($\Delta \approx 200$ mV) instead of room temperature ($\Delta \approx 500$ mV). So the oxidation temperature is an important parameter to be taken into account when comparing the different intermetallics regarding their corrosion resistance.

Murai et al. [208, 209] studied polarisation curves of intermetallics at room temperature and $250^\circ C$ and found higher current densities for the iron containing intermetallics ($ZrFe_2$ and $Zr(FeCr)_2$) in cathodic polarization and higher corrosion resistance / lower anodic currents for $Zr(FeCr)_2$ and $ZrCr_2$ (attributed to their Cr content [208]).

At $250^\circ C$ Zr_2Fe and $ZrFe_2$ were both tested [209] and the current densities were higher for $ZrFe_2$ indicating that the iron content of the precipitates might be one factor increasing the current density. However, the $Zr(Fe,Cr)_2$ precipitates contain more iron than the Zr_2Fe precipitates and they exhibit significantly lower current densities in anodic polarisation.

Comparing these electrochemical results with the microstructural information, it can be observed that the precipitates shifting the rest potential to more noble values, are Zr_2Ni , $Zr_2(Fe,Ni)$ [59], while $Zr(FeCr)_2$ [59] and Zr_3Fe [202] exhibit low rest potentials. An exception from the above category of precipitates is Zr_2Fe reported by Weidinger et al. [59], as it is a metastable phase, stabilized by oxygen impurities [67], not reported for the commercial alloys.

The corrosion resistance of the precipitates is for the materials reported in [208, 209] inverse proportional to their ability to shift the rest potentials to more noble values. Comparing Zr_2Ni and $ZrCr_2$, it is known that $ZrCr_2$ is the more corrosion resistant of the two intermetallics in agreement with the microstructural observations in this study. However, for the intermetallics in the Zr-Fe system the available data are not sufficient to conclude. From the own microstructural results it is suggested that, Zr_3Fe is behaving similar to Zr_2Ni , however the electrochemical confirmation is not available, as not both phases have been tested with the same method.

10.8 Iron oxide formation at the surface

In the case of Zr1%Fe a clear evolution of the presence of iron oxide at the surface has been observed with oxidation time. These observations provide a very good understanding of the behaviour of Fe in Zr alloys. From the results obtained for Zr1%Fe material oxidized for different times, the following evolution of iron oxide precipitation at the surface can be summarized as a function of oxidation time (Figure 104):

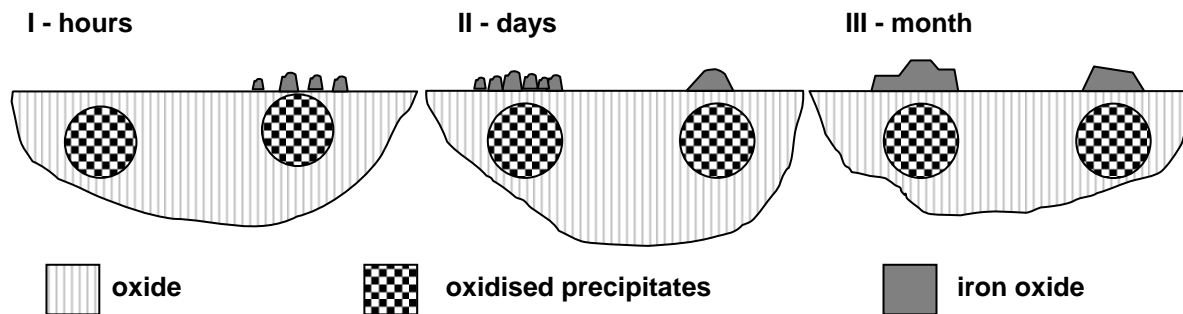


Figure 104: Schematic diagram showing the formation of iron oxide at the surface of Zr1%Fe as a function of time: (a) iron starts to segregate to the surface as pure oxide and forms small crystals above the oxidized precipitates. (b) the density of small iron particles above precipitates increases and more crystals can be observed. (c) large iron oxide crystals have formed some of them are single crystals.

- I – hours: iron segregates from the oxidised precipitates in the oxide to the outer surface, the distance of the oxidised precipitate to the surface and its size control the volume of the formed iron oxide particles and the time for their appearance. A few particles are already developing a crystal shape. (Figure 104a)
- II - days: the segregation process continues and the size of the particles begins to increase. Some particles start to form larger crystals of iron oxide than in stage I. (Figure 104b)
- III - months: the segregation process is finished (can be checked by the absence of Fe in the underlying precipitate) and the small crystals have been replaced by larger iron oxide crystals, which can consist of a single crystal. (Figure 104c)

The presence of iron oxide on the surface above precipitates was observed in earlier studies by Auger spectroscopy [64, 303] electrochemical reduction [177] and TEM [304]. The Auger studies [64, 303] also showed an increase in thickness of the iron oxide layer with time, however, no information about the oxidation state of iron in the oxide was provided (either Fe_2O_3 and Fe_3O_4 [177] from electrochemical measurements). The only TEM results on a binary material beside this study were for a ZrFe_2 intermetallic oxidised in steam at 200°C for 56 days by Abraham and Dietz [304].

Shirvington [177] showed the presence of iron oxide in the form of Fe_2O_3 and Fe_3O_4 on Zr0.7%Fe and Zircaloy-2 oxidised under various conditions using voltage scans and selective reduction. As no high resolution SEM or TEM results could provide further details about this iron oxide, an average iron oxide thickness was calculated based on the precipitate surface fraction and the amount of iron oxide formed. The thickness of the iron oxide on the precipitates was estimated for a continuous coverage of the precipitates to be around 9 nm thick after oxidation for 25h oxygen concentration in the steam seems to have an effect on this phenomenon [177], as in deoxygenated environments no significant amount of iron oxide was detected with electrochemical methods. The present study revealed that iron oxide segregates as crystals with cubic structure (either magnetite - Fe_3O_4 or maghemite - $\gamma\text{-Fe}_2\text{O}_3$)

and not as a continuous layer. Hematite exhibits only a hexagonal crystal structure and can therefore be excluded. As no precession electron diffraction (PED) is available on the used TEM, the two cubic structures cannot be distinguished, due to the very similar lattice constant and structure (magnetite $a = 0.83950$ nm [274] / maghemite $a = 0.8347$ nm [275]), the application of PED to identify the species has been demonstrated for these two iron oxides [305]. Moreover the location of these crystals correlates to the underlying precipitate, which was so far only observed by [64] for a binary Zr-Fe alloy. For the precipitates more than $1\ \mu\text{m}$ away from the surface no segregation of the alloying elements towards the surface was observed. The phenomenon of iron oxide formation above oxidised precipitates containing iron has been observed at different temperatures (300°C [303], 415°C this study and 700°C [198]) and pressures (this study) and if the ZrFe_2 intermetallic is considered the temperature range is extended down to 200°C [304]. So far the other studies assumed just those precipitates in contact with the outer surface to contribute to this phenomenon, a contribution from precipitates close to the surface was not considered. The increase of the iron oxide crystal size with oxidation time is also new information; the previous studies on oxidised Zr alloys [64, 177, 303] were not able to distinguish between an agglomerate of many small iron oxide crystals and a large crystal, as they measured information which was averaged at the micrometer scale and were able to provide estimates of the average iron oxide thickness present.

In the case of Zr-Cr and Zr-Ni binary alloys, such alloying element oxide formation has also been observed but to a much smaller extent [177], which is consistent with this study. However, from the presented results it cannot be claimed that no other alloying element oxide than iron oxide has been observed, and it cannot be excluded that present oxides of chromium and nickel have been missed during surface analysis, although thorough scanning of the surface was performed. On a TEM sample of Zr1%Cr with the finishing by the basic vibratory polisher solution, a higher Cr to Zr ratio was found at the outermost surface of an oxidised precipitate after oxidation in situ for 1 hour, however, no pure chromium oxide could be detected, which might be due to the fact that only a very thin chromium oxide layer was present, which could not be resolved due to the sample thickness. This is in agreement with the very thin chromium rich oxide layer found by Auger electron spectroscopy by Hatano and Sugisaki [200], who found a very thin (~ 0.5 nm thick) layer of chromium rich oxide on the surface of an oxidised $\text{Zr}(\text{Fe},\text{Cr})_2$ precipitate.

For the more complex Zircalloys similar observations of alloying element oxide have been made in several studies. Here the most important ones will be shortly presented to allow a comparison of the different cases:

Iron oxide has also been observed on the surface of Zircaloy-2 by Auger spectroscopy [199] and by controlled potential reduction using a saturated Calomel electrode [177]. In the case of $\text{Zr}(\text{Fe},\text{Cr})_2$ precipitates the outermost layer was consisting of chromium oxide and the inner layer was depleted in iron on an oxidised precipitates [198, 199], the observations were made on samples oxidised for in situ 1 hour at 700°C and 130 Pa vapour pressure [198] and at 400°C for different times at 0.1 MPa steam pressure [199]. Above $\text{Zr}_2(\text{Fe},\text{Ni})$ precipitates only Fe oxide was detected [199]. This order of oxide layers is in accordance with the partial

pressure of oxygen being required to convert the metallic alloying elements into their oxides (Table 23), which is $\text{Cr} < \text{Fe} < \text{Ni}$. However, the explanation proposed by Hatano and Sugisaki [199, 200] for the alloying element oxide formation at the surface does not explain, why iron forms the iron oxide increasing in thickness with oxidation time, as observed in this project and by others [177, 199]. A combination of the oxygen affinity together with the diffusion of the alloying element in the zirconia scale is most probably a much better explanation. Why should otherwise the chromium oxide formation be observed to be similar for different oxidation times [200] and Ni oxide not observed. The depletion in the second alloying element not forming the surface oxide [199, 200] could well be the consequence of a change in oxygen potential underneath the formed alloying element oxide and the conductivity of the oxide. In the case of the presence of iron oxide on the surface it is known that the resistivity of the zirconia is decreased by two orders of magnitude [177].

In this project for Zircaloy-2 the formation of iron and chromium oxide was observed on $\text{Zr}(\text{Fe}, \text{Cr})_2$ precipitates, for $\text{Zr}_2(\text{Fe}, \text{Ni})$ precipitates no observation of iron oxide on the surface has been made for the TEM samples prepared, which might be due to the fact that the precipitates in the oxide of the samples investigated were too far from the surface for the formation of iron oxide at the surface.

10.9 Iron migration to the surface

The presence of iron on the surface above oxidised precipitates can be already observed after less than 1 hour oxidation in situ at 415°C. Therefore it was of interest to estimate the effective transport coefficient of the iron to the surface. Studying the literature, only Iltis et al. [195] have provided an estimate of an iron diffusion coefficient in the zirconia layer formed during oxidation with 10^{-15} cm/s. Other literature sources provide only a relative ranking of the different alloying elements, but do not give diffusion coefficients. For $\text{Zr}(\text{Fe}, \text{Cr})_2$ precipitates segregation into the surrounding zirconia was observed for iron and to a lower extent for chromium reported in [179, 197, 306] and for $\text{Zr}_2(\text{Fe}, \text{Ni})$ precipitates for iron and to a lower extent for nickel [190, 197]. As a result it can be concluded that among the alloying elements studied iron has the highest migration rate in zirconia. This might also explain the formation of the large iron crystals at the surface, while for the other alloying elements this behaviour has not been observed in similar form.

To be able to compare the diffusion coefficient provided by Iltis et al. [195] and others [307-309], an estimate for the diffusion of the iron to the surface was made using the following procedure:

1. Estimate the surface area through which the iron has passed from SEM images
2. Estimate the volume of iron oxide at the actual precipitate from the SEM and TEM images of the same position
3. Estimate the average distance the iron had to migrate to the surface from the TEM image of iron oxide and the underlying oxidised precipitate (Figure 105)

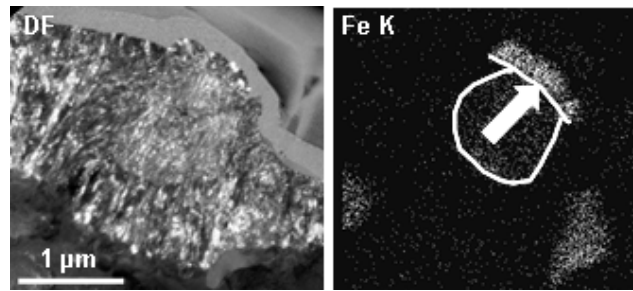


Figure 105: Dark field contrast of oxidized precipitate in oxide with iron oxide on the surface and corresponding EDS map of Fe-K signal. The precipitate and the surface area of the iron oxide are marked by white lines and an arrow indicates iron migration to the surface.

As an example for the TEM data considered for this estimation refer to Figure 105. The amount of iron diffusing was calculated from the observed volume of iron oxide. Integrating Fick's first law and replacing the flux by the amount of iron divided by the surface area and the oxidation time, a diffusion coefficient was estimated assuming constant conditions during the formation of the iron oxide. This is only an idealised description, as the concentration difference (Δc) over the migration distance is reduced with oxidation time and the process is not linear with time! The concentration difference entered into the calculation was the iron concentration in stoichiometric precipitate in oxidised state minus the remaining iron detected with TEM/EDS as upper boundary (iron being transported from precipitate to surface), as on the surface the iron concentration was assumed to be zero with respect to the driving force, as iron oxide was formed.

$$D = \frac{n(Fe)}{A \cdot t} \cdot \frac{\Delta x}{\Delta c}$$

Equation 8: Approximation of the iron diffusion coefficient applying Fick's first law with $n(Fe)$ being the amount of iron in mol, A the area of iron oxide on the surface, t the oxidation time, Δx the migration distance and Δc the concentration difference between depleted precipitate and the surface.

For all conditions for which suitable SEM observations of the iron oxide on the surface and of the precipitate in TEM samples are available, this estimation of the diffusion coefficient was performed (Table 25). The obtained diffusion coefficient (Figure 106) is in a similar range as the one reported by Iltis et al. [195], which was also obtained for a oxidised zirconium alloy without irradiation. The zirconia formed during oxidation exhibits much higher diffusion coefficients for iron than sintered yttria stabilized zirconia [307-309]. The non-surprising difference in iron diffusion coefficient between the different types of yttria stabilized zirconia is the difference between single crystalline material [307] and sintered powder [308, 309], for which surface diffusion in the porosity could be expected, however, the two oxidised zirconium alloys are very similar regarding to their microstructure, so that this parameter will not cause a significant difference between the two materials. Due to the number of assumptions and the associated error, the diffusion coefficients calculated are a good estimate, confirmed by the comparison with Iltis et al. [195]. The difference between the two studies and the described iron migration phenomenon is, that once the iron migrates to the surface and away from the precipitate into the surrounding oxide [195]. As the estimates for

the iron diffusion coefficient for 3 different conditions are in a similar range, the iron diffusion coefficient seems to be fairly similar under the conditions studied. It is not obvious if the small spread of the diffusivity data is due to a low impact of erroneous parameters or because the assumptions are confining the possible range.

Table 25: Estimated diffusion coefficient for the different oxidation conditions and times.

oxidation time	pressure	D / cm ² /sec
1 hour	130 Pa	$1.3 \cdot 10^{-15}$
72 hours	0.1 MPa	$1.4 \cdot 10^{-15}$
72 hours	0.1 MPa	$8.8 \cdot 10^{-16}$
110 days	10.5 MPa	$5.3 \cdot 10^{-16}$
Iltis 400°C [195]	10.3 MPa	$1.0 \cdot 10^{-15}$

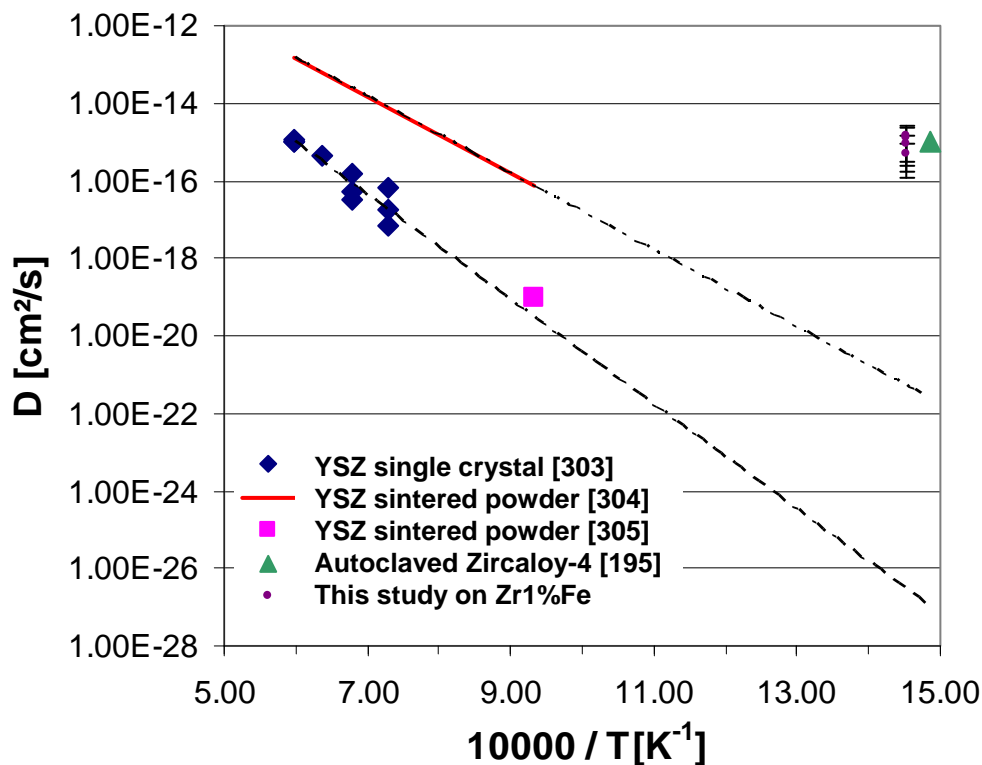


Figure 106: Diffusion coefficients of iron in zirconia reported in the literature for different temperatures, types of zirconia and conditions [195, 307-309].

11 Conclusions

In this work the microstructure of oxides formed on binary zirconium alloys was characterised in order to study the precipitate oxidation behaviour and to understand the influence of different alloying elements and oxidation conditions. Binary zirconium alloys containing 1 wt.% Fe, Cr or Ni and an alloy with 0.6 wt.% Nb as well as pure zirconium and commercial Zircaloy-2 and Zircaloy-4 have been studied after oxidation at 415°C in different oxidation environments.

The studied conditions comprise autoclave oxidation in air as well as steam at ambient pressure (0.1 MPa) for up to three days and in steam at 10.5 MPa for up to 110 days. The oxidation has been also investigated in water vapour at 130 Pa at 415°C for 1 hour in situ in an environmental scanning electron microscope.

The surface of the samples was characterised using scanning electron microscopy and energy dispersive x-ray spectroscopy. In addition the surface of the samples oxidised in the environmental scanning electron microscope was also characterised using atomic force microscopy. The microstructural characterisation of the oxide was performed with scanning electron microscopy, focused ion beam microscopy for transverse and cross-section preparation and transmission electron microscopy including energy dispersive x-ray spectroscopy and electron energy loss spectroscopy. The evolution of the microstructure was characterised for the precipitates in the oxide and their oxidation behaviour determined.

The conclusions are summarised in three points, precipitate oxidation behaviour and possible explanations of this behaviour, iron oxide observed on the surface and protrusions on the surface above oxidised precipitates.

Point 1: From the results of the microstructural characterisation of the oxide and the precipitates in the binary and commercial zirconium alloys the existence of two families of precipitate oxidation behaviour can be concluded:

1. The first family consists of the Zr_3Fe and Zr_2Ni precipitates, as well as the $Zr_2(Fe,Ni)$ precipitates, which exhibit a similar oxidation as that of the surrounding zirconium matrix.
2. The second family comprises the $ZrCr_2$ and the β -Nb precipitates, as well as the $Zr(Fe,Cr)_2$ precipitates, which exhibit a delayed oxidation in comparison with that of the zirconium matrix.

The oxidation behaviour of the precipitates is correlated to their composition :

- Zirconium to alloying element ratio or,
- Free energy of oxide formation per atom in the precipitates.

These two parameters are intrinsically correlated (composition is also reflected in ΔG_{ox}). For those precipitates exhibiting similar oxidation with respect to the zirconium matrix, the zirconium to alloying element ratio is 2 or above and it is 0.5 or below for those exhibiting delayed oxidation with respect to the zirconium matrix. The free energy of oxide formation per atom in the precipitates was estimated from Hess' law, using the formation enthalpy of the precipitates and tabulated data for the free energy of oxide formation of the elements forming

the intermetallics. The precipitate oxidation behaviour observed in other studies accessible in the open literature for other relevant precipitates characterised so far is in agreement with the two families of precipitates reported and the two above mentioned parameters found to be correlated to the precipitate oxidation behaviour.

The matrix oxide was columnar for all environments, only the porosity in form of cracks was significantly increased for the samples oxidised at high pressure and longer times. These cracks observed in the oxide are up to several micrometers long and oriented parallel to the metal-oxide interface. The small cracks formed at the ZrO_2 -precipitate interface in the case of Zr1%Cr and Zr0.6%Nb might act as well dispersed formation sites for somewhat larger cracks, improving the mechanical stability (stress accommodation) of the oxide and thus the corrosion resistance of the alloys. The variation between the different materials exhibiting dissimilar precipitate oxidation is small under the studied conditions; however, in reactor these small differences might well be significant for the performance of the cladding material.

Point 2: In the case of Zr1%Fe pure iron oxide crystals were systematically found on the surface above oxidised precipitates for all conditions. Their size increased from several tens of nanometres after 1 hour of oxidation to more than 1 μm size after 110 days of oxidation. The iron oxide was identified as cubic magnetite. The impact of the iron oxide at the surface on the oxidation resistance could not be clarified in this project. The oxide of the other alloying elements apart from Fe was only observed in rare cases.

Point 3: Protrusions were observed with AFM above oxidised precipitates in contact with the outer surface on the samples of Zr1%Fe and Zr1%Ni. Under the protrusions a locally thicker oxide was found on transverse sections and transmission electron microscope specimens for large precipitates. No large protrusions associated to precipitates could be observed in the case of Zr1%Cr, Zr0.6%Nb and pure zirconium with no precipitates or small precipitates (below 100 nm diameter). For all materials investigated the overall roughness increased from the polished to the oxidised surface; the local protrusions were unambiguously linked to the larger oxidised precipitates in contact with the outer surface. The protrusions are most likely due to a higher Pilling-Bedworth ratio of the precipitates compared to pure zirconium, as the thicker oxide at the protrusions does not explain the protrusion height as sole contributing parameter. In the case of Zr1%Fe the presence of the formed iron oxide on the surface is not sufficient to explain the observed protrusions heights without other contributions. The estimated Pilling-Bedworth ratio of the precipitates, assuming the formation of pure element oxides, described the experimentally observed protrusion heights quite well, taking precipitate size and iron oxide formation into account.

To summarize the findings it could be shown that:

- oxidation behaviour of the precipitates depends on their composition,
- precipitates exhibit a different Pilling-Bedworth ratio than the zirconium matrix,
- iron containing precipitates close to the surface form pure iron oxide crystals on the surface and
- the impact of the two different precipitate oxidation behaviours on the mechanical properties of the oxide has been partly explored.

12 Outlook

The understanding of the local precipitate oxidation behaviour and its impact on the general properties of zirconium alloy during oxidation can still be improved. So far no reliable prediction of the long-term behaviour of zirconium alloys in the corrosive environment inside a nuclear reactor is possible. Even for short-term oxidation in an autoclave the oxidation behaviour cannot yet be fully explained.

For future work on precipitate oxidation behaviour, the investigation of binary zirconium alloys containing copper or vanadium is of interest. These two alloying elements are expected to form precipitates, which cannot fulfil both criteria predicting the precipitate oxidation behaviour for all already characterised precipitate types (both exhibit a similar free energy of oxide formation per oxygen molecule). To investigate if a fixed critical free energy of oxide formation exists, at which the oxidation behaviour changes, precipitates with a free energy of oxide formation between that of $ZrCr_2$ and Zr_2Ni should be tested. These two binary intermetallics exhibit the least difference in free energy of oxide formation and dissimilar oxidation behaviour according to the performed calculations. Possible precipitates which are predicted to have a free energy of oxide formation between $ZrCr_2$ and Zr_2Ni are ZrV_2 and Zr_2Cu (with same predicted free energy of oxide formation per oxygen molecule), additionally $Zr(V,Cr)_2$ with different Cr to V ratio to cover the range between both types of precipitates.

13 References

1. S. Kass, *The Development of the Zircalloys*. ASTM STP **368**, 1964, p. 3-27.
2. H.A. Porte, J.G. Schnizlein, R.C. Vogel and D.F. Fischer, *Oxidation of Zirconium and Zirconium Alloys*. Journal of the Electrochemical Society **107**, 1960 (6), p. 506-515.
3. D.E. Thomas, *The metallurgy of zirconium*, B. Lustman and F. Kerze, Editors, 1955, McGraw-Hill: New York, p. 608-640.
4. P. Chemelle, D.B. Knorr, J.B. Van Der Sande and R.M. Pelloux, *Morphology and composition of second phase particles in Zircaloy-2*. Journal of Nuclear Materials **113**, 1983 (1), p. 58-64.
5. G.P. Sabol, G.R. Kilp, M.G. Balfour and E. Roberts, *Development of a Cladding Alloy for High Burnup*. ASTM STP **1023**, 1989, p. 227-244.
6. M. Harada, M. Kimpara and K. Abe, *Effect of Alloying Elements on Uniform Corrosion Resistance of Zirconium-based Alloys in 360°C Water and 400°C Steam*. ASTM STP **1132**, 1991, p. 368-391.
7. F. Garzarolli, H. Stehle and E. Steinberg, *Behavior and Properties of Zircalloys in Power Reactors: A Short Review of Pertinent Aspects in LWR Fuel*. ASTM STP **1295**, 1996, p. 12-32.
8. A.T. Motta, A. Yilmazbayhan, M.J.G. da Silva, R.J. Comstock, G.S. Was, J.T. Busby, E. Gartner, Q. Peng, Y.H. Jeong and J.Y. Park, *Zirconium alloys for supercritical water reactor applications: Challenges and possibilities*. Journal of Nuclear Materials **371**, 2007 (1-3), p. 61-75.
9. J.Y. Park, B.K. Choi, S.J. Yoo and Y.H. Jeong, *Corrosion behavior and oxide properties of Zr-1.1wt%Nb-0.05wt%Cu alloy*. Journal of Nuclear Materials **359**, 2006 (1-2), p. 59-68.
10. P. Barberis, E. Ahlberg, N. Simic, D. Charquet, C. Lemaignan, G. Wikmark, M. Dahlbäck, M. Limbäck, P. Tägström and B. Lehtinen, *Role of the Second-Phase Particles in Zirconium Binary Alloys*. ASTM STP **1423**, 2002, p. 33-55.
11. E.R. Bradley and A.-L. Nyström, *Microstructure and Properties of Corrosion-Resistant Zirconium-Tin-Iron-Chromium-Nickel-Alloys*. ASTM STP **1245**, 1994, p. 483-498.
12. D. Charquet, *Improvement of the uniform corrosion resistance of Zircaloy-4 in the absence of irradiation*. Journal of Nuclear Materials **160**, 1988 (2-3), p. 186-195.
13. R.A. Graham and C.M. Eucken, *Controlled Composition Zircaloy-2 Uniform Corrosion Resistance*. ASTM STP **1132**, 1991, p. 279-303.
14. E.R. Bradley, J.H. Schemel and A.-L. Nyström, *Influence of Alloy Composition and Processing on the Nodular Corrosion Resistance of Zircaloy-2*. ASTM STP **1132**, 1991, p. 304-318.
15. B.L. Eyre and J.R. Matthews, *Technological impact of microstructural evolution during irradiation*. Journal of Nuclear Materials **205**, 1993, p. 1-15.
16. B. Lustman and F. Kerze, *The metallurgy of zirconium* 1955, New York: McGraw-Hill.
17. J.-P. Mardon, P. Barbéris and P.B. Hoffmann, *Un demi-siècle de développement des alliages de zirconium*. Revue Générale Nucléaire **4**, 2008, p. 38-47.
18. A.V. Nikulina, *Zirconium-Niobium Alloys for Core Elements of Pressurized Water Reactors*. Metal Science and Heat Treatment **45**, 2003 (7), p. 287-292.
19. J.H. Baek and Y.H. Jeong, *Breakaway phenomenon of Zr-based alloys during a high-temperature oxidation*. Journal of Nuclear Materials **372**, 2008 (2-3), p. 152-159.
20. IAEA, *Waterside corrosion of zirconium alloys in nuclear power plants*. IAEA-TECDOC, Vol. 996 1998.
21. T. Isobe, T. Murai and Y. Mae, *Anodic Protection Provided by Precipitates in Aqueous Corrosion of Zircaloy*. ASTM STP **1295**, 1996, p. 203-217.

22. B. Wadman, *Mechanisms of uniform corrosion of zirconium alloys in water and steam*, in *Department of Physics*. 1993, Chalmers University of Technology: Göteborg Sweden.
23. F. Garzarolli, E. Steinberg and H.G. Weidinger, *Microstructure and Corrosion Studies for Optimized PWR and BWR Zircaloy Cladding*. ASTM STP **1023**, 1989, p. 202-212.
24. F. Garzarolli and R. Holzer, *Waterside Corrosion Performance of Light Water Power-Reactor Fuel*. Nuclear Energy-Journal of the British Nuclear Energy Society **31**, 1992 (1), p. 65-85.
25. D. Charquet, E. Steinberg and Y. Millet, *Influence of Variations in Early Fabrication Steps on Corrosion, Mechanical, and Structure of Zircaloy-4 Products*. ASTM STP **939**, 1987, p. 431-447.
26. H.G. Weidinger, F. Garzarolli, C.M. Eucken and E.F. Baroch, *Effect of Chemistry on Elevated Temperature Nodular Corrosion*. ASTM STP **939**, 1987, p. 364-386.
27. T. Andersson, T. Thorvaldsson, A. Wilson and A.M. Wardle, *Influence of Thermal Processing and Microstructure on the Corrosion Behaviour of Zircaloy-4 Tubing*, in *IAEA Int. Symp. on Improvements in Water Reactor Fuel Technology and Utilization*. 1987, IAEA: Stockholm, p. 435-449.
28. J.P. Gros and J.F. Wadier, *Precipitate growth kinetics in Zircaloy-4*. Journal of Nuclear Materials **172**, 1990 (1), p. 85-96.
29. L.F.P. van Swam and S.H. Shann, *The Corrosion of Zircalloy-4 Fuel Cladding in Pressurized Water Reactors*. ASTM STP **1132**, 1991, p. 758-781.
30. R.M. Kruger, R.B. Adamson and S.S. Brenner, *Effects of microchemistry and precipitate size on nodular corrosion resistance of Zircaloy-2*. Journal of Nuclear Materials **189**, 1992 (2), p. 193-200.
31. A. Strasser and M.G. Andrews, *Fundamental Aspects of Corrosion of Zirconium Base Alloys in Water Reactor Environments*, in *IAEA Technical Committee Meeting on Fundamental Aspects of Corrosion of Zirconium Base Alloys in Water Reactor Environments*. 1989, IAEA IWGFPT: Portland, Oregon, p. 88-98.
32. M.M. Stupel, M. Bamberger and B.Z. Weiss, *Determination of Fe Solubility in Alpha-Zr by Mössbauer-Spectroscopy*. Scripta Metallurgica **19**, 1985 (6), p. 739-740.
33. B. Wadman, U. Rolander and H.O. Andren, *Matrix Composition of Zircaloy-4*. Journal De Physique **48**, 1987 (C-6), p. 299-304.
34. K. Loucif, R. Borrelly and P. Merle, *Study by thermoelectric power and resistivity measurements of the precipitation kinetics in zirconium alloys between 450 and 600°C*. Journal of Nuclear Materials **189**, 1992 (1), p. 34-45.
35. R. Borrelly, P. Merle and L. Adami, *Study of the solubility of iron in zirconium by thermoelectric power measurements*. Journal of Nuclear Materials **170**, 1990 (2), p. 147-156.
36. D. Charquet, R. Hahn, E. Ortlieb, J.-P. Gros and J.-F. Wadier, *Solubility Limits and Formation of Intermetallic Precipitates in ZrSnFeCr Alloys*. ASTM STP **1023**, 1989, p. 405-422.
37. E. Vitikainen and P. Nenonen, *Transmission electron microscopy studies on intermetallics in some zirconium alloys*. Journal of Nuclear Materials **78**, 1978 (2), p. 362-373.
38. R.A. Versaci and M. Ipohorski, *Polytype structure of intermetallic precipitates in zircaloy-4 alloys*. Journal of Nuclear Materials **80**, 1979 (1), p. 180-183.
39. J.B. van der Sande and A.L. Bement, *An investigation of second phase particles in Zircaloy-4 alloys*. Journal of Nuclear Materials **52**, 1974 (1), p. 115-118.
40. J.M. Grange, D. Charquet and L. Moulin, *New Intermetallic Compounds in Zircaloy-4*. ASTM STP **754**, 1982, p. 96-104.

41. X.Y. Meng and D.O. Northwood, *Intermetallic precipitates in Zircaloy-4*. Journal of Nuclear Materials **132**, 1985 (1), p. 80-87.
42. X.Y. Meng and D.O. Northwood, *A TEM study of the C15 type Zr(CrFe)₂ Laves phase in Zircaloy-4*. Journal of Nuclear Materials **136**, 1985 (1), p. 83-90.
43. G.M. Hood, *Point defect diffusion in α -Zr*. Journal of Nuclear Materials **159**, 1988, p. 149-175.
44. G.M. Hood and R.J. Schultz, *Tracer Diffusion in Alpha-Zr*. Acta Metallurgica **22**, 1974 (4), p. 459-464.
45. J. Räsänen and J. Keinonen, *Diffusion of Al in ion-implanted α -Zr and α -Hf*. Applied Physics A: Materials Science & Processing **36**, 1985 (4), p. 175-178.
46. G.M. Hood and R. Schultz, *Diffusion of 3D Transition Metals in α -Zr and Zirconium Alloys*. ASTM STP **1023**, 1989, p. 435-450.
47. O.T. Woo and K. Tangri, *Transformation characteristics of rapidly heated and quenched Zircaloy-4-oxygen alloys*. Journal of Nuclear Materials **79**, 1979 (1), p. 83-94.
48. C.E. Lundin and R.H. Cox, in *USAEC Report*. 1962, p. 9.
49. D. Charquet, *Influence of precipitates on the corrosion of Zircaloy-4 in 400°C steam*. Journal of Nuclear Materials **211**, 1994 (3), p. 259-261.
50. Y.H. Jeong, H.G. Kim and T.H. Kim, *Effect of β phase, precipitate and Nb-concentration in matrix on corrosion and oxide characteristics of Zr-xNb alloys*. Journal of Nuclear Materials **317**, 2003 (1), p. 1-12.
51. V.F. Urbanic, B.D. Warr, A. Manolescu, C.K. Chow and M.W. Shanahan, *Oxidation and Deuterium Uptake of Zr-2.5Nb Pressure Tubes in CANDU-PHW Reactors*. ASTM STP **1023**, 1989, p. 20-34.
52. Y.H. Jeong, H.G. Kim, D.J. Kim, B.K. Choi and J.H. Kim, *Influence of Nb concentration in the α -matrix on the corrosion behavior of Zr-xNb binary alloys*. Journal of Nuclear Materials **323**, 2003 (1), p. 72-80.
53. H.-G. Kim, J.-Y. Park and Y.-H. Jeong, *Phase boundary of the Zr-rich region in commercial grade Zr-Nb alloys*. Journal of Nuclear Materials **347**, 2005 (1-2), p. 140-150.
54. J.-Y. Park, S.J. Yoo, B.-K. Choi and Y.H. Jeong, *Oxide microstructures of advanced Zr alloys corroded in 360°C water loop*. Journal of Alloys and Compounds **437**, 2007 (1-2), p. 274-279.
55. H.-G. Kim, J.-Y. Park and Y.-H. Jeong, *Ex-reactor corrosion and oxide characteristics of Zr-Nb-Fe alloys with the Nb/Fe ratio*. Journal of Nuclear Materials **345**, 2005 (1), p. 1-10.
56. C. Toffolon-Masclat, J.-C. Brachet and G. Jago, *Studies of second phase particles in different zirconium alloys using extractive carbon replica and an electrolytic anodic dissolution procedure*. Journal of Nuclear Materials **305**, 2002 (2-3), p. 224-231.
57. J.A. Sawicki, *Mossbauer spectroscopy of tin in unirradiated and neutron irradiated Zircalloys*. Journal of Nuclear Materials **264**, 1999 (1-2), p. 169-179.
58. R.F. Voitvoich and E.I. Golovko, *Oxidation of intermetallic phases containing titanium, zirconium and hafnium*. Soviet Powder Metallurgy and Metal Ceramics **4**, 1978, p. 61-72.
59. H.G. Weidinger, H. Ruhmann, G. Cheliotis, M. Maguire and T.L. Yau, *Corrosion-Electrochemical Properties of Zirconium Intermetallics*. ASTM STP **1132**, 1991, p. 499-535.
60. B.J. Herb, J.M. McCarthy, C.T. Wang and H. Ruhmann, *Correlation of Transmission Electron Microscopy (TEM) Microstructure Analysis and Texture with Nodular Corrosion behaviour for Zircaloy-2*. ASTM STP **1245**, 1994, p. 709-723.

61. H. Zou, G. Hood, J. Roy and R. Schultz, *Formation and stability of Fe-rich precipitates in dilute Zr(Fe) single-crystal alloys*. Metallurgical and Materials Transactions A **25**, 1994 (7), p. 1359-1365.
62. V.P. Filippov, *Potentialities of Mossbauer spectroscopy for studying zirconium alloys and their oxide films*. Metal Science and Heat Treatment **45**, 2003 (11-12), p. 452-460.
63. F. Aubertin, U. Gonser, S.J. Campbell and H.G. Wagner, *An Appraisal of the Phases of the Zirconium-Iron System*. Zeitschrift für Metallkunde **76**, 1985 (4), p. 237-244.
64. R.A. Ploc, *Oxidation Kinetics and Auger Microprobe Analysis of Some Oxidized Zirconium Alloys*. ASTM STP **1023**, 1988, p. 498-514.
65. L.M. Howe, D. Phillips, H.H. Plattner and J.D. Bonnett, *Collision Cascades in Zr₂Fe, Zr₃Fe and ZrFe₂*. Nuclear Instruments & Methods in Physics Research Section B **102**, 1995 (1-4), p. 77-80.
66. A.T. Motta, L.M. Howe and P.R. Okamoto, *Amorphization kinetics of Zr₃Fe under electron irradiation*. Journal of Nuclear Materials **205**, 1993, p. 258-266.
67. F. Stein, G. Sauthoff and M. Palm, *Experimental determination of intermetallic phases, phase equilibria, and invariant reaction temperatures in the Fe-Zr system*. Journal of Phase Equilibria **23**, 2002 (6), p. 480-494.
68. F. Shunk, *Constitution of binary alloys - 2nd Supplement 1969*, New York: McGraw-Hill.
69. A. Grandjean and Y. Serruys, *Metal and oxygen mobilities during Zircaloy-4 oxidation at high temperature*. Journal of Nuclear Materials **273**, 1999 (1), p. 111-115.
70. P. Rudling and G. Wikmark, *A unified model of Zircaloy BWR corrosion and hydriding mechanisms*. Journal of Nuclear Materials **265**, 1999 (1-2), p. 44-59.
71. D.H. Bradhurst, J.E. Draley and Vandrone.C.J., *An Electrochemical Model for Oxidation of Zirconium*. Journal of the Electrochemical Society **112**, 1965 (12), p. 1171-1177.
72. H. Beie, A. Mitwalski, F. Garzarolli and H. Ruhmann, *Examinations of the Corrosion Mechanism of Zirconium Alloys*. ASTM STP **1245**, 1993, p. 615-643.
73. U. Döbler, A. Knop, H. Ruhmann and H.-J. Beie, *On the Initial Corrosion Mechanism of Zirconium Alloy: Interaction of Oxygen and Water with Zircaloy at Room Temperature and 450°C Evaluated by X-Ray Absorption Spectroscopy and Photoelectron Spectroscopy*. ASTM STP **1023**, 1989, p. 644-662.
74. B. Hutchinson and B. Lehtinen, *A theory of the resistance of Zircaloy to uniform corrosion*. Journal of Nuclear Materials **217**, 1994 (3), p. 243-249.
75. B. Cox, *Corrosion of Zirconium and its Alloys*, M.G. Fontana and R.W. Staehle, Editors, 1976, Plenum Press: New York, p. 173-391.
76. B. Cox, *Some thoughts on the mechanisms of in-reactor corrosion of zirconium alloys*. Journal of Nuclear Materials **336**, 2005 (2-3), p. 331-368.
77. IAEA, *Corrosion of zirconium alloys in nuclear power plants*. IAEA-TECDOC, Vol. 684 1993.
78. G.P. Sabol, R.J. Comstock, R.A. Weiner, P. Larouere and R.N. Stanutz, *In-Reactor Corrosion Performance of ZIRLO and Zircaloy-4*. ASTM STP **1245**, 1994, p. 724-744.
79. G.R. Kilp, D.R. Thornburg and R.J. Comstock, *Improvement in zirconium alloy corrosion resistance, in Fundamental Aspects of Corrosion of Zirconium Base Alloys in Water Reactor Environments*, 1990: IWGFPT/34 IAEA, Vienna, p. 145-157.
80. W.E. Berry, D.A. Vaughan and E.L. White, *Hydrogen Pickup During Aqueous Corrosion of Zirconium Alloys*. Corrosion **17**, 1961, p. 109-117.
81. B. Cox, *Effect of Hydrogen Injection on Hydrogen Uptake by BWR Fuel Cladding*. 1983, EPRI-NP-3146: Palo Alto, CA.

82. A.R. Massih and P. Rudling, *Corrosion behavior of Zircaloy-2 and Zircaloy-4 Claddings in Pressurized water reactors*, in *ANS International Topical Meeting on Light Water Reactor Fuel Performance*. 1991: Avignon, France, p. 716-729.
83. ASTM, *Standard Test Method for Corrosion Testing of Products of Zirconium, Hafnium, and Their Alloys in Water at 680°F [360°C] or in Steam at 750°F [400°C]*, in *ASTM G2/G 2M - 06* 2006.
84. D.G. Franklin and P.M. Lang, *Zirconium-Alloy Corrosion: A Review Based on an International Atomic Energy Agency (IAEA) Meeting*. ASTM STP **1132**, 1991, p. 3-32.
85. B. Cox and C. Wu, *Dissolution of zirconium oxide films in 300°C LiOH*. *Journal of Nuclear Materials* **199**, 1993 (3), p. 272-284.
86. A.M. Garde, *Enhancement of Aqueous Corrosion of Zircaloy-4 due to Hydride Precipitation at the Metal-Oxide Interface*. ASTM STP **1132**, 1991, p. 566-594.
87. S. Leistikow and H.V. Berg. *Investigation under nuclear safety aspects of Zircaloy-4 oxidation kinetics at high temperatures in air*. in *Proceeding of the 2nd Workshop of German and Polish Research on High Temperature Corrosion of Metals*, 1987. Julich.
88. T. Arima, K. Miyata, K. Idemitsu and Y. Inagaki, *Oxidation properties of Zr-Nb alloys at 973-1273 K in air*. *Progress in Nuclear Energy* **51**, 2009 (2), p. 307-312.
89. C. Duriez, T. Dupont, B. Schmet and F. Enoch, *Zircaloy-4 and M5 (R) high temperature oxidation and nitriding in air*. *Journal of Nuclear Materials* **380**, 2008 (1-3), p. 30-45.
90. M. Steinbruck, *Prototypical experiments relating to air oxidation of Zircaloy-4 at high temperatures*. *Journal of Nuclear Materials* **392**, 2009 (3), p. 531-544.
91. B. de Gelas, G. Beranger and P. Lacombe, *L'oxydation a haute temperature du zirconium et de ses alliages binaire A faible teneur en element d'addition*. *Journal of Nuclear Materials* **29**, 1969 (1), p. 1-26.
92. E.A. Gulbransen and K.F. Andrew, *Kinetics of the Reactions of Zirconium with O₂, N₂ and H₂*. *Transactions of the American Institute of Mining, Metallurgical and Petroleum Engineers* **185**, 1949 (8), p. 515-525.
93. H. Göhr, J. Schaller, H. Ruhmann and F. Garzarolli, *Long-term in situ corrosion investigation of Zr alloys in simulated PWR environment by electrochemical measurements*. ASTM STP **1295**, 1996, p. 181-202.
94. E.S. Sarkisov, N.T. Chebotarev, A.A. Nevzorova and A.I. Zver'kov, *Oxidation of zirconium at high temperature and structure of the primary oxide film*. *Atomic Energy* **5**, 1958 (5), p. 1465-1470.
95. P. Kofstad, *High temperature corrosion* 1988, New York, USA: Elsevier Applied Science.
96. H. Arashi, T. Yagi, S. Akimoto and Y. Kudoh, *New High-Pressure Phase of ZrO₂ above 35-GPa*. *Physical Review B* **41**, 1990 (7), p. 4309-4313.
97. J.M. Leger, P.E. Tomaszewski, A. Atouf and A.S. Pereira, *Pressure-Induced Structural Phase-Transitions in Zirconia under High-Pressure*. *Physical Review B* **47**, 1993 (21), p. 14075-14083.
98. M. Inagaki, M. Kanno and H. Maki, *Effect of Alloying Elements in Zircaloy on Photo-Electrochemical Characteristics of Zirconium Oxide Films*. ASTM STP **1132**, 1991, p. 437-460.
99. M. Tupin, F. Valdivieso, M. Pijolat, M. Soustelle, A. Frichet and P. Barberis, *Kinetic study of the oxidation by oxygen of a zirconium based alloy: ZrNbO differences between the pre- and post-transition stages*. *High Temperature Corrosion and Protection of Materials* 6, Prt 1 and 2, *Proceedings* **461-464**, 2004, p. 13-20.
100. J.L. Whitton, *Measurement of Ionic Mobilities in Anodic Oxides of Tantalum and Zirconium by a Precision Sectioning Technique*. *Journal of the Electrochemical Society* **115**, 1968 (1), p. 58-61.

101. C.S. Zhang, B.J. Flinn, I.V. Mitchell and P.R. Norton, *The Initial Oxidation of Zr(0001) - 0 to 0.5 Monolayers*. Surface Science **245**, 1991 (3), p. 373-379.
102. P. Steiner, I. Sander, B. Siegwart and S. Hüfner, *Oxidation of Zr and thin (0.2-4nm) Zr films on AG: An ESCA Investigation*. Fresenius Z Anal. Chem. **329**, 1987, p. 272-277.
103. M.C. Deibert, B.P. Thiesen and R. Kahraman, *Investigation by Auger spectroscopy of the composition and surface oxidation characteristics of oxygen saturated zirconium*. Applied Surface Science **35**, 1989 (3), p. 302-316.
104. B. Holmberg and T. Dagerhamn, *X-ray Studies on Solid Solutions of Oxygen in α -Zirconium*. Acta Chemica Scandinavica **15**, 1961, p. 919-925.
105. C.S. Zhang, B.J. Flinn and P.R. Norton, *The Kinetics of Oxidation and Oxide-Growth Mechanisms on Zr(0001)*. Surface Science **264**, 1992 (1-2), p. 1-9.
106. K. Östhagen and P. Kofstad, *Oxidation of Zirconium and Zirconium-Oxygen Alloys at 800°C*. Journal of the Electrochemical Society **109**, 1962 (3), p. 204-207.
107. T. Ericsson, G. Östberg and B. Lehtinen, *Some observations on Zr-O solid solutions with a microprobe and by electron microscopy*. Journal of Nuclear Materials **25**, 1968 (3), p. 322-327.
108. G. Beranger and P. Lacombe, *Contribution a l'etude de la cinetique de l'oxydation du zirconium α et de la diffusion de l'oxygene dans le metal sous-jacent a l'oxyde*. Journal of Nuclear Materials **16**, 1965 (2), p. 190-207.
109. B. Cox and C. Roy, *Transport of Oxygen in Oxide Films on Zirconium Determined by Nuclear Reaction $O^{17} (He^3, \alpha)O^{16}$* . Electrochemical Technology **4**, 1966 (3-4), p. 121-127.
110. C.O. Degonzalez and E.A. Garcia, *Determination of the Diffusion-Coefficients of Oxygen in Zirconium by Means of Xps*. Applied Surface Science **44**, 1990 (3), p. 211-219.
111. I.G. Ritchie and A. Atrens, *The diffusion of oxygen in α -zirconium*. Journal of Nuclear Materials **67**, 1977 (3), p. 254-264.
112. J.P. Pemsler, *Studies on the oxygen gradients in corroding zirconium alloys*. Journal of Nuclear Materials **7**, 1962 (1), p. 16-25.
113. G.R. Wallwork, W.W. Smeltzer and C.J. Rosa, *Parabolic Oxidation Kinetics of Alpha-Zirconium at 850°C*. Acta Metallurgica **12**, 1964 (4), p. 409-415.
114. S. Abolhassani, G. Bart and A. Jakob, *Examination of the chemical composition of irradiated zirconium based fuel claddings at the metal/oxide interface by TEM*. Journal of Nuclear Materials **399**, 2010 (1), p. 1-12.
115. X. Iltis and H. Michel, *Transmission Electron-Microscopy Study of a Locally Ordered Zr-O Solid-Solution Obtained by an Oxidation Treatment of a Zircaloy-4 Alloy*. Journal of Alloys and Compounds **177**, 1991 (1), p. 71-82.
116. A. Motta, A. Yilmazbayhan, R.J. Comstock, J. Partezana, G.P. Sabol, B. Lai and Z. Cai, *Microstructure and Growth Mechanism of Oxide Layers Formed on Zr Alloys Studied with Micro-Beam Synchrotron Radiation*. Journal of ASTM International **2**, 2005 (5), p. 205-232.
117. A. Yilmazbayhan, E. Breval, A.T. Motta and R.J. Comstock, *Transmission electron microscopy examination of oxide layers formed on Zr alloys*. Journal of Nuclear Materials **349**, 2006 (3), p. 265-281.
118. Y. Maeno, M. Yamamoto, S. Naito, M. Mabuchi and T. Hashino, *Change in the Work Function of Zirconium by Oxidation at High-Temperatures and Low Oxygen Pressures*. Journal of the Chemical Society-Faraday Transactions **87**, 1991 (9), p. 1399-1403.
119. C. Morant, J.M. Sanz, L. Galan, L. Soriano and F. Rueda, *An XPS Study of the Interaction of Oxygen with Zirconium*. Surface Science **218**, 1989 (2-3), p. 331-345.

120. K.O. Axelsson, K.E. Keck and B. Kasemo, *AES and EEL spectra from Zr, Zr + O₂ and ZrO₂; peak energy shifts and intensity variations at various stages of oxidation in the pressure range 10⁻⁶-10³ Torr*. *Surface Science* **164**, 1985 (1), p. 109-126.
121. G.R. Corallo, D.A. Asbury, R.E. Gilbert and G.B. Hoflund, *Electron-Energy-Loss Study of Clean and Oxygen-Exposed Polycrystalline Zirconium*. *Physical Review B* **35**, 1987 (18), p. 9451-9459.
122. J.M. Sanz, C. Palacio, Y. Casas and J.M. Martinezduart, *An AES Study of the Oxidation of Polycrystalline Zirconium at Room-Temperature and Low Oxygen Pressures*. *Surface and Interface Analysis* **10**, 1987 (4), p. 177-183.
123. R.L. Tapping, R.D. Davidson, T.E. Jackman and J.A. Davies, *Effect of Analytical Method on Thickness Measurements of Thin Oxide-Films*. *Surface and Interface Analysis* **11**, 1988 (8), p. 441-446.
124. T. Tanabe, M. Tanaka and S. Imoto, *AES and XPS Studies of Oxygen Stabilized Alpha-Zirconium*. *Surface Science* **187**, 1987 (2-3), p. 499-510.
125. M. Yamamoto, S. Naito, M. Mabuchi and T. Hashino, *Kinetics of Oxygen Absorption by Alpha-Zirconium*. *Journal of Physical Chemistry* **93**, 1989 (13), p. 5203-5209.
126. M. Tomita, T. Tanabe and S. Imoto, *An AES Study of Surface Oxidation of Zirconium*. *Surface Science* **209**, 1989 (1-2), p. 173-182.
127. R.L. Tapping and P.R. Norton, *X-Ray and Uv Photoelectron Spectroscopic Study of Implanted and Adsorbed Xenon on Nickel (100) and (111) Surfaces*. *Chemical Physics Letters* **41**, 1976 (2), p. 252-256.
128. T. Tanabe and M. Tomita, *Surface Oxidation of Zirconium above Room-Temperature*. *Surface Science* **222**, 1989 (1), p. 84-94.
129. U. Döbler, A. Knop, H. Ruhmann and H.-J. Beie, *On the Initial Corrosion Mechanism of Zirconium Alloy: Interaction of Oxygen and Water with Zircaloy at Room Temperature and 450°C Evaluated by X-Ray Absorption Spectroscopy and Photoelectron Spectroscopy*. *ASTM STP* **1245**, 1994, p. 644-662.
130. S. Abolhassani, R. Schäublin, F. Groeschel and G. Bart, *AEM and HRTEM analysis of the metal-oxide interface of Zircaloy-4, prepared by FIB*, in *Proceeding of Microscopy and Microanalysis*. 2001: Long Beach, California, USA, p. 250-251.
131. B. Cox, *The Zirconium-Zirconia Interface*. *Journal of the Australian Institute of Metals* **14**, 1969 (3), p. 123-131.
132. A.W. Urquhart and D.A. Vermilyea, *Characterization of Zircaloy Oxidation Films*. *ASTM STP* **551**, 1974, p. 463-478.
133. A. Yilmazbayhan, A.T. Motta, R.J. Comstock, G.P. Sabol, B. Lai and Z. Cai, *Structure of zirconium alloy oxides formed in pure water studied with synchrotron radiation and optical microscopy: relation to corrosion rate*. *Journal of Nuclear Materials* **324**, 2004 (1), p. 6-22.
134. J.S. Bryner, *The cyclic nature of corrosion of Zircaloy-4 in 633 K water*. *Journal of Nuclear Materials* **82**, 1979 (1), p. 84-101.
135. A.J. Maroto, R. Bordoni, M. Villegas, A.M. Olmedo, M. Blesa, A. Iglesias and P. Koenig, *Growth and characterization of oxide layers on zirconium alloys*. *Journal of Nuclear Materials* **229**, 1996 (1), p. 79-92.
136. M. Oskarsson, *Study on the mechanisms for corrosion and hydriding of Zircaloy*, in *Materials Science and Engineering*. 2000, Kungliga Tekniska Högskolan: Stockholm, Sweden.
137. D. Pecheur, J. Godlewski, J. Peybernes and L. Fayette, *Contribution to the Understanding of the Effect of the Water Chemistry on the Oxidation Kinetics of Zircaloy-4 Cladding*. *ASTM STP* **1354**, 2000, p. 793-814.

138. P. Bossis, J. Thomazet and F. Lefebvre, *Study of the Mechanisms Controlling the Oxide Growth Under Irradiation: Characterization of Irradiated Zircaloy-4 and Zr-1Nb-O Oxide Scales*. ASTM STP **1423**, 2002, p. 190-221.
139. G.P. Airey and G.P. Sabol, *Transmission electron microscopy of ion-thinned oxides formed during corrosion of zircaloy-4*. Journal of Nuclear Materials **45**, 1972 (1), p. 60-62.
140. G.P. Sabol, S.G. McDonald and G.P. Airey, *Microstructure of the Oxide Films Formed on Zirconium-Based Alloys*. ASTM STP **551**, 1974, p. 435-448.
141. Lightstone and J.P. Pemsler, *Considerations on the Atomistics of Oxidation*, in *Kinetics of reactions in ionic systems: proceedings of an International Symposium on Special Topics in Ceramics, held June 18-23, 1967, at Alfred University, Alfred, New York*, D. van Frechette and T.J. Gray, Editors. 1969, Plenum Press: New York.
142. B. Wadman, Z. Lai, H.-O. Andrén, A.-L. Nyström, P. Rudling and H. Pettersson, *Microstructure of Oxide Layers Formed During Autoclave Testing of Zirconium Alloys*. ASTM STP **1245**, 1994, p. 579.
143. V.F. Urbanic, P.K. Chan, D. Khatamian and O.T. Woo, *Growth and Characterization of Oxide Films on Zirconium-Niobium Alloys*. ASTM STP **1245**, 1994, p. 116-132.
144. Y. Ding and D.O. Northwood, *The formation of a barrier oxide layer on a Zr-2.5wt.%Nb alloy during corrosion in high temperature pressurized water*. Journal of Alloys and Compounds **187**, 1992 (2), p. 317-330.
145. Y. Ding and D.O. Northwood, *TEM study of the oxide-metal interface formed during corrosion of Zr-2.5wt.%Nb pressure tubing*. Materials Characterization **30**, 1993 (1), p. 13-22.
146. M.B. Elmoselhi, B.D. Warr and S. McIntyre, *A Study of the Hydrogen Uptake Mechanism in Zirconium Alloys*. ASTM STP **1245**, 1994, p. 62-79.
147. H. Stehle, F. Garzarolli, A.M. Garde and P.G. Smerd, *Characterization of ZrO₂ Films Formed In-Reactor and Ex-Reactor to Study the Factors Contributing to the In-Reactor Waterside Corrosion of Zircaloy*. ASTM STP **824**, 1984, p. 483-506.
148. P.M. Rosencrans, *Application of Alternating-Current Impedance Measurements to Characterize Zirconium Alloy Oxidation Films*. ASTM STP **824**, 1984, p. 531-553.
149. F. Garzarolli, H. Seidel, R. Tricot and J.-P. Gros, *Oxide Growth Mechanism on Zirconium Alloys*. ASTM STP **1132**, 1991, p. 395-415.
150. O. Gebhardt, *Investigation of in-pile formed corrosion films on Zircaloy fuel rod claddings by impedance spectroscopy and galvanostatic anodization*. Journal of Nuclear Materials **203**, 1993 (1), p. 17-26.
151. B. Cox, *Pore structure in oxide films on irradiated and unirradiated zirconium alloys*. Journal of Nuclear Materials **148**, 1987 (3), p. 332-343.
152. B.D. Warr, M.B. Elmoselhi, S.B. Newcomb, N.S. McIntyre, A.M. Brennenstuhl and P.C. Lichtenberger, *Oxide Characteristics and Their Relationship to Hydrogen Uptake in Zirconium Alloys*. ASTM STP **1132**, 1991, p. 740-757.
153. J. Lin, H. Li, J.A. Szpunar, R. Bordoni, A.M. Olmedo, M. Villegas and A.J.G. Maroto, *Analysis of zirconium oxide formed during oxidation at 623 K on Zr-2.5Nb and Zircaloy-4*. Materials Science and Engineering A **381**, 2004 (1-2), p. 104-112.
154. Y.P. Lin, O.T. Woo and D.J. Lockwood, *Texture and Phases in Oxide Films on Zr-Nb Alloys*, in *Mat. Res. Soc. Symp. Proc.* 1994, p. 487-492.
155. H. Anada and K. Takeda, *Microstructure of Oxides on Zircaloy-4. 1.0Nb Zircaloy-4 and Zircaloy-2 Formed in 10.3-MPa Steam at 673 K*. ASTM STP **1295**, 1996, p. 35-54.
156. P. Barberis, *Zirconia powders and Zircaloy oxide films: tetragonal phase evolution during 400 °C autoclave tests*. Journal of Nuclear Materials **226**, 1995 (1-2), p. 34-43.

157. J. Godlewski, *How the Tetragonal Zirconia is Stabilized in the Oxide Scale that is Formed on a Zirconium Alloy Corroded at 400°C in Steam*. ASTM STP **1245**, 1994, p. 663-686.
158. J. Godlewski, J.-P. Gros, M. Lambertin, J.-F. Wadier and H.G. Weidinger, *Raman Spectroscopy Study of the Tetragonal-to-Monoclinic Transition in Zirconium Oxide Scales and Determination of Overall Oxygen Diffusion by Nuclear Microanalysis of O18*. ASTM STP **1132**, 1991, p. 416-436.
159. T. Jacquot, R. Guillon, M. Francois, B. Bourniquel and J. Senevat, *Residual Stress of Monoclinic Zircon Obtained by X-Ray Diffraction in ZY4 Oxidized Cladding Tubes*. Materials Science Forum **228**, 1996, p. 845-850.
160. M. Parise, O. Sicardy and G. Cailletaud, *Modelling of the mechanical behavior of the metal-oxide system during Zr alloy oxidation*. Journal of Nuclear Materials **256**, 1998 (1), p. 35-46.
161. B. Cox, *Low temperature (< 300°C) oxidation of Zircaloy-2 in water*. Journal of Nuclear Materials **25**, 1968 (3), p. 310-321.
162. S. Abolhassani, R. Restani, T. Rebac, F. Groeschel, W. Hoffelner, G. Bart, W. Goll and F. Aeschbach, *TEM Examinations of the Metal-Oxide Interface of Zirconium Based Alloys Irradiated in a Pressurized Water Reactor*. ASTM STP **1467**, 2006, p. 467-493.
163. M. Oskarsson, E. Ahlberg and K. Pettersson, *Dissolution of oxygen-enriched Zircaloy-2*. Journal of Nuclear Materials **298**, 2001 (3), p. 291-296.
164. G. Wikmark, P. Rudling, B. Lehtinen, B. Hutchinson, A. Oscarsson and E. Ahlberg, *The Importance of Oxide Morphology for the Oxidation Rate of Zirconium Alloys*. ASTM STP **1295**, 1996, p. 55-73.
165. H. Blank, G. Bart and H. Thiele, *Structural analysis of oxide scales grown on zirconium alloys in autoclaves and in a PWR*. Journal of Nuclear Materials **188**, 1992, p. 273-279.
166. B. Cox, *Chemical dissolution of ZrO₂ during oxide stripping*. Journal of Nuclear Materials **202**, 1993 (3), p. 286-291.
167. S. Abolhassani and P. Gasser, *Preparation of TEM samples of metal-oxide interface by the focused ion beam technique*. Journal of Microscopy **223**, 2006 (1), p. 73-82.
168. P. Bossis, F. Lefebvre, P. Barberis and A. Galerie, *Corrosion of zirconium alloys: Link between the metal/oxide interface roughness, the degradation of the protective oxide layer and the corrosion kinetics*. Materials Science Forum **369-372**, 2001 (), p. 255-262.
169. H. Anada, K.-i. Nomoto and Y. Shida, *Corrosion Behaviour of Zircaloy-4 Sheets Produced Under Various Hot-Rolling and Annealing Conditions*. ASTM STP **1245**, 1994, p. 307-327.
170. R.A. Ploc, *Transmission electron microscopy of thin (<2000 Å) thermally formed ZrO₂ films*. Journal of Nuclear Materials **28**, 1968 (1), p. 48-60.
171. J.N. Wanklyn, *Recent Studies on the Growth and Breakdown of Oxide Films on Zirconium and its Alloys*. ASTM STP **368**, 1964, p. 58-75.
172. R.A. Ploc, *A transmission electron diffraction study of ZrO₂ on α-Zr (0001)*. Journal of Nuclear Materials **110**, 1982 (1), p. 59-64.
173. R.A. Ploc, *Electron diffraction from ZrO₂ on α-Zr(1010)*. Journal of Nuclear Materials **115**, 1983 (1), p. 110-117.
174. R.A. Ploc, *Electron diffraction analysis of ZrO₂ on α-Zr(1120)*. Journal of Nuclear Materials **113**, 1983 (1), p. 75-80.
175. R.A. Ploc, *Transmission electron microscopy of α-ZrO₂ films formed in 573 K oxygen*. Journal of Nuclear Materials **61**, 1976 (1), p. 79-87.
176. N. Ramasubramanian, *Localised electron transport in corroding zirconium alloys*. Journal of Nuclear Materials **55**, 1975 (2), p. 134-154.

177. P.J. Shirvington, *Electron conduction through oxide films on Zircaloy-2*. Journal of Nuclear Materials **37**, 1970 (2), p. 177-202.
178. P.J. Shirvington and B. Cox, *A study of charge transport processes during the oxidation of zirconium alloys*. Journal of Nuclear Materials **35**, 1970 (2), p. 211-222.
179. D. Pecheur, F. Lefebvre, A.T. Motta, C. Lemaignan and J.F. Wadier, *Precipitate evolution in the Zircaloy-4 oxide layer*. Journal of Nuclear Materials **189**, 1992 (3), p. 318-332.
180. R.A. Ploc, *A Scanning Auger Microprobe Analysis of the Oxidation of a Zr₂Ni Alloy*. Journal of Nuclear Materials **165**, 1989 (2), p. 149-155.
181. R.A. Ploc and R.D. Davidson, *Auger Electron Analysis of Oxides grown on dilute Zirconium Alloys*, S.A. Shiels, et al., Editors. 1984, IMS: Philadelphia, p. 131-141.
182. R.A. Ploc and R.D. Davidson, *Auger Electron Analysis of Oxides grown on a dilute Zirconium/Nickel Alloy*, W. Katz and P. Williams, Editors. 1985, Materials Research Society: San Francisco, CA, p. 169-177.
183. D. Pecheur, F. Lefebvre, A.T. Motta, C. Lemaignan and D. Charquet, *Oxidation of Intermetallic Precipitates in Zircaloy-4: Impact of Radiation*. ASTM STP **1245**, 1994, p. 687-708.
184. D. Pecheur, *Oxidation of β -Nb and Zr(Fe,V)₂ precipitates in oxide films formed on advanced Zr-based alloys*. Journal of Nuclear Materials **278**, 2000 (2-3), p. 195-201.
185. D. Pecheur, F. Lefebvre and C. Lemaignan, *Oxidation Processes in Zircaloy*. Journal de Physique IV **3**, 1993 (C7), p. 503-507.
186. Y. Ishii and J.M. Sykes, *Microstructure of oxide layers formed on Zircaloy-2 in air at 450°C*. Materials at High Temperatures **17**, 2000 (1), p. 23-28.
187. T. Kubo and M. Uno, *Precipitate Behaviour in Zircaloy-2 Oxide Films and Its Relevance to Corrosion Resistance*. ASTM STP **1132**, 1991, p. 476-498.
188. E.R. Bradley and R.A. Perkins, *Characterisation of Zircaloy corrosion films by analytical transmission electron microscopy*, in *Fundamental Aspects of Corrosion of Zirconium Base Alloys in Water Reactor Environments*, 1990: IWGFPT/34 IAEA, Vienna, p. 101-106.
189. H. Anada, B.J. Herb, K. Nomoto, S. Hagi, R.A. Graham and T. Kuroda, *Effect of Annealing Temperature on Corrosion Behaviour and ZrO₂ Microstructure of Zircaloy-4 Cladding Tube*. ASTM STP **1295**, 1996, p. 74-93.
190. C. Li, R.L. Zuo, Z.K. Li, S.H. Ying and B.L. Shen, *Transmission electron microscopy investigation of Zr₂(Fe,Ni) particles incorporated in the oxide film formed on a Zirconium alloy*. Thin Solid Films **461**, 2004 (2), p. 272-276.
191. H. Anada, K. Takeda, S. Hagi, T. Murata, A. Oe and T. Miyashita, *Out-of-Pile Corrosion Behaviour and Corrosion Mechanism of NDA for High Burn-up Fuel of PWR*, in *Proceedings of the ANS International Topical Meeting on LWR Fuel Performance*, IAEA. 2000: Park City, p. 445-456.
192. Y.P. Lin and O.T. Woo, *Oxidation of β -Zr and related phases in Zr-Nb alloys: an electron microscopy investigation*. Journal of Nuclear Materials **277**, 2000 (1), p. 11-27.
193. H.G. Kim, B.K. Choi, J.Y. Park, H.D. Cho and Y.H. Jeong, *Analysis of oxidation behavior of the beta-Nb phase formed in Zr-1.5Nb alloy by using the HVEM*. Journal of Alloys and Compounds **481**, 2009 (1-2), p. 867-871.
194. X. Iltis, F. Lefebvre and C. Lemaignan, *Microstructural study of oxide layers formed on Zircaloy-4 in autoclave and in reactor Part I: Impact of irradiation on the microstructure of the zirconia layer*. Journal of Nuclear Materials **224**, 1995 (2), p. 109-120.

195. X. Iltis, F. Lefebvre and C. Lemaignan, *Microstructural study of oxide layers formed on Zircaloy-4 in autoclave and in reactor part II: Impact of the chemical evolution of intermetallic precipitates on their zirconia environment*. Journal of Nuclear Materials **224**, 1995 (2), p. 121-130.
196. S. Abolhassani, D. Gavillet, F. Groeschel, P. Jourdain and H.U. Zwicky, *Recent observations on the evolution of the secondary phase particles in zircaloy-2 under irradiation in a BWR up to a high burn-up*, in *Light-Water-Reactor-Fuel-Performance*. 2000, American Nuclear Society: Park City. Utah, p. 470-484.
197. B. Cox and H.I. Sheikh, *Redistribution of the alloying elements during Zircaloy-2 oxidation*. Journal of Nuclear Materials **249**, 1997 (1), p. 17-32.
198. S. Abolhassani, M.M. Dadras, M. Leboeuf and D. Gavillet, *In situ study of the oxidation of Zircaloy-4 by ESEM*. Journal of Nuclear Materials **321**, 2003 (1), p. 70-77.
199. Y. Hatano and M. Sugisaki, *Oxidation behavior of iron and nickel in Zr₂(Fe,Ni) precipitates in Zircaloy-2*. Journal of Nuclear Science and Technology **33**, 1996 (11), p. 829-833.
200. Y. Hatano and M. Sugisaki, *Auger electron spectroscopy study of oxidation behavior of iron and chromium in Zr(Fe,Cr)₂ precipitate in Zircaloy-4*. Journal of Nuclear Science and Technology **34**, 1997 (3), p. 264-268.
201. S. Davison, R. Kershaw, K. Dwight and A. Wold, *Preparation and characterization of cubic ZrO₂ stabilized by Fe(III) and Fe(II)*. Journal of Solid State Chemistry **73**, 1988 (1), p. 47-51.
202. P. Barberis, B. Baroux and S. Berbenni, *Caractérisation des précipités dans les alliages de zirconium par une étude électrochimique dans le domaine cathodique* La Revue de Metallurgie-CIT/Science et Genie des Materiaux 2000, p. 689-698.
203. D.R. Lutz, S.B. Wisner, D.M. Farkas and R.B. Adamson, *Effects of Fe on Properties of Zr Barriers*, in *Top Fuel 99*. 1999: Avignon, France.
204. T. Murai, T. Isobe, Y. Takizawa and Y. Mae, *Fundamental Study on the Corrosion Mechanism of Zr-0.2Fe, Zr-0.2Cr, and Zr-0.1Fe-0.1Cr Alloys*. ASTM STP **1354**, 2000, p. 623-640.
205. T. Kondo and T. Kimura, *Oxidation and Associated Morphological Changes in Zr-Ni Binary Alloys*. Journal of Nuclear Materials **41**, 1971 (2), p. 121-132.
206. L. Kumar, D.D. Sarma and S. Krummacher, *XPS study of the room temperature surface oxidation of zirconium and its binary alloys with tin, chromium and iron*. Applied Surface Science **32**, 1988 (3), p. 309-319.
207. E.A. Gulbransen and K.F. Andrew, *Oxidation of Series of Dilute Zr Alloys at 500 C in Water Vapor Atmosphere Containing Trace Amounts of Oxygen*. Corrosion **23**, 1967 (8), p. 231-235.
208. T. Murai, T. Isobe and Y. Mae, *Polarization Curves of Precipitates in Zirconium Alloys*. Journal of Nuclear Materials **226**, 1995 (3), p. 327-329.
209. T. Murai, T. Isobe and Y. Mae, *Polarization curves of precipitates in zirconium alloys (2)*. Journal of Nuclear Materials **230**, 1996 (2), p. 178-180.
210. D.F. Taylor, *An Oxide-Semiconductance Model of Nodular Corrosion and Its Application to Zirconium Alloy Development*. Journal of Nuclear Materials **184**, 1991 (1), p. 65-77.
211. J.-Y. Park, H.-G. Kim, Y.H. Jeong and Y.-H. Jung, *Crystal structure and grain size of Zr oxide characterized by synchrotron radiation microdiffraction*. Journal of Nuclear Materials **335**, 2004 (3), p. 433-442.
212. O. Ruff and F. Ebert, *Refractory Ceramics: I, The Forms of Zirconium Dioxide*. Zeitschrift Fur Anorganische Und Allgemeine Chemie **180**, 1929 (1), p. 19-41.
213. D.K. Smith and C.F. Cline, *Verification of Existence of Cubic Zirconia at High Temperature*. Journal of the American Ceramic Society **45**, 1962 (5), p. 249-250.

214. A.H. Heuer and M. Rühle, *Phase Transformations in ZrO₂-Containing Ceramics: II, The Martensitic Reaction in t-ZrO₂*. Advances in Ceramics 1983, p. 14-32.
215. A.H. Heuer and M. Rühle, *Phase Transformations in ZrO₂-Containing Ceramics: I, The Instability of c-ZrO₂ and the Resulting Diffusion Controlled Reactions*. Advances in Ceramics 1983, p. 1-13.
216. P.N.W. Kountouros, *Korrelation zwischen Defektchemie, Phasenstabilisierung und Eigenschaften von stabilisierten ZrO₂-Keramiken*. 1993, Stuttgart.
217. E.H. Kisi and C.J. Howard, *Crystal Structures of Zirconia Phases and their Inter-Relation*. Key Engineering Materials **153-154**, 1998, p. 1-36.
218. S. Block, J.A.H. Dajornada and G.J. Piermarini, *Pressure-Temperature Phase-Diagram of Zirconia*. Journal of the American Ceramic Society **68**, 1985 (9), p. 497-499.
219. Bocquill.G and C. Susse, *High Pressure Phase Diagram of ZrO₂*. Revue Internationale Des Hautes Temperatures Et Des Refractaires **6**, 1969 (4), p. 263-266.
220. R.C. Garvie, R.H. Hannink and R.T. Pascoe, *Ceramic Steel*. Nature **258**, 1975 (5537), p. 703-704.
221. P. Li, I.W. Chen and J.E. Pennerhahn, *Effect of Dopants on Zirconia Stabilization - an X-Ray-Absorption Study: 1. Trivalent Dopants*. Journal of the American Ceramic Society **77**, 1994 (1), p. 118-128.
222. X. Iltis, R. Salot, F. Lefebvre, A.T. Motta and C. Lemaignan. in *Int. Topical Meeting on Light Water Reactor Fuel Performance*, 1994. West Palm Beach, FL, USA.
223. D.L. Porter and A.H. Heuer, *Mechanisms of Toughening Partially Stabilized Zirconia (PSZ)*. Journal of the American Ceramic Society **60**, 1977 (3-4), p. 183-184.
224. N. Petigny, P. Barberis, C. Lemaignan, C. Valot and M. Lallemand, *In situ XRD analysis of the oxide layers formed by oxidation at 743 K on Zircaloy 4 and Zr-1NbO*. Journal of Nuclear Materials **280**, 2000 (3), p. 318-330.
225. N.B. Pilling and R.E. Bedworth, *The oxidation of metals at high temperatures*. Journal of the Institute of Metals **29**, 1923, p. 529-582.
226. C. Lemaignan, *Physical Phenomena Concerning Corrosion Under Irradiation of Zr Alloys*. ASTM STP **1423**, 2002, p. 20-29.
227. J. Godlewski, P. Bouvier, G. Lucazeau and L. Fayette, *Stress distribution measured by Raman spectroscopy in zirconia films formed by oxidation of Zr-based alloys*. ASTM STP **1354**, 2000, p. 877-900.
228. H.X. Zhang, D. Fruchart, E.K. Hlil, L. Ortega, Z.K. Li, J.J. Zhang, J. Sun and L. Zhou, *Crystal structure, corrosion kinetics of new zirconium alloys and residual stress analysis of oxide films*. Journal of Nuclear Materials **396**, 2010 (1), p. 65-70.
229. J.L. Bechade, R. Dralet, P. Goudeau and P. Yvon, *Studies of zirconium alloy oxide layers using synchrotron radiation*. Material Science Forum **347-3**, 2000, p. 471-476.
230. M.G. Glavicic, J.A. Szpunar and Y.P. Lin, *A method for the quantitative phase analysis of ZrO₂ films grown on Zr-2.5% Nb pressure tubes*. Journal of Nuclear Materials **245**, 1997 (2-3), p. 147-151.
231. H.S. Gadiyar and J. Balachandra, *Stress measurements and structural studies during oxidation of zirconium base alloys*. Transactions of The Indian Institute of Metals **28**, 1975 (5), p. 391-391.
232. C. Roy and B. Burgess, *A Study of the Stresses Generated in Zirconia Films During the Oxidation of Zirconium Alloys*. Oxidation of Metals **2**, 1970 (3), p. 235-261.
233. D.H. Bradhurst and P.M. Heuer, *The influence of oxide stress on the breakaway oxidation of Zircaloy-2*. Journal of Nuclear Materials **37**, 1970 (1), p. 35-47.
234. M. Kachanov, *On the Effective Moduli of Solids with Cavities and Cracks*. International Journal of Fracture **59**, 1993 (1), p. R17-R21.
235. M.V. Nevitt, S.K. Chan, J.Z. Liu, M.H. Grimsditch and Y. Fang, *The Elastic Properties of Monoclinic ZrO₂*. Physica B & C **150**, 1988 (1-2), p. 230-233.

236. J. Eichler, U. Eisele and J. Rodel, *Mechanical properties of monoclinic zirconia*. Journal of the American Ceramic Society **87**, 2004 (7), p. 1401-1403.
237. N.N. Ault and H.F.G. Ueltz, *Sonic Analysis for Solid Bodies*. Journal of the American Ceramic Society **36**, 1953 (6), p. 199-203.
238. C.F. Smith and W.B. Crandall, *Calculated High-Temperature Elastic Constants for Zero Porosity Monoclinic Zirconia*. Journal of the American Ceramic Society **47**, 1964 (12), p. 624-627.
239. S.K. Chan, Y. Fang, M. Grimsditch, Z. Li, M.V. Nevitt, W.M. Robertson and E.S. Zouboulis, *Temperature-Dependence of the Elastic-Moduli of Monoclinic Zirconia*. Journal of the American Ceramic Society **74**, 1991 (7), p. 1742-1744.
240. G.C. Wang, F.H. Meng, C.X. Ding, P.K. Chu and X.Y. Liu, *Microstructure, bioactivity and osteoblast behavior of monoclinic zirconia coating with nanostructured surface*. Acta Biomaterialia **6**, 2010 (3), p. 990-1000.
241. O. Bernard, A.M. Huntz, M. Andrieux, W. Seiler, V. Ji and S. Poissonnet, *Synthesis, structure, microstructure and mechanical characteristics of MO CVD deposited zirconia films*. Applied Surface Science **253**, 2007 (10), p. 4626-4640.
242. J. Luo and R. Stevens, *Porosity-dependence of elastic moduli and hardness of 3Y-TZP ceramics*. Ceramics International **25**, 1999 (3), p. 281-286.
243. B.K. Jang and H. Matsubara, *Hardness and Young's modulus of nanoporous EB-PVD YSZ coatings by nanoindentation*. Journal of Alloys and Compounds **402**, 2005 (1-2), p. 237-241.
244. J.W. Adams, R. Ruh and K.S. Mazdiyasi, *Young's modulus, flexural strength, and fracture of yttria-stabilized zirconia versus temperature*. Journal of the American Ceramic Society **80**, 1997 (4), p. 903-908.
245. F. Namavar, G. Wang, C.L. Cheung, R.F. Sabirianov, X.C. Zeng, W.N. Mei, J. Bai, J.R. Brewer, H. Haider and K.L. Garvin, *Thermal stability of nanostructurally stabilized zirconium oxide*. Nanotechnology **18**, 2007 (41), p. -.
246. S. Guo and Y. Kagawa, *Young's moduli of zirconia top-coat and thermally grown oxide in a plasma-sprayed thermal barrier coating system*. Scripta Materialia **50**, 2004 (11), p. 1401-1406.
247. I.M. Ochando, D. Caceres, J. Garcia-Lopez, R. Escobar-Galindo, R.J. Jimenez-Rioboo and C. Prieto, *Influence of the yttria content on the mechanical properties of Y₂O₃-ZrO₂ thin films prepared by EB-PVD*. Vacuum **81**, 2007 (11-12), p. 1457-1461.
248. T. Hilpert and E. Ivers-Tiffée, *Correlation of electrical and mechanical properties of zirconia based thermal barrier coatings*. Solid State Ionics **175**, 2004 (1-4), p. 471-476.
249. N. Zotov, M. Bartsch and G. Eggeler, *Thermal barrier coating systems - analysis of nanoindentation curves*. Surface & Coatings Technology **203**, 2009 (14), p. 2064-2072.
250. B. Basu, *Toughening of yttria-stabilised tetragonal zirconia ceramics*. International Materials Reviews **50**, 2005 (4), p. 239-256.
251. J.W. Hutchinson, *Crack Tip Shielding by Microcracking in Brittle Solids*. Acta Metallurgica **35**, 1987 (7), p. 1605-1619.
252. W. Wang, S. Abolhassani, M.M. Dadras and C. Lemaignan: to be submitted.
253. www.buechiglas.ch
254. www.borel.eu
255. www.buehler.com/
256. www.struers.com
257. L. Giannuzzi, *Introduction to focused ion beams : instrumentation, theory, techniques, and practice* 2005, New York: Springer.
258. N. Jalili and K. Laxminarayana, *A review of atomic force microscopy imaging systems: application to molecular metrology and biological sciences*. Mechatronics **14**, 2004 (8), p. 907-945.

259. J. Goldstein, *Scanning electron microscopy and x-ray microanalysis* 2003, New York: Kluwer Academic/Plenum Publishers.
260. G.D. Danilatos, *Bibliography of Environmental Scanning Electron-Microscopy*. *Microscopy Research and Technique* **25**, 1993 (5-6), p. 529-534.
261. G.D. Danilatos, *Introduction to the ESEM Instrument*, in *Microscopy Research and Technique*, 1993, p. 354-361.
262. D.B. Williams and C.B. Carter, *Transmission electron microscopy : a textbook for materials science* 1996, New York: Plenum Press.
263. www.gatan.com
264. S.L. Lucato, *LINCE (Linear Interception Software) v2.31*. 1998, TU Darmstadt.
265. Y. Golovin, *Nanoindentation and mechanical properties of solids in submicrovolumes, thin near-surface layers, and films: A Review*. *Physics of the Solid State* **50**, 2008 (12), p. 2205-2236.
266. X.D. Li and B. Bhushan, *A review of nanoindentation continuous stiffness measurement technique and its applications*. *Materials Characterization* **48**, 2002 (1), p. 11-36.
267. R.L. Edwards, G. Coles and W.N. Sharpe, *Comparison of tensile and bulge tests for thin-film silicon nitride*. *Experimental Mechanics* **44**, 2004 (1), p. 49-54.
268. A. Karimi, O.R. Shojaei, T. Kruml and J.L. Martin, *Characterisation of TiN thin films using the bulge test and the nanoindentation technique*. *Thin Solid Films* **308**, 1997, p. 334-339.
269. V. Spassov and M. Dadras, *3D imaging application on mechanical properties characterization - Poster*, in *Interdisciplinary Symposium on 3 Dimensional Microscopy*. 2009, SSOM: Interlaken, Switzerland.
270. www.veeco.com
271. N. Simic and E. Ahlberg, *Anodic Oxidation of ZrCr₂ and binary Zr-Cr alloys in sulphuric acid*. not published.
272. B.N.L. Srinivas, *Measurement and Evaluation of Oxide growth in Zirconium Binary Alloys and Zircaloy-2 by Steam Corrosion Test*. 2009, Paul-Scherrer-Institut: Villigen.
273. D. Drouin, A.R. Couture, D. Joly, X. Tastet, V. Aimez and R. Gauvin, *CASINO V2.42 - A fast and easy-to-use modeling tool for scanning electron microscopy and microanalysis users*. *Scanning* **29**, 2007 (3), p. 92-101.
274. G.D. Gatta, I. Kantor, T.B. Ballaran, L. Dubrovinsky and C. McCammon, *Effect of non-hydrostatic conditions on the elastic behaviour of magnetite: an in situ single-crystal X-ray diffraction study*. *Physics and Chemistry of Minerals* **34**, 2007 (9), p. 627-635.
275. A.N. Shmakov, G.N. Kryukova, S.V. Tsybulya, A.L. Chuvilin and L.P. Solovyeva, *Vacancy Ordering in Gamma-Fe₂O₃ - Synchrotron X-Ray-Powder Diffraction and High-Resolution Electron-Microscopy Studies*. *Journal of Applied Crystallography* **28**, 1995, p. 141-145.
276. G. David, R. Geschier and C. Roy, *Study of Growth of Oxide on Zirconium and Zircaloy-2*. *Journal of Nuclear Materials* **38**, 1971 (3), p. 329-339.
277. H.E. Swanson and E. Tatge, *Standard X-Ray Diffraction Patterns*. *Journal of Research of the National Bureau of Standards* **46**, 1951 (4), p. 318-327.
278. C.C. Calvert, A. Brown and R. Brydson, *Determination of the local chemistry of iron in inorganic and organic materials*. *Journal of Electron Spectroscopy and Related Phenomena* **143**, 2005 (2-3), p. 173-187.
279. C. Proff, S. Abolhassani, M.M. Dadras and C. Lemaignan, *In situ oxidation of zirconium binary alloys by Environmental SEM and analysis by AFM, FIB and TEM*. *Journal of Nuclear Materials* **404**, 2010 (2), p. 97-108.
280. C.H. Xu and W. Gao, *Pilling-Bedworth ratio for oxidation of alloys*. *Materials Research Innovations* **3**, 2000 (4), p. 231-235.

281. G. Stefanic, S. Popovic and S. Music, *Influence of Cr₂O₃ on the stability of low temperature t-ZrO₂*. Materials Letters **36**, 1998 (5-6), p. 240-244.
282. G. Stefanic, M. Didovic and S. Music, *The influence of thermal treatment on the phase development of ZrO₂-NiO precursors*. Journal of Molecular Structure **834**, 2007, p. 435-444.
283. R.D. Shannon, *Revised Effective Ionic-Radii and Systematic Studies of Interatomic Distances in Halides and Chalcogenides*. Acta Crystallographica Section A **32**, 1976 (5), p. 751-767.
284. O.T. Woo and M. Griffiths, *The role of Fe on the solubility of Nb in alpha-Zr*. Journal of Nuclear Materials **384**, 2009 (1), p. 77-80.
285. P. Barberis, V. Rebeyrolle, J.J. Vermoyal, V. Chabretou, J.P. Vassault, M. Limback, B. Kammenzind and S.W. Dean, *CASTA DIVA®: Experiments and Modeling of Oxide-Induced Deformation in Nuclear Components*. Journal of ASTM International **5**, 2008 (5), p. 101124-101124.
286. J.K. Dawson, G. Long, W.E. Seddon and J.F. White, *Kinetics and Mechanism of Oxidation of Zircaloy-2 at 350-500 °C*. Journal of Nuclear Materials **25**, 1968 (2), p. 179-200.
287. M. Tupin, M. Pijolat, F. Valdivieso, M. Soustelle, A. Frichet and P. Barberis, *Differences in reactivity of oxide growth during the oxidation of Zircaloy-4 in water vapour before and after the kinetic transition*. Journal of Nuclear Materials **317**, 2003 (2-3), p. 130-144.
288. J. Levitan, J.E. Draley and C.J. van Drunen, *Low-Pressure Oxidation of Zirconium*. Journal of the Electrochemical Society **114**, 1967 (11), p. 1086-1089.
289. C. Toffolon, J.-C. Brachet, C. Servant, L. Legras, D. Charquet, P. Barberis and J.-P. Mardon, *Experimental Study and Preliminary Thermodynamic Calculations of the Pseudo-Ternary Zr-Nb-Fe-(O, Sn) System*. ASTM STP **1423**, 2002, p. 361-383.
290. S.A. Averin, V.L. Panchenko, A.V. Kozlov, L.P. Sinelnikov, V.N. Shishov and A.V. Nikulina, *Evolution of Dislocation and Precipitate Structure in Zr Alloys Under Long-Term Irradiation*. ASTM STP **1354**, 2000, p. 105-121.
291. D.R. Gaskell, *Introduction to Thermodynamics of Materials*. 5th ed 2006, New York: Taylor&Francis.
292. R. DeHoff, *Thermodynamics in materials science* 2006, Boca Raton Fla.: Taylor & Francis.
293. http://www.doitpoms.ac.uk/tlplib/ellingham_diagrams/interactive.php
294. <http://www.engr.sjsu.edu/ellingham/>
295. D. Chakrabarty, *An introduction to physical chemistry* 2001, UK: Alpha Science International Ltd.
296. C. Toffolon, *Formation enthalpy of compounds from thermodynamic database Zircobase*. 2010.
297. P. Barberis, N. Dupin, C. Lemaignan, A. Pasturel and J.M. Grange, *Microstructure and phase control in Zr-Fe-Cr-Ni alloys: Thermodynamic and kinetic aspects*. ASTM STP **1467**, 2005, p. 129-156.
298. Q.T. Guo and O.J. Kleppa, *The standard enthalpies of formation of the compounds of early transition metals with late transition metals and with noble metals as determined by Kleppa and co-workers at the University of Chicago - A review*. Journal of Alloys and Compounds **321**, 2001 (2), p. 169-182.
299. M. Krcmar and C.L. Fu, *First-principles study of point-defect structures in C15 ZrCo₂ and ZrCr₂ and B2 ZrCo*. Physical Review B **68**, 2003 (13), p. 134110.
300. F.R. de Boer, *Cohesion in metals : transition metal alloys* 1988, Amsterdam; New York; New York N.Y. U.S.A.: North-Holland.

301. A.T. Motta, M.J.G. da Silva, A. Yilmazbayhan, R.J. Comstock, Z. Cai and B. Lai, *Microstructural Characterization of Oxides Formed on Model Zr Alloys Using Synchrotron Radiation*. ASTM STP **1505**, 2009, p. 486-506.
302. N. Simic and E. Ahlberg, *Anodic Oxidation of Zr₂Ni and binary Zr-Ni alloys in sulphuric acid*. not published.
303. R.A. Ploc and B. Cox, *Oxidation of some zirconium-based precipitates*, in *Second Phase Particles in Zircalloys*. 1985: Erlangen.
304. D.P. Abraham and N. Dietz, *Role of laves intermetallics in nuclear waste disposal*. Materials Science and Engineering A - Structural Materials Properties Microstructure and Processing **329**, 2002, p. 610-615.
305. S. Nicolopoulos, P. Moeck, Y. Maniette and P. Oleynikov. *Identification / fingerprinting of nanocrystals by precession electron diffraction*. in *EMC 2008 14th European Microscopy Congress*, 2008. Aachen, Germany.
306. Y. Wouters, A. Galerie and J.P. Petit, *Haematite and chromia dissolution in the zirconia matrix during thermal oxidation of Laves-phases Zr(Fe,Cr)₂ on Zircaloy-4*. Materials at High Temperatures **26**, 2009 (1), p. 9-14.
307. C. Argiris, M.A. Taylor, M. Kilo, G. Borchardt, F. Jomard, B. Lesage and O. Kaitasov, *SIMS study of transition metal transport in single crystalline yttria stabilised zirconia*. Physical Chemistry Chemical Physics **6**, 2004 (13), p. 3650-3653.
308. B.A. van Hassel and A.J. Burggraaf, *Oxidation-State of Fe and Ti Ions Implanted in Yttria-Stabilized Zirconia Studied by XPS*. Applied Physics a-Materials Science & Processing **52**, 1991 (6), p. 410-417.
309. M. de Ridder, P.C. van de Ven, R.G. van Welzenis, H.H. Brongersma, S. Helfensteyn, C. Creemers, P. Van Der Voort, M. Baltes, M. Mathieu and E.F. Vansant, *Growth of iron oxide on yttria-stabilized zirconia by atomic layer deposition*. Journal of Physical Chemistry B **106**, 2002 (51), p. 13146-13153.
310. W.C. Oliver and G.M. Pharr, *An Improved Technique for Determining Hardness and Elastic-Modulus Using Load and Displacement Sensing Indentation Experiments*. Journal of Materials Research **7**, 1992 (6), p. 1564-1583.
311. R. Saha and W.D. Nix, *Effects of the substrate on the determination of thin film mechanical properties by nanoindentation*. Acta Materialia **50**, 2002 (1), p. 23-38.
312. S. Veprek, *The search for novel, superhard materials*. Journal of Vacuum Science & Technology A **17**, 1999 (5), p. 2401-2420.
313. M. Shinn, L. Hultman and S.A. Barnett, *Growth, Structure, and Microhardness of Epitaxial TiN/NbN Superlattices*. Journal of Materials Research **7**, 1992 (4), p. 901-911.
314. R.C. Cammarata, T.E. Schlesinger, C. Kim, S.B. Qadri and A.S. Edelstein, *Nanoindentation Study of the Mechanical-Properties of Copper-Nickel Multilayered Thin-Films*. Applied Physics Letters **56**, 1990 (19), p. 1862-1864.
315. B. Jonsson and S. Hogmark, *Hardness Measurements of Thin-Films*. Thin Solid Films **114**, 1984 (3), p. 257-269.
316. X.Y. Zhang and J.L. Yang, *The compressive strength of ceramic microbeads*. Key Engineering Materials **336-338**, 2007, p. 2411-2413.
317. A. Christensen and E.A. Carter, *First-principles study of the surfaces of zirconia*. Physical Review B **58**, 1998 (12), p. 8050-8064.
318. W.R. Tyson and W.A. Miller, *Surface Free-Energies of Solid Metals - Estimation from Liquid Surface-Tension Measurements*. Surface Science **62**, 1977 (1), p. 267-276.
319. E.Y. Fogaing, Y. Lorgouilloux, M. Huger and C.P. Gault, *Young's modulus of zirconia at high temperature*. Journal of Materials Science **41**, 2006 (22), p. 7663-7666.

14 Appendix I – Estimation of precipitate oxygen content for small precipitates

Owing to the size of small precipitates, the EDS signal from the surrounding oxide contributes to the measured signal. Therefore the matrix contribution to the zirconium and oxygen signals has to be subtracted for the estimation of the precipitate oxygen content in case of small precipitates. The oxygen content of the precipitates is therefore derived from the following calculation:

It is assumed that the precipitate ($ZrCr_2$) and the surrounding oxide (ZrO_2) are stoichiometric. The amount of Zr in the matrix is calculated using the measured atomic concentration of chromium / niobium (which exhibit small precipitates) (Eq. 1).

$$c(Zr_{matrix}) = c(Zr_{measured}) - 0.5 \cdot c(Cr_{measured}) \quad \text{Eq. 1}$$

The oxygen content of this oxidised matrix is then subtracted from the total oxygen concentration measured (numerator of Eq. 2). If the numerator is positive, so there is more oxygen than can be present in the matrix around the precipitate, the atomic concentration of oxygen in the precipitate is calculated with Eq. 2.

$$c(O_{SPP}) = \frac{c(O_{measured}) - 2 \cdot c(Zr_{matrix})}{1.5 \cdot c(Cr_{measured}) + \{c(O_{measured}) - 2 \cdot c(Zr_{matrix})\}} \quad \text{Eq. 2}$$

The thickness used for quantification at the precipitate position was derived from the measurement the oxide beside the precipitate, which should yield oxygen to zirconium ratio of 2. Even if the quantification is not fully reliable, this correction provides some useful information about the relative oxygen content of the precipitates with respect to the surrounding oxide.

15 Appendix II – In situ experiments at 700 °C

The samples oxidised at 700 °C in situ for 1 hour at 130 Pa in water vapour aimed at providing experimental insight into the early stage of oxidation at elevated temperatures at which already a commercial zirconium alloy was investigated [198]. Unfortunately, due to the limited time, the samples oxidised at 700 °C were not investigated in detail, as the samples oxidised at 415 °C in situ. A brief overview of what has been done and is available is provided here. Examples for the results are presented for Zr1%Fe, as these represent the experimental results for the binary alloys quite well. At this oxidation temperature the observed changes at the surface were not as distinct as at 415 °C, Figure 107 shows the surface close to an indent made for orientation purposes.

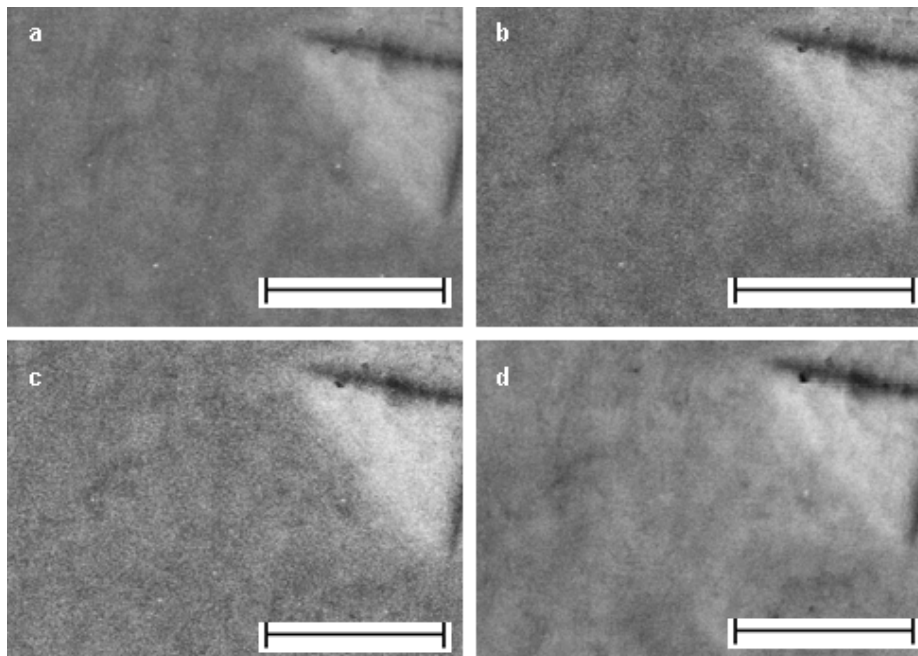


Figure 107: The GSE images of Zr1%Fe oxidised at 700 °C show the surface close to an indent as observed in situ after (a) 1 minute, (b) 11 minutes, (c) 30 minutes and (d) during cooling down to room temperature. All scale bars correspond to 5 μm .

The AFM scans of the surface after oxidation showed some surface roughness (Figure 108), however, as no detailed analysis was performed as for the samples oxidised at 415 °C, further analysis is required before being able to draw conclusions.

The oxide thickness on Zr1%Fe oxidized at 700 °C is homogenous in the observed FIB transverse section (Figure 109). The precipitate oxidation behaviour at the metal-oxide interface seems to be similar as in the material oxidized at 415 °C under similar conditions. However, no TEM sample has been prepared and therefore no conclusions are possible about the precipitate oxidation behaviour at the metal oxide interface and in the oxide.

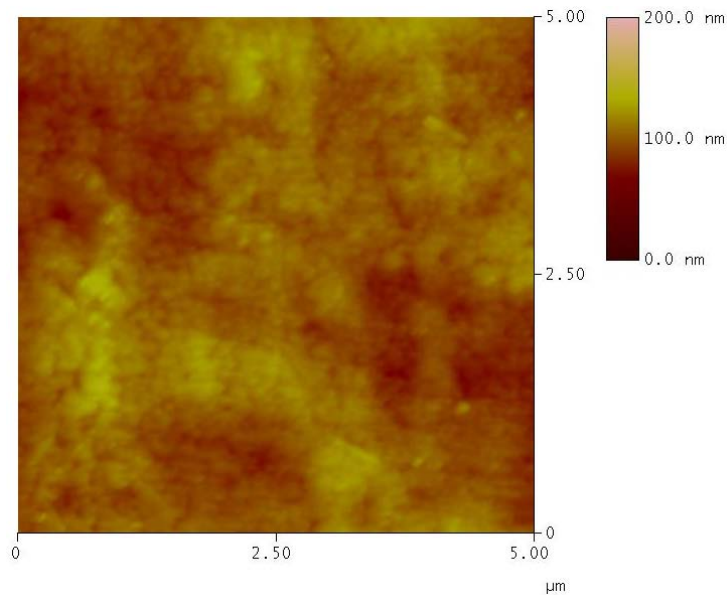


Figure 108: AFM surface profile on Zr1%Fe after oxidation at 700°C in situ.

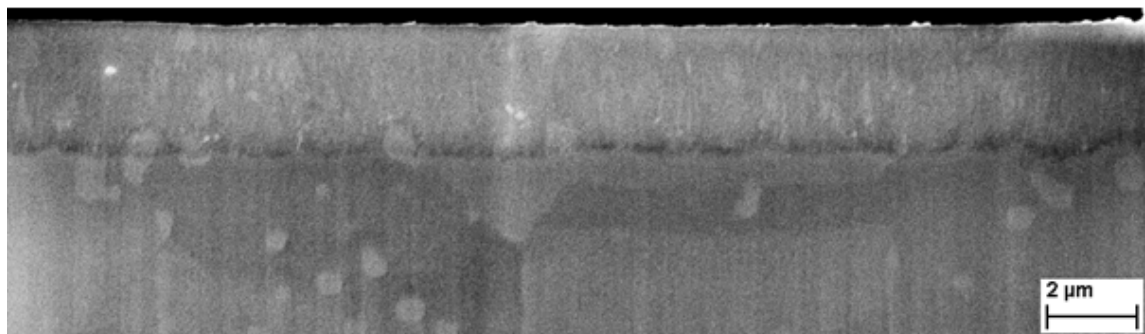


Figure 109: FIB transverse section of Zr1%Fe oxidized at 700°C in situ. Precipitates can be observed in the metal and to some extent in the oxide. View perpendicular to section.

The summarised results for the materials oxidised in situ at 700°C in Table 26 show, that the differences in surface roughness after oxidation is lower than at 415°C (Table 12) and the overall surface roughness obtained is rather low. The three binary alloys containing 1% Fe, Ni or Cr are quite similar to each other regarding their surface roughness; the reason for this is not understood. Interesting is the low average oxide thickness on pure zirconium in this environment compared to the binary alloys, as in general zirconium is observed to exhibit worse corrosion resistance than zirconium alloys in water containing environments.

For a thorough understanding of the behaviour at this oxidation temperature, an extensive characterisation program as performed at 415°C should be completed.

Table 26: parameters of the samples oxidised in situ at 700°C

Alloy	oxidation time / h	Average oxide thickness / μm	RMS polished (5x5 μm) / nm	RMS oxidised (5x5 μm) / nm
Zr1% Fe	1	3.2 ± 0.2	4.3	10.0
Zr1% Ni	1	2.8 ± 0.2	6.3	10.1
Zr1% Cr	1	2.7 ± 0.5	4.3	10.5
Zr0.6% Nb	1	3.2 ± 0.2	3.5	8.4
pure Zr	1	2.4 ± 0.5	5.5	9.6

16 Appendix III – Mechanical properties of oxide on binary alloys

The Young's modulus was determined by nanoindentation of the surface in plain view, with indentation perpendicular to the outer surface. To make sure that the obtained results are not dominated by the mechanical properties of the underlying metal, the indentation depth should not exceed $1/7^{\text{th}}$ of the oxide thickness, as otherwise a contribution of the mechanical properties of the underlying metal will be present in the acquired data. This was confirmed by continuous measurements of the Young's modulus into oxides, which showed always a drop to the Young's modulus of the metal. For indentation depths exceeding a small fraction of the film thickness (20% is already sufficient) an influence of the substrate film cannot be neglected. In the literature a ratio of indentation depth to film thickness of $1/10$ [310] has been proposed to be sufficient to avoid influence of the substrate on the results. The Young's modulus is more sensitive than the hardness to the substrate influence [311], due to the long range elastic field probed by the indenter and in case of soft substrates under stiff films the influence of the substrate is earlier detected than for equal stiffness pairs or soft films, due to substrate yielding, which is also to be expected for the zirconia – zirconium pair. This observation is also in agreement with the different ratios found for different material combinations [311-315]. For thick oxides (4-5 μm) the Young's modulus dropped from the higher surface value (surface effects) to the bulk oxide value around 500 nm indentation depth (depending on the oxide thickness) and exhibited a stable plateau in the metal at a Young's modulus around 100 GPa.

To test the outer surface of the oxide scales 2 mN indentation force was applied, resulting in average indentation depths of around 90 and 150 nm. The general trend of the Young's modulus versus indentation depth was determined by 10 indentations in continuous stiffness measurement mode, allowing to determine the indentation force to be used to measure the bulk properties of the oxide without indenting too deep and obtaining a large contribution from the underlying metal.

Due to the local variation of the obtained data, which is due the fact that the surface is not perfectly flat and possible contamination at some indents, arrays of indents were made, with 100 indents per indentation force (Table 27). The obtained force displacement data were corrected to set the indentation depth to zero at the point where the measured indentation force started to increase, which was not the case for a high proportion of data sets. The Young's modulus was then extracted from the corrected data sets and plotted as frequency versus Young's modulus plots to obtain also information about the spread of the data.

Table 27: Young's modulus of oxide at the surface and in the bulk as obtained by indentation with Vickers indenter. The indentation force for the bulk properties is dependent on the oxide thickness. The oxide scales tested were formed on different binary alloys and pure zirconium by autoclave oxidation.

material	oxide thickness / μm	Atmosphere	surface modulus			bulk modulus		
			indentation Force / mN	modulus / GPa	std. dev modulus / GPa	indentation Force / mN	modulus / GPa	std. dev modulus / GPa
pure Zr	4.12	steam	2	200	66	40	146	42
pure Zr	0.59	air	2	192	24	-	-	-
Zr0.2%Fe	4.19	steam	2	203	85	50	160	32
Zr1%Fe	5	steam	2	198	100	50	166	55
Zr1%Ni	4.15	steam	2	245	104	40	156	36
Zr1%Cr	4.23	steam	2	218	48	40	156	18
Zr0.6%Nb	2.58	steam	2	200	66	20	146	42
Zr0.6%Nb	6.02	air	2	63	16	12	41	7
Zry-4	6.36	steam	2	227	70	70	146	30

A comparison of the Young's modulus close to the surface and in the bulk of the oxide shows, that the Young's modulus at the surface is always higher, but also associated with a larger scatter than those data obtained for the bulk deeper in the oxide scale (Table 27). The larger scatter of the surface data is most probably, to a high extent, caused by the high surface roughness, which poses non-ideal conditions for a high quality determination of the Young's modulus for such low indentation depths. A clear difference can be only observed between the unalloyed pure zirconium and the alloys with Fe, Ni or Cr for the indentation depth probing the bulk. The Nb containing binary alloys as well as Zircaloy-4 are exhibiting a similar Young's modulus as pure zirconium in the same oxidation environment. Due to the scatter it is questionable, if there is a significant difference between the iron containing binary alloys and the other two binary alloys.

17 Appendix IV – Modelling of oxide with different precipitate oxidation

The aim of this modelling is to investigate the stress state of the oxide around the precipitates and to evaluate where the oxide is under tension, which can cause cracking in a brittle material like zirconia. The modelling has been performed for two different precipitate oxidation behaviours, delayed and similar oxidation with respect to the matrix, using ANSYS Multiphysics. As the precipitates have been shown to exhibit a higher volume increase than zirconium, precipitates with similar oxidation as the surrounding matrix will lead to additional compressive stresses. The expansion of oxidised precipitates and oxidising zirconium has been assumed to be isotropic with the Pilling-Bedworth ratios provided in Table 18. The Pilling-Bedworth ratios were converted to linear expansion factors by taking the cubic root (which leads to a value of 15% in the case of Zr/ZrO_2). The obtained linear expansion factors were then transformed to thermal expansion coefficients, as the expansion due to oxidation was modelled with the thermal expansion module in ANSYS.

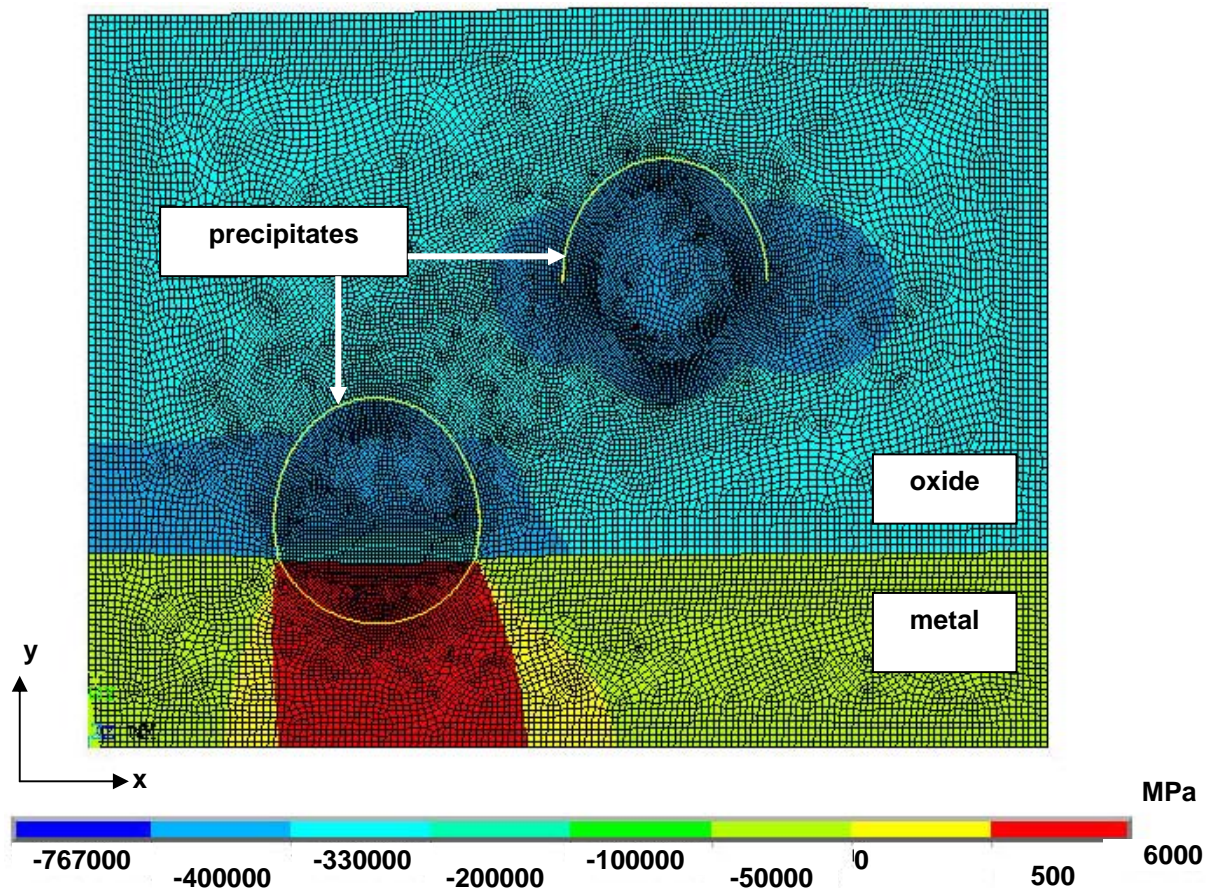


Figure 110: Stresses in x -direction in the model of Zr_3Fe precipitates (300 nm) in the oxide and at the metal-oxide interface. Metal side is partially under tension and the oxide under compression. The stresses are higher on the sides of the precipitates.

For the precipitates oxidising on the oxide side of the metal-oxide interface and in the oxide (Zr_3Fe and Zr_2Ni) with a higher Pilling-Bedworth ratio than zirconium, compressive stresses are induced around the precipitates, a brittle material like zirconia is known to be prone to fail when under tensile stress, as the compressive strength can be quite high (up to 2000 MPa for industrial zirconia [316]). Therefore cracking at the precipitate oxide interface is not expected to occur due to the expansion of the precipitates (300 nm diameter) during oxidation (Figure 110).

For the precipitates exhibiting delayed oxidation in the oxide ($ZrCr_2$ and $\beta-Nb$) with no expansion in the oxide close to the metal-oxide interface, it is observed from the experimental results at different oxidation conditions that the precipitate-oxide interface fails during oxidation on the precipitate side facing the surface (Table 14 on page 118).

In the model the precipitate side facing the surface was modelled with a cohesive contact and the side facing the metal-oxide interface with a rigid interface to allow only cracking on the side facing the surface, otherwise on top and bottom of the precipitates cracks would have appeared in this model. This was done in order to simulate the dynamic oxidation process, during which the oxide front passes the precipitate. First the matrix on the precipitate side facing the outer surface is oxidised and the interface fails, later the matrix on the bottom of the precipitate (towards metal-oxide interface) is oxidised. As the implementation of a moving metal-oxide interface in the model simulating the real oxidation process was not possible (in the available time), this solution was chosen to be able to compare the crack height and shape with the observed examples. The cohesive contact describing the cracking of the precipitate-oxide interface was modelled using the following parameters: interface energy 2 J/m^2 [317, 318], interface stiffness $E = 200 \text{ GPa}$ at 415°C (235 GPa at $400\text{-}500^\circ\text{C}$ [319] and 180 GPa [244] at $400\text{-}500^\circ\text{C}$ could be found and intermediate value been used) and the fracture strength of monoclinic zirconia 200 MPa [236] (experimental value determined at room temperature – also used in model).

Tensile stresses in y-direction are present in the precipitates if no cohesive contact is placed at the interface (not shown here). Therefore cracking at the precipitate oxide interface towards the outer surface is expected for this precipitate oxidation behaviour, as the oxide expands around the still metallic precipitates (Figure 111). The observed crack heights are very similar to experimentally observed precipitates with the same diameter as in the model (50 nm diameter). The experimentally observed crack heights, see Figure 100 on page 146, were quite well reproduced using the cohesive contact model (crack height $\approx 7 \text{ nm}$ for precipitates with 50 nm diameter fully incorporated into the oxide).

It has been shown that undulations can lead to tensile stresses at the metal-oxide interface [160], these stresses do not interfere with the crack initiation at the precipitate-oxide interface of precipitates exhibiting delayed oxidation, as the precipitates are an order of magnitude smaller than the large cracks which form sometimes close to the undulations.

The models predict quite well the observed cracking at precipitates as reported in this work. However, as the presented examples show idealized conditions and do not take the microstructural anisotropy into account, it is not possible to predict cracking of the oxide also within precipitates, as observed experimentally (Figure 63) and formation of the larger cracks

in the oxide with the used models. The obtained stresses are considerably too high (about 30 GPa average compressive stress in the oxide in Figure 111 and around 300 GPa in Figure 110) when compared with the stresses reported in the literature (maximum 2 GPa, see Table 3 on page 34). These values should be further examined as they may reflect a certain weakness of the expansion model used in this study. Other modelling approaches might be necessary to compare with the present scheme. The situation is studied at 415°C and changes due to the different thermal expansion with cooling are not considered.

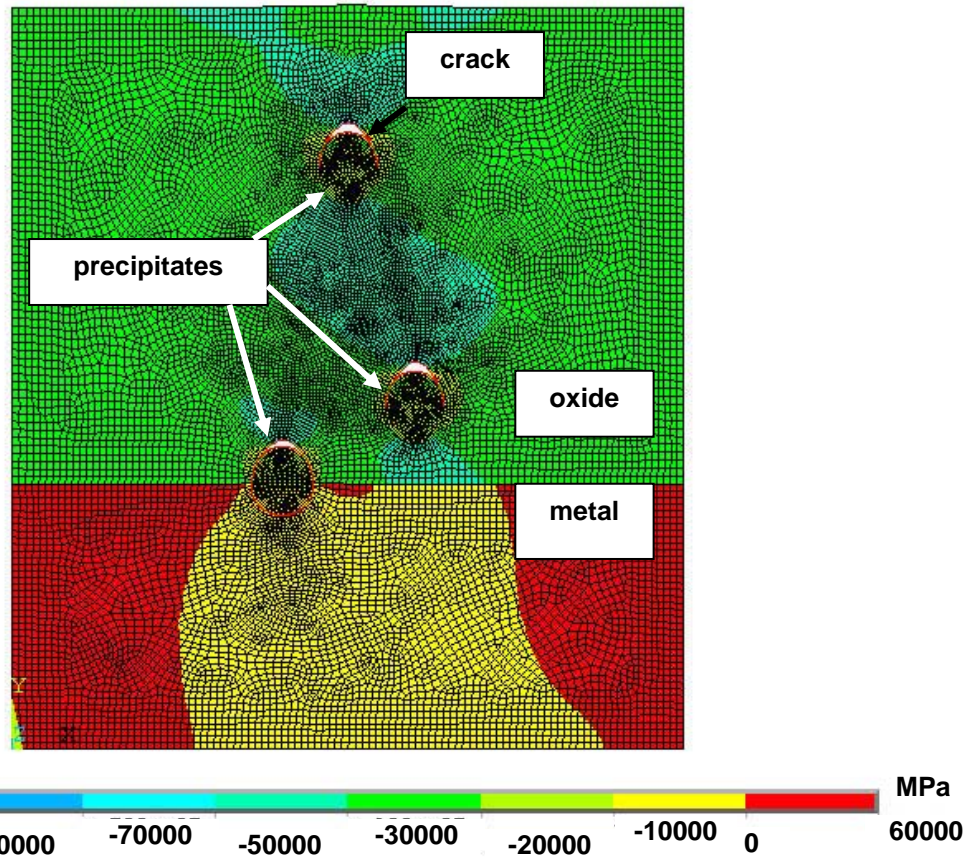


Figure 111: Stresses in x -direction in the model of $ZrCr_2$ precipitates (50 nm) in the oxide and at the metal-oxide interface. Metal side is partially under tension and the oxide under compression. The stresses are reduced on the sides of the precipitates and more compressive above and below.

18 Résumé de thèse en français

18.1 Résumé

Cette thèse est axée sur la caractérisation microstructurale des précipités dans les oxydes des alliages binaires de zirconium (1 wt.% Fe, Cr , Ni ou 0.6 wt.% Nb). La température d'oxydation est fixée au 415°C. Les échantillons sont oxydés dans l'air et dans l'autoclave sous des pressions différentes et dans un microscope électronique à balayages environnemental sous vapeur d'eau.

Les résultats des recherches peuvent être résumés ci-dessous :

- Deux types d'oxydation (retardée et non retardée) ont été observés pour les précipités.
- Le facteur de Pilling-Bedworth des précipités est plus élevé par rapport à celui de zirconium.
- Les précipités contenant du fer entraînent une formation des cristaux de l'oxyde de fer pur à la surface du matériau, quand les précipités sont à la surface ou à la proximité.

Ces observations mènent à la conclusion que le comportement d'oxydation des précipités peut être corrélé à leurs compositions et à la tendance d'oxydation de leurs éléments constituants.

Mots-clés : alliages binaires de zirconium, précipités, corrosion, oxyde, MET, microstructure

Une version électronique de la thèse est accessible sur le serveur:

<http://tel.archives-ouvertes.fr>

(veuillez entrer le titre et le nom de l'auteur afin d'accéder à la thèse S.V.P.)

18.2 Introduction

Les alliages de zirconium sont utilisés dans les centrales nucléaires, par exemple comme matériau de gaine de combustible. Ce type d'alliages avait été retenu pour leurs propriétés intéressantes, notamment leur faible section efficace de capture des neutrons et leur haute résistance à la corrosion dans l'eau ou la vapeur à des températures et pressions élevées. Puisque le zirconium pur n'atteint pas les performances recherchées, des éléments d'alliages sont ajoutés. Certains sont solubles dans la matrice de zirconium pour les concentrations souhaitées alors que d'autres sont pratiquement insolubles et forment donc des précipités.

Les précipités d'alliages de zirconium sont soit des intermétalliques formés par les éléments d'alliage avec le zirconium ou une phase d'élément d'alliage avec le zirconium dans la solution solide. Ces précipités ont démontré un rôle important dans la résistance à la corrosion des alliages de zirconium. Dans les précipités typiques d'alliages de zirconium, un élément d'alliage peut être remplacé dans une certaine mesure par un autre élément d'alliage, de sorte que la composition du précipité soit dépendante de la composition de l'alliage et des paramètres de production. Les précipités $Zr_2(Fe,Ni)$ et $Zr(Fe,Cr)_2$ présents dans les "Zircaloy" en sont des exemples typiques.

Le comportement à l'oxydation des précipités dans les alliages de zirconium commerciaux est connu phénoménologiquement, cependant la compréhension du comportement à l'oxydation des précipités reste limitée et l'influence de différents éléments d'alliage n'est pas fondamentalement assimilée. Du fait de l'importance des précipités pour la résistance à la corrosion des alliages de zirconium, un intérêt est porté sur le comportement des précipités durant l'oxydation et leur influence sur le comportement à l'oxydation de l'alliage entier.

Dans les alliages complexes commerciaux de zirconium, l'interférence entre les différents éléments d'alliage peut masquer le comportement des éléments d'alliage spécifiques ; l'étendue de cette interférence était inconnue jusqu'à présent du fait d'un manque de données pour les précipités d'éléments d'alliage spécifiques. C'est pourquoi des alliages binaires de zirconium ont été choisis pour permettre l'étude du comportement d'un élément d'alliage spécifique pendant l'oxydation, dans différents environnements d'oxydation, sans aucune interférence avec un autre élément d'alliage. Les alliages binaires oxydés ont été caractérisés à l'échelle microscopique par rapport au comportement de l'élément d'alliage dans différents environnements d'oxydation, fournissant une information jusqu'alors non disponible.

Une vue d'ensemble des connaissances sur les alliages de zirconium et leur oxydation est apportée dans l'étude bibliographique de cette thèse. Dans la section suivante le matériau étudié et l'approche expérimentale sont décrits. Les résultats expérimentaux sont introduits en fonction des différents environnements d'oxydation étudiés. La discussion comprend d'une part l'évaluation des limitations des résultats expérimentaux et d'autre part les conséquences des résultats concernant la compréhension de l'oxydation des précipités.

Enfin, l'approche expérimentale utilisée sera résumée et les conclusions les plus importantes récapitulées.

18.3 Littérature

La présence des précipités intermétalliques (particules de phase secondaire – PPS) aide à améliorer la résistance contre la corrosion des alliages de zirconium dans l'eau et dans la vapeur d'eau par une protection anodique. Des alliages de zirconium de même composition mais avec une dissolution complète des éléments dans la matrice de zirconium montrent une résistance à la corrosion inférieure comparé aux ceux avec des précipités. L'influence du traitement thermique sur la distribution de taille et du contenu des éléments chimiques impliqués dans les précipités est bien connue comme la corrélation avec la résistance à la corrosion dans de différents environnements. Le comportement d'oxydation des précipités décrit dans la littérature a été évalué pour une série des alliages commerciaux et nouvellement développés. Pour des alliages binaires seulement le comportement général d'oxydation a été étudié, mais après nos informations la microstructure de l'alliage et des précipités oxydés n'a jamais été analysé en particulier par la MET. Normalement, l'influence de la corrosion des alliages de zirconium sur des aspects mécanique n'est présentée que dans le contexte des propriétés mécaniques de zirconia.

18.4 Matériaux et Méthodes

18.4.1 Matériaux

Les alliages binaires, du zirconium pur et le Zircaloy-4 qui ont été étudié dans ce travail était fournis par CEZUS, France. Les matériaux avaient traités dans un autoclave avec de différents environnements. Le Zircaloy-2 et le Zircaloy-4 sont des alliages commerciaux conformes aux spécifications. Pour les alliages binaires fournis existent des résultats analytiques réalisés précédemment qui comprennent l'augmentation du poids, les changements spectroscopiques d'impédance et du potentiel électrochimique et le comportement d'hydrogénation.

Les compositions des alliages binaires étudiés dans ce projet sont 0.2 wt.% Fe et 1 wt.% Cr, Fe ou Ni et, pour raison de comparaison, du Zr pur. Les alliages sont présentés dans Tableau 28. La fraction volumique des précipités maximale possible est listée, supposant que tout le contenu des éléments secondaires d'alliage est lié dans ces précipités, avec la composition des PPS indiquée. Des échantillons de zirconium-niobium binaire de composition 0.6 wt.% Nb ont été inclus dans l'étude. Ces échantillons étaient obtenus séparément de CEZUS, avec une oxydation dans la vapeur d'eau pour 40 jours et dans l'air ambiant pour 55 jours. Ces échantillons ont servi à une comparaison du comportement corrosif des précipités de Nb avec celui des précipités des autres alliages binaires. Tableau 29 contient un résumé des conditions d'oxydation et des échantillons dont l'épaisseur moyenne de couche d'oxyde étaient déterminés et qui sont utilisés pour ce projet de thèse. A part des conditions décrites il y avait aussi des oxydations d'une et de 24 heures dans l'air à 415°C pour étudier une éventuelle ségrégation des éléments d'alliage à la surface.

Tableau 28: Analyses chimique d'alliages binaires (en ppm ou wt.%) et caractéristiques des précipitées ; données de CEZUS pour Zr1%Fe, Zr1%Ni et Zr1%Cr. Data de précipitées pour Zr0.6%Nb obtenu par calculs.

type d'alliage	Cr / ppm	Fe / ppm	Ni / ppm	Nb	O / ppm	moyenne de taille de grain / μm	type de PPS	PPS fraction de volume / %
Zr0.2%Fe	45	0.22 wt.%	35	-	650	6.2	Zr ₃ Fe	1.13
Zr1%Fe	44	0.99 wt.%	28	-	720	3.1	Zr ₃ Fe	5.71
Zr1%Ni	46	205	1.17 wt.%	-	755	4.6	Zr ₂ Ni	3.70
Zr1%Cr	1.04 wt.%	247	37	-	760	5.2	ZrCr ₂	1.76
Zr0.6%Nb	-	-	-	0.6 wt.%		4.4	ZrNb ₄	1.14

Tableau 29: Résumé des échantillons et épaisseur de couche d'oxyde en μm . L'épaisseur de la couche d'oxyde des échantillons provisionnés par CEZUS (colonne 1-3, foncées) a été déterminée par augmentation du poids, pour tous les autres échantillons oxydés pour ce projet par coupe de FIB.

alliage	Moyenne de couche d'oxyde / μm							
	oxydation dans l'aire CEZUS	oxydation dans la vapeur CEZUS		In situ ESEM à CSEM, Neuchatel		oxydation dans la vapeur, au PSI Limbo 350 autoclave		
	3 jours 415°C 0.1 MPa	3 jours 415°C 0.1 MPa	110 jours 415°C 10.5 MPa	1 heure 415°C 130 Pa	1 heure 700°C 130 Pa	1 heure 415°C 10.5 MPa	1 jour 415°C 10.5 MPa	3 jours 415°C 10.5 MPa
Zr0.2%Fe	0.67	1.61	4.19	—	—	0.42	1.08	—
Zr1%Fe	1.01	1.37	5.00	0.32	3.2	0.62	1.14	1.53
Zr1%Cr	0.79	1.08	4.23	0.35	2.7	0.52	0.94	1.28
Zr1%Ni	0.93	1.26	4.15	0.41	2.8	0.49	—	—
Zr0.6%Nb	6.02 (55 jours)	2.58 (40 jours)	—	0.34	3.2	0.40	—	—
Zr pure	0.63	4.12	—	0.27	2.4	0.62	0.88	—
Zry-2	—	—	—	—	—	0.40	1.15	—
Zry-4	—	—	6.36	—	—	—	—	—

18.4.2 Expériences d'oxydation

Pendant ce projet de thèse, les expériences ont été effectuées pour obtenir des échantillons avec des conditions d'oxydation différentes par rapport à ceux de CEZUS. Les expériences d'oxydation ont été menées in-situ dans un MEBE (microscopie à balayage environnemental), dans un autoclave dans la vapeur d'eau et dans des fours dans l'air sous pression ambiante.

Les expériences d'oxydation in-situ étaient conçues de telle manière qu'un maximum d'information sur la première phase d'oxydation pouvait être obtenu par le MEBE, en étudiant la situation avant et après l'oxydation. Pour étudier les changements par oxydation, la caractérisation des surfaces polies et oxydées a été faite avec AFM (microscopie à force atomique) et MEB (microscopie à balayage). Les expériences in-situ MEBE ont été conduites, tenant les échantillons dans des récipients en platine, pour 60 minutes ou plus longtemps aux conditions désirées (415°C / 700°C dans la vapeur d'eau à 1.3 mbar). Après les analyses avec MEB et AFM, d'autres caractérisations ont été faites avec MEB / EDS (energy dispersive x-ray spectroscopy) sur les surfaces et sur des coupes transversales préparées par FIB (focused ion beam). L'oxydation dans l'autoclave était effectuée pour de petits échantillons à 415°C et avec une pression de 100 bar pour de différentes durées d'oxydation (1 h, 24 h and 72 h). Les expériences d'oxydation dans des fours ont été menées dans l'air ambiant et avec pression ambiante à 415°C pour 1 et 24 heures.

18.5 Méthodes de caractérisation

Les méthodes expérimentales utilisées ont permis de caractériser toute une variété de propriétés des alliages oxydés. Les différentes méthodes seront décrites brièvement selon les procédures de caractérisation appliquées. Des détails seront délivrés pour les techniques non-standards et les paramètres spécifiques pour le système de matériau étudié.

AFM était appliquée pour mesurer le changement de topographie de la surface par oxydation. MEB était utilisée pour la caractérisation de la surface, pour identifier des endroits intéressants pour préparer des échantillons de MET (microscope électronique en transmission) et pour faire des analyses chimiques qualitatives avec EDS. Le MEBE était utilisé pour des expériences d'oxydation dans un milieu avec une pression qui est considérablement augmentée par rapport aux MEB conventionnels et avec la possibilité d'utiliser un chauffage. Dans le MET la microstructure, l'état d'oxydation et la distribution des éléments d'alliages dans la couche d'oxyde étaient étudiés. La distribution de taille des précipités était déterminée dans le MET, et pour l'analyse chimique les méthodes EDS et EELS (electron energy loss spectroscopy) ont été utilisés. La dureté était testé par indentations pour obtenir des indices sur les profils étendus de diffusion d'oxygène et la nano-indentation était utilisée pour mesurer le module de Young dans la couche d'oxyde.

18.5.1 Préparation d'échantillons

Les échantillons étaient coupés des pièces oxydés avec une scie à fil et meulés (papier de SiC) et polis (suspension de diamant neutre) pour éliminer l'endommagement par les étapes de meulage précédent. Quelques échantillons ont vu un traitement final par polissage avec le "Vibromat" dans une solution de silice basic. Pour la détermination de la distribution de tailles des précipités, des disques métalliques minces étaient polis par jet électrolytique pour obtenir une surface assez grande et électro-transparente. Le FIB était appliqué pour préparer des coupes transversales aux endroits spécifiques de l'oxyde pour créer des échantillons de MEB et MET avec la technique de 'lift-out'. Des membranes de zirconia libre pour des 'bulge tests' étaient préparés par polissage électrolytique en éliminant la partie métallique d'un côté dans une zone circulaire ; le côté d'oxyde était protégé par une couche transparente de paraffine.

18.6 Caractérisation du matériau original et expériences d'oxydation

18.6.1 Caractérisation des précipités dans le matériau original

La distribution de taille des précipités était déterminée dans le MET avec des échantillons électro-polis, les résultats sont décrits dans Tableau 30. La distribution complète de taille pour les matériaux avec de grands précipités, Zr1%Fe et Zr1%Ni, est donnée dans figure 1. On peut observer une dispersion de distributions de tailles pour plus étendue pour des précipités Zr_3Fe comparés avec Zr_2Ni . Dans figure 2, les Zr1%Cr et Zr0.6%Nb sont présentés. La part de précipités de taille comprise entre 10 et 40 nm est plus grande pour $ZrCr_2$ par rapport à ceux de $\beta-Nb$, dont la dispersion de taille est aussi plus étendue qu'on peut percevoir par l'écart-type plus large (Tableau 30). Après traitement thermique Zr1%Cr montre des précipités avec une taille en moyenne plus large et avec une dispersion plus étendue par rapport au matériau original.

18.6.2 Résultats des expériences d'oxydation supplémentaires

En plus des échantillons oxydés délivrés par CEZUS, voir colonne 1 à 3 dans Tableau 29, d'autres échantillons ont été oxydés in-situ (colonne 4 et 5) et dans un autoclave dans la vapeur d'eau pour des durées plus courtes (colonne 6 à 8). Ces expériences ont été faites pour obtenir un plus d'information sur le début d'oxydation. A part des alliages binaires et de zirconium pur, aussi Zircaloy-2 et Zircaloy-4 avec des conditions d'oxydation sélectionnées ont été inclus, qui a permis de faire une comparaison des comportements d'oxydation des précipités de ces alliages commerciaux avec ceux des alliages modèles.

18.7 Microstructure d'alliages oxydés in-situ

Pour rendre les informations plus compactes les observations in-situ et les résultats de caractérisation microstructurale ne sont données que pour Zr1%Fe ; les résultats qui restent sont seulement montrés d'une manière générale sans aller dans les détails.

Tableau 30: Distribution de tailles des précipités des échantillons électro-polis MET ; data des tailles de grain de CEZUS (sauf Zr0.6%Nb)

	Zr1%Fe	Zr1%Ni	Zr1%Cr	traitem. therm. Zr1%Cr	Zr0.6%Nb
moyenne de diamètre de précipité / nm	261	252	35	89	47
écart-type / nm	229	120	17	40	24
médiane / nm	167	240	30	80	43
minimum diamètre / nm	23	31	9	23	10
maximum diamètre / nm	861	597	126	282	145
nombre des précipités mesurés	111	109	624	293	286
moyenne de taille de grain du métal / μm	3.1	4.6	5.2	-	4.4
écart-type / μm	1.0	2.2	2.9	-	1.6
nombre des grains mesurés	-	-	-	-	55

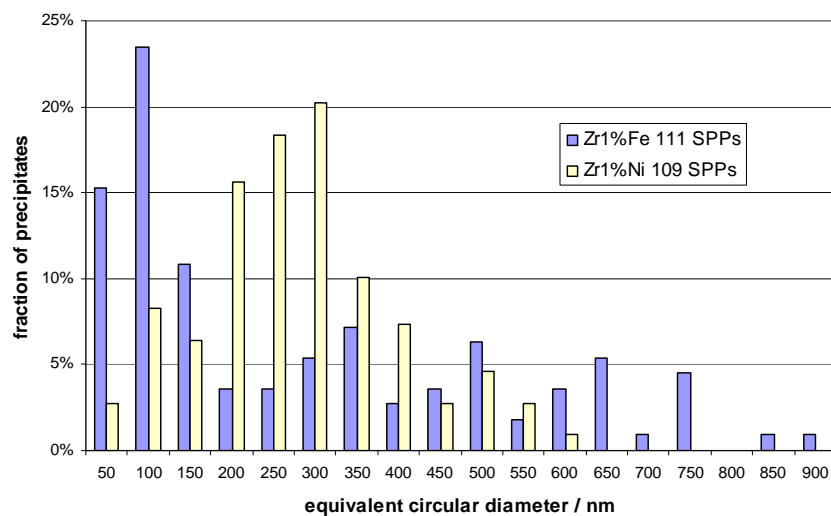


Figure 112: Distribution de taille des précipités pour Zr1%Fe et Zr1%Ni ; précipités d'une classe de taille (50 nm) en fonction du diamètre circulaire équivalent.

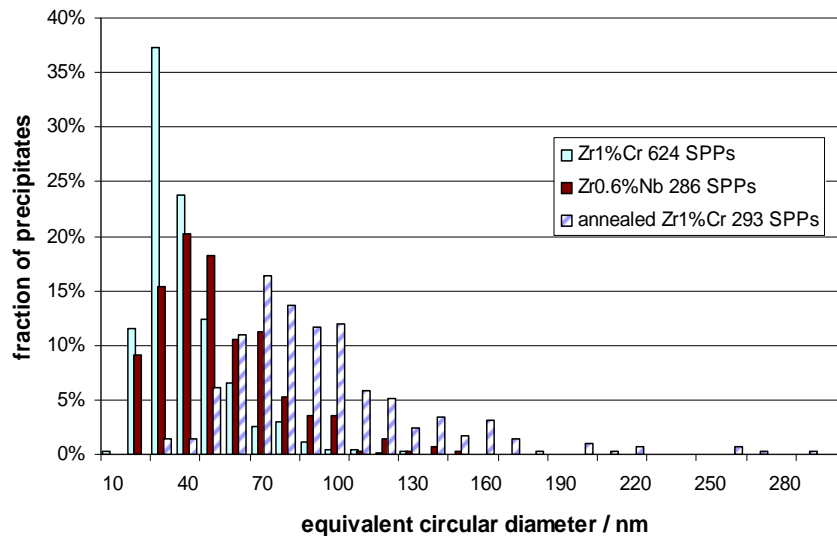


Figure 113: Distribution de taille des précipités pour Zr1%Cr et Zr0.6%Nb ; précipités d'une classe de taille (50 nm) en fonction du diamètre circulaire équivalent.

18.7.1 Oxydation in situ à 415°C

Les expériences in-situ à 415°C ont été effectuées pour obtenir des clarifications expérimentales sur le démarrage d'oxydation, avec la même température que celle utilisée pour les expériences d'autoclave, et pour observer les modifications de la surface et la formation potentielle des fissures. Les observations du procédé d'oxydation par MEBE ont permis dans une lapse de temps adapté aux évolutions de la surface (c'est à dire les premières minutes d'oxydation) d'analyser cette surface; ce qui n'est pas possible par des expériences de corrosion conventionnelles.

Pendant l'oxydation in-situ de Zr1%Fe de petites particules apparaissaient sur la surface (figure 3a-d). Une comparaison des profils de AFM avant et après l'oxydation montraient que de la surface de l'oxyde montre une protubérance pour des particules plus larges, qui n'existaient pas avant l'oxydation (p.ex. Figure 19). On pouvait montrer par EDS que les particules larges sont corrélés avec des précipités qui contiennent du fer. Pour les petites particules à la surface un signal de fer a été enregistré qui était plus élevé que pour les précipités en-dessous ; malheureusement leurs tailles ne permettaient pas une caractérisation plus détaillée dans le MEB. Dans le cas de Zr1%Ni et après polissage neutre, en-dessus des précipités oxydés il n'y avait pas de formation des caractéristique riche en Ni à la surface. Après 2 heures d'oxydation une fissuration de la surface de quelques protubérances oxydés était observée. Zr1%Cr, Zr0.6%Nb et zirconium pur ne montraient pas de changements à la surface pendant les observations in-situ qui pourraient être liés avec la présence des précipités.

En résumé : Les profils de AFM de la surface montraient la présence des protubérances pour Zr1%Fe et Zr1%Ni qui sont liés avec les précipités oxydés en-dessous dans la matrice (Tableau 31). Pour Zr1%Cr, Zr0.6%Nb et zirconium pur, on ne pouvait pas observer des protubérances qui pourrait être liés avec des précipités, surtout à cause de la petite taille des précipités dans les deux alliages binaires. Néanmoins, la rugosité de la surface des trois derniers matériaux était quand même considérable.

Des coupes transversales de FIB confirmaient la corrélation entre les protubérances et les précipités ; aux endroits où il y avait un protubérance à la surface, toujours un précipité pouvait être trouvé en-dessous, comme illustré dans figure 4 avec une flèche noir montrant sur le précipité et une flèche blanche montrant sur le protubérance. L'interface métal-oxyde est ondulée et l'amplitude de l'ondulation est souvent plus élevée aux endroits où se trouvent de précipités oxydés. Ces observations sont comparables pour Zr1%Fe and Zr1% Ni, mais Zr1%Cr, Zr0.6%Nb et zirconium pur présentent pas de précipités ou des précipité beaucoup plus petits en sorte qu'il n'y a pas d'influence sur l'ondulation de l'interface métal-oxyde.

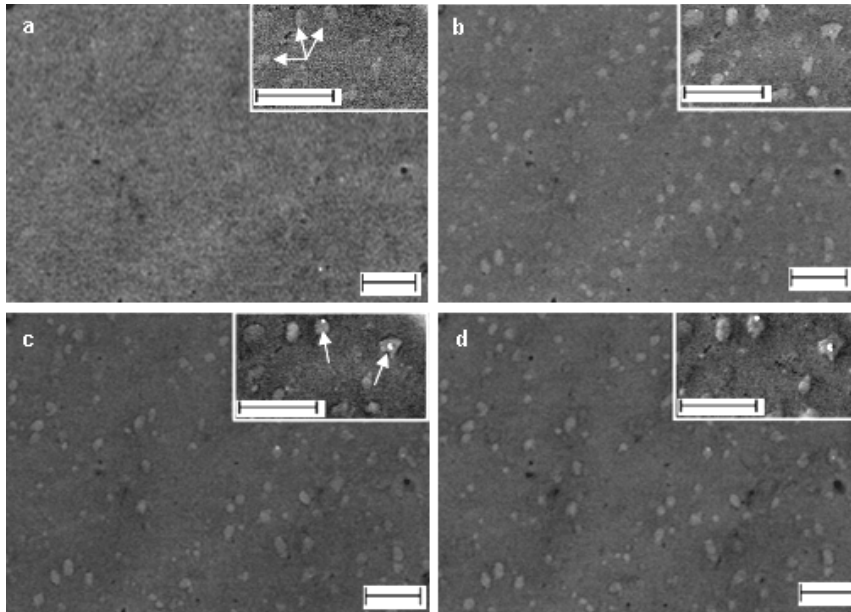


Figure 114: Les images MEBE avec le détecteur GSE de Zr1%Fe à 415°C montrent la surface (a) avant l'oxydation, (b) in-situ après 14 minutes, (c) in-situ après 54 minutes et (d) après refroidissement à la température ambiante. Les petites images insérées présentent des régions avec une magnification plus élevée. Toutes les barres d'échelle représentent 5 µm.

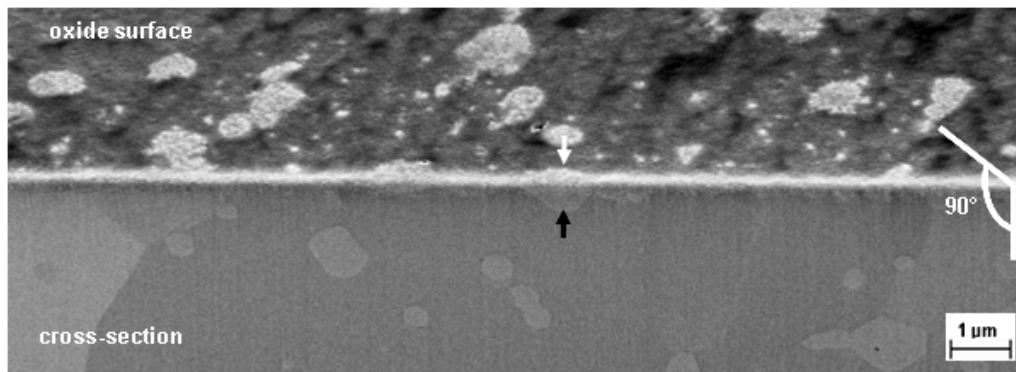


Figure 115: Coupe transversale de FIB de Zr1%Fe ; lien directe entre la caractéristique à la surface (flèche blanche) et le précipité en-dessous (flèche noire).

Tableau 31: paramètres des échantillons oxydés in-situ

Alliage	Moyenne d'épaisseur d'oxyde / µm ϕ	RMS polis (5x5 µm) / nm	RMS oxydé (5x5 µm) / nm	Moyenne d'hauteur des protubérances / nm *	Moyenne de diamètre des protubérances / µm *
Zr1%Fe	0.32 ± 0.11	3.9	21.2 †	68 ± 15	1.1 ± 0.3
Zr1%Ni	0.41 ± 0.11	5.2	10.3 †	19 ± 6	0.7 ± 0.5
Zr1%Cr	0.35 ± 0.07	3.8	8.3	pas possible de détecter	
Zr0.6%Nb	0.34 ± 0.09	5.3	9.3	pas possible de détecter	
Pure Zr	0.27 ± 0.05	3.8	11.2	pas possible de détecter	
Zr1%Ni °	0.24 ± 0.17	3.0	12.2	80 ± 38	
Zr1%Cr °	0.28 ± 0.17	2.7	16.2	53 ± 16	
annealed					

ϕ moyenne des coupes transversales de FIB, † contient les protubérances spécifiques, RMS: root mean square of roughness, * de 10 profiles AFM, ° polissage de vibration

L'interface métal-oxyde et la microstructure des précipités étaient analysés avec le microscope électronique en transmission ; une coupe transversale MET de Zr1%Fe est montrée dans figure 5. Dans le mode en champ sombre, la couche d'oxyde de la matrice et la plus épaisse couche d'oxyde du précipité qui est en contact avec la surface se laissent bien identifier ; des flèches indiquent l'interface métal-oxyde. Une analyse plus détaillée de la microstructure de l'oxyde de précipité révèle des grains fins et axés en même direction. La zircone pure créée sur la matrice montre une structure de grains en forme de colonne. Des cristaux de magnétite pouvaient être trouvés par diffraction d'électrons à la surface de quelques précipités oxydés dans Zr1%Fe, qui eux-mêmes contiennent du fer. Le comportement d'oxydation des précipités dans Zr1%Ni et Zr1%Fe est similaire : dans les deux cas l'oxydation du précipité est accélérée par rapport au reste de la matrice quand le précipité est en contact avec la surface. Si le précipité est encore complètement inclus dans la matrice, le taux d'oxydation du précipité et de la matrice est comparable. Les précipités dans Zr1%Cr et Zr0.6%Nb montrent une oxydation décélérée ; de petites fissures sont produites à l'interface entre le précipité et son oxyde au côté montrant vers la surface extérieure.

L'analyse EDS des précipités donne les informations suivantes : Les précipités dans Zr1%Fe et Zr1%Ni sont oxydés dans et comme l'oxyde de la matrice. Les précipités dans Zr1%Cr et Zr0.6%Nb présentent moins d'oxygène que la matrice voisine ; la méthode de différentiel entre le signal de la matrice et du précipité est décrite dans le chapitre de discussion. A cause de la taille de très petits précipités dans Zr1%Cr qui ne permettait pas une analyse d'une potentielle ségrégation pendant l'oxydation, des tests avec prétraitement thermique ont été faits. Le matériau traité présente des précipités plus larges (voir Tableau 31). Les précipités de ce Zr1%Cr forment aussi des protubérances à la surface, mais seulement une couche très mince en contact avec la surface s'oxyde et le reste du précipité reste métallique pendant cette phase d'oxydation. Comme il n'y avait pas d'analyses des couches d'oxyde plus épaisses, il n'est pas possible de conclure l'épaisseur finalement nécessaire pour faire oxyder ces précipités plus larges.

18.8 Microstructure des alliages oxydés en autoclave

Suivant la procédure ASTM G2, la surface des échantillons ont été décapés à l'acide avant l'oxydation en autoclave, induisant un état de surface plus rugueux. Les échantillons ont été testés dans l'air et dans la vapeur d'eau à la pression atmosphérique pendant 3 jours et sous 10.5 MPa pendant 110 jours. Le choix de ces environnements révèle l'influence de l'air et de la vapeur aussi bien que de la pression et du temps d'oxydation. Cependant, pour les échantillons disponibles, les changements de paramètres étant simultanés, l'identification des effets paramètre par paramètre est impossible.

18.8.1 Oxydation pendant 3 jours dans l'air à la pression ambiante

L'examen par MEB et EDS de la surface de Zr1%Fe a révélé, pour cet environnement, la présence d'oxyde de fer sous la forme d'agglomérats de petits cristaux déposés en surface (Figure 50). Pour Zr1%Ni, Zr1%Cr et Zr0.6%Nb, aussi bien que pour Zr pur, ce phénomène n'a pas été observé. Dans cette condition d'oxydation, des fissures de surface d'une longueur

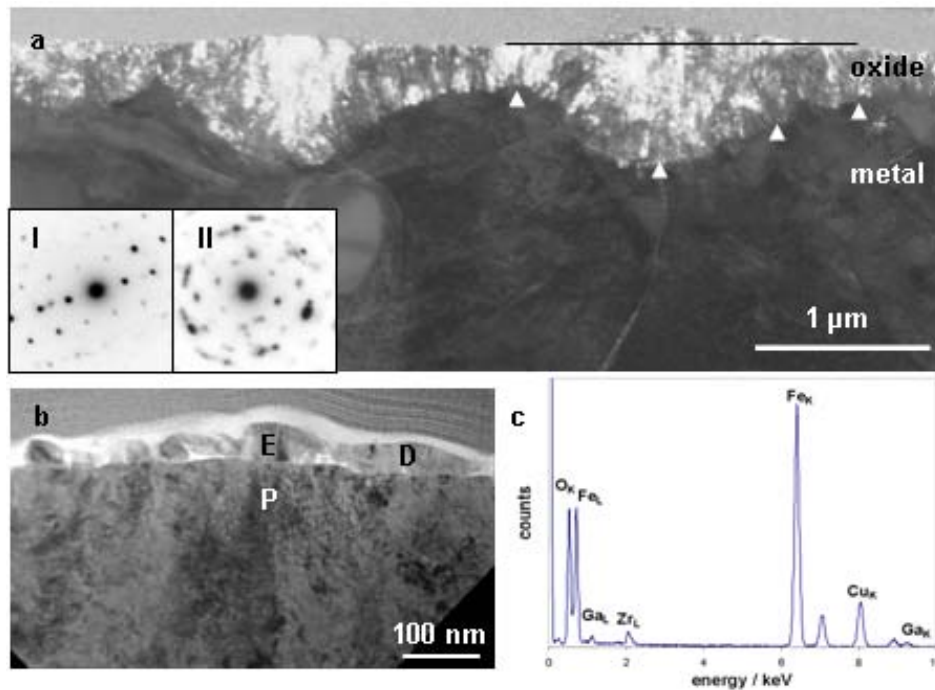


Figure 116: (a) Contraste en champ sombre de Zr1%Fe. Ondulations de l'interface d'oxyde et bosses de surface peuvent être observées lorsque le précipité est en contact avec la surface. (b) Contraste champ clair montrant les cristaux d'oxyde de fer formés à la surface de l'oxyde. (c) Spectre EDS du cristal de la figure (b) à la position marquée E. Le signal Cu provient de la grille FIB-MET et le signal Ga provient de l'implantation pendant la préparation de l'échantillon MET. En E, la composition est de 63.5 at.% O, 34 at.% Fe et 2 at.% Zr, et en P 69 at.% O, 3.5 at.% Fe et 27 at.% Zr. Les deux encarts dans la figure (a) montrent la figure de diffraction d'un cristal d'oxyde de fer (I) en D et du précipité oxydé sous-jacent (II) en P.

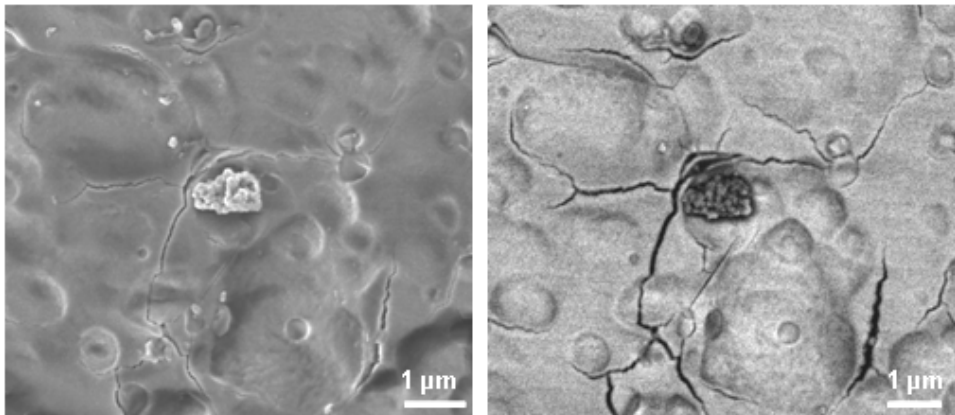


Figure 117: Micrographies MEB de la surface de Zr1%Fe montrant l'agglomérat d'oxyde de fer à la surface et des fissures dans le dépôt d'oxyde.

allant jusqu'à plusieurs micromètres ont été trouvées. Ces fissures de surface sont souvent présentes dans les cratères produit par le décapage à l'acide dans le cas de Zr1%Fe et Zr1%Ni, alors que les autres matériaux avec de plus petit, voir pas, de précipités ne présentent pas de tels cratères.

La rugosité de surface induite par les cratères de décapage peut aussi s'observer sur les sections transverses obtenues par FIB. L'interface métal-oxyde est ondulée et l'épaisseur de l'oxyde varie considérablement.

Les micrographies MET révèlent un comportement de type oxydation de précipités, qui peut-être divisé en oxydation similaire à la matrice environnante (Zr1%Fe et Zr1%Ni) et oxydation de précipités différée (Zr1%Cr et Zr0.6%Nb). Les micrographies de la Figure 52 montrent le dépôt d'oxyde complet ainsi que l'interface métal-oxyde et l'agglomérat de cristaux d'oxyde de fer (flèche blanche). Un précipité Zr_3Fe partiellement oxydé est visible sur la Figure 53 à l'interface métal-oxyde.

Les précipités oxydés ont un aspect finement granulé qui contraste avec la matrice colonnaire environnante. Des fissures de l'ordre du micromètre sont aussi visibles. Les précipités présents dans l'oxyde étaient complètement oxydés dans le cas de Zr1%Fe; dans le cas de Zr1%Cr et Zr0.6%Nb, un niveau d'oxygène plus faible que dans la matrice environnante a été mesuré.

18.8.2 Oxydation sous vapeur pendant 3 jours à pression ambiante

Pour Zr1%Fe, les analyses MEB et EDS ont révélé la présence d'oxyde de fer sous la forme d'agglomérats de petits cristaux en surface (Figure 61). Dans quelques cas, de plus gros cristaux d'oxyde de fer d'une taille de l'ordre de quelque centaine de nanomètres ont été trouvés. Pour cet environnement et cette durée d'oxydation, des fissures de surface ont été observées sur tous les échantillons. Pour Zr1%Ni, de petits cristaux riches en nickel ont été observés à la surface externe de certains précipités. Les sections transverses FIB montrent un film d'oxyde d'épaisseur variable et de larges fissures orientées parallèlement à la surface (Figure 62) pour Zr1%Fe, ceci étant aussi valable pour les autres matériaux. Les micrographies MET présentées Figure 63 montrent les cristaux d'oxyde à la surface et l'interface métal-oxyde de Zr1%Fe. Pour les précipités proches de la surface externe, de petits cristaux d'oxyde de fer sont observés à leur verticale en surface pour Zr1%Fe. Pour Zr1%Ni, les petits précipités riches en nickel ont été identifiés comme nickel métallique par le biais de l'analyse EDS et de la diffraction électronique. Les précipités à l'interface métal-oxyde (Figure 63c) montrent un comportement à l'oxydation similaire à la matrice de zirconium environnante (Zr1%Fe et Zr1%Ni), aucun précipité métallique n'étant observé dans l'oxyde. Pour Zr1%Cr et Zr0.6%Nb une oxydation différée a été observée accompagnée par de petites fissures à l'interface précipité-oxyde en face de la surface extérieure. L'oxyde de la matrice est de type colonnaire et orienté parallèlement à la direction de croissance de l'oxyde. Dans le précipité oxydé, une petite fissure orientée perpendiculairement à la direction de croissance de l'oxyde est observable.

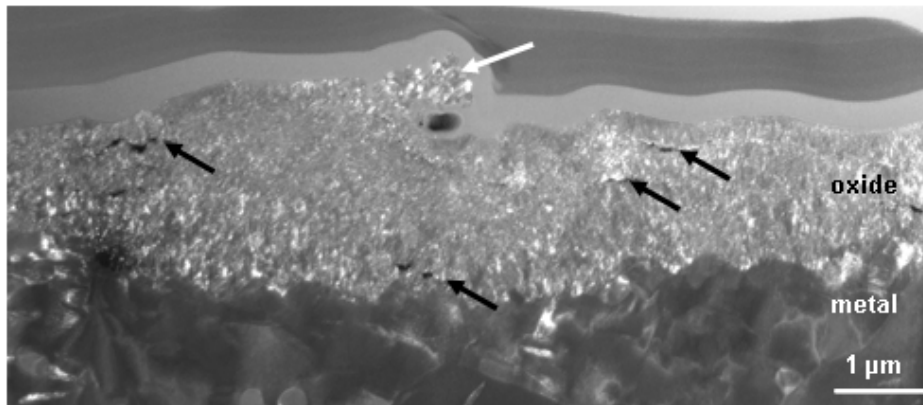


Figure 118: Contraste en champ sombre de l'oxyde formé sur Zr1%Fe oxydé pendant 3 jours à l'air avec une particule d'oxyde de fer à la surface (flèche blanche). Les fissures dans l'oxyde sont repérées par des flèches noires.

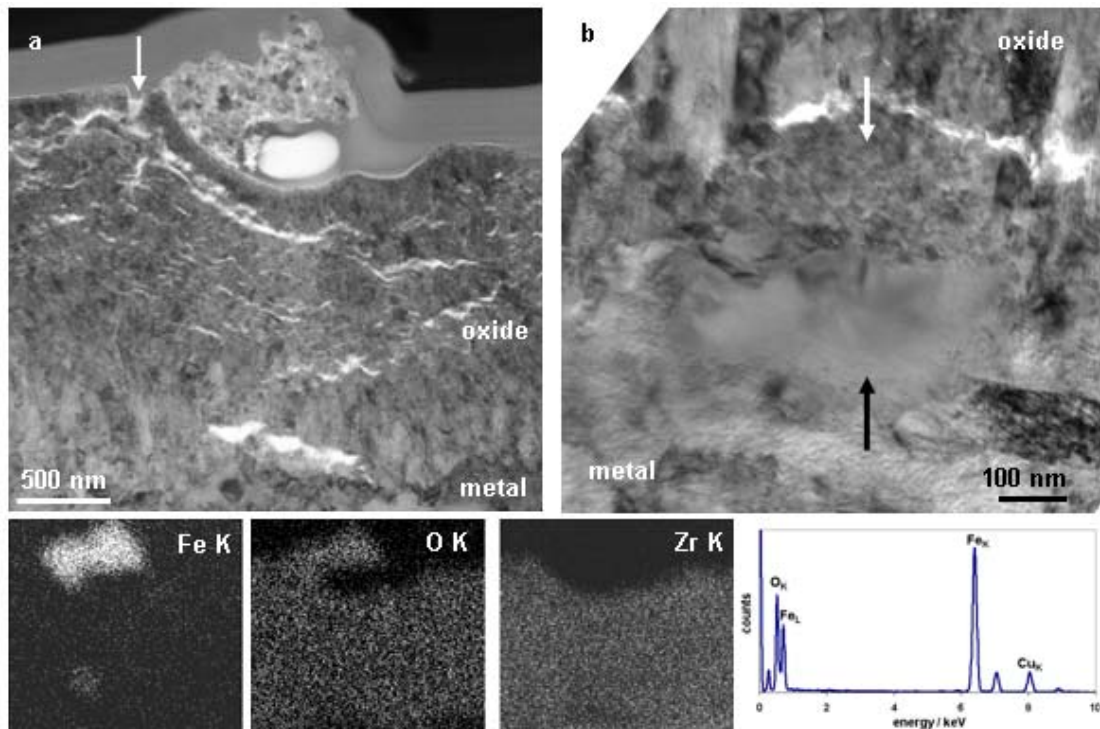


Figure 119: Contraste en champ clair des particules d'oxyde de fer en surface de l'échantillon présenté aussi Figure 52. La carte EDS correspondante démontre que les particules à la surface sont constituées d'oxyde de fer pur (la carte présente une faible rotation par rapport à la micrographie champ clair). L'analyse EDS ponctuelle montre que seul l'oxyde de fer est présent, exclusion faite du cuivre de la grille MET ainsi que de l'oxygène et du fer. (b) Contraste en champ clair présentant un précipité partiellement oxydé à l'interface métal-oxyde ; la partie oxydée est repérée par une flèche blanche et la partie métallique par une flèche noire.

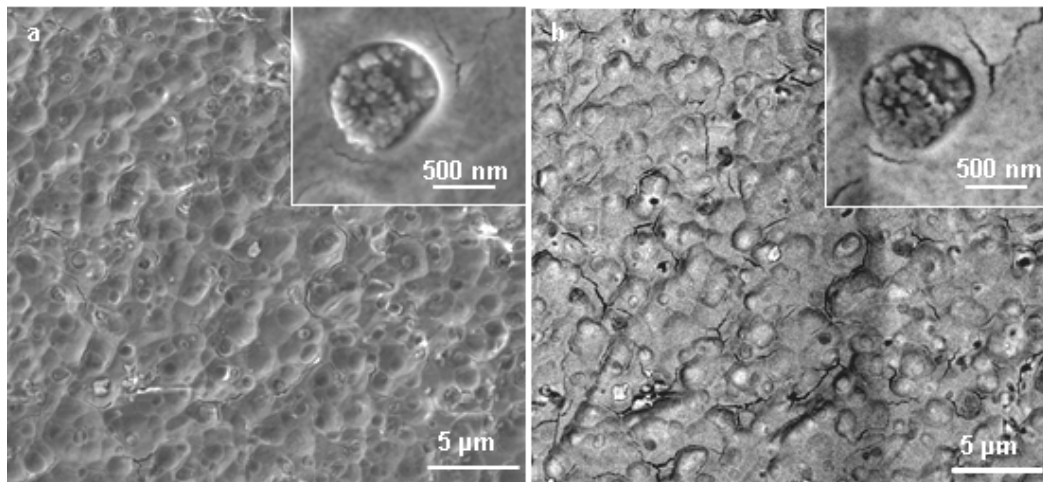


Figure 120: Surface de Zr1%Fe montrant les cristaux en surface. (a) image MEB et (b) image MEB en mode BSE de la même région. Les régions gris sombres sur l'image (b) correspondent aux cristaux d'oxyde de fer et les régions noires sont dues à la contamination pendant les manipulations et le stockage. Les encarts montrent un cristal d'oxyde de fer en fort grossissement. Des fissures sont visibles à la surface.

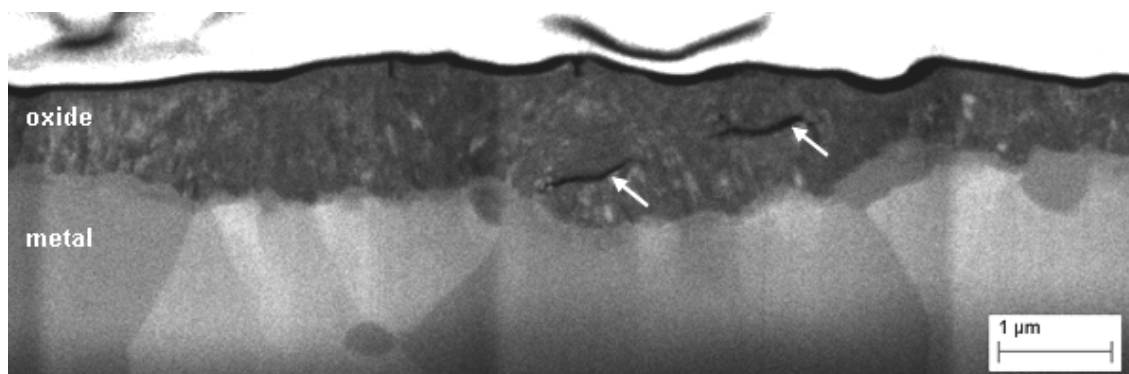


Figure 121: Section transverse FIB de Zr1%Fe oxyde sous vapeur pendant 3 jours. Les flèches blanches repèrent des fissures importantes dans le dépôt d'oxyde.

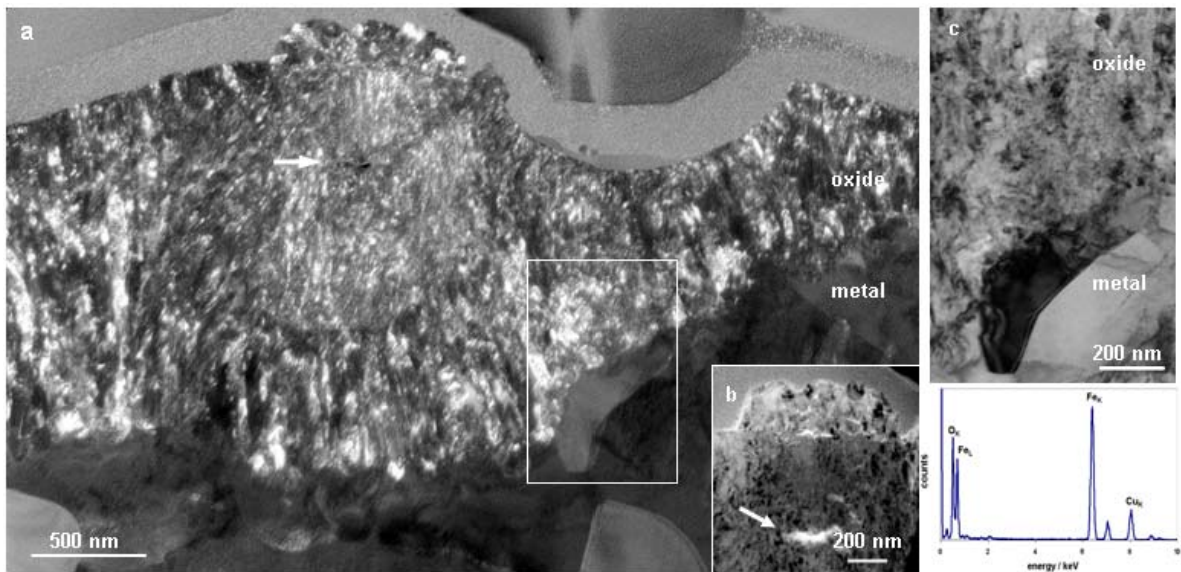


Figure 122: (a) image MET en champ sombre de Zr1%Fe oxydé pendant 3 jours sous vapeur montrant les particules d'oxyde de fer pur à la surface et la matrice à structure colonnaire. (b) Contraste en champ clair montrant les particules d'oxyde de fer pur en surface. (c) Contraste en champ clair d'un précipité partiellement oxydé à l'interface métal-oxyde; la position est indiquée par la flèche blanche sur l'image (a). Le spectre EDS provient d'une particule d'oxyde de fer en surface.

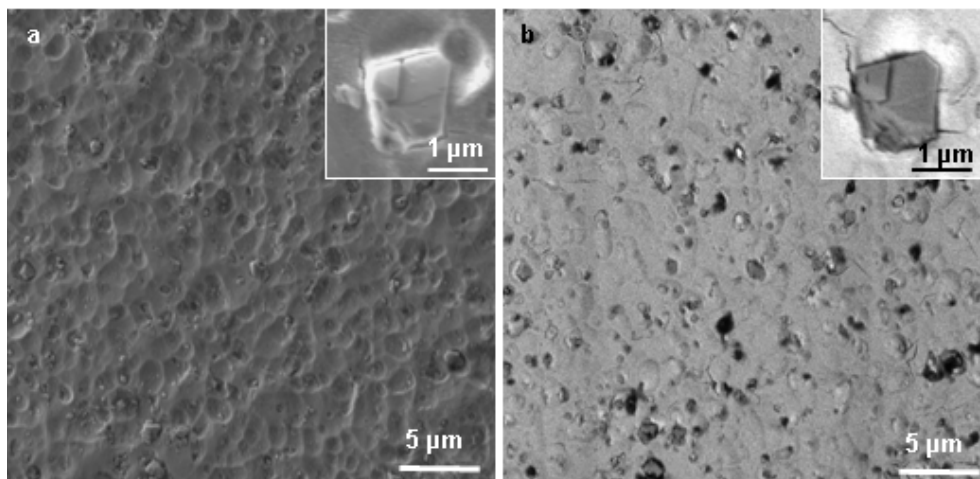


Figure 123: Surface de Zr1%Fe oxydé pendant 110 jours sous vapeur d'eau montrant les cristaux d'oxyde de fer en surface. (a) Image MEB et (b) image MEB-BSE de la même région. Les régions gris sombres sur l'image (b) correspondent aux cristaux d'oxyde de fer et les régions noires sont dues à la contamination pendant les manipulations et le stockage.

18.8.3 Oxydation sous vapeur à 10.5 MPa pendant 110 jours

A la surface de Zr1%Fe oxydé pendant 110 jours en autoclave, l'analyse MEB etEDS a révélé la présence de larges cristaux d'oxyde de fer en surface. Les fissures présentes à la surface ont une longueur pouvant aller jusqu'à plusieurs microns pour tous les alliages binaires et sont souvent présentes aux cratères de décapage pour Zr1%Fe et Zr1%Ni.

Les fissures dans l'oxyde (par exemple Figure 72) sont orientées perpendiculairement à la direction de croissance de l'oxyde et sont présentes dans tout le dépôt d'oxyde. Les ondulations de l'interface métal-oxyde sont corrélées avec la présence de fissures importantes dans l'oxyde; l'épaisseur de l'oxyde est souvent réduite pour les régions ne présentant pas de fissures importantes proches de l'interface métal-oxyde. Ces sections n'ont pas révélé de corrélation particulière entre les ondulations de l'interface métal-oxyde et la présence de précipités. Concernant la présence d'importantes fissures et les ondulations de l'interface métal-oxyde, on peut constater que la présence de fissures semble aller de pair avec un front d'oxydation différée. Cependant, il n'est pas possible de quantifier ce phénomène plus avant et il n'est ainsi pas possible de conclure lequel de ces deux phénomènes est la cause et lequel est la résultante.

Pour Zr1%Fe et Zr1%Ni, une oxydation précipitée similaire à la matrice environnante peut être justifiée par la présence de gros précipités à l'interface métal-oxyde observés sur les sections FIB, ces derniers étant oxydés du côté de l'oxyde et métallique du côté du métal.

En analyse MET, l'oxyde de fer à la surface de Zr1%Fe a été identifié par diffraction électronique comme étant de la magnétite (Figure 74). La diffraction X n'a pas permis de fournir une réponse car les pics observés étaient trop étendus et faibles pour permettre une identification non-ambigüe de la phase d'oxyde de fer, de plus le spectre EELS n'était pas spécifique à un type d'oxyde de fer (Figure 75). L'oxyde affiche d'importantes fissures orientées perpendiculairement à la direction de croissance, la plus grande fissure s'étendant sur environ 2 μm sur la micrographie présentée. L'existence de telles fissures est commune à tous les alliages binaires. A l'interface métal-oxyde, les précipités de Zr1%Fe et Zr1%Ni présentent un front d'oxydation similaire à la matrice environnante, voir aussi encart II de la Figure 75. Dans Zr1%Cr et Zr0.6%Nb, une oxydation précipitée différée a été observée pour des précipités dans l'oxyde jusqu'à une distance de 1 μm de l'interface métal-oxyde.

Pour les précipités dans Zr1%Fe, il a été possible de montrer par analyse EELS que l'état d'oxydation du fer dans les précipités de l'oxyde et celui de l'oxyde de fer pur étaient identiques. Ainsi, la présence possible de fer non-oxydé dans l'oxyde n'a pas été observée pour les alliages binaires étudiés ici. A partir des résultats obtenus, nous n'avons pas de preuve de l'existence de précipités ayant un état d'oxydation différent de celui des éléments d'alliage qu'il contient. Pour Zr₂Ni cela n'a pas été démontré (pas d'analyse EELS).

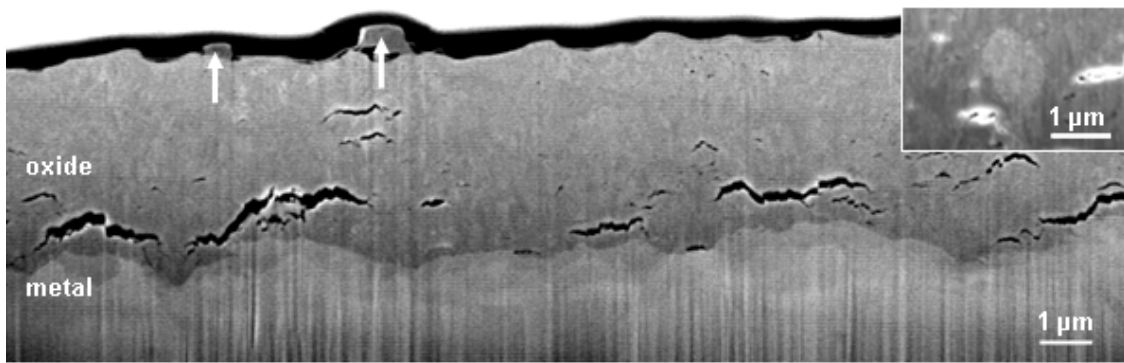


Figure 124: Section FIB de Zr1%Fe oxydé pendant 110 jours sous vapeur d'eau montrant une épaisse couche d'oxyde et une interface métal-oxyde ondulée. Deux cristaux d'oxyde de fer peuvent être observés en surface (flèches blanches). Les précipités dans l'oxyde ont un contraste plus brillant que la matrice de zircone (encart), la structure colonnaire étant là aussi observable.

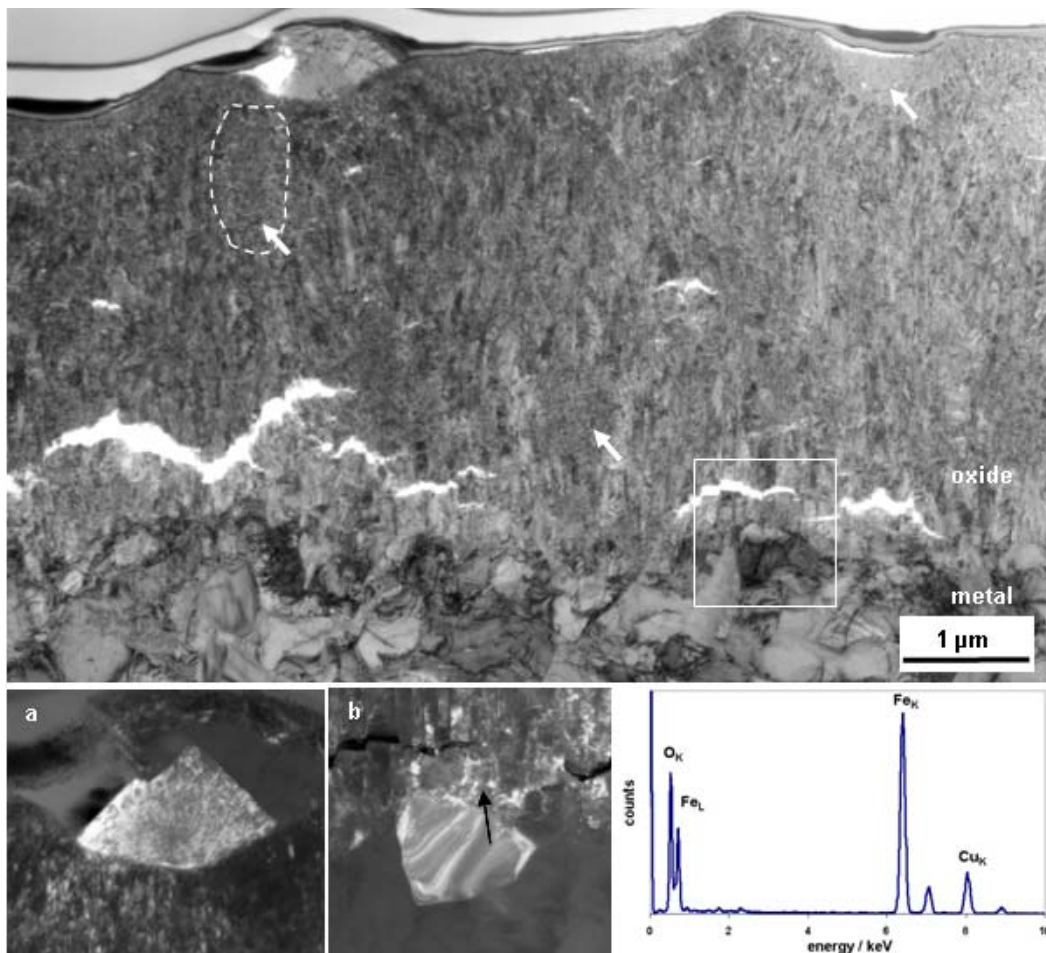


Figure 125: Contraste en champ clair de Zr1%Fe oxydé pendant 110 jours sous vapeur montrant un cristal d'oxyde de fer pur en surface, la matrice colonnaire de la couche d'oxyde épaisse et l'interface métal-oxyde ondulée. Les précipités présentent un oxyde equiaxé (repéré par des flèches blanches). L'encart 1 présente, en champ sombre, uniquement la partie cristalline de l'oxyde de fer en surface. Un précipité partiellement oxydé à l'interface métal-oxyde est visible dans le cadre blanc (encart 2). Le spectre EDS provient du cristal d'oxyde de fer en surface.

18.8.4 Comparaison du comportement du fer sous différentes conditions d'oxydation

Pour toutes les conditions d'oxydation, la formation de cristaux d'oxyde de fer a été observée à la surface des échantillons Zr1%Fe. Après 1 heure, les cristaux d'oxyde de fer étaient petits et disséminés sur quelques précipités dans l'oxyde. Pour les oxydations pendant 1 et 3 jours, la quantité de cristaux d'oxyde de fer présents sur les précipités oxydés était plus importante après 1 heure, et après 110 jours, d'importants cristaux d'oxyde de fer d'une taille allant jusqu'à quelques microns s'étaient formés. L'analyse par diffraction électronique a révélé la présence d'une phase cubique avec une figure de diffraction similaire à celles généralement observées pour la magnétite ou la maghémite. Pour les précipités oxydés sous-jacents à l'oxyde de fer en surface, une déplétion graduelle en fer a été observée, cette déplétion augmentant au cours du temps. À partir de la quantité d'oxyde de fer et de l'estimation de la surface couverte, un coefficient de diffusion effectif pour le transport du fer en surface a pu être estimé (voir discussion **Error! Reference source not found.**). L'oxydation *in-situ* et dans sur des échantillons non décapés démontre que ce phénomène n'est pas restreint aux surfaces décapées ou à l'oxydation sous vapeur d'eau.

18.8.5 Comparaison des différents alliages binaires et de leurs conditions d'oxydation

La matrice d'oxyde est de structure colonnaire pour tous les matériaux étudiés, les grains de l'oxyde étant orientés dans la direction de croissance de l'oxyde. Aucune différence significative n'a été observée entre les grains colonnaires des différents matériaux. Plus le temps d'oxydation est important, plus il est fréquent d'observer des fissures importantes dans le dépôt d'oxyde. De petites fissures ont été systématiquement observées dans la partie externe de l'oxyde, proches de la surface extérieure. La structure de l'oxyde est finement granulée et avec des précipités oxydés equiaxés dans Zr1%Fe, Zr1%Cr et Zr0.6%Nb, comme cela est visible sur les micrographies. Pour Zr1%Ni, à cause de l'absence d'observations claires de la partie oxydée des précipités, il n'est pas possible de déterminer la microstructure de l'oxyde.

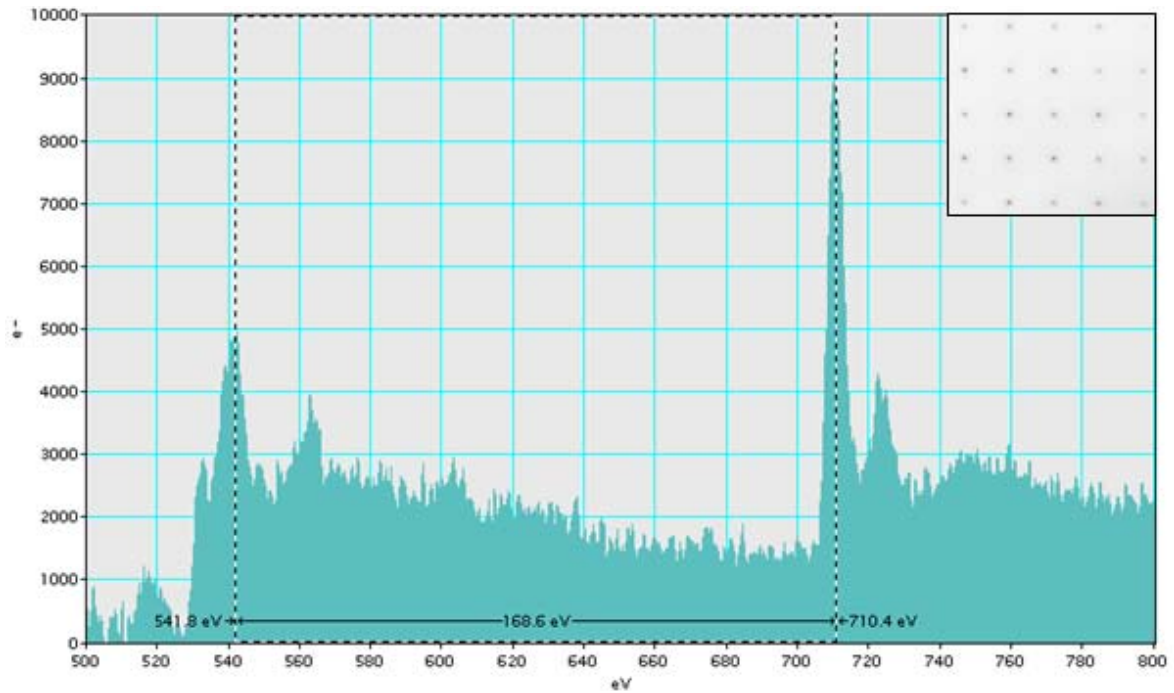


Figure 126: Les spectres de perte d'énergie, indiquent la présence des signaux de Fe- $L_{2,3}$ et O-K pour les cristaux d'oxyde de fer à la surface. Le cliché de diffraction avec l'axe de zone [100] correspond à une maille cubique avec un paramètre de maille de 0.82 nm.

Table 32: Exemples représentatifs pour différentes conditions d'oxydation concernant la présence des cristaux d'oxyde de fer à la surface et correspondance en chaque cas avec les précipités immédiatement en-dessous de la surface.

	SE	BSE	TEM	EDS
in situ (ESEM) 130 Pa 1 hour vapeur				
autoclave 0.1 MPa 3 days steam				
autoclave 10.5 MPa 110 days steam				

18.9 Autres conditions d'oxydation choisies

18.9.1 Autres conditions d'oxydation pour les alliages binaires

Le comportement à l'oxydation dans l'air de précipités en contact avec la surface extérieure a été examiné par cuisson en four à 415°C pendant 1 et 24 heures d'échantillons polis. Ces oxydations montrent que la formation d'oxyde de fer en surface des alliages binaire contenant du fer peut être observée aussi pour une oxydation à l'air aussi bien qu'à l'eau. Pour les autres éléments d'alliage, la formation d'oxyde de l'élément d'alliage en surface n'a pas été observée. Les échantillons préparés avec un polissage non-neutre sont sujet à une attaque accélérée de précipités en comparaison aux échantillons préparés par un procédé neutre.

18.9.2 Oxydation des Zircaloy en autoclave sous vapeur à 415°C

Le comportement à l'oxydation des précipités $Zr_2(Fe,Ni)$ a été étudié sur un échantillon de Zircaloy-2 oxydé à 415°C pendant 1 jour sous vapeur à une pression de 415°C. Pour cet échantillon, les précipités $Zr_2(Fe,Ni)$ ont été observés à l'interface métal-oxyde à l'état oxydé du côté de l'oxyde et à l'état métallique du côté du métal. Les précipités $Zr(Fe,Cr)_2$ dans le Zircaloy-2 et le Zircaloy-4 présentent un comportement de type oxydation différée et aucune différence n'a été observée entre eux. Ce comportement à l'oxydation est similaire à celui observé pour les précipités correspondant dans les alliages binaires, les précipités $Zr_2(Fe,Ni)$ ayant une structure semblable aux précipités Zr_2Ni et les précipités $Zr(Fe,Cr)_2$ ayant la même structure que les précipités $ZrCr_2$.

18.10 Discussion

18.10.1 Influence de la préparation de la surface sur les résultats

Il a été observé que la préparation de la surface influence le comportement du précipité à l'oxydation sur la surface extérieure. Trois procédures différentes de préparation de surface ont été utilisées pour l'oxydation des échantillons. Cette section aborde les implications de chacune de ces procédures. Les procédés de polissage suivi d'un décapage suppriment les précipités de grande taille en contact avec la surface extérieure. Dans le cas des échantillons préparés par cette procédure, le comportement à l'oxydation des précipités ne peut être étudié que pour ceux qui ne sont pas en contact avec la surface après le décapage. La surface est rugueuse dans le cas d'alliages avec des précipités de grande taille. Les échantillons préparés avec des morceaux de diamant de 1 µm en suspension lors de la dernière étape de polissage ont donné lieu à une surface lisse sans attaque notable de précipités à la surface. Le polissage en dernière étape avec une solution contenant des particules de silice de 60 nm et un pH de 9,5 avec une tribofinition par vibreur a engendré la surface lisse avec la plus basse rugosité ; cependant une attaque des précipités a été observée.

18.10.2 Mesures EDS quantitatives

Quelques précautions ont dû être prises pour les mesures EDS quantitatives dans le MET. Le volume d'interaction du faisceau avec le faisceau d'électrons primaire est beaucoup plus petit que dans le MEB ; toutefois même dans ce cas le volume analyse devrait être homogène

en composition afin de permettre une quantification correcte. Puisque les mesures quantitatives EDS se concentrent principalement sur les sites des précipités, il est intéressant comment les différentes géométries matrice-précipités trouvées dans les échantillons de MET doivent être exploitées afin d'obtenir un maximum de données du point de vue de la fiabilité.

Pour les précipités trop petits pour voir leur teneur en oxygène mesurée directement du fait de la contribution de la matrice, une procédure de soustraction de la matrice de zirconium et de la contribution d'oxygène a été développée, en assumant une composition stœchiométrique du précipité et du zirconia.

Pour une quantification correcte de l'oxygène et les éléments d'alliage (Fe, Cr et Ni), plusieurs changements de paramètres dans la routine d'EDS ont du être appliqués. La routine optimale de quantification nécessite d'abord la quantification avec la ligne L du zirconium afin d'obtenir le montant correct d'oxygène dans l'oxyde et ensuite une quantification avec la ligne K du zirconium afin de déterminer le bon ratio zirconium/alliage. Cette procédure a été testée, et pour des petits précipités de $ZrCr_2$ la correction de l'influence de la matrice augmente le résultat sur la teneur en oxygène des précipités. L'influence de différents paramètres de l'échantillon, tels que l'épaisseur et la densité, sur la quantification obtenue, est discutée dans cette section en rapport avec les domaines possibles de ces paramètres et les erreurs introduites.

18.10.3 Changement de la topographie de surface Durant l'oxydation

Les mesures d'AGM sur la topographie de surface avant et après oxydation des surfaces polies ont révélé la formation de protubérances sur quelques alliages binaires. Dans ce cas, les observations seront discutées et des explications possibles ainsi qu'une approche du phénomène par un modèle ANSYS seront présentées. La hauteur des protubérances avec l'AFM sur les larges précipités en surface après oxydation des surfaces polies (non décapées) peut avoir plusieurs origines :

1. Un ratio de Pilling-Bedworth plus haut que celui de la matrice de zirconium
2. L'oxyde formé est plus épais au niveau des précipités en contact avec la surface extérieure
3. Les espèces diffusantes vers la surface extérieure.

Les hauteurs de protubérance observées expérimentalement peuvent être expliquées seulement avec les modèles ANSYS dans le cas d'un ratio de Pilling-Bedworth plus élevé ; il faut considérer les précipités complètement oxydés et la diffusion du fer vers la surface pour Zr1%Fe.

Pour ce calcul un ratio de Pilling-Bedworth hypothétique a été calculé en assumant une formation de zirconia pure et d'oxyde pur d'élément d'alliage, les valeurs obtenues sont 1,87 pour Zr_3Fe et Fe_2O_3 , 1,59 pour Zr_2Ni et la formation de NiO , 1,78 pour $ZrCr_2$ et la formation de Cr_2O_3 , et 1,51 pour Zr et la formation de ZrO_2 .

18.10.4 Influence des conditions d'oxydation sur l'oxydation de précipité

La pression n'a pas été identifiée comme ayant une influence sensible sur le comportement à l'oxydation des précipités. Puisque seuls les échantillons oxydés à 415°C ont été caractérisés, aucune donnée microstructurale n'est disponible et ne peut être utilisée pour l'étude de la température sur le comportement des précipités à l'oxydation.

18.10.5 Le comportement des précipités à l'oxydation

18.10.5.1 Le comportement des précipités à l'oxydation dans l'oxyde des alliages binaires

La tendance à l'oxydation observée (Tableau 33) pour les précipités qui ne sont pas en contact avec la surface externe est la suivante : $Zr_3Fe \approx Zr_2Ni \approx$ matrice de $Zr > \beta-Nb \approx ZrCr_2$, représentée aussi schématiquement par la Figure 127. En comparant les phénomènes observés et les différents types de précipités, une classification du comportement des précipités à l'oxydation dans les trois catégories suivantes couvre toutes les observations microstructurales de cette étude :

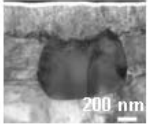
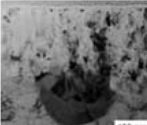
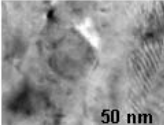
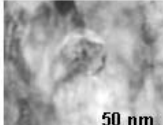
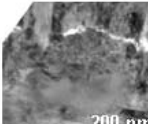
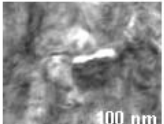
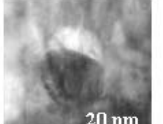
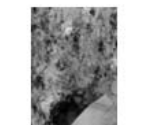


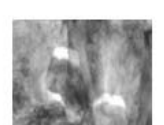

1. Pour les alliages de $Zr1\%Fe$ et $Zr1\%Ni$, les précipités en contact avec la surface extérieure montrent une vitesse d'oxydation apparente plus élevée que pour la matrice de zirconium, résultant en une protubérance de l'oxyde à la surface et une interface métal-oxyde ondulée. Ce comportement peut être associé au procédé de nucléation des nodules. Les précipités qui ne sont pas en contact avec la surface extérieure s'oxydent avec une vitesse proche de celle de la matrice de zirconium environnante (Zr_3Fe & Zr_2Ni).
2. L'élément d'alliage diffuse vers la surface extérieure et forme un oxyde pur ($Zr1\%Fe$)
3. Pour les alliages $Zr1\%Cr$ et $Zr0,6\%Nb$, les précipités s'oxydent après la matrice et une fois qu'ils sont entourés par l'oxyde proche de l'interface ($\beta-Nb$ & $ZrCr_2$).

Les précipités dans le $Zr1\%Cr$ et $Zr0,6\% Nb$ affichent des concentrations en oxygène plus basses que les matrices d'oxyde environnantes du fait de leur faible taille, et l'état métallique des précipités avec diffraction par électron n'a pas pu être confirmé. Des fissures en forme de croissant au-dessus des précipités faisant face à la surface extérieure ont été observées dans le cas du $Zr1\%Cr$ et $Zr0,6\%Nb$. Il est à noter que ces fissures n'ont pas été observées dans le cas du $Zr1\%Fe$ et $Zr1\%Ni$. Il est suggéré que ces fissures sont le résultat d'une oxydation retardée des précipités, puisqu'elles ont été observées seulement dans le cas des précipités avec une teneur en oxygène dans l'oxyde relativement basse.

18.10.5.2 Fissures sur les précipités présentant une oxydation retardée

La taille des fissures présentées au dessus des précipités affichant une oxydation retardée a été étudiée dans le cadre de l'expansion de la matrice durant l'oxydation. Les hauteurs de fissures possibles pour les différents cas envisageables (par exemple l'expansion isotropique, unidirectionnelle, avec et sans oxydation de précipités) ont été comparées avec les données expérimentales. La comparaison a montré que les hauteurs des fissures sont proches du modèle pour une expansion isotropique de la matrice pendant oxydation. Le procédé de préparation avec la sonde ionique focalisée a plus tendance à ouvrir les fissures qu'à les refermer, ce qui indique que le modèle avec les hauteurs de fissures similaires ou inférieures à celles mesurées expérimentalement décrivent au mieux la situation réelle.

Tableau 33: Vue d'ensemble du comportement des précipités à l'oxydation au niveau de l'interface métal-oxyde

	Zr1%Fe	Zr1%Ni	Zr1%Cr	Zr0,6%Nb
in situ (ESEM) 130 Pa 1 heure Vapeur				
autoclave 0.1 MPa 3 jours Air				
autoclave 0.1 MPa 3 jours Vapeur				55 days
autoclave 10.5 MPa 110 jours vapeur				

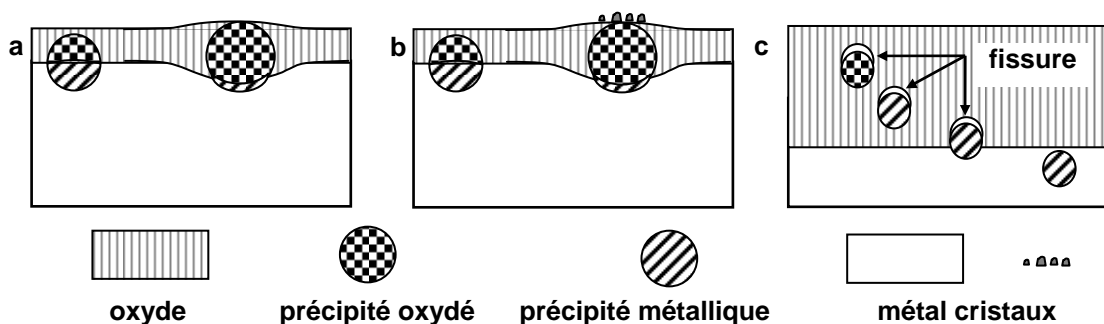


Figure 127: Vue schématique de l'interface métal-oxyde et de l'état d'oxydation du précipité (a) comportement à l'oxydation des précipités observé pour Zr_3Fe & Zr_2Ni , (b) formation de cristaux d'oxyde tels qu'observés pour le Zr_3Fe , (c) comportement à l'oxydation des précipités observé pour $ZrCr_2$ et $\beta-Nb$.

18.10.5.3 Paramètres susceptibles d'affecter le comportement à l'oxydation des précipités

Les paramètres influençant le comportement à l'oxydation des précipités, et qui ont été suggérés auparavant, sont la taille de précipité et la structure du cristal. Dans cette étude, le ratio de teneur zirconium/élément d'alliage pour les précipités et l'énergie libre d'oxydation par molécule d'oxygène dans les précipités oxydés ont été suggérés comme paramètres possibles.

La comparaison avec la littérature et les résultats obtenus ont fait de la taille des précipités et de la structure cristalline des paramètres improbables, puisqu'aucune corrélation entre les deux paramètres et le comportement à l'oxydation des précipités n'a pu être observée. Dans le cas du ratio atomique zirconium/élément d'alliage dans les précipités déterminant le comportement à l'oxydation des précipités, tous les précipités avec un ratio de 0,5 ou au-delà ($ZrCr_2$, $Zr(Fe,Cr)_2$, $Zr(Fe,V)_2$ et $Zr(Fe,Nb)_2$ et β -Nb (20%Zr)) ont présenté une oxydation retardée. Pour Zr_2M (ratio de 2, par exemple le cas du Zr_2Ni , $Zr_2(Fe,Ni)$ et $(Zr,Nb)_2Fe$) et des teneurs en Zr plus élevées dans les précipités (Zr_3Fe), une oxydation similaire à celle de la matrice de zirconium environnante a été observée. Aussi dans le cas de l'énergie libre d'oxydation par molécule d'oxygène dans les précipités oxydés, une corrélation entre le comportement à l'oxydation observé et un classement de l'énergie libre calculée a été trouvée. Les deux derniers critères sont seulement en désaccord sur la prédiction du comportement à l'oxydation de ZrV_2 et Zr_2Cu (Tableau 34 et Figure 128).

18.10.6 Oxydation des précipités à la surface

Les précipités en contact avec la surface extérieure montrent une oxydation favorable par rapport à la matrice de zirconium environnante, ce qui s'exprime en un oxyde localement plus épais (solution neutre avec morceaux de diamants sur la surface \rightarrow n'induit aucune modification majeure de la surface). Ils présentent une oxydation plus rapide que la matrice de zirconium environnante avec un oxyde localement plus épais (Figure 127). Pour les écailles d'oxydes formés pendant les expériences in situ, une ondulation accrue de l'interface métal-oxyde a été observée, en tant que conséquence de l'oxyde plus épais au niveau des précipités oxydés.

18.10.7 Formation d'oxyde de fer à la surface

L'oxyde de fer en forme de petits cristaux sur la surface au-dessus des précipités oxydés peut être déjà observé après moins d'une heure d'oxydation et le montant d'oxyde de fer augmente avec le temps d'oxydation (Figure 129). Parallèlement à l'augmentation du montant d'oxyde de fer à la surface, la teneur en fer des précipités oxydés décroît après 110 jours d'oxydation. Il a été observé que les précipités avec de grands cristaux d'oxyde de fer sur la surface sont complètement pauvres en fer. Ce phénomène de formation d'oxyde de fer a été clairement observé dans des études précédentes et l'oxyde de fer a été identifié comme de la magnétite et hématite, mais la forme dans laquelle l'oxyde de fer était présent n'avait pas pu être montrée, puisque les études plus vieilles étaient soit électrochimiques sans aucune résolution latérale ou leur technique fournissait une information en résolution trop faible pour permettre l'identification de cristaux d'oxydes de fer.

Tableau 34: Energie libre d'oxydation calculée pour les phases rencontrées dans les alliages de zirconium, normalisée au nombre d'atomes de métal dans l'intermétallique. Pour plus de détails concernant le calcul, se référer au texte.

phase	ratio Zr / élément d'alliage		ΔG_{ox} / kJ/(mols oxygène)		$\Delta H_{formation}$ / kJ/mol intermétallique		Etat de l'oxydation de précipité observe dans l'oxyde
	(1)	(2)	(1)	(2)	Diverses sources	Zircobase	
Zr-matrix	1	0	-965	-965	-	-	-
Zr ₃ Fe	3	1	-867	-869	-13.5 t	-3.1	oxydé
Zr ₂ Ni	2	1	-830	-833	-31.2 e	-24.2	oxydé
ZrCr ₂	1	2	-757	-755	-14.5 e	-18.7	oxydation retardée
β -Nb (20%Zr)	1	4	-727	-728	3-4 t	10.6 *	oxydation retardée
β -Zr (20%Nb)	4	1	-891	-891	3-4 t	-	oxydé
Zr(Fe,Cr) ₂	1	2	-717	-704	-	-31.6	oxydation retardée
Zr ₂ (Fe,Ni)	2	1	-839	-833	-	-15.2	oxydé
Zr(Fe,V) ₂	1	2	-746	-746	-	-	oxydation retardée
Zr(Fe,Nb) ₂	1	2	-703	-702	-	-3.4	oxydation retardée
(Zr,Nb) ₂ Fe	2	1	-826	-825	-	-4.7	oxydé
ZrV ₂	1	2	-818	-824	-5.0 t	9.1 *	Non disponible
Zr ₂ Cu	2	1	-805	-815	-25.0 t	-	Non disponible
ZrMo ₂	1	2	-628	-630	-8.0 t	-	Non disponible

* dénote les enthalpies de formation positives pour les phases métastables depuis la Zircobase, qui sont présentes à cause des contraintes thermodynamiques. Enthalpie de formation : e dénote les valeurs expérimentales et t les valeurs théoriques. (1) dénote les valeurs d'énergie libre d'oxydation dérivées en utilisant diverses sources pour l'enthalpie de formation et (2) les enthalpies de formation à 415°C depuis la Zircobase.

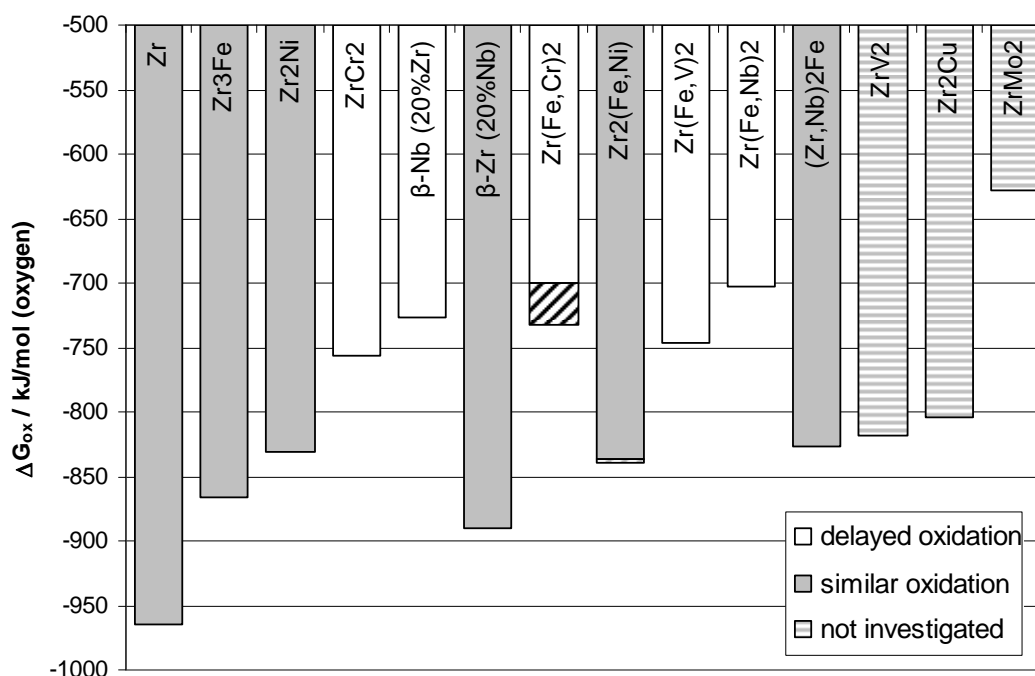


Figure 128: Energie libre d'oxydation pour les différentes phases rencontrées dans les précipités d'alliages de zirconium normalisée au nombre de molécules d'oxygène dans le précipité oxydé du Tableau 34. Les pointilles marquent la limite en énergie pour laquelle un changement depuis une oxydation retardée vers une oxydation similaire à la matrice est observé. Les données affichées sont issues du Tableau 34 (colonne d'énergie libre de gauche).

18.10.8 Migration de fer vers la surface

Une estimation grossière du coefficient de diffusion du fer depuis les précipités vers la surface pour différents temps d'oxydation a fourni des coefficients de diffusion (tableau 8) similaires au seul cas reporté de diffusion de zirconia formée sur un alliage de zirconium durant l'oxydation.

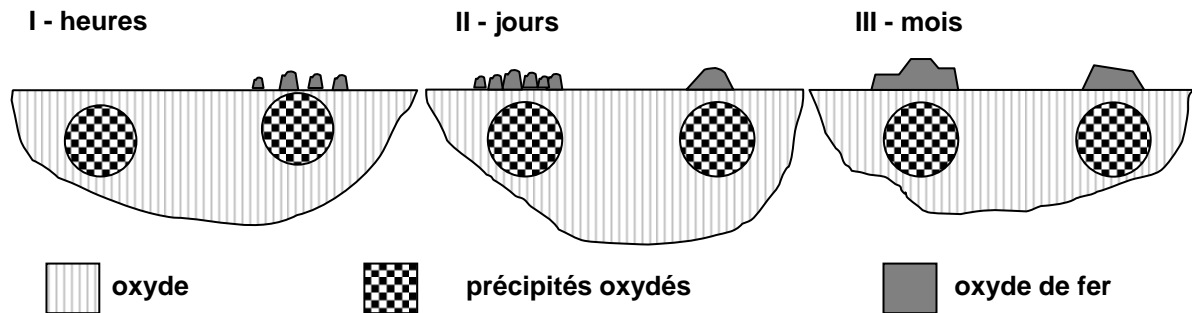


Figure 129: Diagramme schématique montrant la formation d'oxyde de fer à la surface de $Zr1\%Fe$ en fonction du temps : (a) le fer commence à se séparer de la surface en oxyde pur et forme des petits cristaux au-dessus des précipités oxydés, (b) la densité des petites particules de fer au-dessus des précipités augmente et plus de cristaux peuvent être observés, (c) de grands cristaux d'oxyde de fer sont formés, certains d'entre eux sont des cristaux singuliers.

Tableau 35: Coefficient de diffusion estimé pour les différentes conditions et durées d'oxydation.

Durée d'oxydation	pression	D / cm ² /sec
1 heure	130 Pa	$1.3 \cdot 10^{-15}$
72 heures	0.1 MPa	$1.4 \cdot 10^{-15}$
72 heures	0.1 MPa	$8.8 \cdot 10^{-16}$
110 jours	10.5 MPa	$5.3 \cdot 10^{-16}$
Iltis et al. JNM 1995 400°C	10.3 MPa	$1.0 \cdot 10^{-15}$

18.11 Conclusions

Dans ce travail la microstructure des oxydes formés dans des alliages binaires de zirconium a été caractérisée afin d'étudier le comportement à l'oxydation des précipités et afin de comprendre l'influence des différents éléments d'alliage et conditions d'oxydation. Des alliages binaires de zirconium contenant 1 % de Fe, Cr, Ni ou bien 0,6 % de Nb ainsi que du zirconium pur et les alliages commerciaux Zircaloy-2 et Zircaloy-4 ont été étudiés après oxydation à 415°C dans différents environnements d'oxydation.

Les conditions étudiées incluent l'oxydation en autoclave dans un mélange d'air et de vapeur à pression ambiante (0,1 MPa) pendant des durées atteignant jusqu'à trois jours et dans la vapeur à 10,5 MPa pendant des durées atteignant jusqu'à 110 jours. L'oxydation a été examinée dans la vapeur d'eau à 130 Pa et 415°C pendant une heure in situ avec un microscope électronique à balayage environnemental.

La surface des échantillons a été caractérisée par microscopie électronique à balayage et analyse dispersive en énergie. De plus, la surface des échantillons oxydés dans un microscope électronique à balayage environnemental a été caractérisée par microscopie à force atomique.

La caractérisation microstructurale de l'oxyde a été réalisée par microscopie électronique à balayage, sonde ionique focalisée pour les préparations des sections transverses et normales et par microscopie électronique en transmission incluant l'analyse dispersive en énergie et spectroscopie des pertes d'énergie. L'évolution de la microstructure a été caractérisée pour les précipités dans l'oxyde et le comportement à l'oxydation déterminé.

Les conclusions s'articulent sur trois points :

- Explications possibles pour le comportement à l'oxydation des précipités,
- Morphologie de l'oxyde de fer observé sur la surface et
- Formation des protubérances sur la surface au-dessus des précipités oxydés.

1^{er} point: D'après les résultats de la caractérisation microstructurale de l'oxyde et des précipités dans les alliages binaires et commerciaux, l'existence de deux familles de comportements à l'oxydation de précipités est mise en évidence. :

1. La première famille se compose des précipités de Zr_3Fe et de Zr_2Ni ainsi que les précipités $Zr_2(Fe,Ni)$, qui présentent une oxydation similaire à celle de la matrice de zirconium environnante.
2. La seconde famille comprend les précipités $ZrCr_2$ et $\beta-Nb$, aussi bien que les précipités $Zr(Fe,Cr)_2$, qui présentent une oxydation retardée par rapport à celle de la matrice de zirconium.

Le comportement à l'oxydation des précipités est corrélé à leur composition :

- Ratio zirconium / élément d'alliage, ou
- Energie libre d'oxydation par molécule d'oxygène dans le précipité oxydé.

Le ratio zirconium / élément d'alliage est de 2 ou au-delà pour les précipités présentant une oxydation similaire à celle de la matrice de zirconium, et de 0,5 ou en-deçà pour ceux présentant une oxydation retardée par rapport à celle de la matrice de zirconium.

L'énergie libre d'oxydation par molécule d'oxygène dans le précipité oxydé a été estimée par la loi de Hess, en utilisant l'enthalpie de formation des précipités et des valeurs tabulées pour l'énergie libre d'oxydation des éléments formant les intermétalliques. Le comportement à l'oxydation des précipités, observé dans les autres études de la littérature pour les autres précipités d'intérêt caractérisés jusqu'à présent, est en accord avec les deux familles de précipités reportées et les deux paramètres identifiés précédemment cités pour lesquels une corrélation a été établie avec le comportement à l'oxydation des précipités.

De point de vue microstructurale, la matrice d'oxyde était colonnaire pour tous les environnements, et seule la porosité en forme de fissure était sensiblement accrue pour les échantillons oxydés à haute pression pour des temps plus longs. Ces fissures observées dans les oxydes sont longues, jusqu'à plusieurs micromètres, et orientées parallèlement à l'interface métal-oxyde. Les petites fissures formées à l'interface ZrO_2 -précipité dans les cas du Zr 1%Cr et Zr 0,6%Nb pourraient agir comme sites de formation bien dispersés pour les fissures plus larges, améliorant la stabilité mécanique (accommodation à l'effort) de l'oxyde et donc une résistance à la corrosion des alliages. La variation entre les matériaux présentant une oxydation des précipités différente est faible dans les conditions étudiées ; cependant, dans les conditions en réacteur sous irradiation, ces différences pourraient bien être considérables en ce qui concerne la performance du matériau de la gaine.

2^{ème} point: Dans le cas du Zr 1%Fe, des cristaux d'oxyde de fer pur ont été trouvés pour toutes les conditions à la surface au-dessus des précipités oxydés. Leur taille a augmenté de plusieurs dizaines de nanomètres après une heure d'oxydation jusqu'à 1 micromètre après 110 jours d'oxydation. L'oxyde de fer a été identifié sous la forme magnétite cubique. L'impact de l'oxyde de fer sur la surface envers la résistance à l'oxydation n'a pas pu être clarifié dans ce projet.

3^{ème} point: Des protubérances ont été observées par MFA au-dessus des précipités oxydés en contact avec la surface extérieure pour les échantillons de Zr 1%Fe et Zr 1%Ni. Sous les protubérances, un oxyde plus épais a été détecté localement sur les échantillons en section transverse et MET. Aucune protubérance large associée aux précipités n'a pu être observée dans les cas du Zr 1%Cr, Zr 0,6%Nb et zirconium pur avec absence de précipités ou présence de précipités en dessous de 100 nanomètres de diamètre. Pour tous les matériaux étudiés la rugosité globale a augmenté depuis la surface polie vers la surface oxydée ; les protubérances ont été liées sans ambiguïté aux précipités oxydés de plus grande taille, en contact avec la surface extérieure. Les protubérances sont très probablement dues à un ratio de Pilling-Bedworth plus élevé pour les précipités que pour le zirconium pur, puisque l'oxyde plus épais au niveau des protubérances ne justifie pas la hauteur de dernier comme seul paramètre contribuant à cet effet. Dans le cas du Zr 1%Fe, la présence d'oxyde de fer formé sur la surface n'est pas suffisante pour expliquer sans aucune autre contribution les hauteurs des protubérances observées. Les ratios de Pilling-Bedworth des précipités, estimés en assumant la formation d'oxydes d'éléments purs, décrivent très convenablement les hauteurs de protubérances observées expérimentalement, en prenant en compte la taille des précipités et la formation d'oxyde de fer.

Il a donc été trouvé que :

- le comportement à l'oxydation des précipités dépend de la composition, en général deux familles de comportements sont mises en évidence: a- une oxydation retardée ou b-une oxydation similaire par rapport à celle de la matrice de zirconium,
- les précipités présentent un ratio de Pilling-Bedworth différent de celui de la matrice de zirconium, ce qui affecte la formation des protubérances.
- les précipités proches de la surface qui contiennent du fer forment des cristaux d'oxyde de fer purs à la surface.

18.12 Perspectives

La compréhension du comportement de l'oxydation locale des précipités et son impact sur les propriétés générales de l'alliage de zirconium durant l'oxydation peuvent encore être améliorées. Jusqu'à présent, il est impossible d'obtenir une prédiction fiable à long terme du comportement des alliages de zirconium dans un environnement corrosif dans un réacteur nucléaire. Même en ce qui concerne l'oxydation à court terme dans un autoclave, le comportement à l'oxydation ne peut pas encore être entièrement expliqué.

Pour un prochain travail sur le comportement des précipités à l'oxydation, l'investigation des alliages binaires de zirconium contenant du cuivre ou du vanadium présentent un intérêt. Ces deux éléments d'alliage devraient former des précipités qui ne remplissent pas les critères prévoyant le comportement d'oxydation des précipités pour tous les types de précipités déjà caractérisés. Afin de déterminer s'il existe une énergie libre critique fixée pour laquelle le comportement à l'oxydation change, des précipités avec une énergie libre d'oxydation située entre celle du $ZrCr_2$ et Zr_2Ni doivent être testés. Ces deux alliages binaires intermétalliques présentent la plus faible différence en énergie libre d'oxydation et se distinguent du comportement à l'oxydation selon les calculs effectués. Les précipités possibles d'avoir une énergie libre d'oxydation comprise entre celle du $ZrCr_2$ et du Zr_2Ni sont ZrV_2 et Zr_2Cu et $Zr(V,Cr)_2$ avec différents ratios Cr / V.